

Bachelor of Science Thesis title

“Thermochromic Vanadium Dioxide for energy saving applications: A study on solution-based synthetic approach”

University of Crete

Department of Chemistry

and

Foundation for Research and Technology - Hellas

Institute of Electronic Structure and Laser

Supervisors: *Prof. Anastasiadis S., department of chemistry*

Prof. Kiriakidis G., department of physics

Dr. Binas V., Forth-IESL

Laboratory: *TCMD, Forth-IESL*

B.Sc. Student:	Leila Zouridi
Studies:	Chemistry
Student ID:	1579
Birth date:	1993/08/02
e-mail:	l.zouridi@campus.fct.unl.pt

Heraklion, October 2017

[page intentionally left blank]

TABLE OF CONTENTS	i - v
Abstract	1
Περίληψη	3
List of Abbreviations and Symbols	5
CHAPTER 1. Introduction - Literature Review	7
1.1 Motivation.....	7
1.1.1. Thermochemical Materials	7
1.1.2. Research Challenge	8
1.2 Properties of Vanadium Oxides	10
1.2.1. Vanadium (V) Oxide.....	10
1.2.2. Vanadium (IV) Oxide.....	11
1.2.2.a Structural properties of VO ₂	11
1.2.2.b Electronic properties of VO ₂	14
1.2.2.c Electrical properties of VO ₂	16
1.2.2.d Thermal properties of VO ₂	17
1.2.2.e Optical properties of VO ₂	17
1.2.3. Reduction of V ₂ O ₅ to VO ₂ and its polymorphs complications	19
1.2.4. Doping of Vanadium (IV) Oxide	25
1.3 Technological applications of Thermochemical Thin Films	27
CHAPTER 2. Methodology and Protocol	28
2.1 Reagents/Materials	28
2.2 Synthetic Procedure.....	28
2.2.1. Changing Parameters.....	29
2.2.2. The Hydrothermal Method.....	29
2.3 Characterization Techniques.....	31
2.3.1. Introduction	31
2.3.2 X-Ray diffraction (XRD).....	31
2.3.3 Differential Scanning Calorimetry (DSC).....	33
2.3.4 Scanning Electron Microscope (SEM).....	33
2.3.5 Energy-Dispersive X-Ray Spectroscopy (EDX)	35
2.3.6 Thermogravimetric Analysis (TGA)	35
CHAPTER 3. Experimental Results	37
3.1 Parameter: Molar Ratio of precursors.....	38
3.1.1. Before annealing (“as obtained” products).....	38
3.1.1.a. XRD patterns for the as obtained at 18 g/L V ₂ O ₅ concentration	38
3.1.1.b. XRD patterns for the as obtained at 9 g/L V ₂ O ₅ concentration	39
3.1.1.c. XRD patterns for the as obtained at 3 g/L V ₂ O ₅ concentration.....	40
3.1.2. After annealing (“final” products).....	41

3.1.2.a.	XRD patterns for the final products at 18 g/L V ₂ O ₅ concentration	41
3.1.2.b.	XRD patterns for the final products at 9 g/L V ₂ O ₅ concentration	42
3.1.2.c.	XRD patterns for the final products at 3 g/L V ₂ O ₅ concentration	43
3.2	Parameter: V ₂ O ₅ concentration	44
3.2.1.	Before annealing (“as obtained” products)	44
3.2.1.a.	XRD patterns for the as obtained at 1:1.5 molar ratio	44
3.2.1.b.	XRD patterns for the as obtained at 1:2 molar ratio.....	45
3.2.1.c.	XRD patterns for the as obtained at 1:3 molar ratio.....	45
3.2.1.d.	XRD patterns for the as obtained at 1:4 molar ratio	46
3.2.1.e.	XRD patterns for the as obtained at 1:6 molar ratio	46
3.2.1.f.	XRD patterns for the as obtained at 1:8 molar ratio	47
3.2.1.g.	XRD patterns for the as obtained at 1:10 molar ratio	47
3.2.1.h.	XRD patterns for the as obtained at 1:12 molar ratio	48
3.2.2.	After annealing (“final” products).....	48
3.2.2.a.	XRD patterns for the final products at 1:1.5 molar ratio.....	48
3.2.2.b.	XRD patterns for the final products at 1:2 molar ratio	49
3.2.2.c.	XRD patterns for the final products at 1:3 molar ratio	49
3.2.2.d.	XRD patterns for the final products at 1:4 molar ratio	50
3.2.2.e.	XRD patterns for the final products at 1:6 molar ratio	50
3.2.2.f.	XRD patterns for the final products at 1:8 molar ratio	51
3.2.2.g.	XRD patterns for the final products at 1:10 molar ratio.....	52
3.2.2.h.	XRD patterns for the final products at 1:12 molar ratio	52
3.3	Conclusions over the effect of the synthetic reagents concentrations	53
3.4	Parameter: synthesis volume	55
3.4.1.	Before annealing (“as obtained” products)	56
3.4.2.	After annealing (“final” products).....	57
3.5	Parameter: pH of synthesis	58
3.6	Effect of additives	60
3.6.1.	Effect of additive Sulfuric Acid, H ₂ SO ₄	60
3.6.2.	Effect of additive additive Thiourea, SC(NH ₂) ₂	62
3.7	Effect of dopants	65
3.7.1.	Effect of doping with Tungstic Acid, H ₂ WO ₄	65
3.7.2.	Effect of doping with Magnesium Sulfate, MgSO ₄	69
3.7.3.	Effect of co -doping with H ₂ WO ₄ and MgSO ₄	72
3.8	Structural transition properties	74
3.8.1.	DSC results of basic configurations	75
3.8.2.	DSC results of configurations with additives	81
3.8.3.	DSC results of configurations with dopants	84
3.8.3.	Conclusions over the structural transition.....	90
3.9	Elemental analysis.....	93
3.9.1.	EDX results of W-doped samples.....	93
3.9.2.	EDX results of Mg-doped samples.....	98
3.9.3.	EDX results of W, Mg co-doped samples.....	102

3.10	Morphology	105
3.10.1.	SEM results on the thiourea effect.....	105
3.10.2.	SEM results on W-doping effect	106
3.10.3.	SEM results on Mg-doping effect.....	108
3.10.4.	SEM results on W, Mg co-doping effect.....	109
3.10.5.	Conclusions over morphology of samples.....	110
3.11	Thermal decomposition and annealing step	112
CHAPTER 4. Conclusions		114
4.1	Summary and conclusion.....	114
4.2	Future suggestions - perspectives	115
REFERENCES		117
CURRICULUM VITAE		125

[page intentionally left blank]

ABSTRACT

Vanadium dioxide is one of the most promising thermochromic solid-state materials. It has potential application in the field of smart windows and glazings, due to its unique optical properties related to its inherent and reversible structural transition at a critical temperature of $T_c = 68\text{ }^\circ\text{C}$. In this thesis we present the motivations, challenges and results of our project “Thermochromic Vanadium Dioxide for energy saving applications: A study on solution-based synthetic approach”. In our hydrothermal synthesis approach, we started with reagents V_2O_5 as the vanadium source and oxalic acid as its reducing agent. Then a study of the effects of different parameters on the solution-based synthesis of VO_2 was conducted by focusing on each parameter and characterizing the resulting products. We preferred to experiment with the chemical parameters of our synthesis, such as reagents concentration (molar ratio of precursors and V_2O_5 density in solution), synthesis volume (20 vs 40 mL), synthesis pH (acidic to basic), effect of additives (H_2SO_4 and thiourea) and effect of dopants (W and Mg). The as obtained products were characterized by x-ray diffraction (XRD), differential scanning calorimetry (DSC), field emission scanning electron microscopy (SEM), energy dispersive x-ray (EDX) and thermogravimetric analysis (TGA). During the hydrothermal reduction, V_2O_5 was reduced into different vanadium oxides and also into different VO_2 crystalline polymorphs. Then, in order to achieve better crystallinity and to fully convert the products to the desired thermochromic polymorph, our samples were annealed in a furnace under constant nitrogen gas flow, to avoid the oxidation of our samples. The final products were also characterized by the same techniques and results were discussed in comparison to the as obtained data and the synthesis parameter changes. We achieved to produce powders of high crystallinity pure thermochromic VO_2 in high yields, and with good thermochromic properties with T_c ranging from $59\text{ }^\circ\text{C}$ to $67\text{ }^\circ\text{C}$ depending from the synthesis parameters configuration used. An optimized hydrothermal route for achieving better crystallinity products in high yields is proposed, and a possible explanation of the mechanism behind our synthesis is discussed.

Keywords: vanadium dioxide, thermochromic, synthesis, solution-based, hydrothermal, synthesis optimization, synthesis mechanism, chemical parameters, molar ratio, reagents concentration, pH, synthesis volume, additives, dopants, structural transition

[page intentionally left blank]

ΠΕΡΙΛΗΨΗ

Το διοξείδιο του Βαναδίου αποτελεί το πιο πολλά υποσχόμενο θερμοχρωμικό υλικό στερεάς κατάστασης. Οι πιθανές του εφαρμογές βρίσκονται στον τομέα των “έξυπνων” παραθύρων και τζαμιών, λόγω των μοναδικών του οπτικών ιδιοτήτων οι οποίες προέρχονται από την εγγενή και αναστρέψιμη δομική μετάβαση του σε μια κρίσιμη θερμοκρασία $T_c = 68 \text{ }^\circ\text{C}$. Σε αυτή την διατριβή παρουσιάζουμε τα κίνητρα, τις προκλήσεις και τα αποτελέσματα του πειραματικού μας σχεδίου με τίτλο “Θερμοχρωμικό Διοξείδιο του Βαναδίου για εφαρμογές στην εξοικονόμηση ενέργειας: Παραμετροποίηση της μεθοδολογίας σύνθεσης σε διάλυμα”. Για την υδροθερμική σύνθεση του υλικού χρησιμοποιήσαμε τα αντιδραστήρια V_2O_5 ως πηγή βαναδίου και οξαλικό οξύ ως αναγωγικό παράγωγα. Στην συνέχεια μελετήθηκε η επίδραση από διαφορετικές παραμέτρους στην σύνθεση με βάση το διάλυμα του VO_2 , εστιάζοντας σε κάθε παράμετρο και χαρακτηρίζοντας τα προϊόντα. Προτιμήσαμε να εξετάσουμε τις χημικές παραμέτρους της σύνθεσης μας, όπως για παράδειγμα οι συγκεντρώσεις των αντιδρώντων (μοριακή αναλογία των πρόδρομων ενώσεων και πυκνότητα του V_2O_5 στο διάλυμα), ο όγκος της σύνθεσης (20 vs 40 mL), το pH της σύνθεσης (από όξινο έως βασικό), η επίδραση πρόσθετων αντιδραστηρίων (H_2SO_4 και θειουρία) και η επίδραση των προσμείξεων (W και Mg). Τα “ως ληφθέντα” προϊόντα χαρακτηρίστηκαν από τις τεχνικές: x-ray diffraction (XRD), differential scanning calorimetry (DSC), field emission scanning electron microscopy (SEM), energy dispersive x-ray (EDX) and thermogravimetric analysis (TGA). Κατά την διάρκεια της υδροθερμικής αναγωγής του V_2O_5 μετατράπηκε σε διαφορετικά οξειδία του βαναδίου καθώς και σε διαφορετικά κρυσταλλικά πολύμορφα του VO_2 . Έπειτα, προκειμένου να πετύχουμε καλύτερη κρυσταλλικότητα στα υλικά και να μετατρέψουμε τα προϊόντα μας πλήρως στο επιθυμητό θερμοχρωμικό πολύμορφο, τα υλικά μας εκτέθηκαν σε υψηλές θερμοκρασίες σε ένα κατάλληλο φουρνο υπό ροή σταθερού αέριου αζώτου, ώστε να αποφύγουμε την οξειδωσή τους. Τα “τελικά” προϊόντα χαρακτηρίστηκαν επίσης με τις ίδιες τεχνικές και τα αποτελέσματα συζητήθηκαν συγκριτικά με τα δεδομένα από τα “ως ληφθέντα” και ως προς τις διαφορετικές συνθετικές παραμέτρους. Καταφέραμε να συνθέσουμε σε υψηλές αποδόσεις σκόνες υψηλής κρυσταλλικότητας καθαρού VO_2 , και με καλές θερμοχρωμικές ιδιότητες, T_c από $59 \text{ }^\circ\text{C}$ έως $67 \text{ }^\circ\text{C}$ αναλόγως την πειραματική πορεία διαφορετικών παραμέτρων. Στην εργασία αυτή, προτείνουμε μια βελτιστοποιημένη υδροθερμική πορεία για την σύνθεση προϊόντος καλής κρυσταλλικότητας σε καλές αποδόσεις και επιδιώκουμε να εξηγήσουμε τον μηχανισμό πίσω από τις χημικές διεργασίες.

Λέξεις κλειδιά: διοξείδιο του βαναδίου, θερμοχρωμισμός, σύνθεση, με βάση το διάλυμα, υδροθερμική μέθοδος, βελτιστοποίηση σύνθεσης, μηχανισμός σύνθεσης, χημικές παράμετροι, μοριακή αναλογία, συγκέντρωση αντιδραστηρίων, pH, όγκος σύνθεσης, πρόσθετα, προσμείξεις, δομική μετάβαση

[page intentionally left blank]

List of Abbreviations and Symbols

ox	Oxalic acid
VO ₂ (M)	Thermochromic Monoclinic Vanadium Dioxide
VO ₂ (R)	Thermochromic Rutilic Vanadium Dioxide
VO ₂ (B)	"Non-Thermochromic" Metastable Monoclinic Vanadium Dioxide
VO ₂ (A)	"Non-Thermochromic" Metastable Tetragonal Vanadium Dioxide
MIT	Metal-to-insulator Transition
SMT	Semiconductor-to-metal transition
IR	Infrared (spectra)
UV-Vis	Ultraviolet-visible (spectra)

[page intentionally left blank]

CHAPTER 1. Introduction - Literature Review

1.1 Motivation

The building sector contributes up to 30% of global annual green house gas emissions and consumes up to 40% of all energy.^[1.1.1] Some of that energy and emissions are to be attributed to inadequate heat insulation of the building. With windows capable of regulating solar/heat transmission for energy efficiency and comfort, also called smart windows, there is the potential to moderate the energy consumption of buildings.

1.1.1. Thermochromic Materials

“Chromeogenic” materials are those that exhibit changes in their optical properties due to some external stimulus. The most common of these are photochromic, thermochromic and electrochromic materials, where the stimuli are irradiation by light (photons), change in temperature, and an applied electric field, respectively. Thus, a thermochromic material changes colour upon reaching a characteristic ‘transition temperature’. In short, thermochromism is the temperature-dependent changes in the optical properties of a material. It involves a structural phase change at the transition temperature, which [phase change] can be first- or second-order in nature, and may be reversible or irreversible, as governed by the thermodynamics of the system. Thermochromism offers potential for technological applications, for example, in thermometers (fever indicators, gadgets, design applications, etc), temperature sensors for safety, in laser marking, imaging, warning signals, memory devices, surface coating and even smart windows.^[1.1.2]

The most widely studied thermochromic material for applications to smart windows is VO_2 with the monoclinic (M) phase (shown as $\text{VO}_2(\text{M})$), which is able to execute a reversible phase transition at a critical temperature ($T_c = 68^\circ\text{C}$): below T_c the material is monoclinic, insulating and quite infrared transparent ($\text{VO}_2(\text{M})$), and above T_c it is tetragonal, metallic and infrared reflecting ($\text{VO}_2(\text{R})$). More on the properties of vanadium oxides are noted at the section 1.2.

1.1.3. Research Challenge

Vanadium Dioxide is been studied for its thermochromic phase transition since 1959 when F. J. Morin reported the temperature dependent metal-insulator transition occurring in the material.^[1.1.3]

Since then a lot of progress have been made on understanding the properties of this material, and how to synthesize it. Still some challenges remain. First of all, the ability of vanadium atoms to possess multiple stable oxidation states results in the easy conversion between oxides of different stoichiometry by oxidation or reduction, thus making their study more complicated with all various oxides along with the many crystal phases of each one playing a role on the chemistry and synthesis of our material.

Moreover, VO₂-based films with high thermochromic quality can be deposited by various mostly physical deposition methods in laboratory. Some of these include pulsed laser deposition (PLD)^[1.1.31], reactive sputtering in oxygen environment from a V target^[1.1.32], reactive evaporation^[1.1.33], sol-gel method^[1.1.34], chemical vapor deposition (CVD)^[1.1.35], and various post-deposition annealing techniques where either over-oxidized phases such as V₂O₅ are reduced to VO₂ by annealing^[1.1.36] or pure V films are annealed in oxygen to achieve the VO₂ stoichiometry^[1.1.37].

However, there are some barriers for these techniques which restrict the production of these films in low-cost and large- scale. To solve the problem, the route for the synthesis of VO₂/polymer composite films has been proposed, by dispersing solid vanadium dioxide in a liquid polymer and then solidified as an active film. Nowadays, polymer science has been greatly developed. Up to now, highly transparent and durable films are commercially available and a variety of functional fillers have been widely used. While the VO₂ powder is considered as a kind of filler, it can be asserted that all other technical problems have been solved except the availability of high quality filler. Therefore, the fabrication of low-cost and large-scale VO₂(M) powders is crucial for materials scientists.^[1.1.4]

So far, various technologies have been developed for producing VO₂(M) powders. These methods generally can be cataloged to reduction of high-valance vanadium oxides^{[1.1.5],[1.1.6]}, pyrolysis of vanadium containing precursor^{[1.1.7],[1.1.8]}, soft-chemical route^{[1.1.9],[1.1.10]}, transforming from VO₂(B)^{[1.1.11],[1.1.12]} or VO₂(A)^[1.1.13] to VO₂(M) at elevated temperatures, direct confined-space combustion^[1.1.14], sol-gel synthesis^[1.1.15] and hydrothermal synthesis^[1.1.16-1.1.23]. However, most of them are much complex, low efficiency and high cost. Besides, their experimental conditions are very harsh and energy-consuming. Thus, they are not suitable for coating the surface of substrates with a large

surface area and industrial applications. On the contrary, in recent years, the hydrothermal synthesis has been paid increasing attention owing to its simple route, low cost, large-scale and mass production.

Various publications has reported success in synthesizing, isolating and characterizing thermochromic vanadium dioxide particles by a hydrothermal synthetic route. Still, in order to acquire the right VO₂ crystal phase in a one-step hydrothermal procedure, most either use highly-toxic and not easy-to-handle chemical reagents, like hydrazine, or high temperatures during the hydrothermal step and prolonged reaction times.^{[1.1.18],[1.1.24],[1.1.25],[1.1.26]} Most of the published work requires more than one step for the successful synthesis of thermochromic VO₂, and the majority of the experimentation has focused on the physical parameters of the procedure (duration and temperature of hydrothermal step and/or of further steps needed).^{[1.1.27],[1.1.28],[1.1.29]}

In the authors' best knowledge, very few works have been published experimenting with the chemical parameters of the hydrothermal synthesis.^{[1.1.4],[1.1.23],[1.1.28],[1.1.30]} Therefore, with this project our aim was to further experiment with the chemical parameters of the synthetic procedure, in particular the hydrothermal step, in order to optimize the synthetic route to achieve better yields of a good quality thermochromic vanadium dioxide.

1.2 Properties of Vanadium and its Oxides

Vanadium is a transition metal with an atomic number 23 and atomic mass of $50.9415 \text{ g}\cdot\text{mol}^{-1}$. The melting point of vanadium is $1910 \text{ }^\circ\text{C}$ and its boiling point is $3407 \text{ }^\circ\text{C}$. There are five isotopes of vanadium. Its electronic configuration is $[\text{Ar}] 3d^3 4s^2$. The vanadium is a rare, soft, ductile gray-white element found combined in certain minerals and used mainly to produce certain alloys. Common oxidation states of this element include +2, +3, +4 and +5. After vanadium has been oxidized, it can produce different vanadium oxides with different colours, transition temperature, melting point and boiling point.^{[1.2.0],[1.2.1]} Table 1.1 shows a list of Vanadium Oxides and some of their properties.

Vanadium Oxide	Oxidation state of Vanadium	Colour	Critical temperature of phase transition ($^\circ\text{C}$)
V_2O_5 orthorhombic	+5	orange	257
V_3O_7 monoclinic	+4.6		
V_6O_{13} monoclinic	+4.3		-123
VO_2 (M) monoclinic	+4	blue black	68
V_2O_3 monoclinic	+3	Black	-105

Table 1.1. Properties of Vanadium Oxides

In the following sections we will discuss the two most important oxides for this project, vanadium (V) oxide and, of course, vanadium (IV) oxide.

1.2.1. Vanadium (V) Oxide, V_2O_5

Vanadium (V) oxide, V_2O_5 , with $M_r = 181.88 \text{ amu}$, is orange yellow in color and is traded as a solid in the form of fused flakes or powder. The vanadium cation of V_2O_5 has a high oxidation state (+5) and the material can act both as an amphoteric oxide and an oxidizing agent. From the industrial perspective, it is the most important compound of vanadium, being principal precursor to alloys of vanadium and is a widely used industrial catalyst. At normal temperature and pressure V_2O_5 is thermodynamically most stable.^[1.2.1]

Regarding their structure vanadium ions in V_2O_5 may be considered to be either distorted trigonal bi-pyramid (five V-O bond lengths of $1.58\text{-}2.02 \text{ \AA}$), distorted tetragonal pyramid or a distorted octahedron (the sixth V-O bond length of 2.79 \AA). On Figure 1.1 (a) the idealized structure of trigonal bi-pyramid V_2O_5 , (b) the perspective view of the orthorhombic V_2O_5 crystal lattice and (c) the oxygen

coordination around vanadium atom of the orthorhombic V_2O_5 , are presented.^[1,2,2] The common orthorhombic V_2O_5 phase consists of layers of edge- and corner-sharing octahedra along the ab planes. These layers are connected at corners to give a three-dimensional lattice pattern. Regarding its thermochromic properties it undergoes a Mott and phase transition at 257 °C.

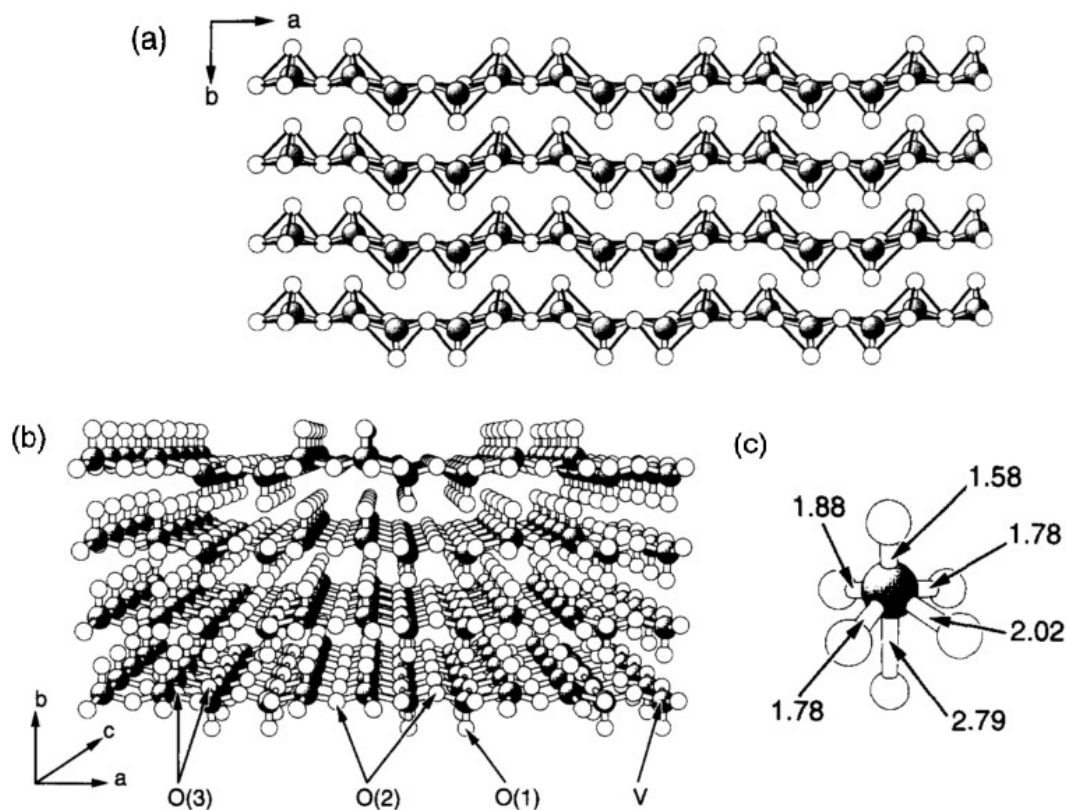


Figure 1.1: (a) Idealized structure of V_2O_5 of $(0\ 0\ 1)$ plane projection drawn as trigonal bi-pyramids. (b) Perspective view of the orthorhombic V_2O_5 crystal lattice. The location of the vanadium centers, V, and surface oxygen sites, O(1)-O(3), are indicated and labeled. (c) Oxygen coordination around vanadium atom of the orthorhombic V_2O_5 . The V-O distances are written in Å. ^[1,2,2]

1.2.2. Vanadium (IV) Oxide, VO_2

Vanadium (IV) oxide, VO_2 , with $M_r = 82.94$ amu, is a dark blue solid, with the vanadium cation in the +4 oxidation state. Vanadium dioxide is amphoteric, dissolving in non-oxidising acids to give the blue vanadyl ion, $[VO]^{2+}$, and in alkali to give the brown $[V_4O_9]^{2-}$ ion, or at high pH $[VO_4]^{4-}$.

1.2.2.a. Structural properties of VO_2

As many studies have shown, VO_2 can exist in multiform poly-morphic stable and metastable forms. It is reported that VO_2 has at least seven polymorphs (except for the hydrates), among which

rutile VO₂(R), monoclinic VO₂ (M) and triclinic VO₂ (T) phase are similar in structure, and there are other four VO₂ phases designated as tetragonal VO₂ (A), monoclinic VO₂ (B), paramontroseite VO₂ and VO₂ with new body centered-cubic (bcc) structure, respectively.^[1.2.3] Some of these VO₂ polymorphs that are of interest for this project are presented on Table 1.2 :

Crystallographic phase			Phase transition	Space group	
VO ₂ (B)	monoclinic	Meta-stable phases	Magnetic properties change transition below 25 °C	T > T _c *	C2/m
VO ₂ (A)	tetragonal		Phase Transition at 162 °C	T < T _c *	P4 ₂ /ncc
VO ₂ (M)	monoclinic	Stable phases	Metal-to-Insulator Transition at 68 °C	T < T _c *	P2 ₁ /c
VO ₂ (R)	rutile			T > T _c *	P4 ₂ /mnm

Table 1.2. Thermochromic properties of VO₂. (*) T is the temperature at which the specific phase can be detected in comparison with the transition temperature, T_c, whose average value is mentioned in the “Phase Transition” column of the table. ^{[1.2.14][1.2.4][1.2.5][1.2.6][1.2.7]}

The monoclinic VO₂ (M) polymorph is the one that exhibits a fully reversible phase transition to the rutile VO₂ (R) accompanied by a first order phase transition, VO₂ (M) ↔ VO₂ (R), shown in Figure 1.2. This low temperature insulating phase of VO₂ (M) at 25 °C consists of a lattice with unit cell parameters: a = 5.75 Å, b = 4.52 Å, c = 5.38 Å and β = 122.60° (space group P2₁/c). The lattice is the result of the distortion and doubling in size of the high temperature metallic tetragonal phase. The structure involves V⁴⁺–V⁴⁺ pairing with alternate shorter (0.266 nm) and longer (0.313 nm) V⁴⁺–V⁴⁺ distances along the monoclinic axis, and tilting with respect to the rutile c-axis. The pure VO₂ (M) phase is also sometimes referred to as M1, since doping of vanadium (IV) oxide results in another monoclinic arrangement, M2 (space group C2/m).^[1.2.4, 1.2.8] For the purposes of this project the monoclinic phase of vanadium dioxide will be referred to simply as (M).

When temperature is higher than the critical temperature, thermochromic VO₂ will transition to the rutile phase, VO₂ (R). This high temperature rutile structure of metallic VO₂ is based on a simple tetragonal lattice (space group P4₂/mnm). The vanadium atoms are located at the equidistant Wyck-off positions (4f), (0, 0, 0) and (½, ½, ½), with a V⁴⁺–V⁴⁺ distance of 0.288 nm and each V atom is surrounded by an edge-sharing octahedron of oxygen atoms, VO₆, which occupy the positions at ± (u, u, 0) and ±(½ + u, ½ - u, ½).^[1.2.4, 1.2.8]

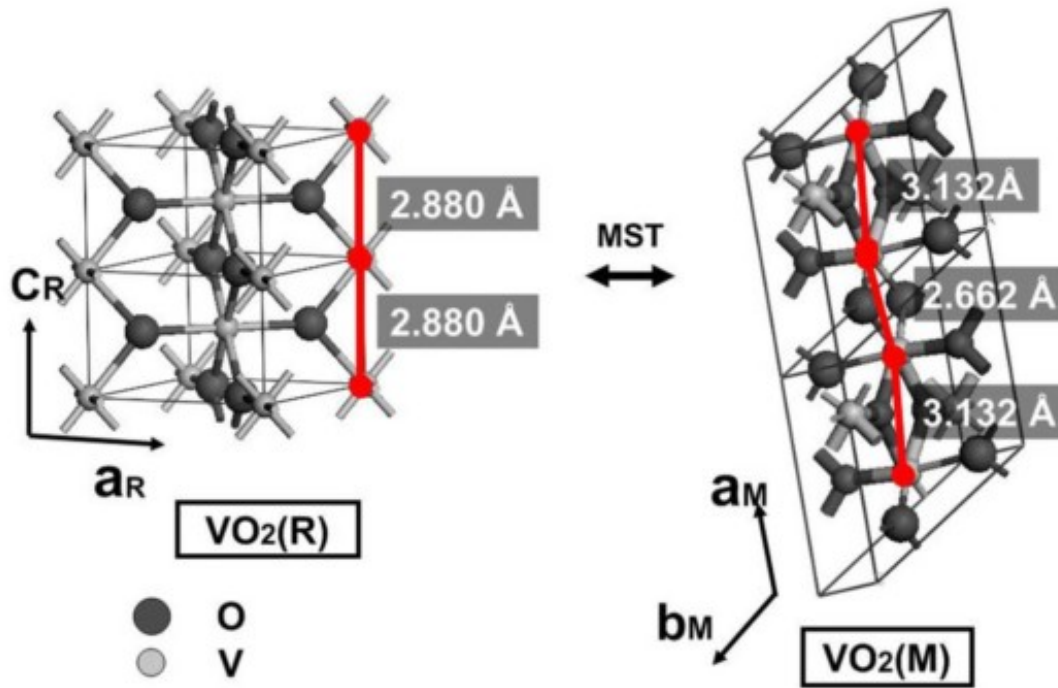


Figure 1.2 The crystallographic structure of $\text{VO}_2(\text{M})$ (to the right) and $\text{VO}_2(\text{R})$ (to the left). After the Mott transition, linear and equal-distant (2.880 Å) V-V chains along C_R axis in tetragonal (R) phase become distorted with alternative distances at 3.132 Å and 2.662 Å with unit cell doubled in monoclinic (M) phase.^[1.2.4]

The tetragonal VO_2 (A) polymorph undergoes a metal-to-semiconductor phase transition at $T_c = 162$ °C, accompanied by a crystallographic transition between a low temperature phase (LTP, P4/ncc, 130 below 162 °C) and a high temperature phase (HTP, I4/m, 87 above 162 °C).^[1.2.7]

The monoclinic VO_2 (B) polymorph has become of great interest owing to its layered structure, high energy capacity along with moderate work potential, thus being promising for applications in the field of energy technologies.^{[1.2.17][1.2.18][1.2.15]}

Both structures, as shown in Figure 1.3, are characterized by oxygen sites forming an fcc lattice with one-ninth vacant and with vanadium atoms occupying four-ninths of the octahedral sites. The planes (110) of VO_2 (A) and (001) of VO_2 (B) exhibit an identical structure (i.e. a VO_6 octahedral sheet).

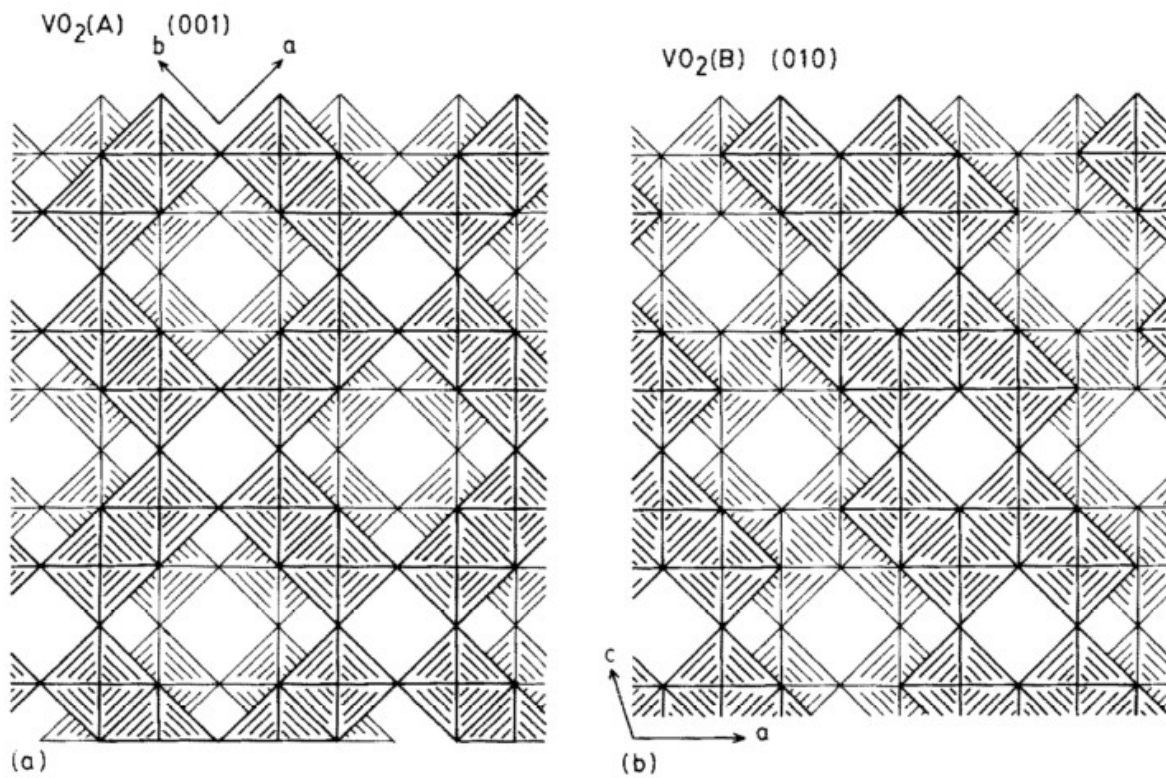


Figure 1.3 Idealized structures showing superpositions of the VO₆ sheets: (a) VO₂ (A) viewed along the c-axis; (b) VO₂ (B) viewed along the b-axis.^[1.2.5]

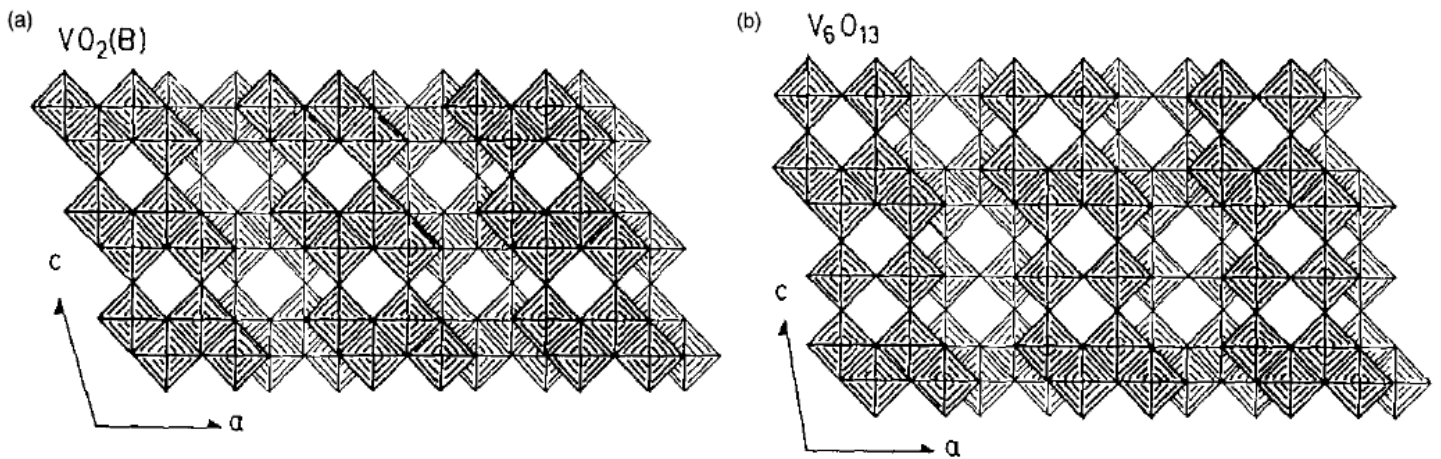


Figure 1.4 Diagrammatic illustrations of the structures of (a) VO₂ (B) and (b) V₆O₁₃.^[1.2.6]

1.2.2.b. Electronic properties of VO₂

In the tetragonal structure, VO₂ is meant to be in its metallic state and it has V⁴⁺ ion at the center of an O octahedron. For the fact of symmetry, the degenerate five 3d atomic orbitals of V are split in doubly degenerate e_g (d_{3z²-r², d_{xy}) levels and triply degenerate t_{2g} (d_{x²-y², d_{xz}, d_{yz}) levels. The e_g orbitals}}

are directed towards O ligands and hybridized with the O 2p orbitals. They form the σ and σ^* bands with the O 2p orbitals. The π and π^* bands, and the $d_{||}$ band are formed from the t_{2g} orbitals which point in between the ligands and this results from the V $3d_{xy}$ orbitals along the c-axis.

As we can see in Figures 1.5 and 1.6, the overlap of the $d_{||}$ and π^* bands at Fermi level of $\text{VO}_2(\text{R})$ is the cause behind its metallic properties. The low temperature phase, $\text{VO}_2(\text{M})$, causes the V-O hybridization to change and V-V bonding is stronger and π^* rises above Fermi level. The $d_{||}$ band separates into an empty and filled band due to the doubling of the unit cell, thus VO_2 has insulating properties with a band gap of about 0.7 eV. The insulating phase of VO_2 can have anomalous effects due to the doping of magnetic impurities and it is in the boundary of being a magnetic insulator. The metal-to-insulator transition (MIT) of VO_2 , which is sometimes also referred to as semiconductor-to-metal transition (SMT)^{[1.2.9], [1.2.10]}, is shown on Figure 1.2, in the previous section “1.2.2.a Structural properties of VO_2 ”.

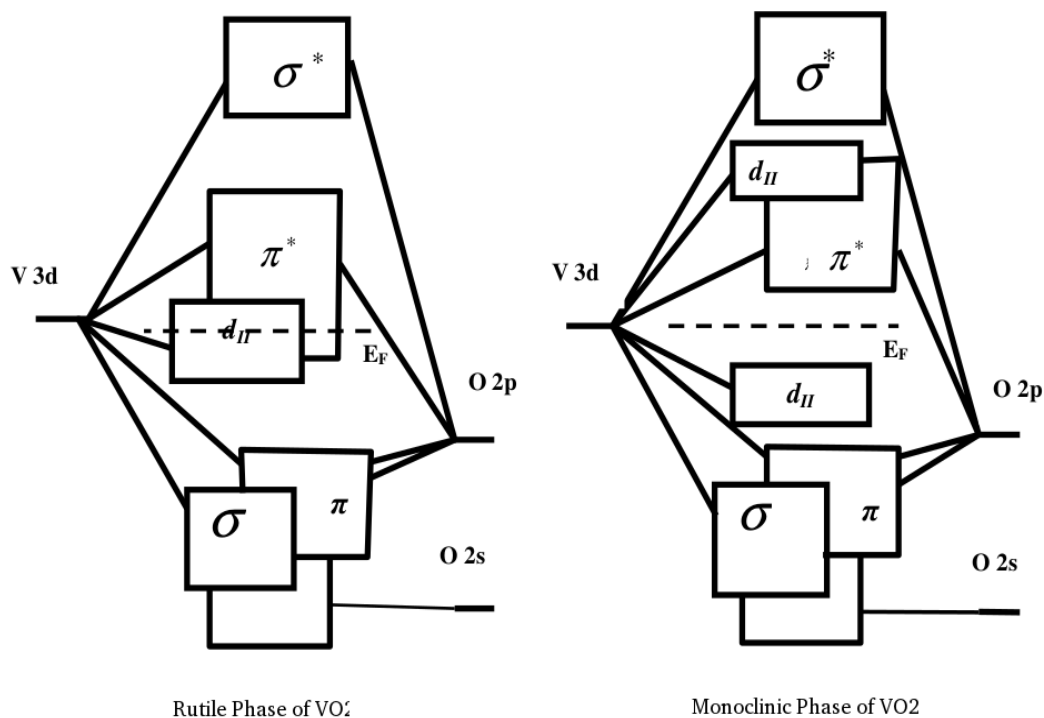


Figure 1.5 The metallic rutile phase of VO_2 showing no band gap (to the left), and the semiconductor monoclinic phase showing a band gap (to the right).

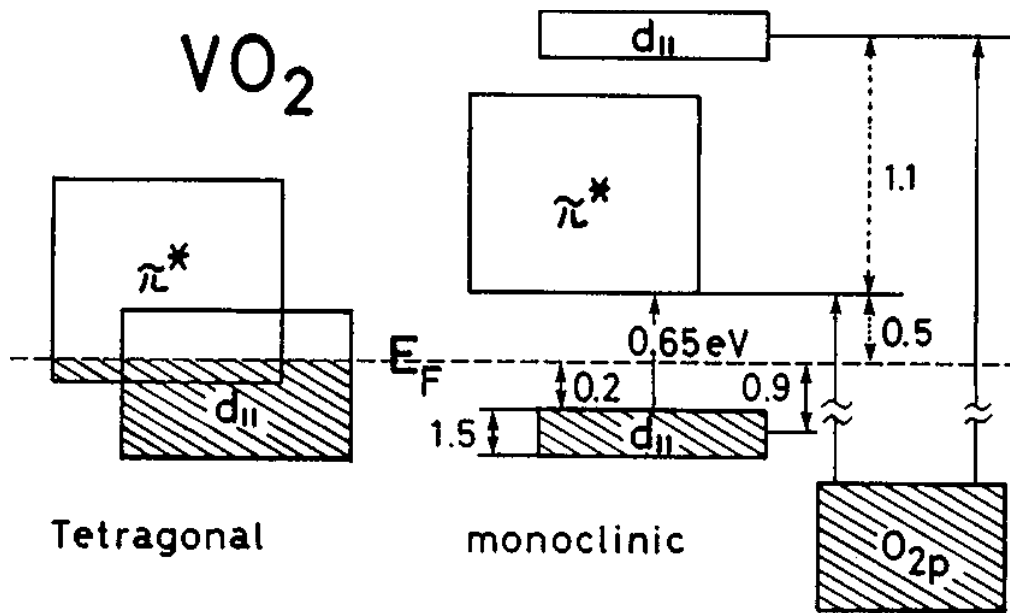


Figure 1.6 Schematic band structure diagram of VO_2 . The hybridisation of the V 3d and O 2p levels reflects the symmetries of the atomic arrangement in the crystal lattice.^[1.2.10]

The nature of the MIT in vanadium dioxide has been investigated via computational, experimental and theoretical studies. The prime mechanism of the transition still remains a phenomenon under investigation and research. The Mott-Hubbard model of correlating electrons were initially postulated.^[1.2.9] Goodenough (1971) proposed a useful explanation of the two phases of vanadium (IV) oxide, based on molecular orbitals and a band structure diagram, as shown on Figure 1.6.^[1.2.10] An anti-ferroelectric transition was considered as the potential driving force for the MIT in vanadium (IV) oxide. It was suggested that $\text{V}^{4+}\text{-V}^{4+}$ pairing in the tetragonal phase becomes energetically stable after cooling, following rearrangement of the band structure to give the monoclinic phase. Subsequently, the onset of anti-ferroelectric and crystallographic distortion was found to occur at two different temperatures, but happen to be synchronized for vanadium (IV) oxide. Goodenough concluded that the anti-ferroelectric component of the monoclinic low temperature phase in VO_2 is the driving force of the distortion. Furthermore, the transition temperature, T_c , is not controlled by thermal excitation of electrons into the anti-bonding bands, but by the entropy of the lattice vibrational modes.

1.2.2.c. Electrical properties of VO_2

During the MIT, VO_2 undergoes a $\approx 10^5$ decrease in resistivity when switching to the metallic state, as shown on Figure 1.7. The sharpness or the lack of thereof, of these changes in electrical proper-

ties has been related to disorientation between grains, and grain size and other morphologic faults.

It has been determined that the variations in the VO₂ switching are due to the level of internal or external stress, which can be modified by mismatch between lattice constants, expansion coefficients on different substrates, or even by ion bombardment.

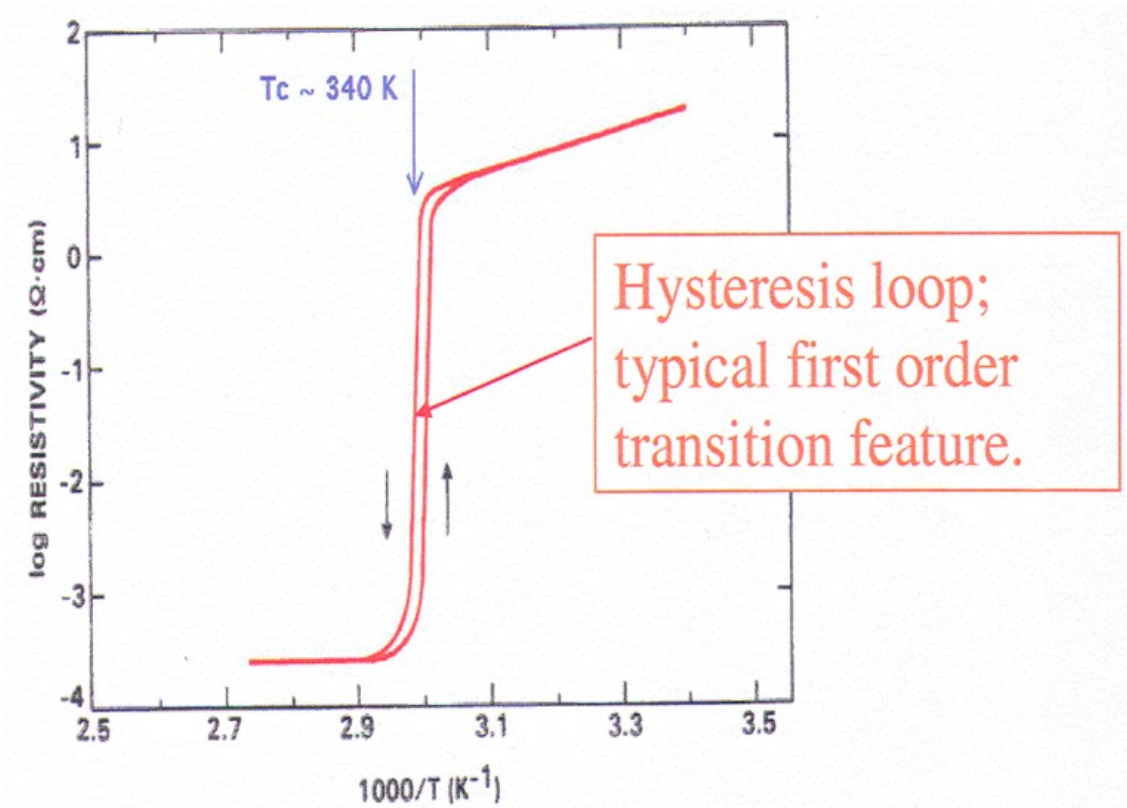


Figure 1.7 The variation of VO₂ electrical resistivity with temperature

1.2.2.d. Thermal properties of VO₂

In metals, electrons carry both charge and heat. As a consequence, electrical conductivity and the electronic contribution to the thermal conductivity are typically proportional to each other. Lee *et al.* (2017) found a large violation of this so-called Wiedemann-Franz law near the MIT in VO₂ nanobeams. In the metallic phase, the electronic contribution to thermal conductivity was much smaller than what would be expected from the Wiedemann-Franz law. The results can be explained in terms of independent propagation of charge and heat in a strongly correlated system.^[1.2.11]

1.2.2.e. Optical properties of VO₂

To this point it has been made clear that the MIT of VO₂ manifests along with many other switching of properties. Still, the one of major interest for this project is the optical switching that occurs dur-

ing the MIT of VO₂. As stated in previous sections, upon passing through the transition temperature (T_c), VO₂ undergoes a dramatic increase in infrared reflectivity with virtually no change in the visible region. Above T_c, the material reflects infrared radiation (IR). Yet, below T_c, it is IR-transparent, thus exhibiting the desired thermochromic effect which is the property of interest for using VO₂ as a thin film coating for “intelligent” architectural glazing.

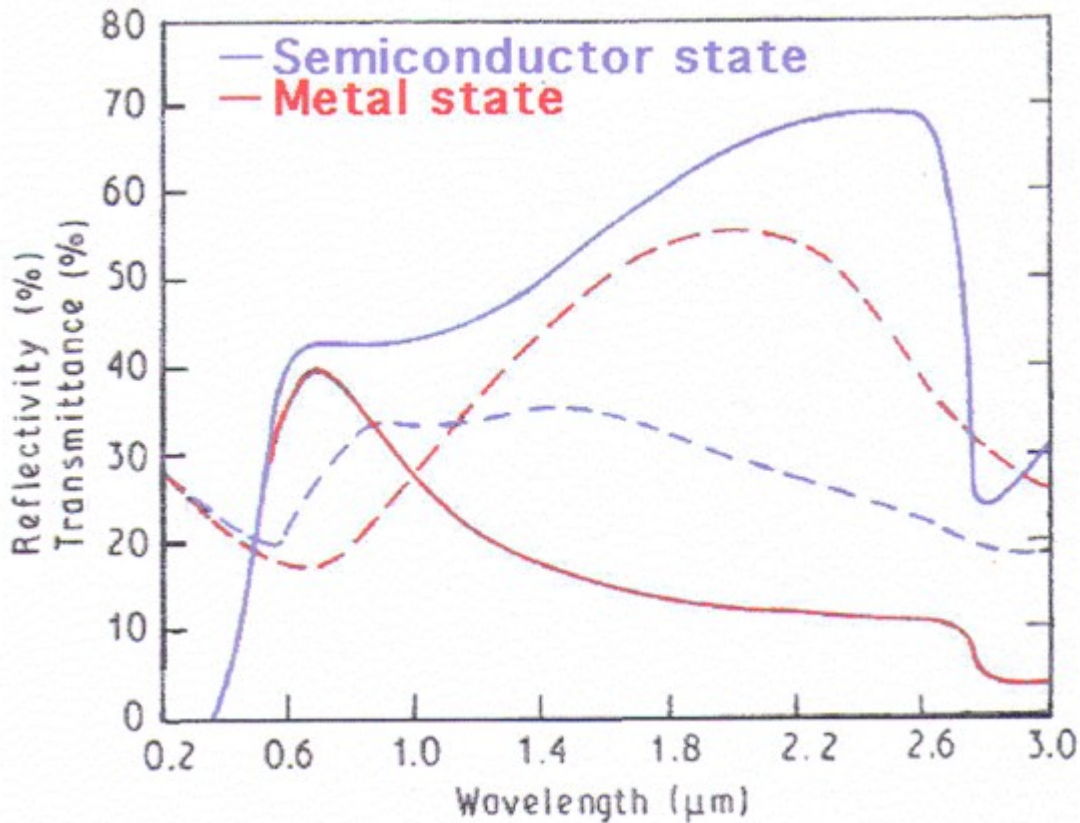


Figure 1.8 Optical transmittance (-) and reflectivity (--) of a VO₂ 85 nm thin film [6] deposited on a silica substrate. (blue lines) at room temperature and (red lines) 100°C

It has been shown that the MIT (or SMT) in VO₂ occurs gradually: first metallic puddles nucleate, then their size grows until the metallic phase percolates throughout the whole material. During the transition, there is coexistence of spatially separate metallic and insulating phases. When the wavelength of the incident radiation is comparable with the characteristic size of the metallic puddles, enhanced scattering is expected which would lead to the decline in reflection. The typical size of the metallic puddles in the middle of the transition can be estimated to be 1–2 μm. Further growth of the metallic puddles results in complete merging of the metallic phase and consequently an increase of the reflectance. Enhanced scattering is then expected at $\lambda = 1\text{--}2 \mu\text{m}$. ^[1.2.12, 1.2.13]

1.2.3. Reduction of V_2O_5 to VO_2 and its polymorphs complications

Of all the oxides of transition metals, the vanadium–oxygen system is truly remarkable and even, in a certain sense, unique. The point is that vanadium forms more than ten distinct oxide phases with different electronic properties, ranging from metallic to semiconducting/insulating: VO, V_2O_3 , VO_2 , Magneli (V_nO_{2n-1}) and Wadsley ($V_{2n}O_{5n-2}$) homologous series, and V_2O_5 . Many of these have interesting properties, like metal-to-insulator phase transitions, and are of great interest in the advanced materials research sector.

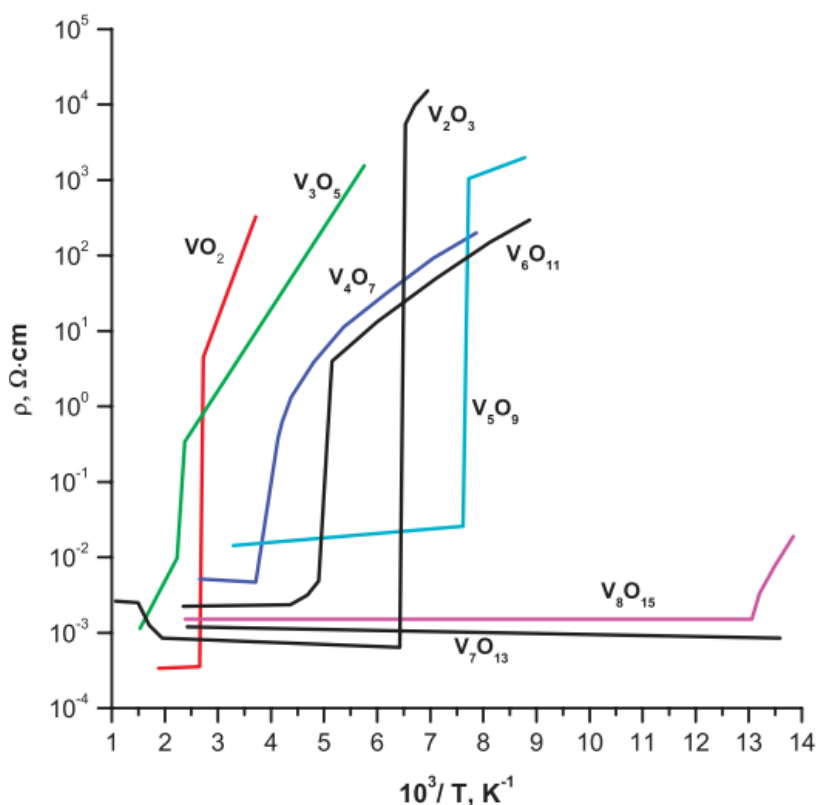


Figure 1.9 Metal-Insulator Transitions of Vanadium Oxides^[1.2.16]

This multitude of vanadium oxides is the result of a very basic property of the vanadium atom, since it can be found in many oxidation states (+2, +3, +4, +5); so, in vanadium (V) oxide vanadium has a valence of five (+5) while in vanadium (IV) oxide has a valence of four (+4). This implies that V_2O_5 can be converted to VO_2 by reducing the oxygen content, and valence of vanadium is reduced from +5 to +4. Vanadium pentoxide can form other phases before VO_2 is produced:



In their 1997 work, Haber J. et al. Suggested a mechanism for the reduction from vanadium pentox-

ide (oxidation state +5) to V_6O_{13} (oxidation state +4.3). “On long exposure of the sample [V_2O_5] to ultrahigh vacuum in the electron beam in the LEED chamber, streaks in the normal pattern begin to appear, then starting from the (0 0) spot every second spot of each column and each row weakens and disappears completely. In the final stage a parallelogram structure is obtained representing a two dimensional pattern of the V_6O_{13} (0 1 0) surface”, continuing, “... As a possible mechanism one can suggest that in the first stage oxygen is lost from the top V-O layer disturbing the periodicity in the a-direction. When sufficient amount of oxygen has been removed V_6O_{13} becomes a more stable configuration and by diffusion through the channels, the oxygen concentration of the top layer is restored to the requirements of the corresponding lattice.”

This can be understood better by looking at the structures of the two oxides, on *Figure 1.10*. The reduction happens as a transformation of the structure of V_2O_5 , which consists of corner-linked V-O octahedra, into that of V_6O_{13} , which consists of edge-linked octahedra. The structure of V_6O_{13} can be obtained from that of V_2O_5 by taking away every third oxygen layer parallel to the (0 1 0) plane (oxygen atoms removed are marked as black spheres) and rearranging the V-O bonds through a crystallographic shear. In the remaining V-O layers only the relative positions of the atoms change resulting in all vanadium being in the same plane instead of being warped as in V_2O_5 . The top layer of V_6O_{13} corresponds thus to a stretched V_2O_5 top layer with slightly different dimensions which accounts for the appearance of the parallelogram unit mesh.

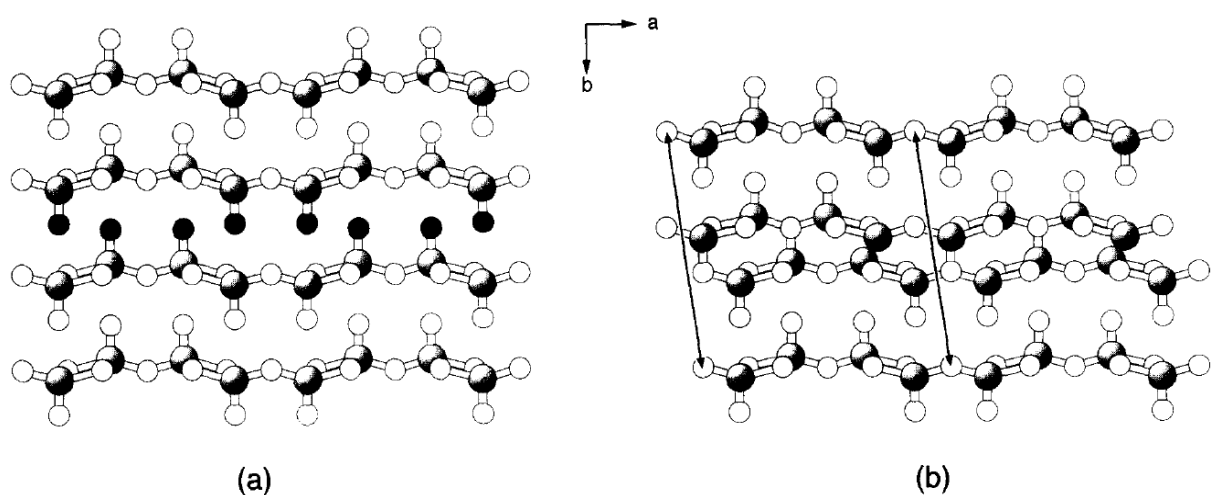


Figure 1.10 Mechanism of formation of a crystallographic shear plane. (a) The layer of oxygen to be removed marked by black spheres. (b) Rearrangement of the layers.

n in formula V_nO_{2n-1}	Oxide	T_t , K
(1)	VO	—
(2)	V_2O_3	150
3	V_3O_5	450
4	V_4O_7	240
5	V_5O_9	130
6	V_6O_{11}	170
7	V_7O_{13}	—
8	V_8O_{15}	70
(∞)	VO_2	340
(-6) ^{*)}	V_6O_{13}	150
(-2)	V_2O_5	—

^{*)} V_6O_{13} and V_2O_5 formally correspond to the series V_nO_{2n-1} with negative n , though actually they belong to the Wadsley phases $V_{2n}O_{5n-2}$.

Table. 1.3 Vanadium Oxides chemical formula and Temperatures of Transitions.^[1.2.16]

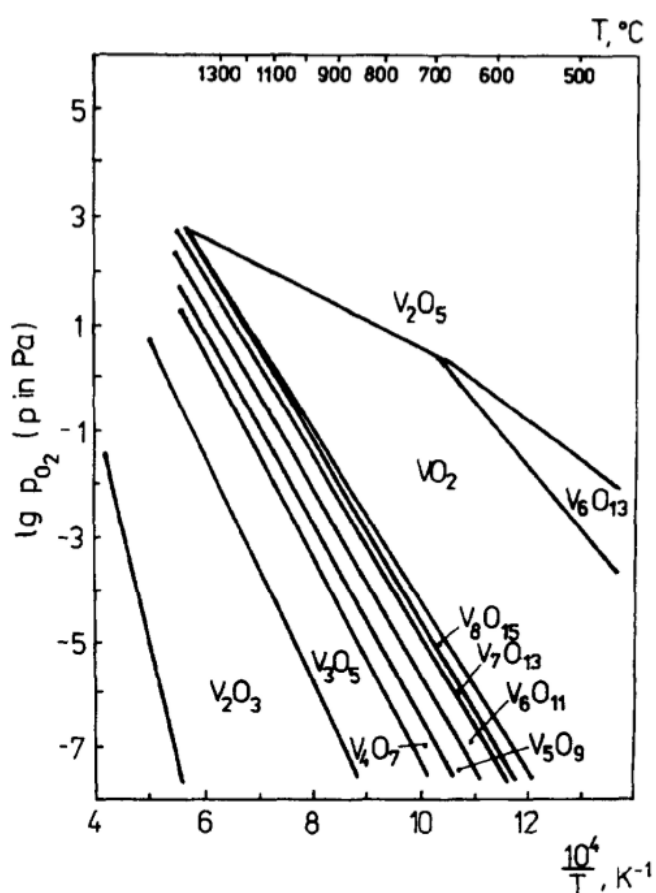


Figure 1.11 Phase diagram of the V~O system. The equilibrium oxygen pressures over two coexisting vanadium oxide phases as a function of temperature.^[1.2.2]

In 2002, Ningyi Y. et al.^[1.2.20] reported this valence reduction sequence while synthesizing VO₂ from V₂O₅ powders via a *sol-gel* route. Later on, other studies confirmed this sequence^[1.2.21]. Thus reduction of highly-oxidized vanadium oxides became the most studied way to obtain VO₂ by a solution-based chemical methods.

Regarding the *hydrothermal procedure*, which is also a solution-based method, the most commonly-used reagents as a vanadium source are V₂O₅ or, less frequently, ammonium metavanadate, NH₄VO₃; both having V at an oxidation state of +5. To reduce the oxide to the +4 oxidation state of vanadium in VO₂ many different reducing agents have been used, from the more drastic and toxic, hydrazine hydrate, to more mild and common organic acids, like oxalic acid (C₂H₂O₄), citric acid (C₆H₈O₇) and ascorbic acid (C₆H₈O₆)^{[1.2.22],[1.2.23],[1.2.42]}. For this project we chose to reduce solid V₂O₅ using *oxalic acid*, as the bibliography suggested to be more effective and still more easy-to-handle and less toxic.^{[1.2.23],[1.2.42]} Thus, the basic reaction we employed for the hydrothermal synthesis of VO₂ has been formulated in the following equation:



Still, the challenge of synthesizing the desired thermochromic polymorph of vanadium dioxide remains. In 1977, Théobald^[1.2.24] first reported the synthesis of VO₂(M) above 350°C by *hydrothermal reaction* in the V₂O₃–V₂O₅–H₂O system. Thereafter, there has been few literatures reported on the hydrothermal synthesis of VO₂(M), suggesting the difficulty in obtaining VO₂(M) at low temperature by one step reaction. Up until 2001, when Gui et al.^[1.2.25] mentioned the formation of VO₂(R) by a long-time hydrothermal reduction of NH₄VO₃ by N₂H₄ (at 220°C for 15 days). But no details about the formed VO₂(R) were given in their paper. More recently, VO₂(R) hollow spheres with nanorods aggregating on their surface were successfully synthesized by a surfactant-assisted hydrothermal process^[1.2.26]. Then, Son et al.^[1.2.27] reported the synthesis of micro- and nano-crystals of VO₂(M) by a hydrothermal method by the hydrothermal reaction of V₂O₅, H₂SO₄, and N₂H₄·H₂O at 230°C for 48 h. Ji et al.^[1.2.28] directly synthesized VO₂(R) nanorods via the hydrothermal reduction of V₂O₅ by oxalic acid. However, other studies^{[1.2.29],[1.2.30],[1.2.31][1.2.32]} found that only the (B) and (A) polymorphs of VO₂ can be successfully obtained by a single-step hydrothermal reaction of V₂O₅ and oxalic acid.

More specifically, Y. Zhang et al. (2012 and 2013)^{[1.2.31],[1.2.32]} showed that VO₂(B) is the first intermediate polymorph followed by the second intermediate polymorph VO₂(A) in the route to synthesize VO₂(M) hydrothermally. Such results are also in good accordance by other theoretical^[1.2.19] and

experimental^[1.2.33] results of other publications, as presented in *Figure 1.2* and *Figure 1.13*, respectively.

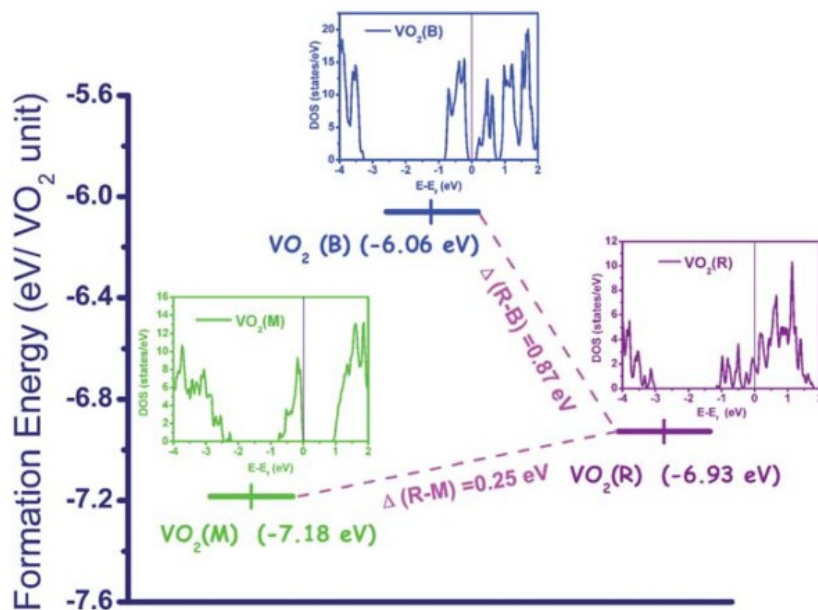


Figure 1.12 The calculated formation energy for $\text{VO}_2(\text{M})$, $\text{VO}_2(\text{R})$ and $\text{VO}_2(\text{B})$ according to the hybrid density functional theory.^[1.2.19]

According to the calculations of this work^[1.2.19] the formation energy of $\text{VO}_2(\text{B})$ are calculated to be higher than those of $\text{VO}_2(\text{M})$ and $\text{VO}_2(\text{R})$ by 1.12 eV and 0.87 eV per VO_2 unit, respectively, verifying that the rutile phase is indeed a thermodynamically stable phase. Although $\text{VO}_2(\text{R})/\text{VO}_2(\text{M})$ has the superior structural stability, the solution-based synthetic procedures like the hydrothermal will most likely lead to the metastable phases, rather than the thermodynamically stable phase of $\text{VO}_2(\text{R})$. Likewise, in the work of^[1.2.33] the incremental formation of $\text{VO}_2(\text{M})$ nanorods by nucleation and growth of $\text{VO}_2(\text{B})$, is observed experimentally by optical, structural and thermal measurements of the samples.

These results match the notion that V_2O_5 , when in a reducing environment, will reduce to the structurally similar V_6O_{13} due to the oxygen vacancies formed and then since V_6O_{13} is also of a similar structure to $\text{VO}_2(\text{B})$ polymorph (see “1.2.2.a Structural properties of VO_2 ”) this metastable polymorph will become the next kinetically stable intermediate to the reduction progress.

More on the characterization techniques for identification of the different polymorphs of VO_2 , as well as the influence of different additives and of chemical parameters of the synthesis will be discussed later on in this report (on “Chapter 3. Experimental Results”).

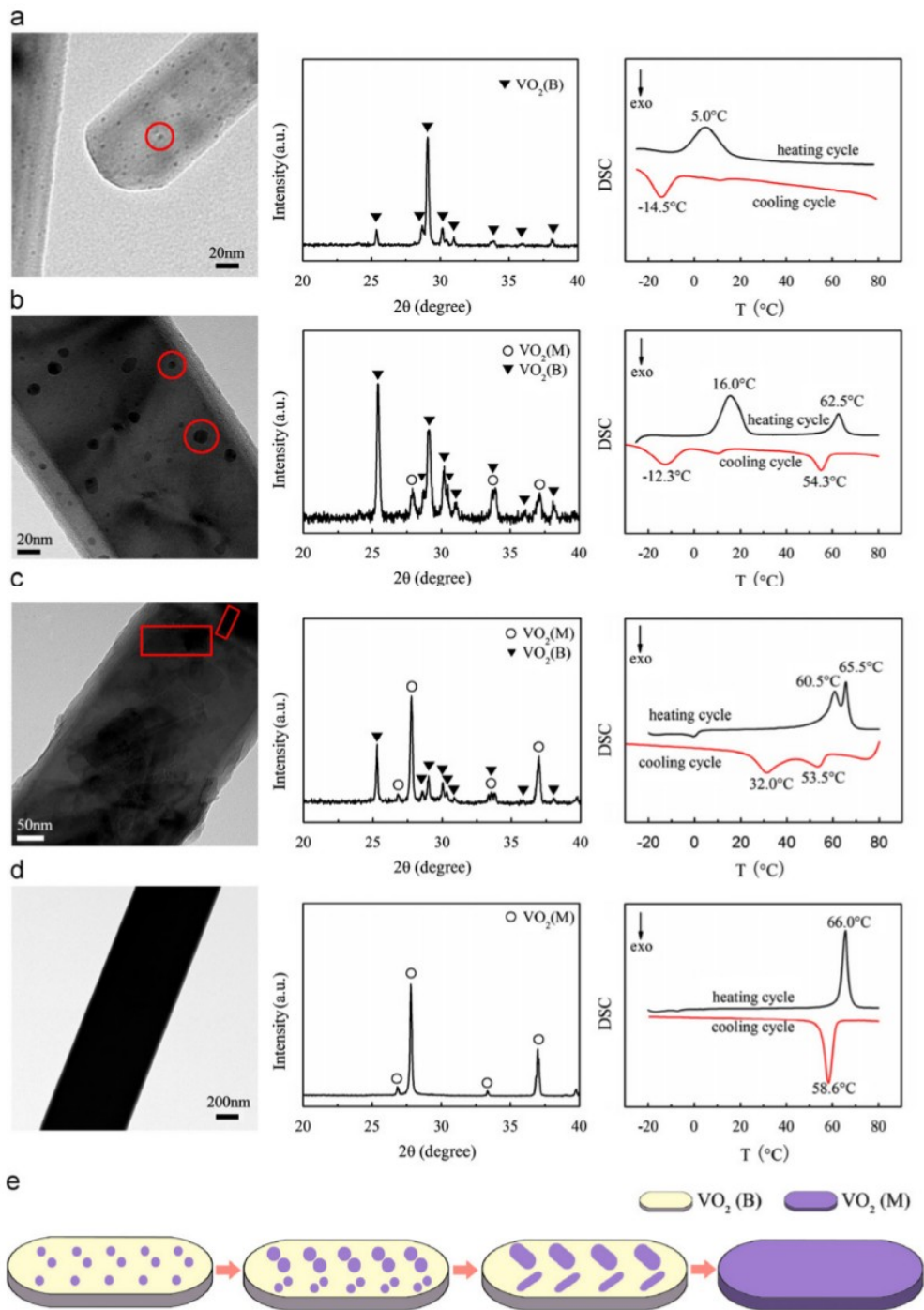


Fig. 1.13 TEM images (left), XRD patterns (middle) and DSC curves (right) of samples prepared by the hydrothermal treatment at 260°C for (a) 4 h, (b) 16 h, (c) 18 h, and (d) 20 h. The red marks are to highlight the nanobumps. (e) SCHEME: nucleation and growth mechanism of $\text{VO}_2(\text{B})$ nanorods to $\text{VO}_2(\text{M})$ nanorods. ^[1.2.33]

1.2.4. Doping of Vanadium (IV) Oxide

Doping is the intentional introduction of impurities into the crystal structure of our material, in order to create some lattice defects. The addition of substitutional and intercalative dopants is well-known to modify the phase stabilities of solid-state materials and either induce or hinder phase transformations by selective stabilization of one region of the phase diagram or by providing low-energy alternatives to processes that otherwise have high energetic barriers for pure materials.

Substitutional doping of the vanadium sub-lattice of VO_2 with other transition metals can strongly modify the phase-transition temperature and hysteresis and has commonly been used to shift the phase transition in closer proximity to room temperature. J. P Pouget, et al. (1974, 1975) found that doping with Al and Cr can result in stabilization of the metastable M2 phase of VO_2 .^{[1.2.34],[1.2.35]} Alternatively, doping the oxide sub-lattice with fluoride is also known to cause a depression of the phase-transition temperature. Doping the vanadium sub-lattice with tungsten yields a depression in the transition temperature of 20 to 26 °C per W %atom^{[1.2.36],[1.2.37],[1.2.38]}, whereas for other common dopants, Mo, Ti, and Nb, the induced decrease in the transition temperature is about half of that value on a per atom basis.^[1.2.36]

Regarding the mechanism behind the doping effect on the vanadium dioxide phase transition, Tang et al.^[1.2.39] demonstrated that the depression in phase transition upon W doping arises from destabilization of the V-V dimers in the M1 phase. According to their model, W^{6+} penetrates into the crystal lattice of VO_2 and substitutes the V^{4+} ion. In order to maintain charge neutrality of the lattice, two distinctive pairs are formed along the α -axis of $\text{VO}_2(\text{M})$ cell, with valencies of $\text{V}^{3+}-\text{V}^{4+}$ and $\text{V}^{3+}-\text{W}^{6+}$. With the enhancement of the electron concentration from the presence of W donors, the loss of $\text{V}^{4+}-\text{V}^{4+}$ pairs becomes more and more obvious, resulting that the insulating phase becomes destabilized and the band gap is reduced. Thus, the temperature of the MIT is decreased. In addition, Netsianda et al.^[1.2.40] have further calculated that there is a greater stabilization (more negative solution energy) associated with doping W within the rutile (R) phase of VO_2 as compared to the solution energy gained by doping the M1 phase. Additionally, the ionization of the tungsten dopant to W^{6+} adds two electrons to the band structure of VO_2 , which further increases the carrier density and coaxes the system toward transformation to the metallic state. Based on all the above results, the research about mechanism of reducing the T_c of $\text{VO}_2(\text{M})$ and (R) by doping still requires a lot of effort by scientists.

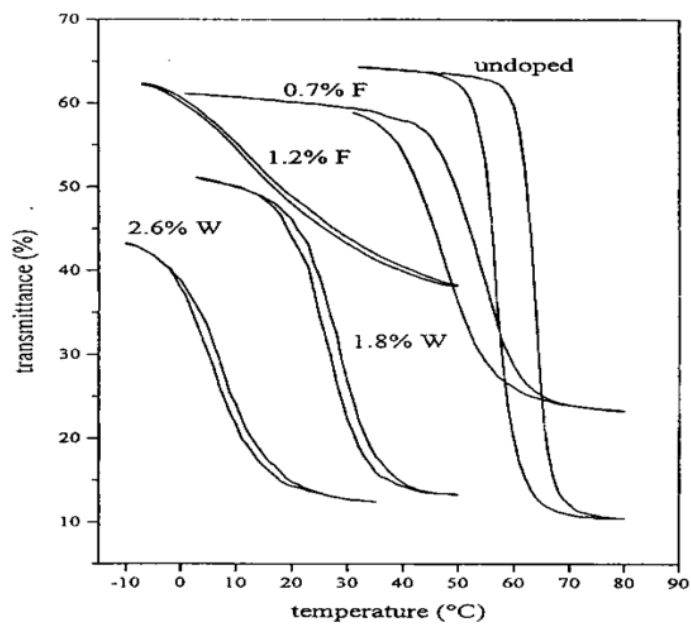


Figure 1.14 Hysteresis loops of optical switching of undoped, W-doped and F-doped VO_2 films.

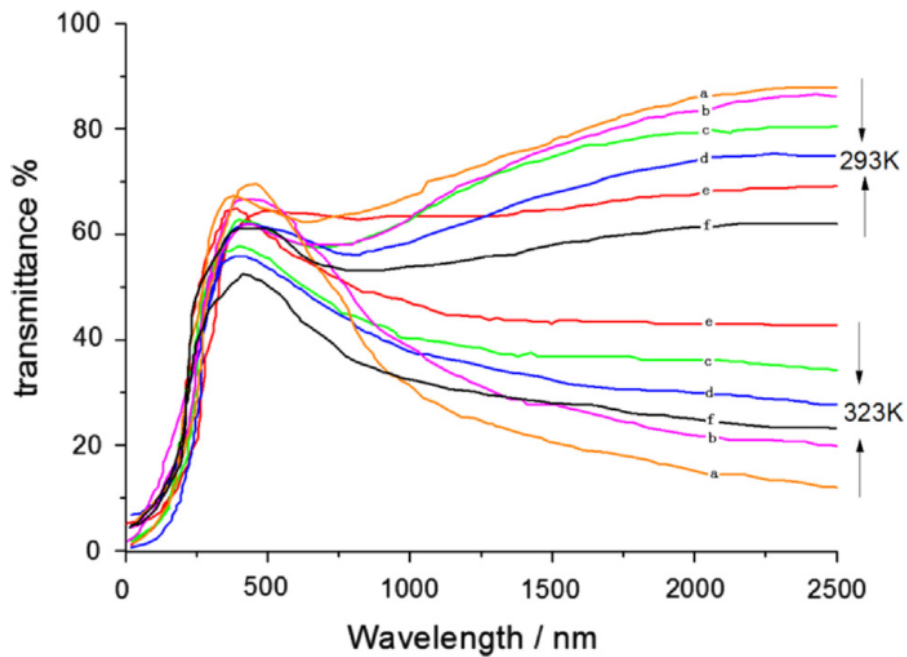


Fig. 1.15 Transmittance spectra for films with Mo-W-co-doped $\text{VO}_2(\text{R})$ at different contents of the dopants.^[1.2.41]

1.3 Technological applications of VO₂ Thermo-chromic Thin Films

As it has been already stated, solar control coatings can be applied to commercial or residential glazing, with the potential of improving the energy efficiency of buildings. Gold-doped vanadium (IV) oxide thin films have also received attention as fast optical switches. Other potential applications of VO₂ thin films to exploit the ultra-fast switching could include solid-state devices, such as thermal-switches, computational switches, optical mirrors and data storage or memory devices.^[1.2.8]

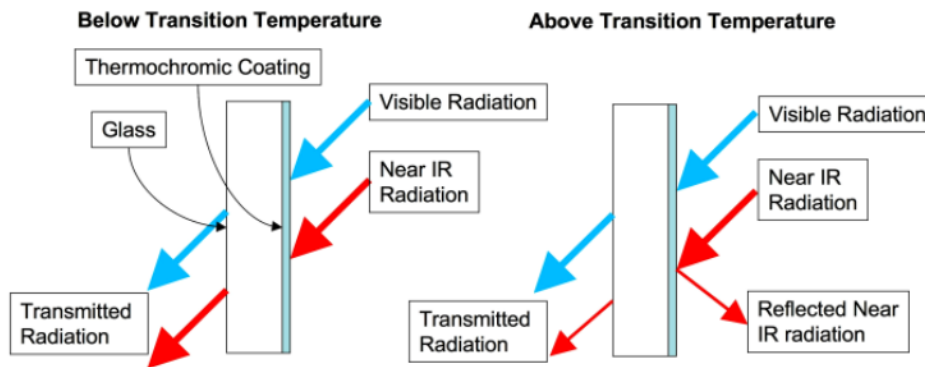


Figure 1.16 Visual representation of thermo-chromic VO₂ applied as a smart window coating.^[1.2.8]

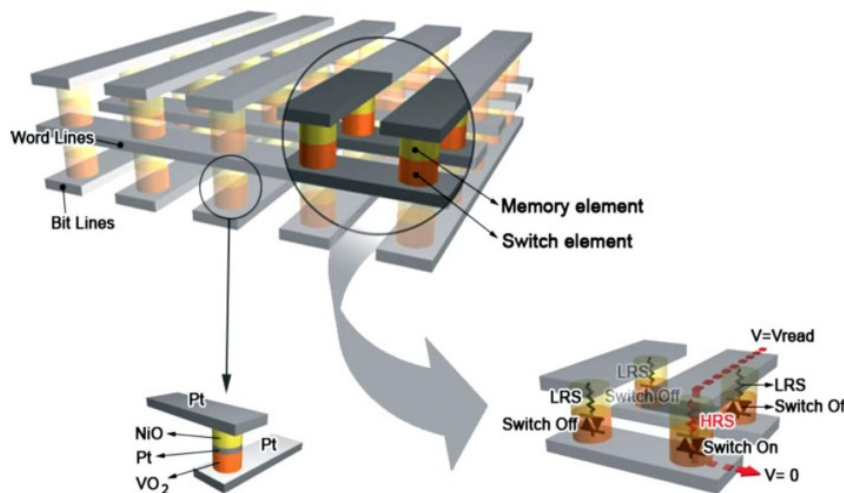


Figure 1.17 Application of VO₂ as a switching element in an oxide based memory with high speed and high density. It consists of a memory element (Pt/NiO/Pt) with non-volatile resistance switching behavior, and a switching element (Pt/VO₂/Pt) with threshold resistance switching behavior^[1.2.8]

CHAPTER 2. Methodology and Protocol

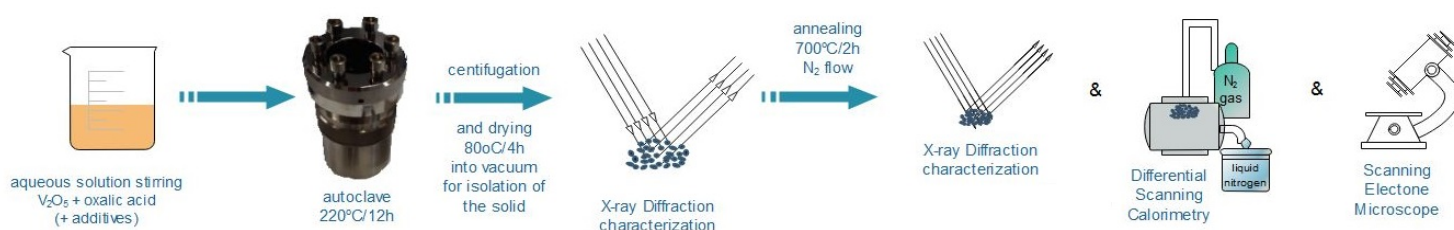


Figure 2.1 Overall schematic representation of protocol applied on this project.

2.1 Reagents/Materials

The VO₂ powders were synthesized by a hydrothermal procedure using solid Vanadium (VI) Oxide, V₂O₅ (98+%), as the source of vanadium, and solid Oxalic Acid dihydrate, H₂C₂O₄ · 2H₂O (≥99.0%), as the reducing agent. For the doping of our material solid Tungstic Acid, H₂WO₄ (≥99.0%), was used, as well as Magnesium Sulfate, MgSO₄ (≥99.5%). Other reagents were used as additives such as solid Sodium Hydroxyde, NaOH (98-100.5% pellets); liquid Hydrochlorich Acid, HCl (≥37%, Fluka); Sulfuric Acid, H₂SO₄ (95-97%); and solid Thiourea, SC(NH₂)₂ (≥99.0%). All reagents mentioned were used without further purification and purchased from Sigma-Aldrich, except tungstenic acid and hydrochlorich acid which were purchased and used as obtained by Fluka.

2.2 Synthetic Procedure

In a typical procedure, appropriate amounts of *solid* V₂O₅ (usually 0.365 g) and *solid* H₂C₂O₄ · 2 H₂O (usually 1.012 g) were dissolved in 40 mL of *deionised water*. After 15 minutes of stirring the original dark yellow mixture turned into a dark green - blue solution. During this step, some of the *additional reagents* were added in specific batches (see section 2.3 *Changing parameters*). Then, for the hydrothermal treatment to take place, the precursor mixture was transferred into a 125 mL *Parr Teflon-lined autoclave* of stainless steel and into a furnace at 220 °C for 12 hours with non-dynamic vacuum applied (at about -0.1 MPa). After the hydrothermal treatment, the autoclave was cooled naturally to room temperature. The obtained 'as prepared' (usually blue-black coloured) solid *product was isolated* from the synthesis solution *via centrifugation*, and then *dried* in a furnace with *dynamic vacuum* applied (at about -0.1 MPa) at 80 °C for 4 hours. Finally, to acquire the desired crystalline phase of thermochromic VO₂ the solid product was *annealed* at 700 °C for 2 hours, with a heating rate of 5°C/min, under constant *nitrogen gas flow* of 3 mL/min.

2.2.1. Changing Parameters

The main focus of this project was to study the solution-based synthetic approach for this material and how, by changing the chemistry of the system, we can obtain an optimized synthetic procedure. For this to happen, we needed to examine the correlation of changing the chemical parameters in regard to the final material gained. The basic parameters we moderated were: the *molar ratio* of the solid reagents, the *concentration* of our reagents in solution, the *pH* of the synthesis, the presence of *additives* and the *doping* levels. Only parameters regarding to the chemistry of the system were tested, since the alteration of physical parameters for such synthesis, such as synthesis temperature and duration, has been already studied, as explained at the Introductory part of this report.

The *molar ratio* between the two precursors was changed from a minimum of 1:1.5 to a maximum of 1:12, as in V_2O_5 mol : oxalic acid mol, by raising the oxalic acid mass while keeping the vanadium precursor mass constant. The *concentration* of the vanadium precursor in solution was changed from 9 g/L to 18 g/L, either by changing the original mass of solid V_2O_5 used or by reducing the volume of our precursor mixture by half (thus dissolving the reagents in 20 mL of deionised water instead of 40 mL). These test were also done for different molar ratios between the two precursors. The *pH* of the synthesis was changed by adding various amounts of pH-regulating *additives* such as HCl or NaOH solutions, in order to reach various pH values from 0 to 8. Other *additives* used were H_2SO_4 and thiourea. *Dopants* used were solid $MgSO_4$ and solid H_2WO_4 for single or co- doping of our synthetically optimized material. Doping levels varied from 0.5 mol% to 10 mol% depending on the dopant used.

2.2.2. The Hydrothermal Method

The term "hydrothermal" is of geologic origin. Geochemists and mineralogists have studied hydrothermal phase equilibria since the beginning of the twentieth century, establishing the foundations of this method. Originally, hydrothermal synthesis could be defined as a method of synthesis of single crystals that depends on the solubility of minerals in hot water under high pressure. The crystal growth is performed in an apparatus consisting of a steel pressure vessel called an *autoclave*, in which a nutrient (reagent) is supplied along with water. A temperature gradient is maintained between the opposite ends of the growth chamber. At the hotter end the nutrient solute dissolves, while at the cooler end it is deposited on a seed crystal, growing the desired crystal.

Today, hydrothermal synthesis is commonly used to synthesize nanostructures, as this method allows for the generation of unique nanoscale morphology. It opens up the possibility of structure control not afforded by traditional high-temperature solid-state reactions. Hydrothermal synthesis,

involving water-soluble precursors at a low temperature, is cost effective and sensitive to synthesis parameters such as time, temperature, pH, concentration, pressure, and reducing agents, which are useful to obtain desired morphologies and explore new phases.

Advantages of the hydrothermal method over other types of crystal growth include the ability to create crystalline phases which are not stable at the melting point. Also, materials which have a high vapour pressure near their melting points can be grown by the hydrothermal method. The method is also particularly suitable for the growth of large good-quality crystals while maintaining control over their composition. Disadvantages of the method include the need of expensive autoclaves, and the impossibility of observing the crystal as it grows. Although autoclaves may be expensive laboratory equipment, still they are less expensive than other solid-state synthesis techniques, especially when working with nano- structures, and depending on the case. On *Figure 2.2* we present a photograph along with a detailed schematic of the teflon-lined autoclave used for this project.

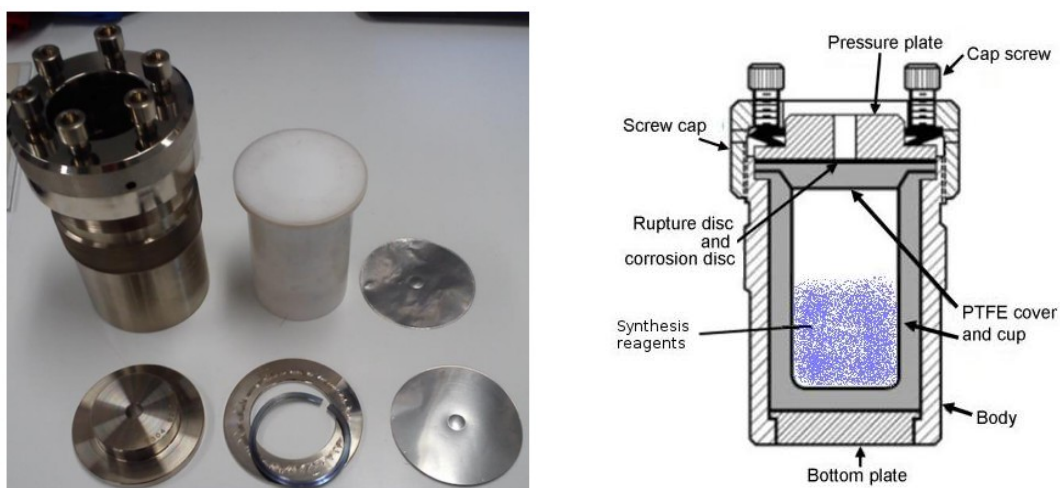


Figure 2.2 Parr acid digestion vessel. Model 4748 has a 125 mL, removable PTFE cup in a stainless steel body with six cap screws in the screw cap to seal the flanged PTFE cup.

2.3 Characterization Techniques

The morphology of the solid product was examined by Field Emission Scanning Electron Microscopy (SEM, Jeol 7000), operating at 15 keV, and equipped with an Energy Dispersive X-ray (EDX) spectrometry system. The phase identification of the VO₂ powders was performed using X-ray diffraction (XRD, RIGAKU RINT 2000) with Cu-K α radiation source of $\lambda_{\text{CuK}\alpha}$ =1.54 Å, from 10-80° with a step of 0.2°/sec. The thermochromic transition was studied by Differential Scanning Calorimetry (DSC, Perkin-Elmer), from 20 °C to 170 °C with 10 °C/min under Nitrogen flow of 20 cc/min, connected with a liquid nitrogen cooling system. To test the thermal stability of our materials Thermogravimetric Analysis (TGA, SDT Q600 V8.3 Build 101) was used to measure the mass loss percentage of our materials through a temperature ramp from 30 °C to 800 °C with a heating range of 5 °C/min under Argon flow. A more in depth explanation of these techniques will be presented in the next subsections of this chapter.

2.3.1. Introduction

Inorganic and Polycrystalline Solid Materials can be characterized and studied through many different characterization techniques, using either radiation (x-rays, electrons, etc) or by exploiting other physiochemical properties of our materials, depending on the specific application under examination. Here, in these subsections the characterization techniques used for this project will be presented, as well as a short explanation on their *basic principles*.

2.3.2 X-Ray diffraction (XRD)

X-Ray diffraction (XRD) is a versatile, non-destructive technique that reveals detailed information about the chemical composition and crystallographic structure of natural and manufactured materials. The X-ray diffraction methods have qualitative and quantitative analysis. Qualitative analysis involves the identification of phase or phases in a specimen by comparison with the reference pattern (i.e. data collected by someone else), and relative estimation of proportions of different phases in multiphase specimens by comparing peak intensities attributed to the identified phase. The quantitative analysis of diffraction data involves the determination of amounts of different phases in multi-phase samples. In quantitative analysis, an attempt is made to determine structural characteristics and phase proportions with quantifiable numerical precision from the experimental data itself. The most successful quantitative analysis usually involves modeling diffraction pattern such that the calculated pattern(s) duplicates the experimental one. All quantitative analysis requires precise and accurate determination of the diffraction pattern for a sample in terms of both peak positions and intensities.

Generation of X-rays

X-rays are short-wavelength with high-energy electromagnetic radiation and having the properties of both waves and particles. They can be described in terms of photon energy (E) or wavelength λ and frequency ν . The relation of between energy, frequency or wavelength can be defined as follows:

$$E = h\nu = hc/\lambda \quad \text{eq.(2.1)}$$

X-rays are produced from the interaction of high energetic electrons with the metal target. The X-ray tube must contain (a) a source of electron, (b) a high accelerating voltage, (c) a metal target.

Bragg's Law

Since atoms are arranged periodically in a lattice, x-rays scattered from a crystalline solid can constructively interfere and produce a diffracted beam through these atoms. In 1912, W.L. Bragg recognized the predictable relationship among several factors, as are expressed in Bragg's Law:

$$n\lambda = 2d \sin\theta \quad \text{eq.(2.2)}$$

where, n : an integer 1, 2, 3...etc [$n=1$ for calculations]; λ : the wavelength of the incident X-radiation; θ : the diffraction angle in degrees; and d : the distance between similar atomic planes of a mineral, which is called d-spacing and is usually measured in angstroms.

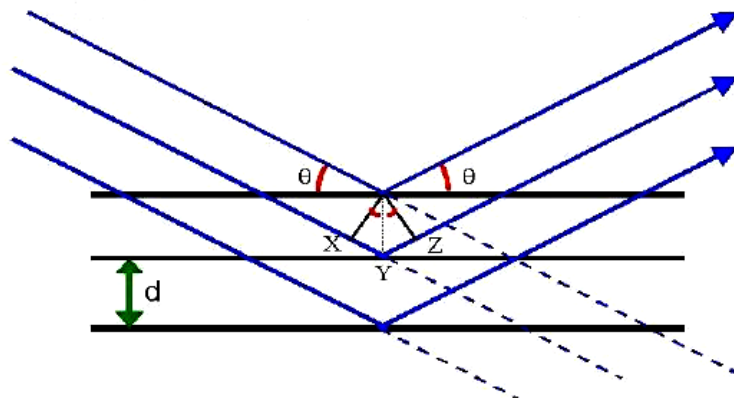


Figure 2.3 Bragg diffraction on a periodic structure (crystalline solid).

By varying the angle theta, the Bragg's Law conditions are satisfied by different d-spacings in the polycrystalline materials. Plotting the angular positions and intensities of the resultant diffracted peaks of radiation produces a pattern, which is characteristic of the sample. Where a mixture of different phases is present, the resultant diffractogram is formed by addition of the individual pattern.

2.3.3 Differential Scanning Calorimetry (DSC)

Differential Scanning Calorimetry (DSC) is a thermoanalytical technique in which the difference in the amount of heat required to increase or decrease the temperature of a sample in order to keep up with a reference sample is measured as a function of temperature, by monitoring the material's heat capacity (C_p). A sample of known mass is heated or cooled and the changes in its heat capacity are tracked as changes in the heat flow. This allows the detection of transitions such as melts, glass transitions, phase changes, and curing. Basically, DSC can detect any change that alters the heat flow in and out of a sample. This includes more than just glass transitions and melting. You can see solid state transitions such as eutectic points, melting and conversions of different crystalline phases like polymorphic forms, dissolution and precipitation from solutions, crystallization and re-crystallizations, curing exotherms, degradation, loss of solvents, and chemical reactions. The biggest advantage of DSC is the ease and speed with which it can be used to see transitions in materials.

In our current work DSC was used to monitor the metal-to-insulator (MIT) phase transition of our thermochromic material and to deduct/calculate useful data, like the specific critical temperature of this structural transition, T_{cr} , as well as the hysteresis loop between the heating and cooling temperatures, $\Delta T_{cr} = | T_{cr}^{heating} - T_{cr}^{cooling} |$.

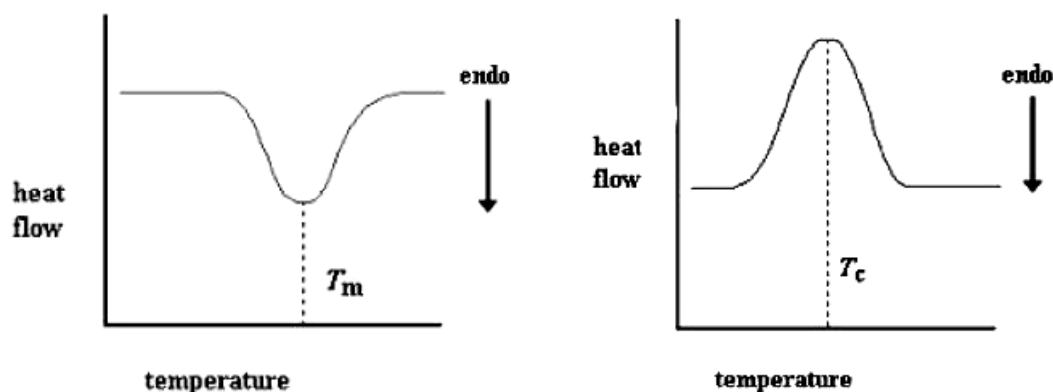


Figure 2.4 Heating peak of the transition and $T^{heating}$ transition temperature, here “ T_m ” (on the left). Cooling peak of the transition and $T^{cooling}$ transition temperature, here “ T_c ” (on the right).

2.3.4 Scanning Electron Microscope (SEM)

A scanning electron microscope is a type of electron microscope that produces images of a sample by scanning the surface with a focused beam of electrons. The electrons interact with atoms in the

sample, producing various signals that contain information about the sample's surface topography and composition. The most common SEM mode is detection of secondary electrons emitted by atoms excited by the electron beam. The number of secondary electrons that can be detected depends, among other things, on specimen topography. By scanning the sample and collecting the secondary electrons that are emitted using a special detector, an image displaying the topography of the surface is created. SEM can achieve resolution better than 1 nanometer. Specimens can be observed in high vacuum in conventional SEM, or in low vacuum or wet conditions in variable pressure or environmental SEM, and at a wide range of cryogenic or elevated temperatures with specialized instruments.

In more detail, primary electrons are filled-emitted by cathode filament (W or LaB6) or field-emission gun (W-tip) and after that accelerated with high energy typically 1 to 30 KeV. Electron beam is steered with scanning coils over the area of the interest. During the interaction of the beam with material, the primary electrons decelerate and lose their energy by inelastic transfer to the other atomic electron and to the lattice. Due to continuous scattering events the primary beam spread up with different energies depending on origin source, as shown in *Figure 2.5-a*. The interaction volume with the various electrons emitted and their respective energy is shown in *Figure 2.5-b*. Secondary electrons of about 1 to 50 eV are mostly used for imaging the topographically contrast and reproduce the surface. High energy elastically backscattered electrons depends on the atomic number (Z) of the element, which is useful to obtain Z-contrast. For the qualitative and quantitative analysis of the elemental composition and distribution in the sample, the X-ray characteristic is commonly used (see next subsection on "*Energy-Dispersive X-Ray Spectroscopy*").

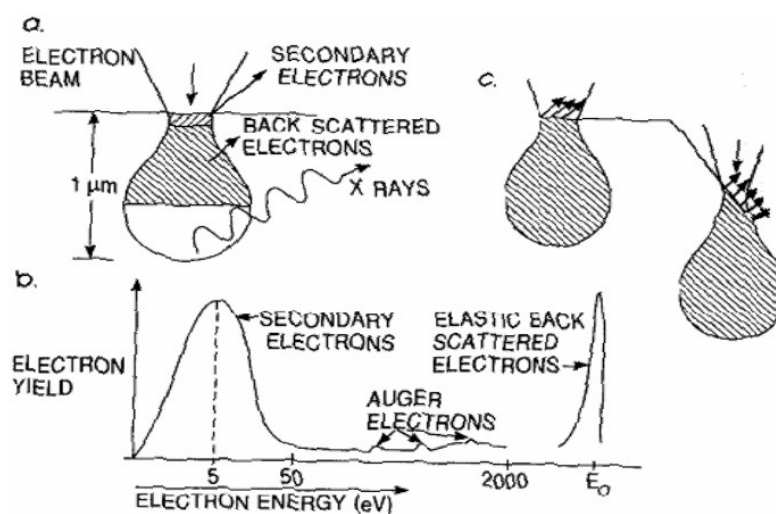


Figure 2.5 (a) The interactions of electrons with the surface during bombardment. (b) Type of electrons and corresponding energies of the emitted electrons after element interaction. (c) Showing the effect of surface topography on electron emission.

2.3.5 Energy-Dispersive X-Ray Spectroscopy (EDX)

The EDX system, also sometimes called EDS, is connected to electron microscopes such as SEM, FE-SEM and HR-TEM. The EDX spectra of the corresponding elements of the sample are obtained by measuring the energy of x-rays emitted from the sample during e-beam bombardment. X-rays are produced as a result of ionization of an atom when an inner shell electron has been removed by the incident electrons. When an ionized atom returns from its excited state to its ground state, an electron from a higher energy outer shell fills the vacant inner shell and then releases an amount of energy equal to the potential energy difference between the two shells. This energy, which is unique for every atomic transition, will be emitted either as an x-ray or as Auger electron. In EDX analysis, the detector analyzes these emitted x-ray photons from the sample, which can be utilized for quantitative and qualitative composition analysis

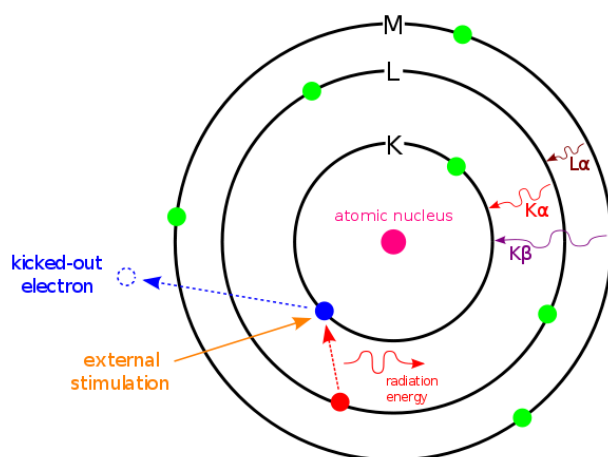


Figure 2.6 Principle of EDX

2.3.6 Thermogravimetric Analysis (TGA)

Thermogravimetric analysis or thermal gravimetric analysis (TGA) is a method of thermal analysis in which the mass of a sample is measured over time as the temperature changes. This measurement provides information about physical phenomena, such as phase transitions, absorption and desorption; as well as chemical phenomena including chemisorptions, thermal decomposition, and solid-gas reactions (e.g., oxidation or reduction).

TGA is conducted on an instrument referred to as a thermogravimetric analyzer. A thermogravimetric analyzer continuously measures mass while the temperature of a sample is changed over time. Mass, temperature, and time in thermogravimetric analysis are considered base measurements while many additional measures may be derived from these three base measurements.

A typical thermogravimetric analyzer consists of a precision balance with a sample pan located inside a furnace with a programmable control temperature. The temperature is generally increased at constant rate (or for some applications the temperature is controlled for a constant mass loss) to incur a thermal reaction. The thermal reaction may occur under a variety of atmospheres (ambient air, vacuum, inert gas, oxidizing/reducing gases, etc) as well as a variety of pressures.

The thermogravimetric data collected from a thermal reaction is compiled into a plot of mass or percentage of initial mass on the y-axis versus either temperature or time on the x-axis. This plot, which is often smoothed, is referred to as a TGA curve.

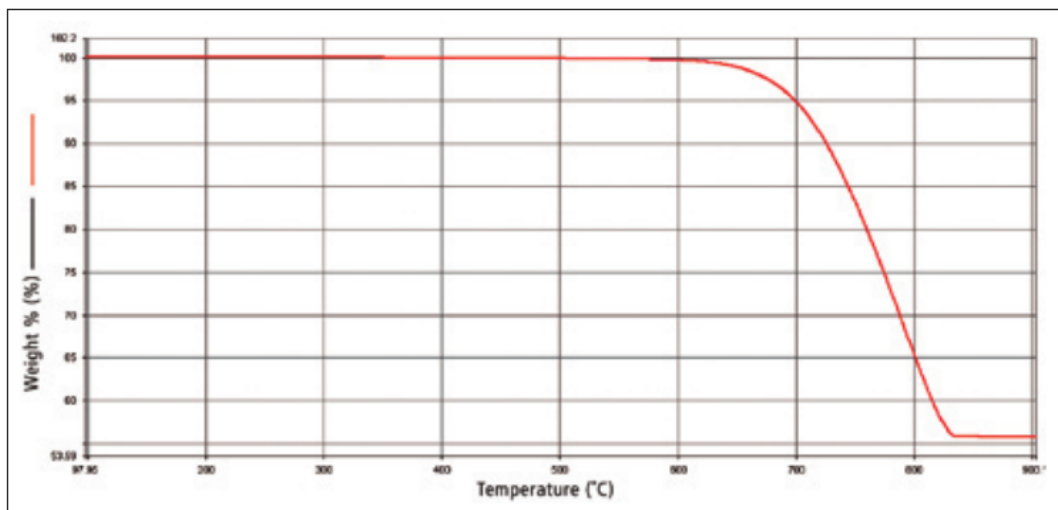


Figure 2.7 A typical TGA curve, with the Weight % on the y-axis versus the Temperature on the x-axis.

CHAPTER 3. Experimental Results

In this section we will present the most prominent of our experimental results. In total we tested 44 different synthetic parameter configurations. These results will be presented in different sections based on a parameter change at a time. The experimental data presented for these configurations/batches will be mostly by means of XRD patterns, in order to identify the product of each batch and compare results between different configurations. Furthermore, in each chapter data will be presented for our samples both prior (“*as obtained*”) and after (“*final*”) the annealing process. The comparison of these data is of interest, since the annealing of our “*as obtained*” samples can distort the crystalline lattices to adopt more thermodynamically stable phases of thermochromic VO₂ as well as increase the crystallinity of our materials, thus achieving better quality products.

The yields of the products of our synthetic procedures were also calculated by dividing the mass of the hydrothermal “*as obtained*” product to the original mass of our reagent, V₂O₅, and multiplying by 100%, as in equation (2):

$$\text{Yield \%} = \frac{\text{final mass}}{\text{starting mass}} \cdot 100 \% \quad \text{eq. (2)}$$

The results of our calculations for the as prepared products in regard to the two main changing parameters, molar ratio of precursors and concentration of vanadium precursor, are presented in *Table 3.1*. Note that these as obtained hydrothermal products aren't necessary the desired thermochromic polymorph of VO₂ (more on the identification of this samples in the following sections).

V ₂ O ₅ : Oxalic acid molar ratio	V ₂ O ₅ concentration		
	3 g/L	9 g/L	18 g/L
1:1.5	83.6 %	95.4 %	-
1:2	-	91.9 %	-
1:3	-	41.2 %	-
1:4	82.5 %	78.2 %	85.1 %
1:6	82.4 %	77.5 %	-
1:8	79.4 %	77.5 %	-
1:10	79.6 %	73.3 %	-
1:12	73.4 %	-	-

Table 3.1. Calculated Yields% of hydrothermal procedure, in regard to molar ratio of precursors and concentration of V₂O₅ precursor.

3.1 Parameter: Molar Ratio of precursors

The synthesis process was initiated by reducing V_2O_5 in the presence of oxalic acid to VO_2 under ambient conditions during the stirring process. The final formation of VO_2 crystals in the more studied configurations occurred during the subsequent hydrothermal step and is summarized by the chemical reaction equation (1), as explained in previous sections (see "1.2.3. Reduction of V_2O_5 to VO_2 and its polymorphs complications").



The molar ratio of the precursors plays a crucial role in fully reducing the vanadium to the desired +4 oxidation state, making it a critical factor in the preparation of VO_2 phases. Based on the chemical reaction of eq. (1), the molar ratio between V_2O_5 and oxalic acid should be at least 1:2 to fully reduce V^{5+} to V^{4+} . For the purpose of this project, we experimented with molar ratios of 1:1.5, 1:2, 1:3, 1:4, 1:6, 1:8, 1:10 and 1:12, in order to see the effect of an excess of the reducing agent, while other synthetic parameters, like concentration, pH, temperature and duration, were kept constants.

3.1.1. Before annealing (“as obtained” products)

3.1.1.a. XRD patterns for the as obtained at 18 g/L V_2O_5 concentration

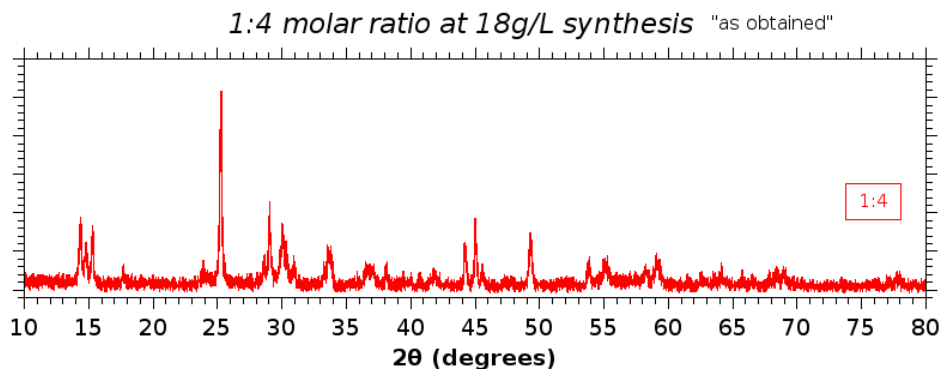


Figure 3.1 X-ray diffraction patterns of “as obtained” sample with a configuration of 18 g/L V_2O_5 and 1:4 molar ratio of the reagents.

For the synthesis with high concentration of vanadium precursor, we tested the configuration with a molar ratio of 1:4. From the XRD pattern shown on Figure 3.1 we have identified the monoclinic $VO_2(B)$ and the tetragonal $VO_2(A)$ polymorphs. For these and for all of the XRD data in this project identification of the samples was done using the XRD identification programs: JADE and EVA.

3.1.1.b. XRD patterns for the as obtained at 9 g/L V_2O_5 concentration

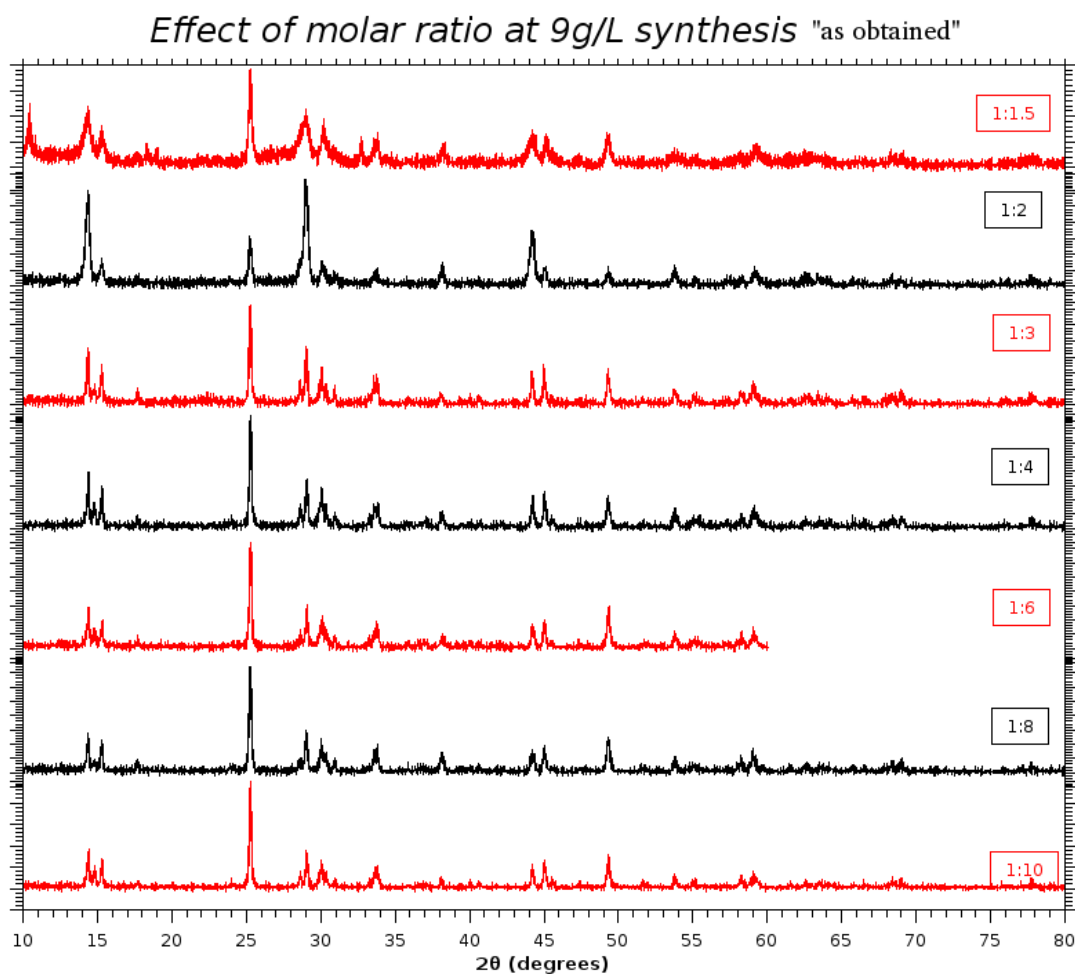


Figure 3.2 X-ray diffraction patterns of “as obtained” samples with configurations of 9 g/L V_2O_5 and various molar ratios of the reagents.

For the synthesis with medium concentration of vanadium precursor, we tested the configurations with a molar ratio of 1:1.5, 1:2, 1:3, 1:4, 1:6, 1:8 and 1:10. From the XRD patterns shown on Figure 3.2 we can deduce several conclusions. The 1:1.5 molar ratio batch consists of a mixture of the hydrated vanadium oxide, $V_6O_7 \cdot H_2O$ (oxidation state of +2.3), the monoclinic $VO_2(B)$ and the tetragonal $VO_2(A)$ with less intense peaks. Still, the 1:2, 1:3, 1:4, 1:6, 1:8 and 1:10 molar ratio batches consist of a mixture of the two metastable vanadium dioxide polymorphs, the monoclinic $VO_2(B)$ and the tetragonal $VO_2(A)$ only. The structures of these two polymorphs were presented in the introductory section of this project. The peaks corresponding to the monoclinic (B) polymorph are more intense than the peaks of the tetragonal (A) polymorph in all of these batches. Specifically, an increase of the main peaks of the tetragonal polymorph can be observed from 1:2 to 1:4 and 1:6, whereas on higher molar ratios the peaks of the tetragonal (A) are reduced and the crystallinity of the products seem to diminish, suggesting that an oxalic acid excess of x2 to x3 times higher than the suggested by chemical eq. (1) can produce better materials, for 9 g/L of V_2O_5 configurations.

3.1.1.c. XRD patterns for the as obtained at 3 g/L V_2O_5 concentration

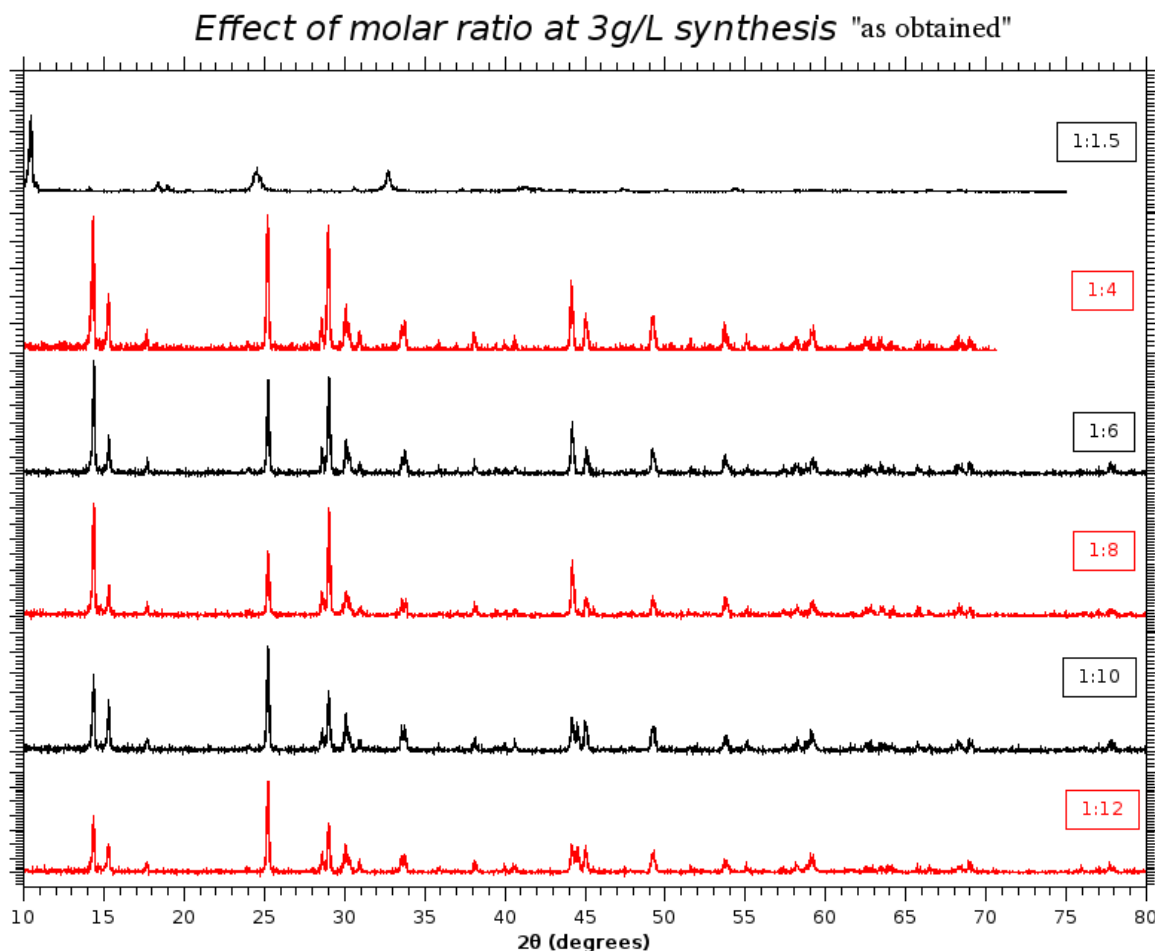


Figure 3.3 X-ray diffraction patterns of “as obtained” samples with configurations of 3 g/L V_2O_5 and various molar ratios of the reagents.

For the synthesis with low concentration of vanadium precursor, we tested the configurations with a molar ratio of 1:1.5, 1:4, 1:6, 1:8, 1:10 and 1:12. From the XRD patterns shown on Figure 3.3 we can deduce several conclusions. The 1:1.5 molar ratio batch consists of a mixture of unidentifiable peaks, with some of them attributed to the hydrated vanadium oxides, $V_3O_7 \cdot H_2O$ (oxidation state of +4.7) and $V_5O_{12} \cdot 6H_2O$ (oxidation state of +4.8), as expected since the reducing agent is less than the necessary to reduce V^{+5} to V^{+4} . In contrast, the 1:4, 1:6, 1:8, 1:10 and 1:12 molar ratio batches consist of a mixture of the two metastable vanadium dioxide polymorphs, the monoclinic $VO_2(B)$ and the tetragonal $VO_2(A)$. The structures of these two polymorphs were presented in the introductory section of this project. The peaks corresponding to the monoclinic (B) polymorph are more intense than the peaks of the tetragonal (A) polymorph in all of these batches. Higher crystallinity was achieved in the 1:4 and 1:6 molar ratio batches, suggesting again that an oxalic acid excess of x2 to x3 times higher than the suggested by chemical eq. (1) can produce better materials, for the low concentration of vanadium precursor configurations.

3.1.2. After annealing (“final” products)

3.1.2.a. XRD patterns for the final products at 18 g/L V_2O_5 concentration

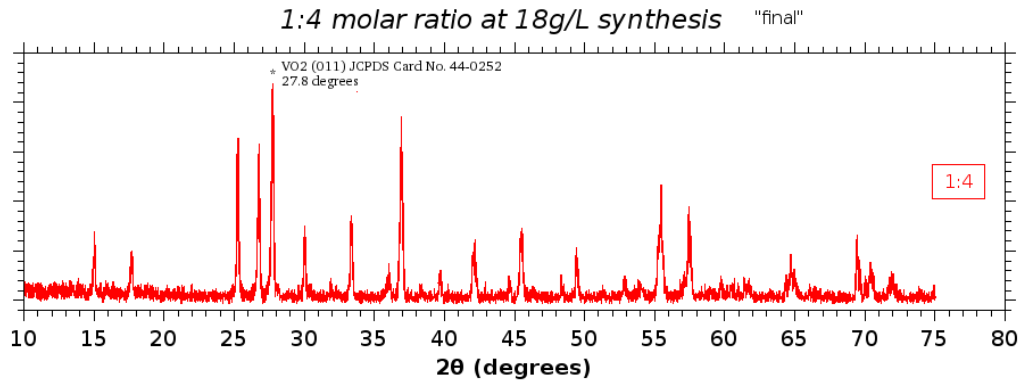


Figure 3.4 X-ray diffraction patterns of “final” sample with a configuration of 18 g/L V_2O_5 and 1:4 molar ratio of the reagents (the characteristic 27.8 degrees peak of $VO_2(M)$ has been noted with an asterisk).

From the XRD pattern shown on Figure 3.4 we have identified the thermochromic polymorph monoclinic $VO_2(M)$ (JCPDS Card No. 44-0252, $P21/c$, $a=4.506 \text{ \AA}$, $b=2.899 \text{ \AA}$, $c=4.617 \text{ \AA}$ and $\beta=91.79^\circ$) and the oxide V_6O_{13} (ox. state +4.3). The characteristic peak of $VO_2(M)$ is visible at 27.8 degrees, along with other peaks of the V_6O_{13} oxide impurity.

3.1.2.b. XRD patterns for the final products at 9 g/L V_2O_5 concentration

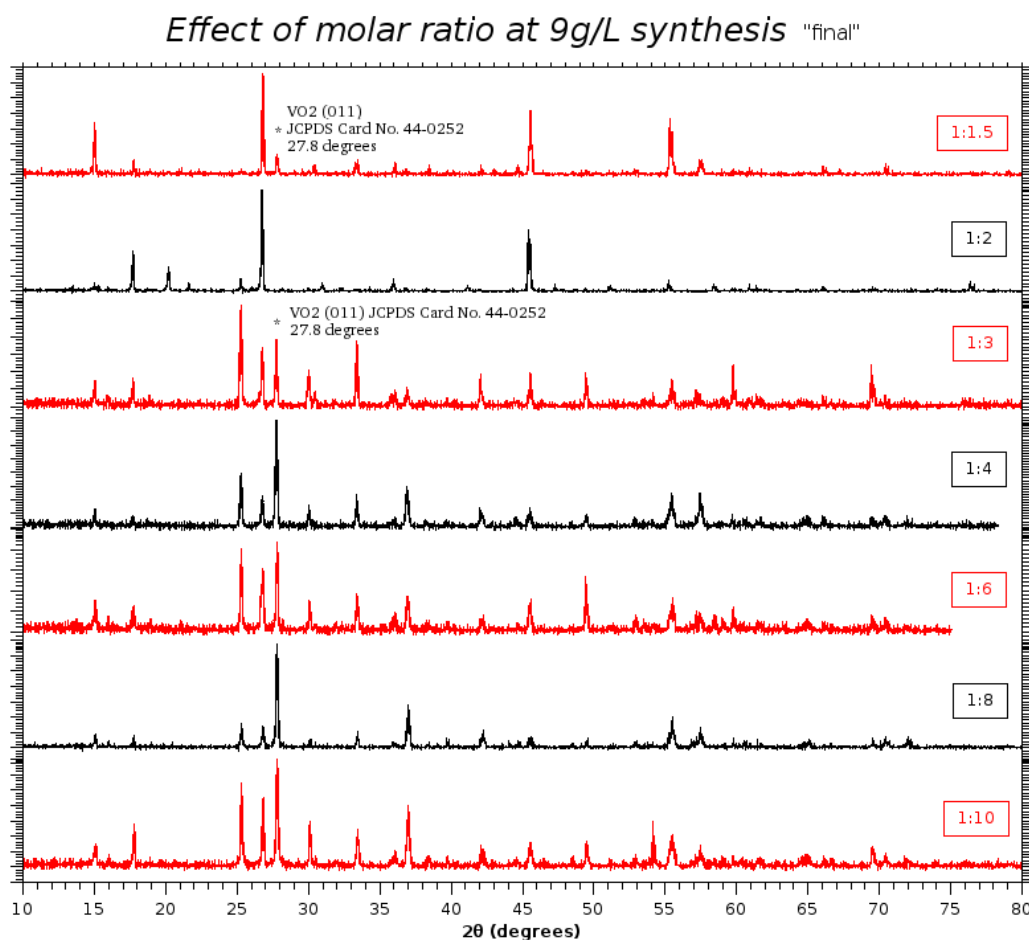


Figure 3.5 X-ray diffraction patterns of “final” samples with configurations of 9 g/L V_2O_5 and various molar ratios of the reagents (the characteristic 27.8 degrees peak of $VO_2(M)$ has been noted with an asterisk).

From the XRD patterns shown on Figure 3.5 we can deduce several conclusions. The 1:1.5 molar ratio batch consists mostly of vanadium oxide V_6O_{13} (oxidation state of +4.3), with the presence of small peaks of the monoclinic thermochromic crystalline phase $VO_2(M)$ (JCPDS Card No. 44-0252). Still, the 1:2 molar ratio batch consists of a mixture of vanadium oxides V_6O_{13} and V_2O_5 (oxidation state of +5), possibly due to some partial oxidation of the material during the annealing process, since the rest of the batches with 1:3, 1:4, 1:6, 1:8 and 1:10 molar ratio have a strong presence of the $VO_2(M)$ peaks, along with the vanadium oxide V_6O_{13} . Batches 1:4 and 1:8, in the case of the 9 g/L vanadium precursor, seem to have a greater presence of the monoclinic thermochromic polymorph, than the +4.3 vanadium oxidation state oxide, whereas the rest of the batches have either less of the desired thermochromic phase or a very high impurity of V_6O_{13} . The structures of these oxides were presented in the introductory section of this project.

3.1.2.c. XRD patterns for the final products at 3 g/L V_2O_5 concentration

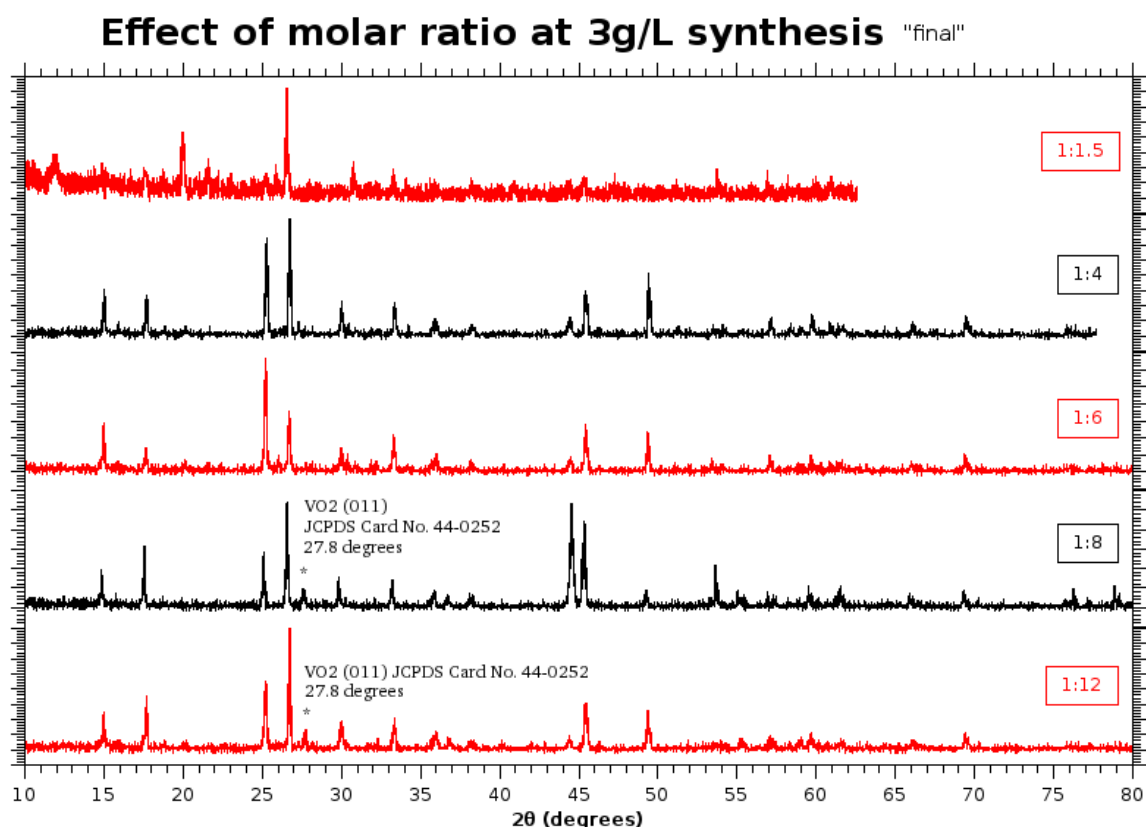


Figure 3.6 X-ray diffraction patterns of “final” samples with configurations of 3 g/L V_2O_5 and various molar ratios of the reagents (the characteristic 27.8 degrees peak of $VO_2(M)$ has been noted with an asterisk).

From the XRD patterns shown on Figure 3.6 we can deduce several conclusions. The 1:1.5 molar ratio batch consists of a mixture of vanadium oxides, the V_6O_{13} (oxidation state of +4.3) and the V_4O_9 (oxidation state of +4.5). Then, the 1:4 and 1:6 molar ratio batches consist of a mixture of vanadium oxides V_6O_{13} and V_2O_5 (oxidation state of +5). The rest of the batches with 1:8 and 1:12 molar ratio have a subtle presence of the $VO_2(M)$ peaks, along with the oxides V_4O_9 and $VO_2(A)$ for 1:8 and oxide V_6O_{13} for 1:12. Unfortunately, no 1:10 molar ratio batch was saved after the annealing for structural characterization. So, for the case of the low (3 g/L) concentration of vanadium precursor, we can deduce that only with an oxalic acid excess of x4 or x6 times higher than the suggested by chemical eq. (1) we can detect peaks of the desired thermochromic polymorph.

3.2 Parameter: V_2O_5 concentration

As we already seen by the results in the previous section, different concentrations of the vanadium precursor will result to different vanadium oxides and/or polymorphs. In this section the same data will be presented, but in regards to the effect of V_2O_5 concentration. For the purpose of this project, we experimented with V_2O_5 concentrations of 3 g/L, 9 g/L and 18 g/L, in order to see the effects, while other synthetic parameters, like the molar ratio, pH, temperature and duration, were kept constants.

3.2.1. Before annealing (“as obtained” products)

3.2.1.a. XRD patterns for the as obtained at 1:1.5 molar ratio

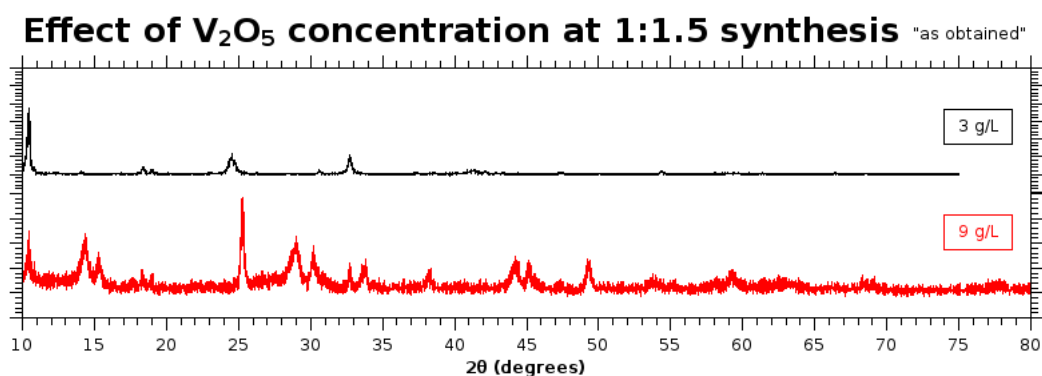


Figure 3.7 X-ray diffraction patterns of “as obtained” samples with configurations of 1:1.5 molar ratios of the reagents and various concentrations of V_2O_5 .

For the synthesis with 1:1.5 precursors molar ratio, we tested the configurations with a V_2O_5 concentrations of 3 g/L and 9 g/L. From the XRD patterns shown on Figure 3.7 we can deduce several conclusions. The 3 g/L batch consists of a mixture of unidentifiable peaks, with some of them attributed to the hydrated vanadium oxides, $V_3O_7 \cdot H_2O$ (oxidation state of +4.7) and $V_5O_{12} \cdot 6H_2O$ (oxidation state of +4.8), whereas the 9 g/L batch consists of a mixture of the hydrated vanadium oxide, $V_6O_7 \cdot H_2O$ (oxidation state of +2.3), the monoclinic $VO_2(B)$ and the tetragonal $VO_2(A)$ with less intense peaks. As stated previously, the 1:1.5 molar ratio according to the chemical eq. (1) is not enough to fully reduce the V^{5+} to V^{4+} , as shown by the results of the 3 g/L configuration. Still when increasing to a higher concentration of vanadium precursor, we can achieve a partial oxidation to the V^{4+} .

3.2.1.b. XRD patterns for the as obtained at 1:2 molar ratio

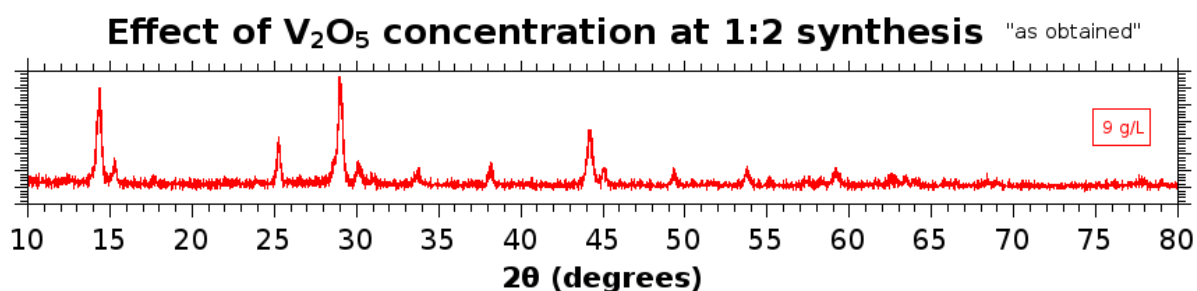


Figure 3.8 X-ray diffraction pattern of “as obtained” sample with configurations of 1:2 molar ratios of the reagents and a 9 g/L concentration of V₂O₅.

For the synthesis with 1:2 precursors molar ratio, we tested only the configuration with a V₂O₅ concentration of 9 g/L. From the XRD pattern shown on Figure 3.8 we identified the material as a mixture of the two metastable vanadium dioxide polymorphs, mostly of the monoclinic VO₂(B) and in very small traces the tetragonal VO₂(A).

3.2.1.c. XRD patterns for the as obtained at 1:3 molar ratio

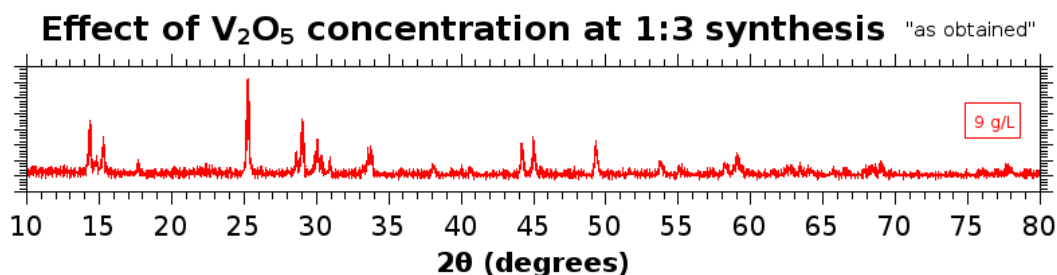


Figure 3.9 X-ray diffraction pattern of “as obtained” sample with configurations of 1:3 molar ratios of the reagents and a 9 g/L concentration of V₂O₅.

For the synthesis with 1:3 precursors molar ratio, we tested only the configuration with a V₂O₅ concentration of 9 g/L. From the XRD pattern shown on Figure 3.9 we identified the material as a mixture of the two metastable vanadium dioxide polymorphs, of the monoclinic VO₂(B) and the tetragonal VO₂(A), with peaks of the monoclinic VO₂(B) having about three times higher intensity than the peaks of the tetragonal VO₂(A).

3.2.1.d. XRD patterns for the as obtained at 1:4 molar ratio

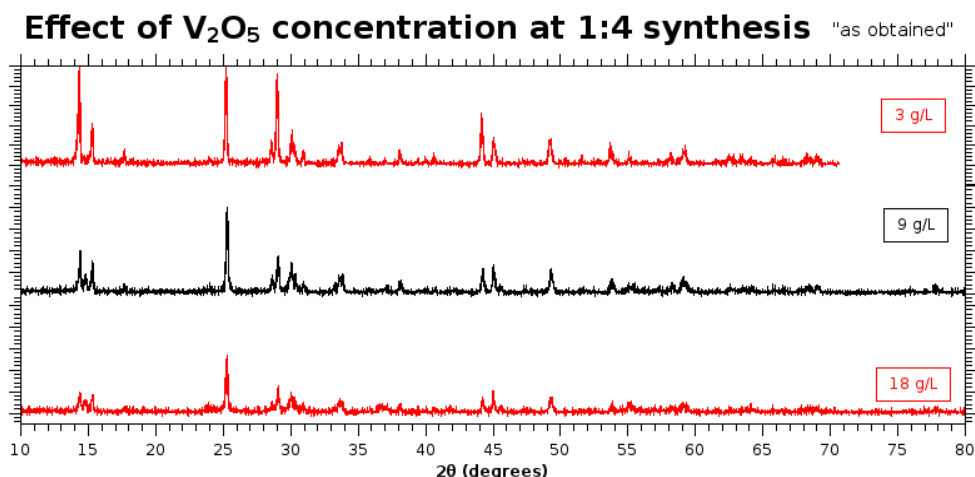


Figure 3.10 X-ray diffraction patterns of “as obtained” samples with configurations of 1:4 molar ratios of the reagents and various concentrations of V₂O₅.

For the synthesis with 1:4 precursors molar ratio, we tested the configurations with a V₂O₅ concentrations of 3 g/L, 9 g/L and 18 g/L. From the XRD patterns shown on *Figure 3.10* all of the tested batches were identified as a mixture of the two metastable vanadium dioxide polymorphs, the monoclinic VO₂(B) and the tetragonal VO₂(A), with the 3 g/L batch having little presence of the tetragonal VO₂(A) polymorph. Higher V₂O₅ concentrations seem to promote the formation of tetragonal metastable VO₂(A) polymorph over the monoclinic metastable VO₂(B) polymorph.

3.2.1.e. XRD patterns for the as obtained at 1:6 molar ratio

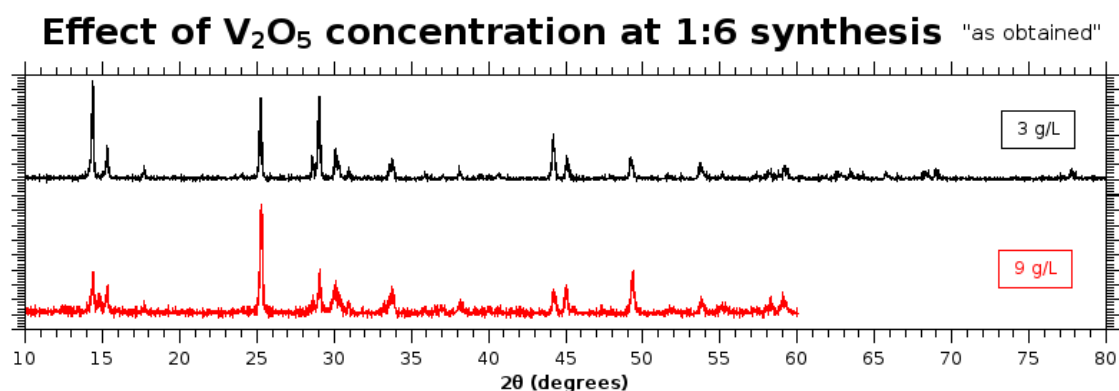


Figure 3.11 X-ray diffraction patterns of “as obtained” samples with configurations of 1:6 molar ratios of the reagents and various concentrations of V₂O₅.

For the synthesis with 1:6 precursors molar ratio, we tested the configurations with a V₂O₅ concentrations of 3 g/L and 9 g/L. From the XRD patterns shown on *Figure 3.11* we can observe the same pattern with previous results. The low concentration batch was identified as pure VO₂(B), whereas the medium concentration batch was identified as a mixture of VO₂(B) and VO₂(A) polymorphs.

3.2.1.f. XRD patterns for the as obtained at 1:8 molar ratio

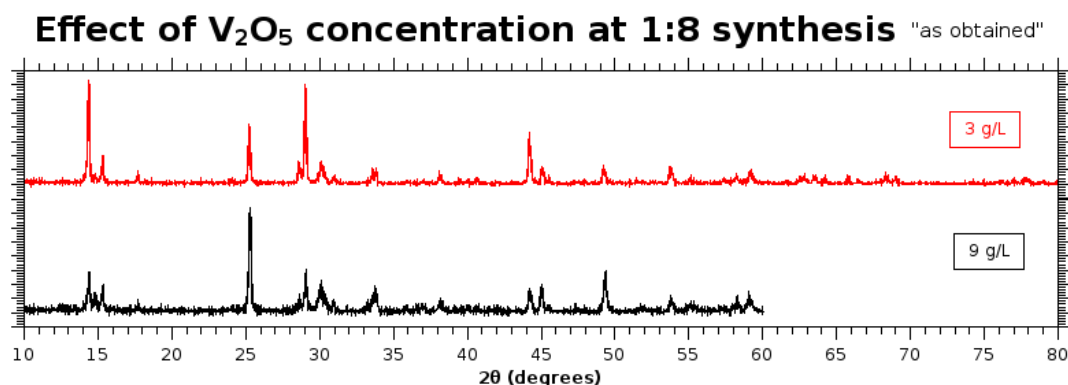


Figure 3.12 X-ray diffraction patterns of “as obtained” samples with configurations of 1:8 molar ratios of the reagents and various concentrations of V₂O₅.

For the synthesis with 1:8 precursors molar ratio, we tested the configurations with a V₂O₅ concentrations of 3 g/L and 9 g/L. From the XRD patterns shown on Figure 3.12 we can observe the same pattern with previous results. Both tested batches were identified as a mixture of the two metastable vanadium dioxide polymorphs, the monoclinic VO₂(B) and the tetragonal VO₂(A), with the 3 g/L batch having little presence of the tetragonal VO₂(A) polymorph. Again, higher V₂O₅ concentrations seem to promote the formation of tetragonal metastable VO₂(A) polymorph over the monoclinic metastable VO₂(B) polymorph.

3.2.1.g. XRD patterns for the as obtained at 1:10 molar ratio

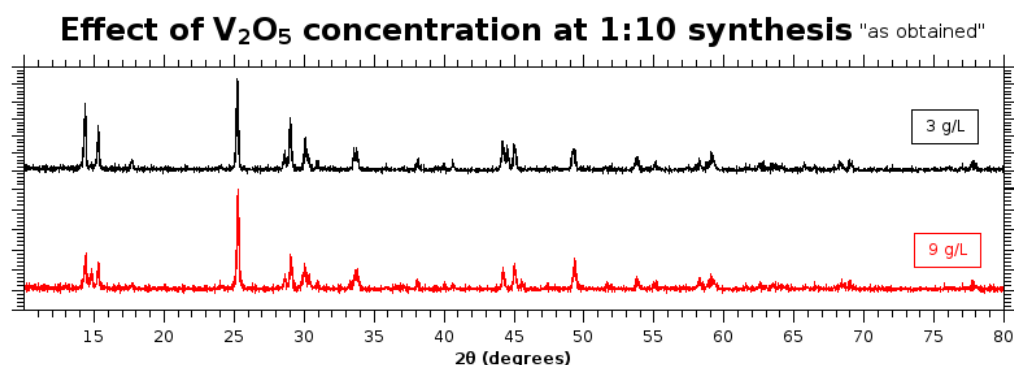


Figure 3.13 X-ray diffraction patterns of “as obtained” samples with configurations of 1:10 molar ratios of the reagents and various concentrations of V₂O₅.

For the synthesis with 1:10 precursors molar ratio, we tested the configurations with a V₂O₅ concentrations of 3 g/L and 9 g/L. From the XRD patterns shown on Figure 3.13 we can observe the same pattern with previous results. Both tested batches were identified as a mixture of the two metastable

vanadium dioxide polymorphs, the monoclinic VO₂(B) and the tetragonal VO₂(A), with the 3 g/L batch having little presence of the tetragonal VO₂(A) polymorph. Again, higher V₂O₅ concentrations seem to promote the formation of tetragonal metastable VO₂(A) polymorph over the monoclinic metastable VO₂(B) polymorph.

3.2.1.h. XRD patterns for the as obtained at 1:12 molar ratio

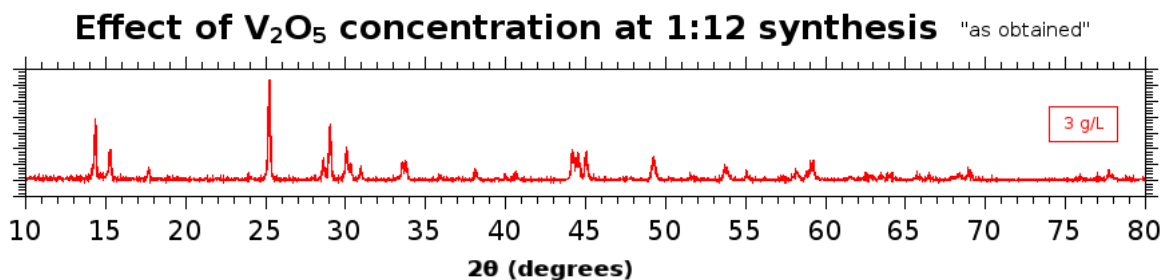


Figure 3.14 X-ray diffraction patterns of “as obtained” sample with configurations of 1:12 molar ratios of the reagents and a 3 g/L concentration of V₂O₅.

For the synthesis with 1:12 precursors molar ratio, we tested only the configuration with a V₂O₅ concentration of 3 g/L. From the XRD pattern shown on Figure 3.14 we can observe the same pattern with previous results. Our sample identified as a mixture of the two metastable vanadium dioxide polymorphs, with a strong presence of the monoclinic VO₂(B) and a little presence of the tetragonal VO₂(A) polymorph.

3.2.2. After annealing (“final” products)

3.2.2.a. XRD patterns for the final products at 1:1.5 molar ratio

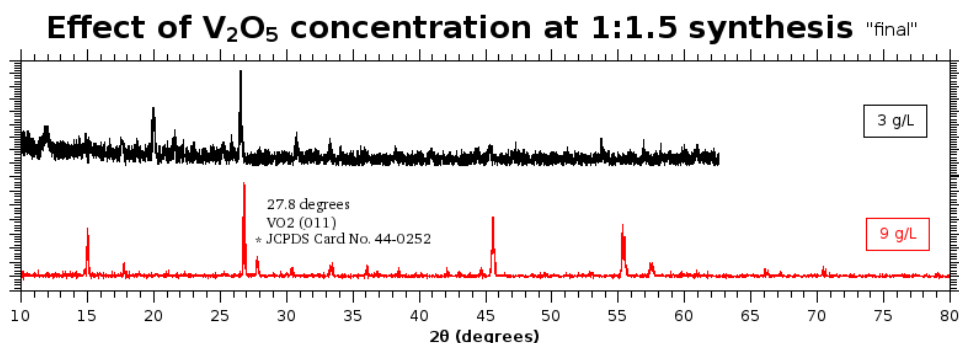


Figure 3.15 X-ray diffraction patterns of “final” samples with configurations of 1:1.5 molar ratios of the reagents and various concentrations of V₂O₅ (the characteristic 27.8 degrees peak of VO₂(M) has been noted with an asterisk).

From the XRD pattern shown on *Figure 3.15* we can deduce several conclusions. The 3 g/L batch consists of a mixture of vanadium oxides, the V_6O_{13} (oxidation state of +4.3) and the V_4O_9 (oxidation state of +4.5). Whereas, the 9 g/L batch consists mostly of vanadium oxide V_6O_{13} (oxidation state of +4.3), with the presence of small peaks of the monoclinic thermochromic crystalline phase $VO_2(M)$ (JCPDS Card No. 44-0252). These results confirm that the concentration of the vanadium precursor has a crucial role over the formation of the desired thermochromic polymorph of vanadium dioxide, even when the reducing agent is in deficiency (1:1.5 molar ratio).

3.2.2.b. XRD patterns for the final products at 1:2 molar ratio

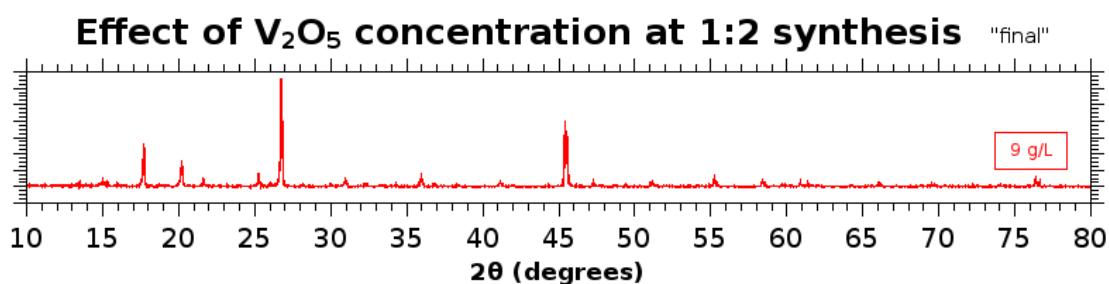


Figure 3.16 X-ray diffraction patterns of “final” samples with configurations of 1:2 molar ratios of the reagents and a 9 g/L concentration of V_2O_5 .

For the synthesis with 1:2 precursors molar ratio, we tested only the configuration with a V_2O_5 concentration of 9 g/L. From the XRD pattern shown on *Figure 3.16* we identified the sample as a mixture of the vanadium oxides V_6O_{13} (oxidation state of +4.3) and V_2O_5 (oxidation state of +5), possibly due to some partial oxidation of the material during the annealing process.

3.2.2.c. XRD patterns for the final products at 1:3 molar ratio

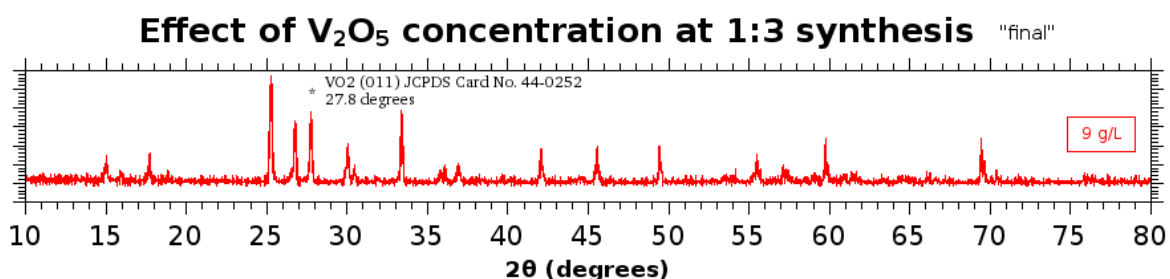


Figure 3.17 X-ray diffraction patterns of “final” samples with configurations of 1:3 molar ratios of the reagents and a 9 g/L concentration of V_2O_5 (* : 27.8 degrees peak of $VO_2(M)$).

For the synthesis with 1:3 precursors molar ratio, we tested only the configuration with a V_2O_5 concentration of 9 g/L. From the XRD pattern shown on *Figure 3.17* we identified the sample as a mixture of the $VO_2(M)$ thermochromic polymorph, along with strong vanadium oxide V_6O_{13} impurities.

3.2.2.d. XRD patterns for the final products at 1:4 molar ratio

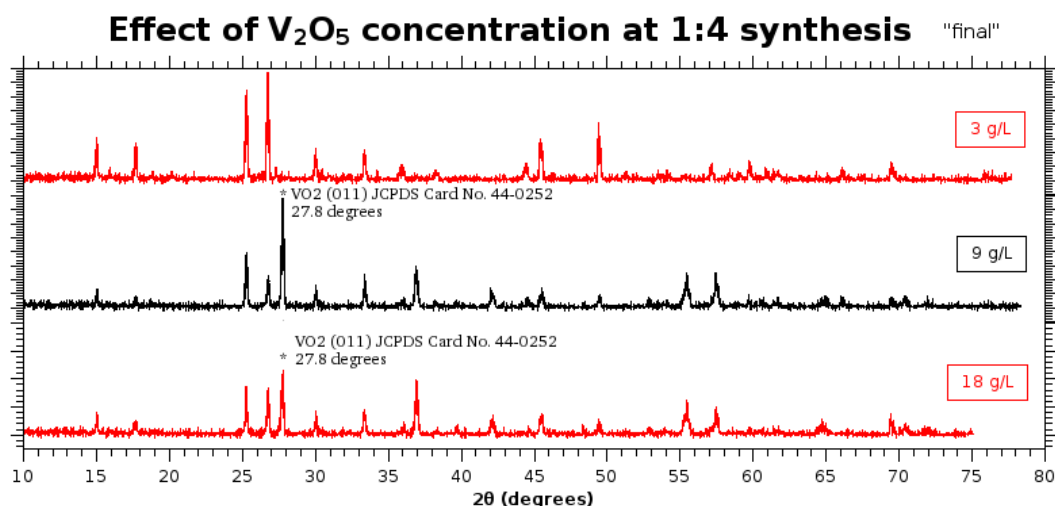


Figure 3.18 X-ray diffraction patterns of “final” samples with configurations of 1:4 molar ratios of the reagents and various concentrations of V_2O_5 (the characteristic 27.8 degrees peak of $VO_2(M)$ has been noted with an asterisk).

For the synthesis with 1:4 precursors molar ratio, we tested configurations with all three V_2O_5 concentrations, 3 g/L, 9 g/L and 18 g/L. From the XRD pattern shown on Figure 3.18 we can deduce several conclusions. The 3 g/L batch consists of a mixture of vanadium oxides, the V_6O_{13} (oxidation state of +4.3) and the V_2O_5 (oxidation state of +5). Whereas, the 9 g/L and 18 g/L batches consist mostly of the thermochromic polymorph $VO_2(M)$, along with some vanadium oxide V_6O_{13} impurities. The medium concentration (9 g/L) configuration seems to give products of better crystallinity than that of higher concentration (18 g/L).

3.2.2.e. XRD patterns for the final products at 1:6 molar ratio

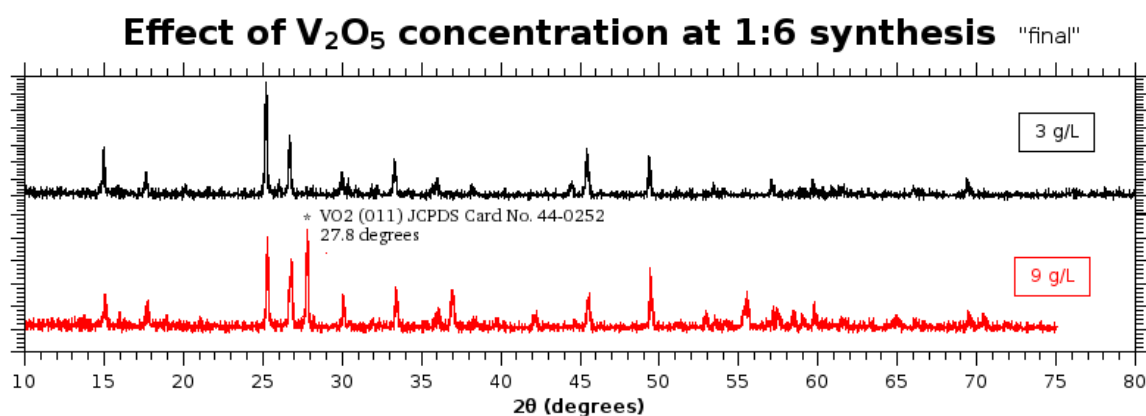


Figure 3.19 X-ray diffraction patterns of “final” samples with configurations of 1:6 molar ratios of the reagents and various concentrations of V_2O_5 (the characteristic 27.8 degrees peak of $VO_2(M)$ has been noted with an asterisk).

For the synthesis with 1:6 precursors molar ratio, we tested configurations with V_2O_5 concentrations 3 g/L and 9 g/L. From the XRD pattern shown on *Figure 3.19* we can deduce several conclusions. The 3 g/L batch consists of a mixture of vanadium oxides, the V_6O_{13} (oxidation state of +4.3) and the V_2O_5 (oxidation state of +5). Whereas, the 9 g/L batch consists of a mixture of the thermochromic polymorph $VO_2(M)$ and the oxide V_6O_{13} . Again, these results confirm that the concentration of the vanadium precursor has a crucial role over the formation of the desired thermochromic polymorph of vanadium dioxide.

3.2.2.f. XRD patterns for the final products at 1:8 molar ratio

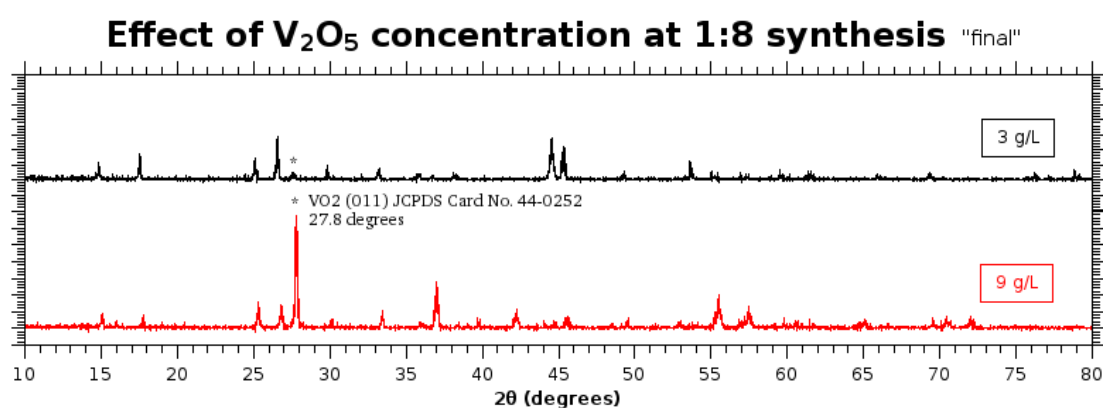


Figure 3.20 X-ray diffraction patterns of “final” samples with configurations of 1:8 molar ratios of the reagents and various concentrations of V_2O_5 (the characteristic 27.8 degrees peak of $VO_2(M)$ has been noted with an asterisk).

For the synthesis with 1:6 precursors molar ratio, we tested configurations with V_2O_5 concentrations 3 g/L and 9 g/L. From the XRD pattern shown on *Figure 3.20* we can deduce several conclusions. For the 3 g/L batch a subtle presence of the $VO_2(M)$ peaks, along with the oxides V_4O_9 (oxidation state of +4.5) and $VO_2(A)$ was identified, whereas for the 9 g/L a strong presence of the $VO_2(M)$ peaks, along with little vanadium oxide V_6O_{13} (oxidation state of +4.3) impurities. Again we see, as with previous results, the importance of the concentration of the vanadium precursor to the hydrothermal synthesis for thermochromic VO_2 .

3.2.2.g. XRD patterns for the final products at 1:10 molar ratio

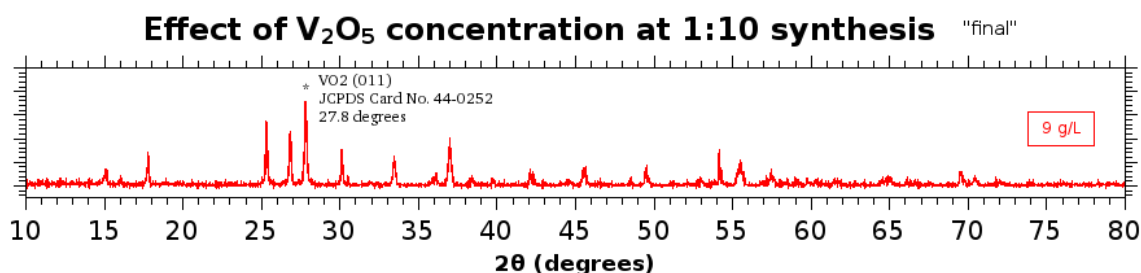


Figure 3.21 X-ray diffraction patterns of “final” samples with configurations of 1:10 molar ratios of the reagents and a 9 g/L concentration of V₂O₅.

Unfortunately, no “3 g/L & 1:10” batch material was saved after the annealing for structural characterization. Still, from the characterization of the XRD pattern shown on *Figure 3.20* we identified the 9 g/L as the thermochromic monoclinic VO₂(M) polymorph, along with visible vanadium oxide V₆O₁₃ (oxidation state of +4.3) impurities.

3.2.2.h. XRD patterns for the final products at 1:12 molar ratio

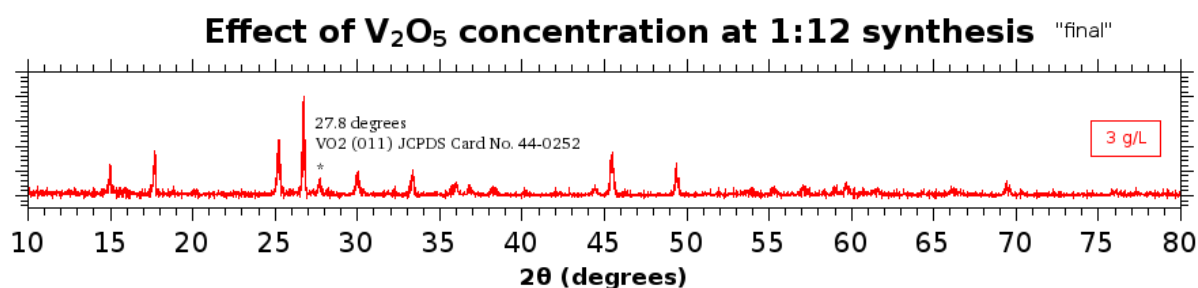


Figure 3.22 X-ray diffraction patterns of “final” samples with configurations of 1:12 molar ratios of the reagents and a 3 g/L concentration of V₂O₅.

For the synthesis with 1:12 precursors molar ratio, we tested only the configuration with a V₂O₅ concentration of 3 g/L. From the XRD pattern shown on *Figure 3.22* we can observe the same pattern with previous results. Our sample identified as a mixture of the oxide V₆O₁₃ (oxidation state of +4.3) mostly, along with a small presence of the thermochromic monoclinic VO₂(M) polymorphs.

3.3 Conclusions over the effect of the synthetic reagents concentrations

In the previous two chapters we discussed the effect of both the synthetic reagents concentrations over our hydrothermal synthesis and the products obtained, either by an expression of reagents molar ratio with an change in the moles of oxalic acid used, or by an expression of the concentration of the vanadium precursor in our reagents solution. From the data presented, we can sum up the conclusions of these two separate parameters in order to agree on an optimal configuration of reagents concentrations, for the following tested parameters.



Regarding the oxalic acid, we concluded that a higher concentration, up to x2 or x3 times the suggested amount from the chemical equation (1), can promote the formation of the second intermediate metastable polymorph $\text{VO}_2(\text{A})$ over the formation of the first intermediate metastable polymorph $\text{VO}_2(\text{B})$ for the “as obtained” products, thus leading to an increase in the formation of $\text{VO}_2(\text{M})$ over the products mixtures/impurities for the “final” products, confirming the suggestions of our bibliography^{[1.2.31],[1.2.32]}. Also, it promotes the formation of higher crystallinity materials in both stages of our synthetic procedure. This is the case especially for the higher concentrations of vanadium precursor.

In accordance, regarding the vanadium precursor V_2O_5 , we concluded that a medium to high concentration, of 9 g/L or 18 g/L, can promote the formation of the second intermediate metastable polymorph $\text{VO}_2(\text{A})$ over the formation of the first intermediate metastable polymorph $\text{VO}_2(\text{B})$ for the “as obtained” products, thus leading to an increase in the formation of $\text{VO}_2(\text{M})$ over the products mixtures/impurities for the “final” products, as in the case above, especially when with higher concentrations of oxalic acid. In contrast, it won't always promote the formation of higher crystallinity materials, making it a more unrelated parameter to the quality of the final products.

In conclusion, by combining the best results of both concentrations, a configuration of optimized parameters can be achieved, between the 1:4 – 1:8 reagents molar ratio and 9 g/L of vanadium precursor.

synthetic optimisation through reagents concentrations

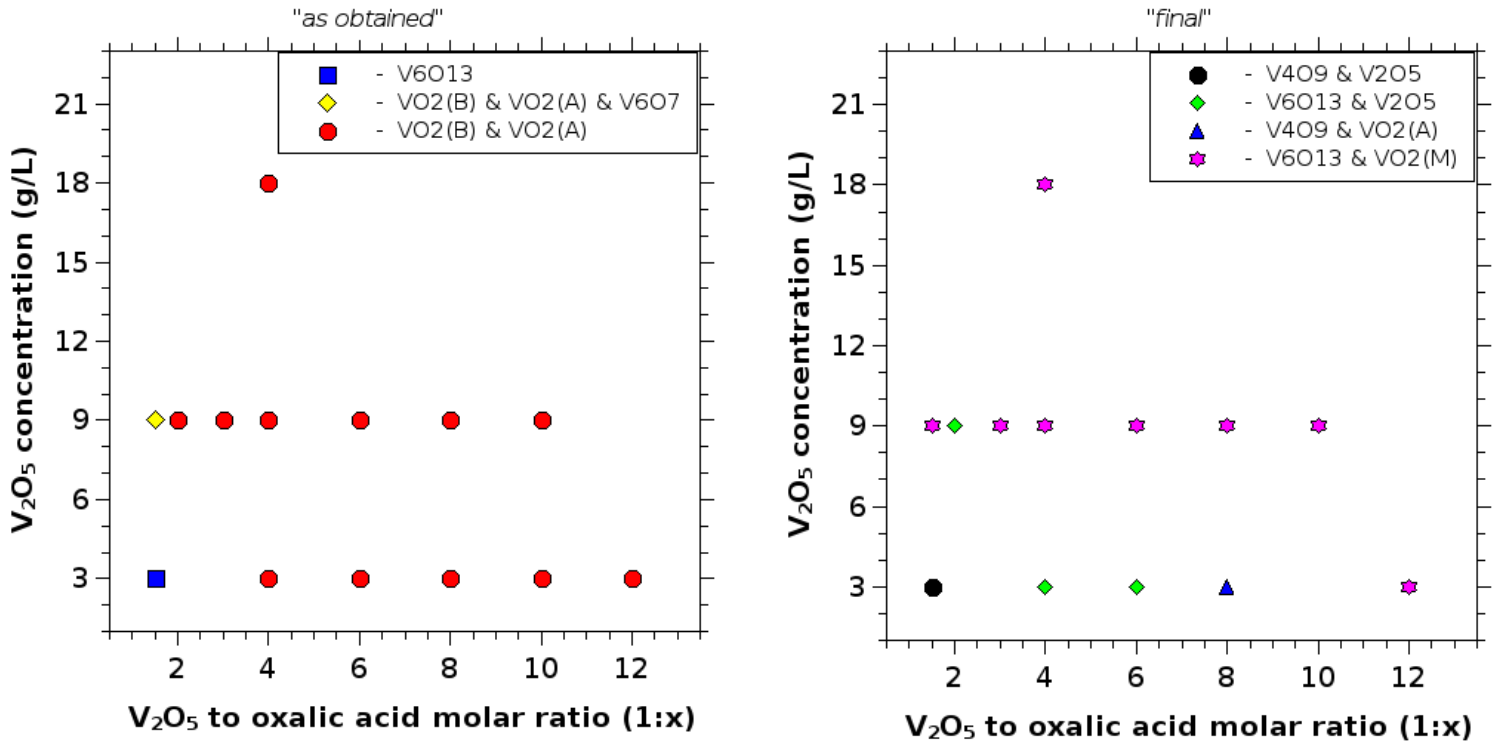


Figure 3.23 Graphical overview of XRD identification results of batches with configurations of different concentrations of reagents, before (left) and after (right) the annealing process. Optimal configuration and high quality materials can be achieved at a minimum of 9 g/L V₂O₅ and 1:4 V₂O₅ : oxalic acid molar ratio for our hydrothermal procedure.

3.4 Parameter: synthesis volume

Since the concentration of our reagents play a crucial role to the results of our synthetic procedures we deemed right to try some synthetic configurations on high concentrations of V_2O_5 . To do so, we still had to abide by the limits of maximum pressure and mass loadings suggested by the manufacturer company of the autoclave used. Thus, we decided to test these configurations on half the volume of our previous configurations used, so 20 mL of deionized water instead of 40 mL, and thus also experiment with the possible effect of reducing the synthesis volume.

When the volume of reagents solution is reduced, the pressure applied inside the autoclave during the hydrothermal procedure will be lower and the reaction will be less vigorous than with the configurations with higher loadings. As shown by our results, the only difference in reducing the synthesis volume is the slight increase of impurities at both our “as obtained” and “final” products.

For this parameter change we experimented with molar ratios of 1:1.5, 1:4, 1:8 and 1:12, while keeping a 18 g/L V_2O_5 concentration. Figure 3.24 shows the only configuration we have tested both on full synthesis volume and half synthesis volume. As stated above, the only effect for the “1:4 & 18 g/L” configurations is an increase on impurities when reducing the synthesis volume by half.

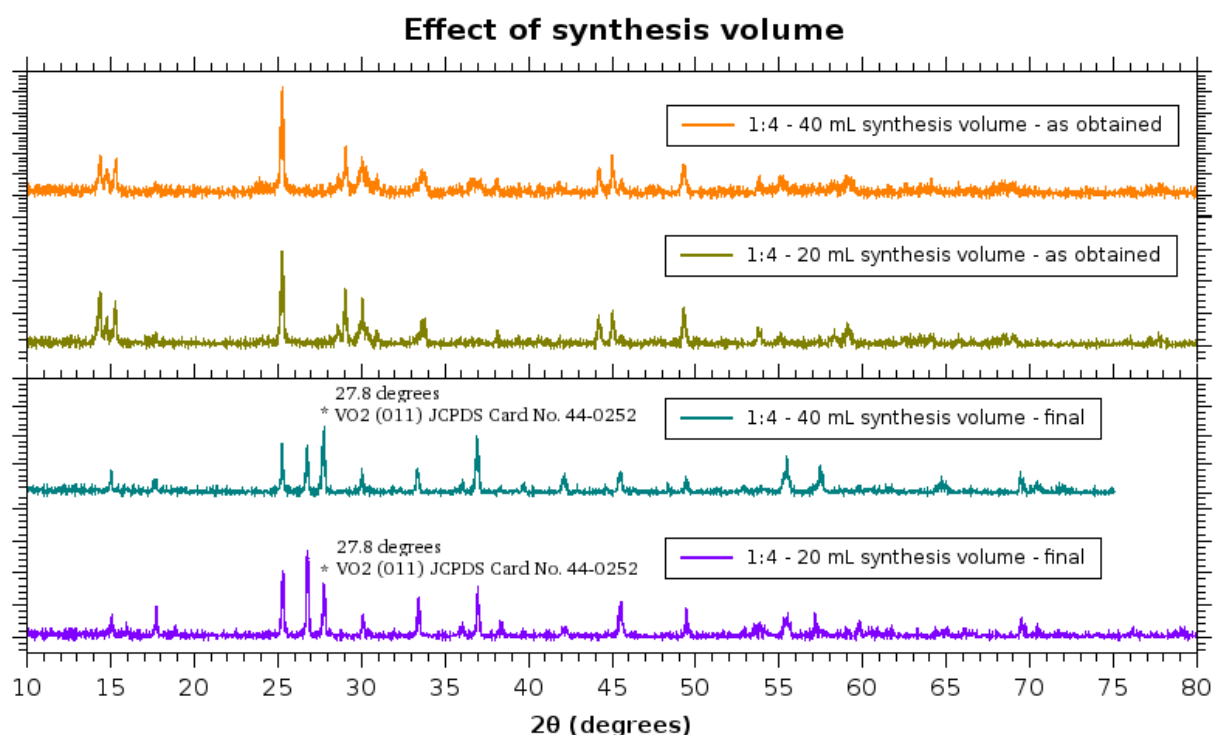


Figure 3.24 X-ray diffraction patterns of “as obtained” and “final” samples with configurations of 18 g/L V_2O_5 concentration, 1:4 reagents molar ratio and two different solution synthesis volume.

All of the configurations tested in the half volume synthesis parameter will be presented in the two following sections as “before” and “after” annealing results.

3.4.1. Before annealing (“as obtained” products)

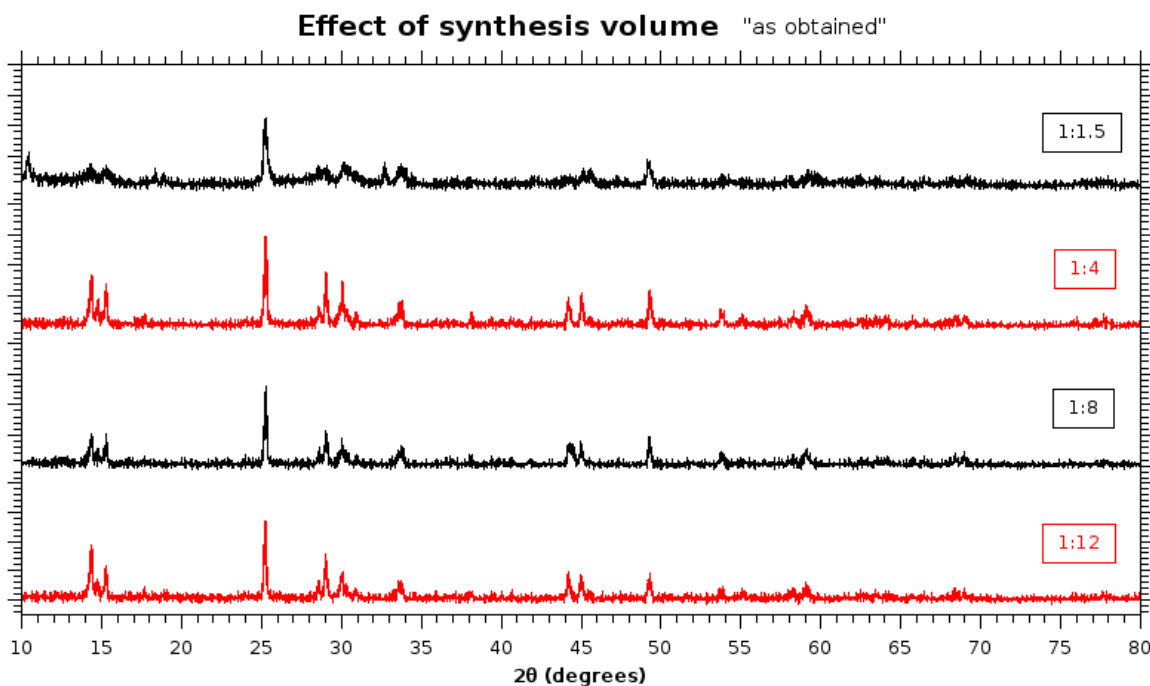


Figure 3.25 X-ray diffraction patterns of “as obtained” samples with configurations of 18 g/L concentration of V_2O_5 , half the reagents solution volume and various reagents molar ratios.

From the XRD data collected, shown on *Figure 3.25*, we can deduce several conclusions. The 1:1.5 molar ratio batch consists of a mixture of the metastable monoclinic $VO_2(B)$ polymorph and the hydrated vanadium oxide $V_6O_7 \cdot H_2O$ (oxidation state of +2.3). Still, the rest of the batches, 1:4, 1:8 and 1:12 consist of a mixture of the two metastable polymorphs, monoclinic $VO_2(B)$ and tetragonal $VO_2(A)$.

3.4.2. After annealing (“final” products)

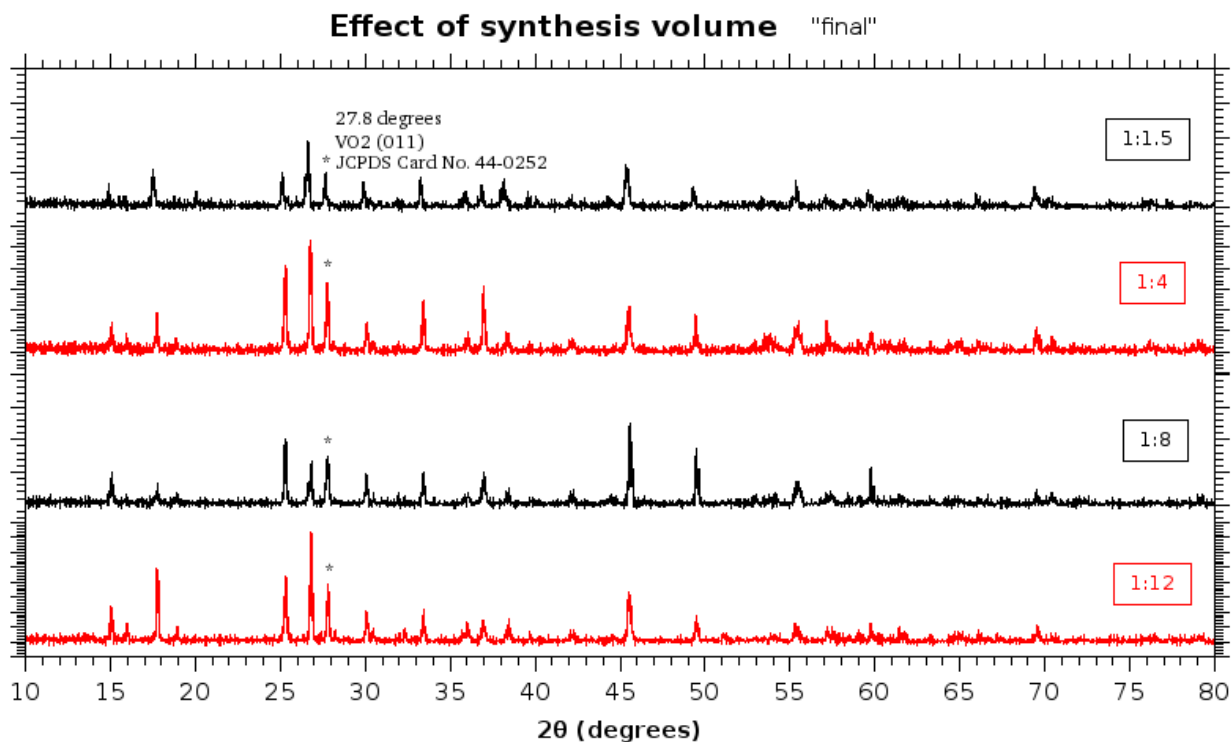


Figure 3.26 X-ray diffraction patterns of “final” samples with configurations of 18 g/L concentration of V₂O₅, half the reagents solution volume and various reagents molar ratios.

From the XRD patterns shown on Figure 3.26, we can identify a mixture of the vanadium oxides V₆O₁₃ (oxidation state of +4.3) and the thermochromic monoclinic VO₂(M) polymorph for all of the patches tested, along with some impurities of V₂O₅ (oxidation state of +5) on batch 1:1.5 and some impurities of V₁₂O₂₆ (oxidation state of +4.3) on 1:4.

3.5 Parameter: pH of synthesis

Since, at the time of our experimental procedures the “1:4 & 9 g/L” configuration seemed to be the batch with the better results, as explained above, we mostly used this to experiment with the rest of the changing chemical parameters. In everyone of our previously presented batches pH measurements were taken after each of every step of our synthetic procedure when possible. The pH measurements during the synthetic procedure for our basic configuration are presented below:

<i>Synthetic Step</i>	<i>pH value</i>
After 15 min of stirring the reagents solution	0.6
After 12h of hydrothermal procedure at 220°C	2.4

Table 3.2. pH values of our basic “1:4 & 9 g/L” configuration during different synthetic steps.

The idea was to experiment with the change of the pH value of our solution before the hydrothermal step, in order to find the optimal pH for this synthesis. This was achieved by addition of either NaOH solution for pH regulation to more basic values or HCl solution for pH regulation to more acidic values. *Table 3.3* summarizes the batches tested along with their pH values measured on both synthetic steps. As shown below, by adding extra solvents concentration of V₂O₅ drops, so the new values for each synthesis solution has been calculated.

pH regulation after the 15 min stirring step		New calculated V ₂ O ₅ concentration	After hydrothermal step	notes
≈ 10 mL NaOH 1M	pH = 2.0	≈ 7 g/L	pH = 6.3	Not enough solid product
≈ 14 mL NaOH 1M	pH = 4.2	≈ 7 g/L	pH = 6.8	Yield% = 12.1%
≈ 16 mL NaOH 1M	pH = 6.0	≈ 6.5 g/L	pH = 6.8	No solid products precipitated
≈ 20 mL NaOH 1M	pH = 8.0	≈ 6 g/L	pH = 6.8	No solid products precipitated
≈ 20 mL HCl 0.1M	pH = 0.4	≈ 6 g/L	pH = 1.7	Yield% = 57.8%
≈ 8 mL HCl 1M	PH = 0.1	≈ 7 g/L	pH = 1.8	Not enough solid product

Table 3.3. Characteristics of configurations with pH regulation prior the hydrothermal step.

As noted, most of these configurations produced no to little solid products. Even the batch with the best results (pH=0.4 regulation by HCl) gave a solid product at low yields (57.8%). For comparison, our basic configuration “1:4 & 9 g/L” has a higher yield (around 80%) and pH values after the 15 min stirring step are of 0.6 without any regulation.

On Figure 3.27 the XRD patterns of the two configurations that gave enough solid product for characterization are presented. Unfortunately, an even less amount from the “pH = 4.2 NaOH regulated” batch was recovered after the annealing process making it impossible to characterize with the equipment available to us. In contrast, the “pH = 0.4 HCl regulated” batch mass was enough for characterizations both prior and after the annealing process. To compare, the XRD patterns of our standard batch are also presented.

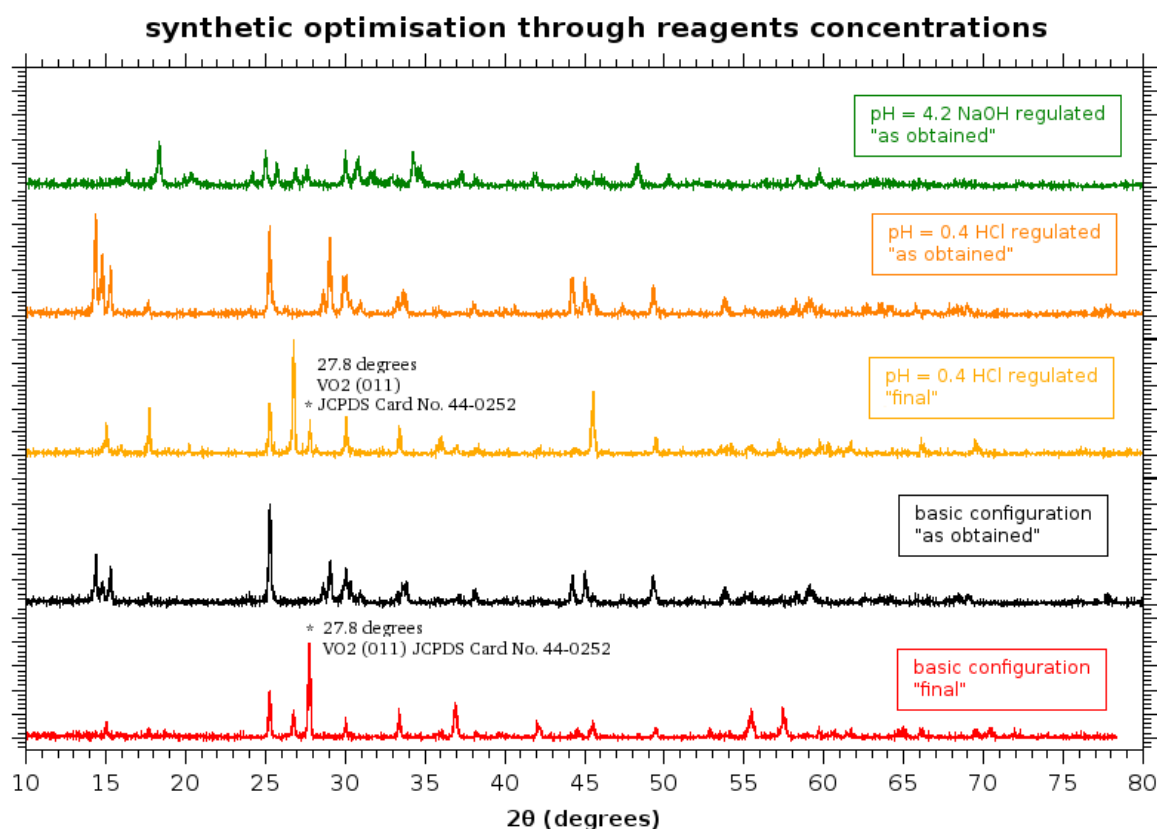


Figure 3.27 X-ray diffraction patterns of pH regulated samples prior and after the annealing process, along with patterns of our most basic configuration “1:4 & 9 g/L” for comparison.

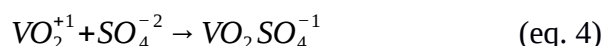
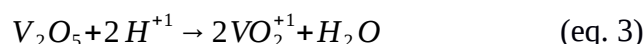
Not only the yields of our pH regulated batches are poor, we also identify them as mixtures of different compounds. On the “as obtained” NaOH regulated batch we can identify the oxide NaV_2O_5 along with other impurities of compounds of sodium. Still, that is not the case for the “as obtained” HCl regulated batch which was found to consist of a mixture of the two metastable polymorphs, monoclinic $\text{VO}_2(\text{B})$ and tetragonal $\text{VO}_2(\text{A})$. On the “final” HCl regulated batch we can identify the oxides V_6O_{13} (ox. state of +4.3), V_2O_5 (ox. state of +5) and the thermochromic monoclinic $\text{VO}_2(\text{M})$ polymorph. No chloride compounds were found in these configurations. From these results we can empirically conclude that for our synthetic procedure *no pH regulation is needed*, since the results are better when starting on a non regulated pH value of about “0.6”.

3.6 Effect of additives

As by now, we have found an optimized configuration by means of reagents concentrations, synthesis volume and starting pH for our hydrothermal synthesis. The next step was to try the effects of different additives, mostly based on suggestions from novel research of our bibliography. In this chapter we will present and discuss the results of two series of configurations: a series with additive Sulfuric Acid, H_2SO_4 , and another with additive Thiourea, $SC(NH_2)_2$. Additives used for doping will be discussed separately in the next chapter (see “3.7 Effect of dopants”).

3.6.1. Effect of additive Sulphuric Acid, H_2SO_4

As suggested by some novel research papers of our bibliography^{[3.1],[3.2],[3.3]}, sulphuric acid can be used as either an assistant in the formation and morphology control of $VO_2(R)$ in the hydrothermal process, as a pH regulator during the reagents mixture preparation, or as an additive to increase the vanadium leaching to the reaction solution. As explained by Tavakoli et al.^[3.3], by having sulphate/bi-sulphate anions in our reaction solution along with the pentavanadyl cations (VO_2^+), the dominant vanadium cation in acidic aqueous solutions (equation 3), the monosulphate complex VO_2HSO_4 can be formed (equation 4 and 5). Thus, an increase in vanadium solubility can be achieved due to this complexation, promoting the leaching of vanadium in reducing solutions from the 5+ oxidation state of the solid precursor to the 4+ soluble oxide ion, and enriching the overall solution chemistry of the system (overall reaction at low pH, equation 6).



To test the relevance of these observations to our own experimental system, we tested the effect of additive H_2SO_4 to our basic “1:4 & 9 g/L” configuration as well as for configuration “1:10 & 9 g/L” by adding 6-7 drops of dense H_2SO_4 solution before the hydrothermal procedure step. Results presented in *Figure 3.28* show the effect of additive H_2SO_4 to our system.

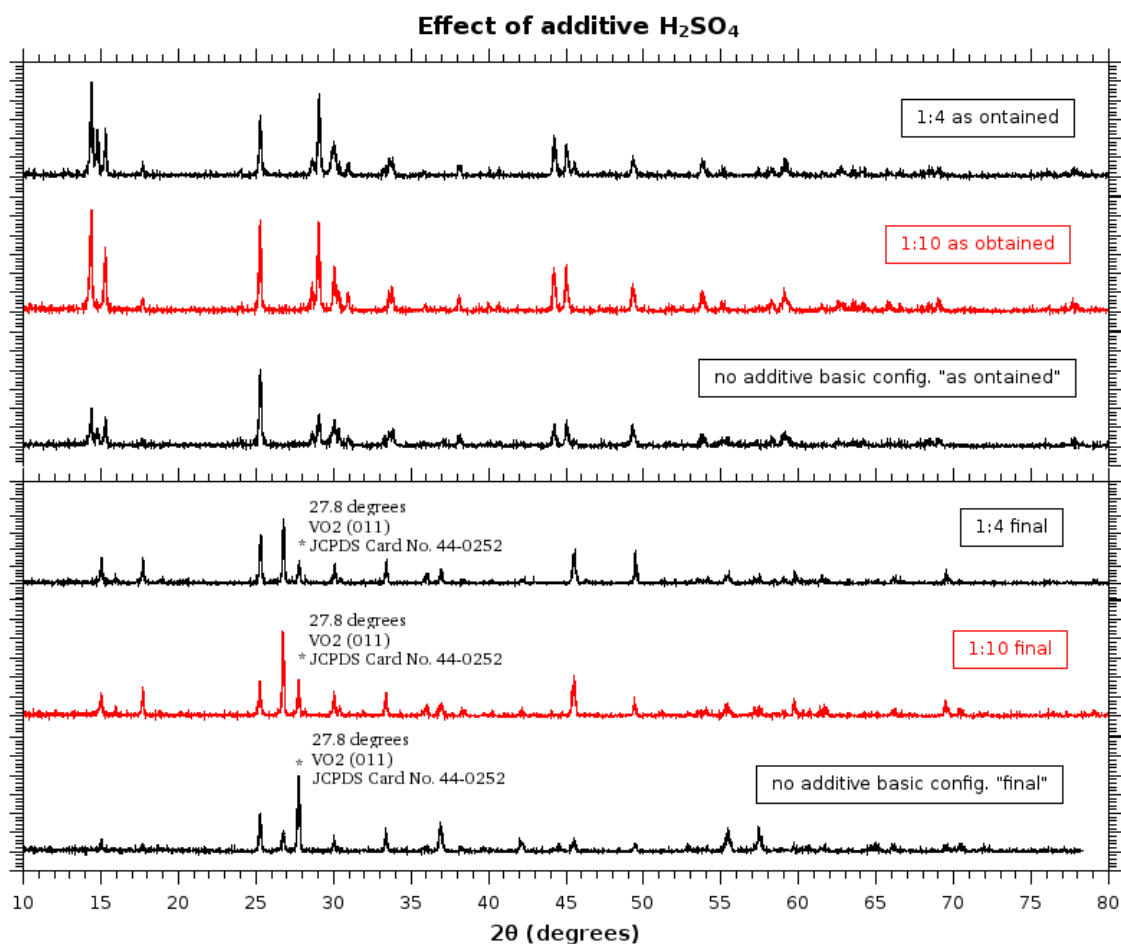


Figure 3.28 X-ray diffraction patterns of configurations with additive H_2SO_4 and of our basic configuration, prior and after the annealing process.

Compared to the results of our basic configuration, sulphuric acid seems to promote $VO_2(B)$ and (A) formation during the hydrothermal step of our synthesis, giving higher crystallinity products. However, after the annealing process we seem to get products with greater V_6O_{13} oxide impurities and $VO_2(M)$ peaks are of lower crystallinity. Thus, we can conclude that additive sulphuric acid can be used as an pH regulator and assistant additive for the more efficient formation of the metastable phases of VO_2 , as suggested by the work of Li R. and Liu C.^[3,2]

In addition, pH measurements were done prior and after the addition of sulphuric acid to our reagents solution, as presented on Table 3.4 :

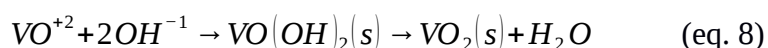
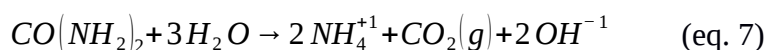
configuration	pH before H_2SO_4 addition	pH after H_2SO_4 addition
“1:4 & 9 g/L”	0.47	0.28
“1:10 & 9 g/L”	0.45	0.30

Table 3.4. pH values of configurations with H_2SO_4 addition prior the hydrothermal step.

3.6.2. Effect of additive Thiourea, $SC(NH_2)_2$

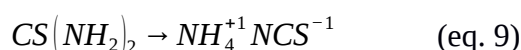
As a continuation of our experimentation presented through this chapter, after having tested additive H_2SO_4 we kept looking for novel research and reports of additives used on hydrothermal procedures similar to our own, to experiment with. In few papers we found suggestions of additive urea to be linked with the formation of our final desired product^{[3.4],[3.5],[3.6]}, achieving greater crystallinity and morphology control of thermochromic VO_2 product.

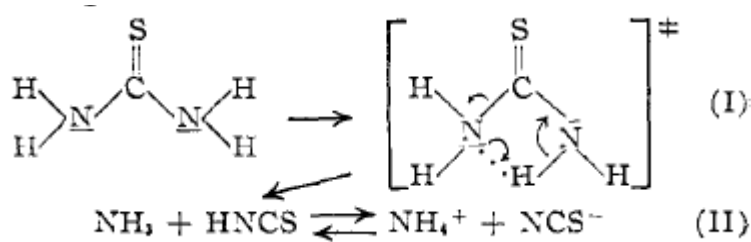
In literature urea is referred to be of used as a homogeneous precipitation agent for various transition metal oxides.^{[3.5][3.7]} Its decomposition will produce ammonia and carbon dioxide for temperatures over 60 °C accompanied by a *slow, gradual and uniform rise in pH throughout the whole solution* which can result in the nucleation and growth of uniformly nanosized particles. In our case, for the hydrothermal synthesis of thermochromic VO_2 , Li W. et al.^[3.5] suggested that through the dissolution of urea in aqueous media (equation 7), the pentavanadyl cations (VO_2^+), the dominant vanadium cation in acidic aqueous solutions, can gradually be precipitated by a slowly pH shift from the original acidic to alkaline (equation 8) as VO_2 , for the hydrothermal reducing reaction system.



When discussing our observations from the addition of sulphate/bi-sulphate anions in our reaction solution, by the sulphuric acid additive in the previous subsection, along with the suggestions mentioned in the bibliography of this subsection on using additive urea, the idea of testing similar but untested reagents that are available to us was the next logical step. Thus we decided to explore the effect that additive thiourea will have in our system.

According to the literature^{[3.8][3.9]} when thermally heated in an oven thiourea will be either decomposed to ammonia and carbodiimide (around 180 °C), or else will be decomposed to ammonia, isothiocyanic acid, H_2S and carbodiimide (above 220 °C). But these are the products of the dry thermal decomposition of thiourea. However, in the absence of acids and bases, when in an aqueous media and heated to 90 - 130 °C thiourea dissolves to ammonium and cyanate ions (equation 9). Whereas, for the aqueous decomposition in concentrated acid solutions of $pH < 2$, the thiocyanate ion begins to hydrolyze to ammonium ion (equation 10). A possible mechanism of the aqueous decomposition of thiourea can be seen below as equation 11.^[3.10]





(eq. 11) : Mechanism of thiourea aqueous decomposition is presumed to be pH independent since it assumes an intramolecular hydrogen transfer.^[3,10]

The equilibrium in the second step (from (I) to HNCS complex) should lie far to the right in aqueous solutions since HNCS -unlike HNCO- is a strong acid. Formation of the activated complex in Step I is assumed to involve the partial intramolecular transfer of a hydrogen ion from one nitrogen atom to the next, making the mechanism pH independent.^[3,10]

As we discussed above the decomposition of urea resulted in a *gradual and uniform pH increase*, with OH^- ions also promoting the pentavanadyl cation (VO_2^+) precipitation as $\text{VO}(\text{OH})_2$. In a similar fashion, we here mentioned that when heated thiourea in aqueous media will decompose to NH_4^+ and NCS^- . So, if applied to our system, we would expect that thiocyanate ions would either start to hydrolyze to ammonium ion due to the low pH of our synthesis solution (eq. 10), thus accelerating the gradual pH increase of the synthesis solution, or would act in the same manner as hydroxyl ions for urea decomposition, promoting the pentavanadyl cation (VO_2^+) precipitation, but this time as “ $\text{VO}(\text{SCN})_2$ ” or other similar entity to the equivalent $\text{VO}(\text{OH})_2$ for the additive urea. Both of these paths would probably result in an increase of vanadium solubility in the solution thus enriching the solution chemistry of the system.

To examine our hypothesis validity we tested the effect of additive thiourea to our basic “1:4 & 9 g/L” configuration by adding solid thiourea to our reagents mixture before the hydrothermal procedure step, with a thiourea to vanadium precursor molar ratio of either 25% or 50%. The results presented in *Figure 3.29* show some interesting and unexpected results. While our basic synthetic procedure produces a mixture of the metastable phases of VO_2 which are then annealed to acquire the desired thermochromic $\text{VO}_2(\text{M})$ polymorph, when adding solid thiourea in our reagents solution the as obtained product can be identified as a mainly amorphous V_6O_{11} solid (+3.6 ox. state). However, after the annealing process the results show a high purity $\text{VO}_2(\text{M})$ product, with even higher crystallinity than any of the other results of this project, with no V_6O_{13} nor other impurities detected.

In the best of our knowledge, no current work has been published with similar results, nor the effect of additive thiourea has been tested (nor hypothesized, explained).

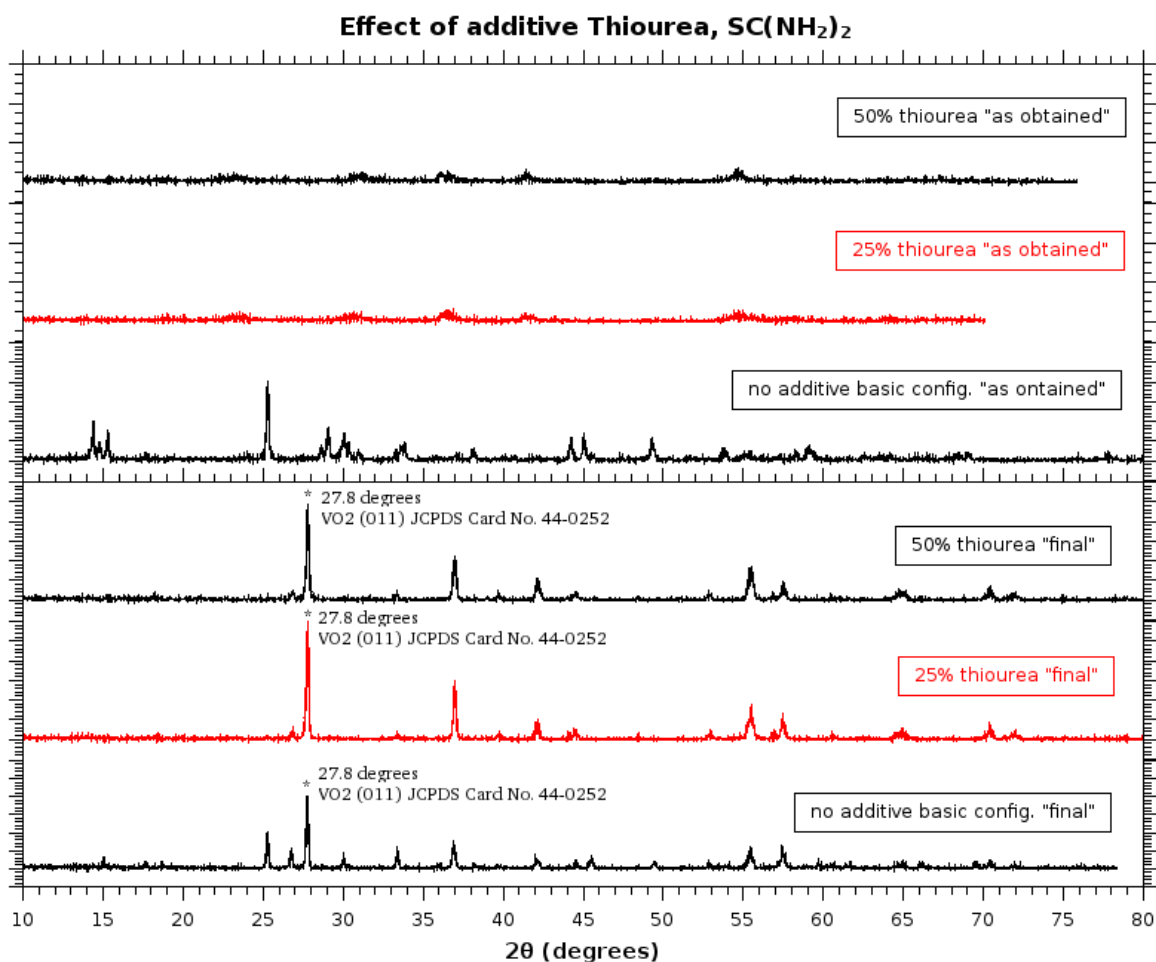


Figure 3.29 X-ray diffraction patterns of configurations with additive Thiourea, prior and after the annealing process, and of our basic configuration after annealing, for comparison purposes.

Comparison between the two different thiourea concentration, reveals that using 25% of thiourea to vanadium pentoxide molar ratio seem to produce slightly higher crystallinity products that the use of 50% additive. Also, the yields percentage of these configurations was calculated as in previous chapters (eq. 2). Again, the 25% configuration showed slightly better results, as presented below:

Thiourea : V ₂ O ₅ molar ratio	Hydrothermal synthesis yield, %
0% - no additive (basic configuration)	78.2 %
25%	87.4 %
50%	84.9 %

Table 3.5. Calculated Yields% of hydrothermal procedure, for thiourea and basic configurations.

Thus, we concluded that thiourea as an additive can promote the formation of our desired thermochromic VO₂(M) polymorph, in greater yields and better crystallinity for our solid product.

3.7 Effect of dopants

As explained in the introductory chapter of this thesis, elemental doping of VO₂ is an efficient strategy that has been extensively employed to modify the thermochromic property of the material mainly by affecting the T_c and the hysteresis loop width. Mechanically this is possible due to the effect of dopants acting as lattice imperfections in the material, thus destabilizing the V-V dimers structure of the insulating phase of VO₂, reducing band gap and making the structural transition to the metallic phase (MIT) more facile.

For the purpose of testing the effect of dopants to our system, we used H₂WO₄ as the source of tungsten dopant and MgSO₄ as the source of magnesium dopant to various of our configuration as explained in each sub-section below.

3.7.1. Effect of doping with Tungstic Acid, H₂WO₄

For the W-doped VO₂ series we synthesized materials from our basic configurations “1:1.5 & 9 g/L”, “1:4 & 9 g/L” and “1:8 & 9 g/L”, as well as a series of configurations with 25% additive thiourea. The configurations tested, along with the dopant molecular (mol%) and atomic percentage (at.%), and the yield% of each of these configurations are presented in *Table 3.6*, below.

V ₂ O ₅ :Oxalic acid molar ratio	V ₂ O ₅ concentration	Thiourea:V ₂ O ₅ molar ratio	W-doping mol%	W-doping at. %	Yield%
1:1.5	9 g/L	No additive	10 mol%	5 at%	-
1:4	9 g/L	No additive	10 mol%	5 at%	83.4%
1:8	9 g/L	No additive	10 mol%	5 at%	-
1:4	9 g/L	25%	0.5 mol%	0.3 at%	85.8%
1:4	9 g/L	25%	1 mol%	0.5 at%	85.0%
1:4	9 g/L	25%	1.5 mol%	0.8 at%	85.8%

Table 3.6 Calculated characteristics of configurations with W-doping.

For the calculations of the dopant percentages and yields equations 12, 13 and 14 were used:

$$\text{mol\%} = \frac{H_2WO_4 \text{ moles}}{V_2O_5 \text{ moles}} \cdot 100\% \quad \text{eq. (12)}$$

$$at.\% = \frac{W\ atoms}{V\ atoms + W\ atoms} \cdot 100\% \quad \text{eq. (13)}$$

$$Yield\% = \frac{final\ mass}{starting\ mass(V_2O_5 + dopant)} \cdot 100\% \quad \text{eq. (14)}$$

Results presented in *Figure 3.30* and *Figure 3.31* show the effect of dopant H_2WO_4 to our system.

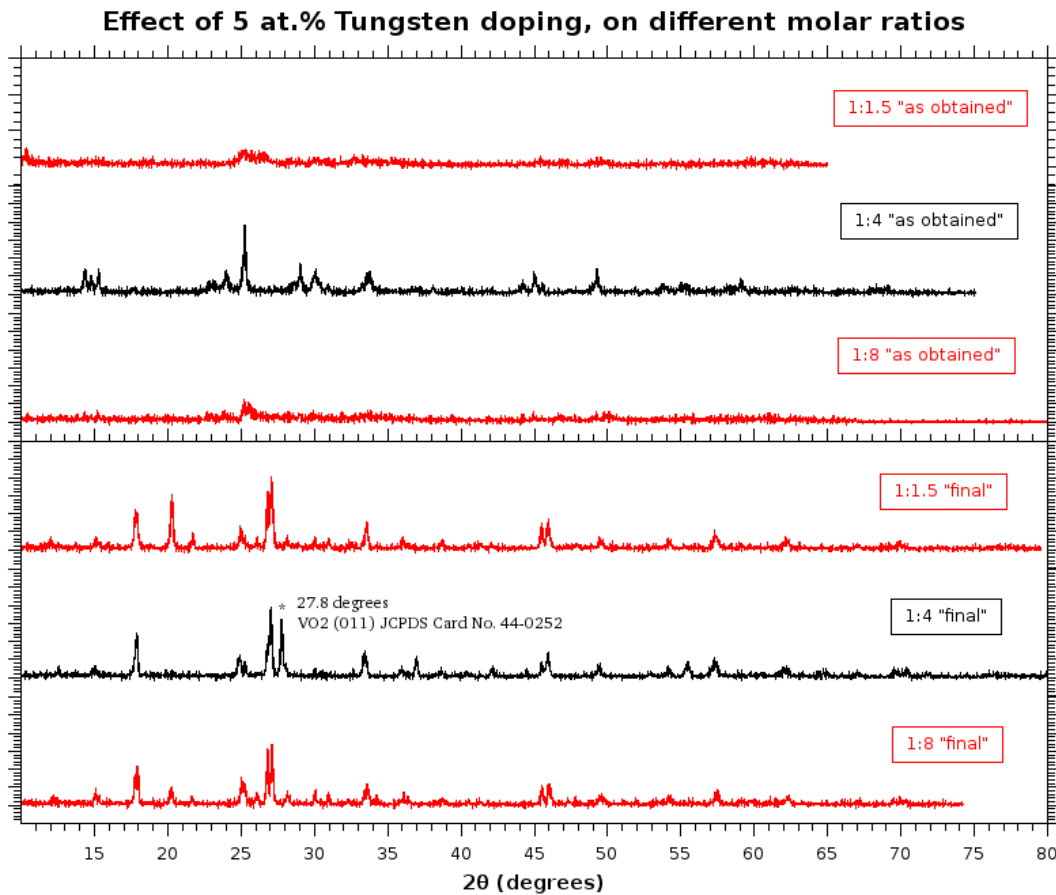


Figure 3.30 X-ray diffraction patterns of configurations with 5 at.% Tungsten doping on configurations of various molar ratios, prior and after the annealing process.

From the XRD patterns shown on *Figure 3.30*, we can identify the products of our 5 at.% W-doped configurations. Prior to the annealing process, the “as obtained” products of configuration with 1:1.5 molar ratio consists of an amorphous structure identified by the EVA and Jade programs as $VO_2(B)$; the 1:4 consists of a mixture of the metastable vanadium dioxide phases VO_2 (A) and (B) and some impurities of WO_3 , suggesting that tungsten has not been fully incorporated in the VO_2 lattice; and the 1:8 again as in 1:1.5 configuration consist of an amorphous structure identified as $VO_2(B)$ and WO_3 . In the case of the annealed “final” samples of these configurations, we identify our products as mixtures of vanadium oxides, with 1:1.5 having peaks of V_6O_{13} , WV_2O_6 and some

weak VO₂(M) peaks; 1:4 as a mixture of V₆O₁₃, V₂O₅ and VO₂(M); and 1:8 as V₂O₅, V₃O₇ and V₆O₁₃. These results indicate of no incorporation or very low incorporation of Tungsten in our products structures, with H₂WO₄ additive most likely here contributing on the production of lower crystallinity products. This may be the case of an imbalance on the solution equilibrium of ions interacting in our optimized reagents configuration, forced to our reagents system due to the addition of H₂WO₄ additive.

However, when additive H₂WO₄ was tested as a dopant on the optimized “1:4, 9 g/L & 25% thiourea” synthetic configurations, results seem to be more predictable. From the XRD patterns shown on *Figure 3.31*, we can identify the products of our W-doped 25% thiourea configurations. Prior to the annealing process, the “as obtained” products of 0.3 at.%, 0.5at.% and 0.8 at.% consist of amorphous unidentifiable structures, whereas for the annealed “final” samples of the same configurations, we identify all three our products as pure VO₂(M) polymorph. These results suggest that tungsten incorporation in our materials may have been achieved.

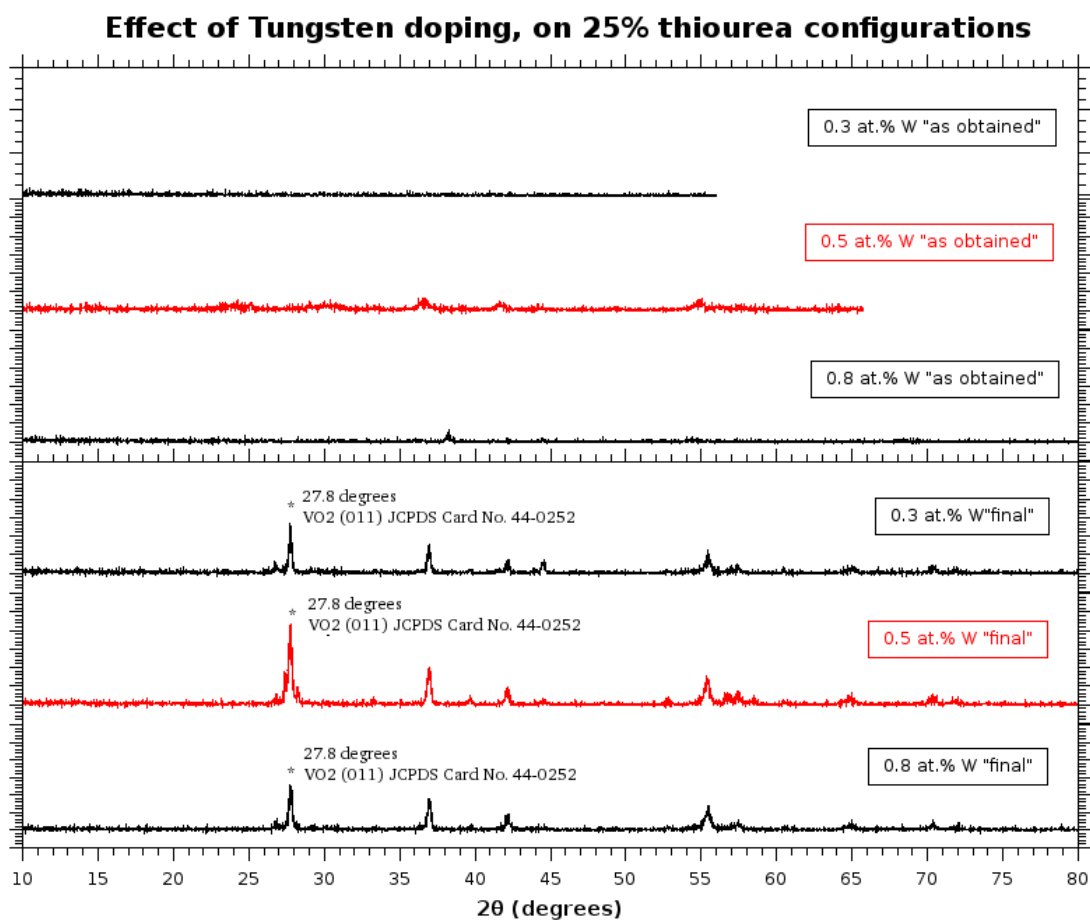


Figure 3.31 X-ray diffraction patterns of configurations with various at.% Tungsten doping on optimized 25% thiourea configuration, prior and after the annealing process.

A more in depth analysis on the case of W incorporation in our products will be discussed in the following chapters where results from EDX analysis will be presented. Still, there is another way to examine the case from our XRD data. As already discussed in the Introduction, doping of our material means substitution of Vanadium ions in the monoclinic lattice. Due to the fact that the radius of V ions is smaller than that of W ions, their substitution will result to strain applied to the crystal lattice of $\text{VO}_2(\text{M})$. Thus an expansion of the adjacent inter-planar distance will take place, resulting to a shift of all of the XRD peaks towards a lower angle according to the Scherrer equation ($2d \cdot \sin \theta = \lambda$), confirming that W had been successfully incorporated into the crystal lattice of $\text{VO}_2(\text{M})$. The shift monitoring of the major peak of thermochromic VO_2 at 27.8° is the most efficient indirect method used by experimentalists to determine the W incorporation in $\text{VO}_2(\text{M})$.^{[3.5][3.11]}

On *Figure 3.32*, we examine the case of W incorporation by monitoring the major peak of our “final” $\text{VO}_2(\text{M})$ samples. No apparent relation of the dopant at.% and the major peak value was noted, giving no further clues about the W incorporation in our material lattice. The dopant is either not in the material lattice or it is in very small quantities, below the detection levels of the XRD.

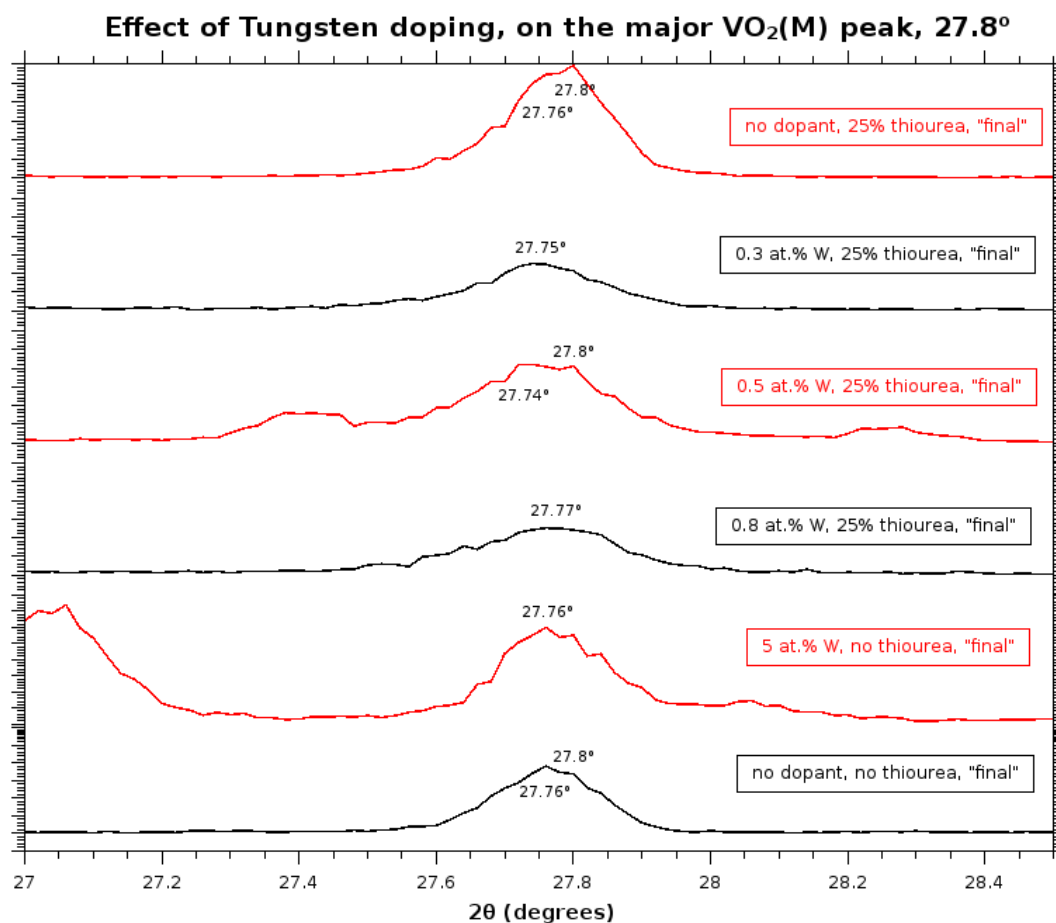


Figure 3.32 Narrow XRD patterns ($27^\circ \leq 2\theta \leq 28.5^\circ$) of $\text{VO}_2(\text{M})$ samples of various at.% W.

3.7.2. Effect of doping with Magnesium Sulfate, $MgSO_4$

For the Mg-doped VO_2 series we synthesized materials from our basic configurations “1:1.5 & 9 g/L”, “1:4 & 9 g/L” and “1:8 & 9 g/L”, as well as a series of configurations with 25% additive thiourea. The configurations tested, along with the dopant molecular (mol%) and atomic percentage (at.%), and the yield% of each of these configurations are presented in *Table 3.7*, below.

V_2O_5 :Oxalic acid molar ratio	V_2O_5 concentration	Thiourea: V_2O_5 molar ratio	Mg-doping mol%	Mg-doping at.%	Yield%
1:1.5	9 g/L	No additive	10 mol%	5 at%	99.7%
1:4	9 g/L	No additive	10 mol%	5 at%	82.3%
1:8	9 g/L	No additive	10 mol%	5 at%	81.2%
1:4	9 g/L	25%	4 mol%	2 at%	83.2%
1:4	9 g/L	25%	6 mol%	3 at%	83.0%
1:4	9 g/L	25%	8 mol%	4 at%	82.7%

Table 3.7 Calculated characteristics of configurations with Mg-doping.

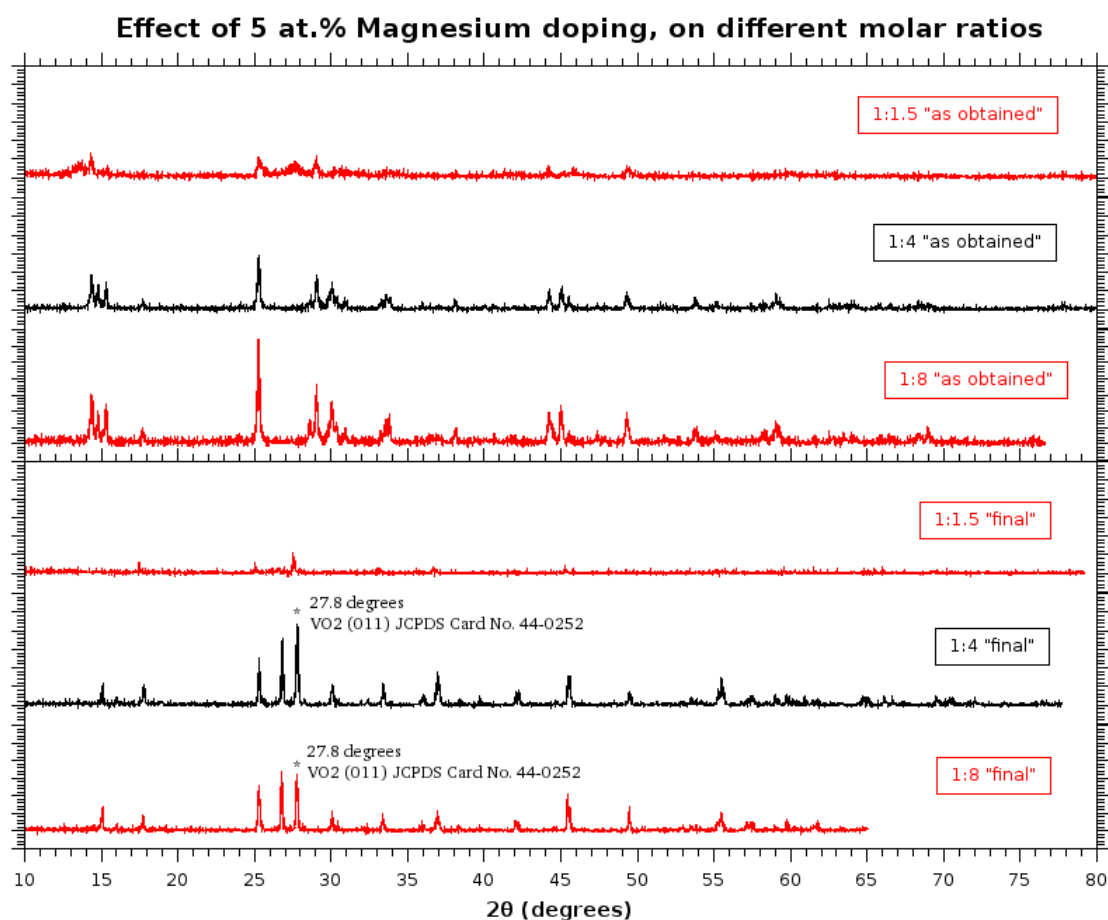


Figure 3.33 X-ray diffraction patterns of configurations with 5 at.% Tungsten doping on configurations of various molar ratios, prior and after the annealing process.

From the XRD patterns shown on *Figure 3.33*, we can identify the products of our 5 at.% Mg-doped configurations. Prior to the annealing process, the “as obtained” products of configuration with 1:1.5 molar ratio consists of an amorphous unidentifiable structure; the 1:4 consists of a mixture of the metastable vanadium dioxide phases VO₂ (A) and (B), as expected our basic configuration results; as well as for the 1:8 which consist of the expected mixture of the metastable vanadium dioxide phases VO₂ (A) and (B). In the case of the annealed “final” samples of these configurations, we identify our products as mixtures of vanadium oxides, with 1:1.5 a product of low crystallinity with some weak peaks identified as V₆O₁₃, V₄O₉ and VO₂(M); 1:4 is identified as a mixture of V₆O₁₃ and VO₂(M); as well as 1:8 which is also identified as a mixture of V₆O₁₃ and VO₂(M). Since no impurities of Magnesium were detected, these results indicate that Mg is either in our products as a dopant (undetectable by XRD) or it hasn't reacted to precipitate from the solution at all. Results of additive MgSO₄ on our basic configurations seem to give more predictable results than with additive H₂WO₄.

Again, additive MgSO₄ was also tested as a dopant on the optimized “1:4, 9 g/L & 25% thiourea” configurations. From the XRD patterns shown on *Figure 3.34*, we can identify the products of our Mg-doped 25% thiourea configurations. Prior to the annealing process, the “as obtained” products of 2 at.%, 3 at.% and 4 at.% consist of amorphous unidentifiable structures, whereas for the annealed “final” samples of the same configurations, we identify all three our products as pure VO₂(M) polymorph. These results suggest that Mg incorporation in our materials may have been achieved.

On *Figure 3.35*, we examine the case of Mg incorporation by monitoring the major peak of our “final” VO₂(M) samples, as we did in the case of W-doped samples. Again, no apparent relation of the dopant at.% to the major peak value was noted, giving no further clues about the Mg incorporation in our material lattice. The dopant is either not in the materials lattice or it is in very small quantities, below the detection levels of the X-ray Diffraction. More on the dopants incorporation will be discussed in the following chapters, with the results of EDX of these samples.

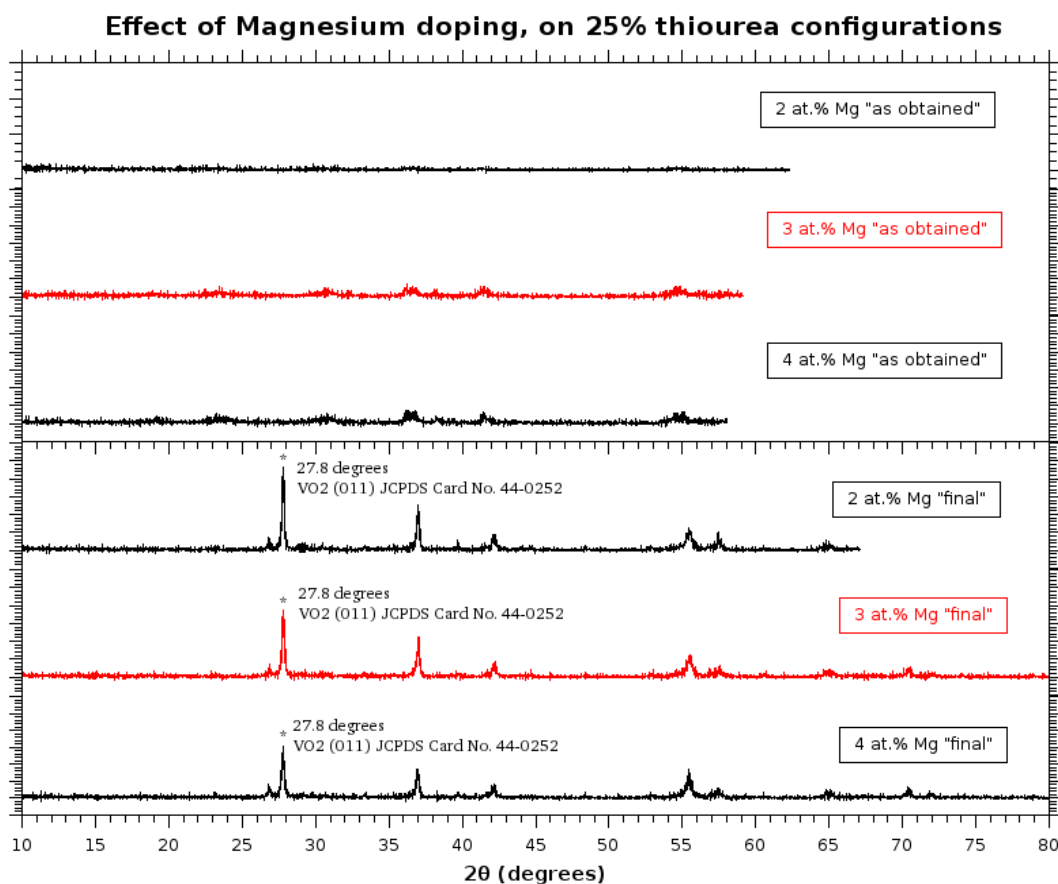


Figure 3.34 X-ray diffraction patterns of configurations with various at.% Magnesium doping on optimized 25% thiourea configuration, prior and after the annealing process.

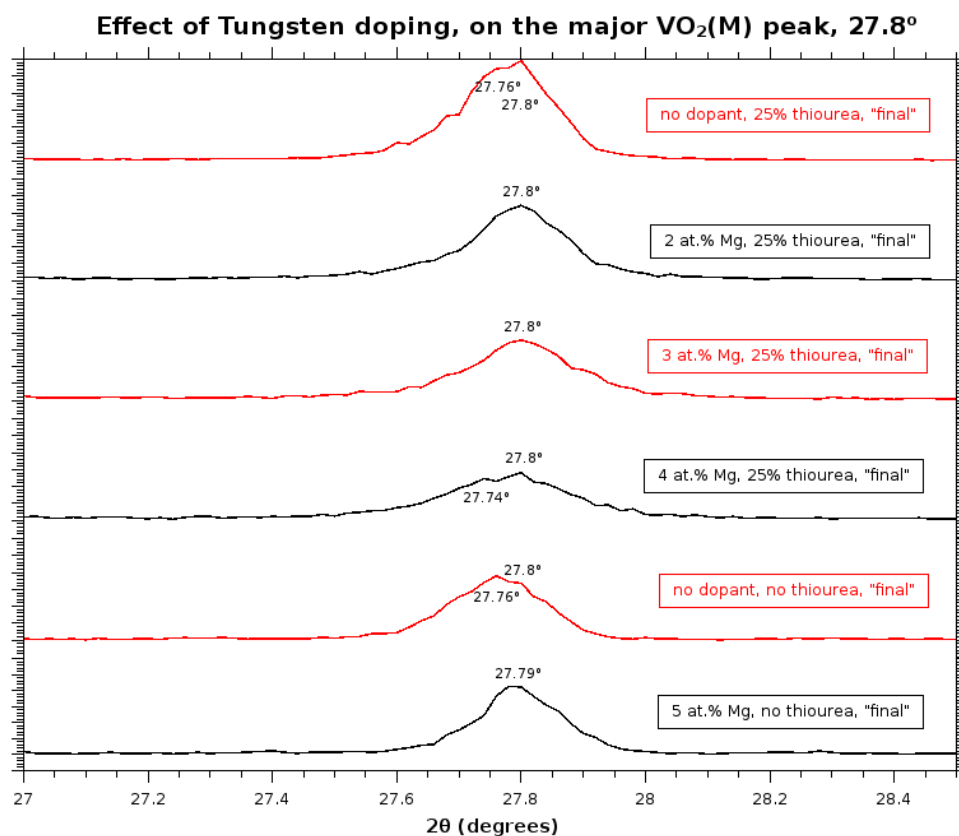


Figure 3.35 Narrow XRD patterns ($27^\circ \leq 2\theta \leq 28.5^\circ$) of $VO_2(M)$ samples of various at.% W.

3.7.3. Effect of co-doping with H_2WO_4 and $MgSO_4$

For the W, Mg co-doped VO_2 series we synthesized materials using our basic configuration with 25% additive thiourea. The configurations tested, along with the dopants molecular (mol%) and atomic percentage (at.%), and the yield% of each of these configurations are presented in Table 3.8, below.

V_2O_5 :Oxalic acid molar ratio	V_2O_5 concentration	Thiourea: V_2O_5 molar ratio	W-doping mol%	W-doping at. %	Mg-doping mol%	Mg-doping at. %	Yield %
1:4	9 g/L	25%	0.5 mol%	0.3 at%	4 mol%	2 at%	82.6%
1:4	9 g/L	25%	0.5 mol%	0.3 at%	6 mol%	3 at%	80.7%
1:4	9 g/L	25%	0.5 mol%	0.3 at%	8 mol%	4 at%	82.3%

Table 3.8 Calculated characteristics of configurations with W, Mg co-doping.

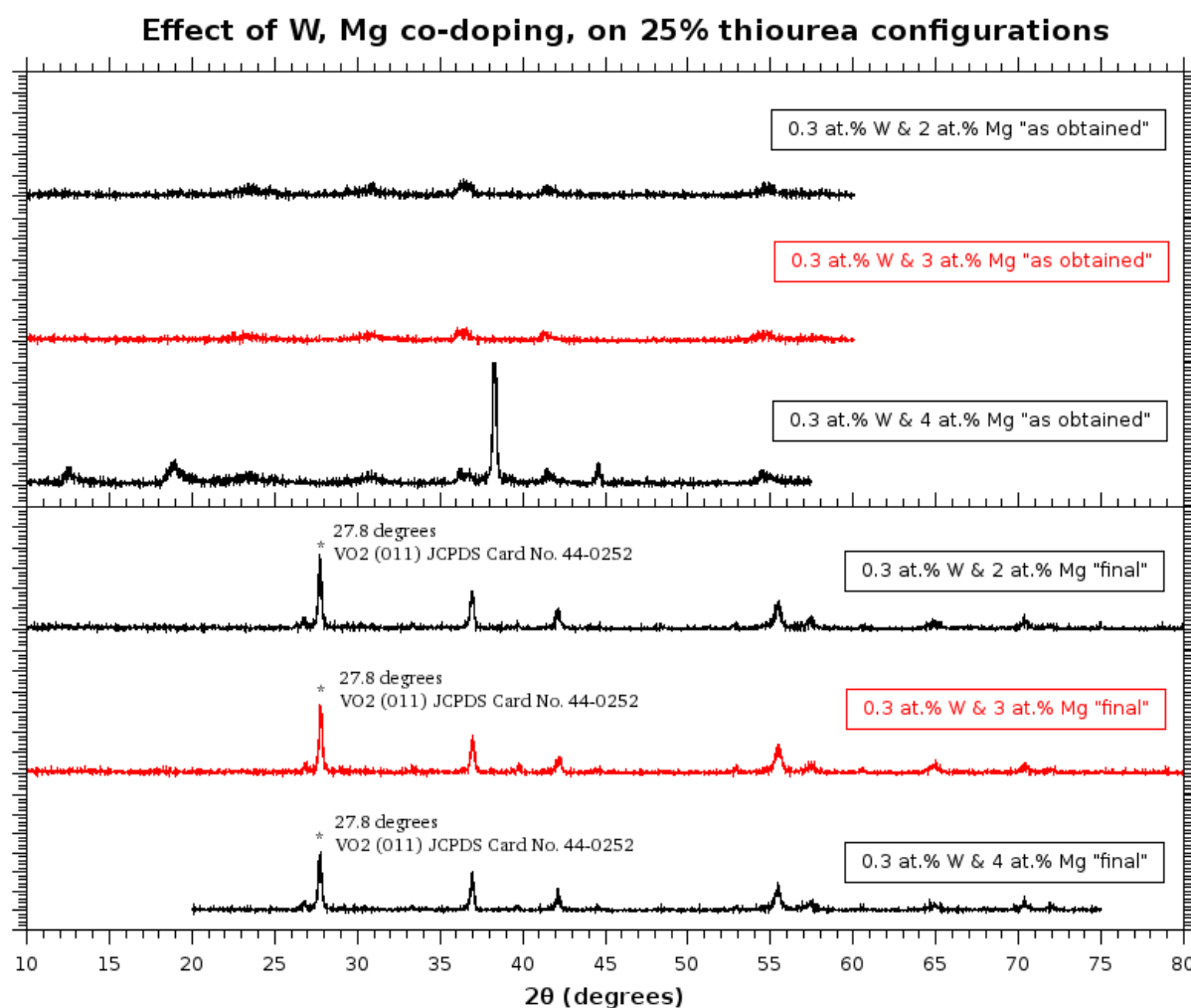


Figure 3.36 X-ray diffraction patterns of configurations with various at.% Mg- and 0.3 at.% W- co-doping on optimized 25% thiourea configuration, prior and after the annealing process.

From the XRD patterns shown on *Figure 3.36*, we can identify the products of our “1:4, 9 g/L & 25% thiourea” co-doping configurations. Prior to the annealing process, the “as obtained” products of 0.3 at.% W and 2 at.%, 3 at.% and 4 at.% Mg co-doping consist of amorphous unidentifiable structures, with the exception of 0.3 at.% - 4 at.% where we can see some strong but unidentifiable -in regards of our materials used- peaks, that most probably belong to the holder of our sample, and can be accounted as an experimental error. For the annealed “final” samples of the same configurations, we identify all three our products as pure VO₂(M) polymorph. Again results suggest that dopants W and Mg could be incorporated in our materials.

In order to test this W and Mg incorporation, on *Figure 3.37*, we examine the case by monitoring the major peak of our “final” VO₂(M) samples. Again, no apparent relation of the dopants total at.% to the major peak value was noted, giving no further clues about the W and Mg incorporation in our material lattice. The dopant is either not in the materials lattice or it is in very small quantities, below the detection levels of the X-ray Diffraction. More on the dopants incorporation will be discussed in the following chapters, with the results of EDX of these samples.

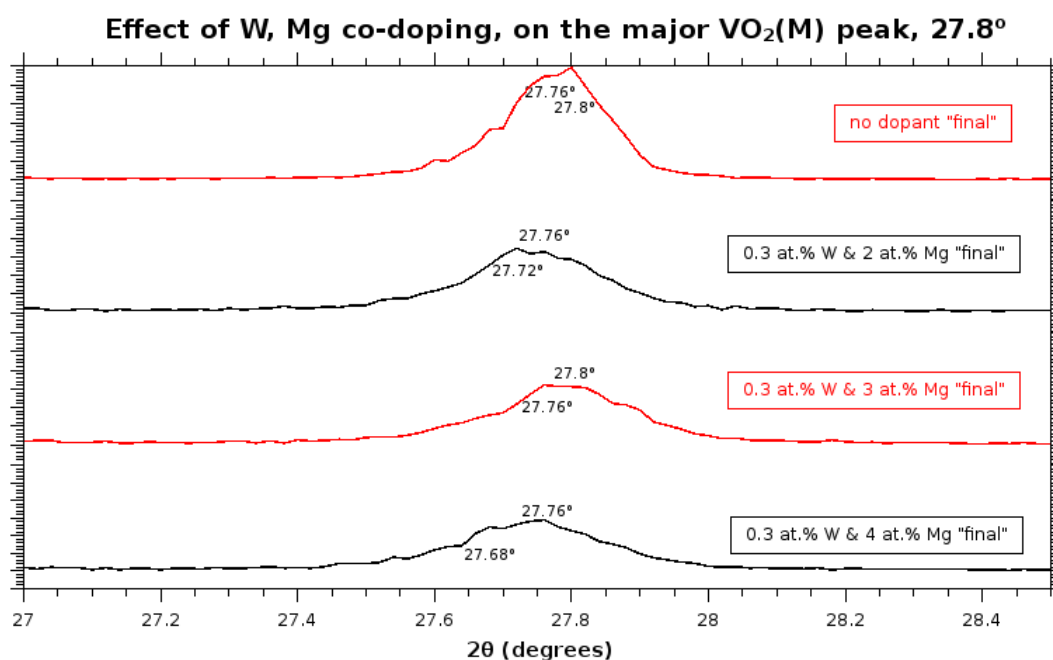


Figure 3.37 Narrow XRD patterns ($27^{\circ} \leq 2\theta \leq 28.5^{\circ}$) of W, Mg co-doped VO₂(M) samples.

3.8 Structural transition properties

The thermochromic behavior of our materials was examined by monitoring the structural transition (polymorphs R \leftrightarrow M) by DSC measurements, as mentioned in the Introductory part of this thesis. Properties like the critical temperature of the transition, T_{cr} or T_c and the hysteresis loop between the heating and cooling temperatures, ΔT_{cr} or ΔT_c , were calculated from the DSC data. The T_c corresponds to the average of the maximum ($T_c^{cooling}$) and the minimum ($T_c^{heating}$) value of the peaks, $T_c = (T_c^{cooling} + T_c^{heating})/2$, and the hysteresis can be calculated as: $\Delta T_c = |T_c^{heating} - T_c^{cooling}|$.

Configuration	xrd identification	T_c (°C)	ΔT_c (°C)
1:4, 9g/L, 5at.% W	V_6O_{13} , $VO_2(M)$, V_2O_5	59.27	7.11
1:4, 9g/L, 0.5at.% W, 25% Thiourea	$VO_2(M)$	64.37	11.39
1:4, 9g/L, 0.8at.% W, 25% Thiourea	$VO_2(M)$	64.53	9.11
1:4, 9g/L, 0.3at.% W, 25% Thiourea	$VO_2(M)$	65.04	9.79
1:4, 9g/L, 0.3at.% W, 2at.% Mg, 25% Thiourea	$VO_2(M)$	65.06	9.92
1:4, 9g/L, 0.3at.% W, 4at.% Mg, 25% Thiourea	$VO_2(M)$	65.12	9.55
1:4, 9g/L, 0.3at.% W, 3at.% Mg, 25% Thiourea	$VO_2(M)$	65.36	9.96
1:8 & 3 g/L	V_4O_9 , $VO_2(A)$, $VO_2(M)$	65.53	6.45
1:4 & 9 g/L	$VO_2(M)$, V_6O_{13}	65.79	9.02
1:4, 9g/L, 3at.% Mg, 25% Thiourea	$VO_2(M)$	65.84	9.59
1:8, 18 g/L, half volume synthesis	$VO_2(M)$, V_6O_{13}	65.88	8.61
1:4, 9g/L, 50% Thiourea	$VO_2(M)$	65.94	11.59
1:4, 9g/L, 2at.% Mg, 25% Thiourea	$VO_2(M)$	66.02	9.31
1:4, 9g/L, 4at.% Mg, 25% Thiourea	$VO_2(M)$	66.08	8.86
1:8, 9g/L	$VO_2(M)$, V_6O_{13}	66.18	8.57
1:12, 3g/L	V_6O_{13} , $VO_2(M)$	66.28	6.59
1:10, 9g/L	$VO_2(M)$, V_6O_{13}	66.36	7.88
1:4, 9g/L, 25% Thiourea	$VO_2(M)$	66.52	12.12
1:3, 9g/L	V_6O_{13} , $VO_2(M)$	66.52	7.48
1:10, 9g/L, H_2SO_4	V_6O_{13} , $VO_2(M)$	66.61	8.37
1:4, 9g/L, H_2SO_4	V_6O_{13} , $VO_2(M)$	66.67	7.19
1:1.5 & 9g/L	$VO_2(M)$, V_6O_{13}	66.7	6.54
1:4, 18g/L	$VO_2(M)$, V_6O_{13}	66.75	9.88
1:6, 9g/L	V_6O_{13} , $VO_2(M)$	66.85	9.26

Table 3.9 DSC overall data from various configurations measured, arranged by ascending T_c .

On the following configuration type based sub-sections more detailed graphs of the DSC curves will be presented and discussed. The area of the curve is analogue to the crystallinity of the material, so in polymer science is used to calculate the rate of crystallinity of polymers. Here no such calculations are required, since we have a crystallinity estimation by the X-ray powder diffraction data. However a comparison of results between the two characterization methods can be of interest, since only the thermochromic VO₂ polymorph of the samples will contribute in the structural transition from the Rutile to Monoclinic and vice versa, thus making the area of curves an indicator of the crystallinity of thermochromic VO₂ polymorphs of our samples. At the section end, a concluding sub-section will be provided with an overview of results and a comparison between our samples, along with XRD measurements of two of our samples in different temperatures, above and below T_c, to observe the structural face change effect in the lattice of our material.

3.8.1. DSC results of basic configurations

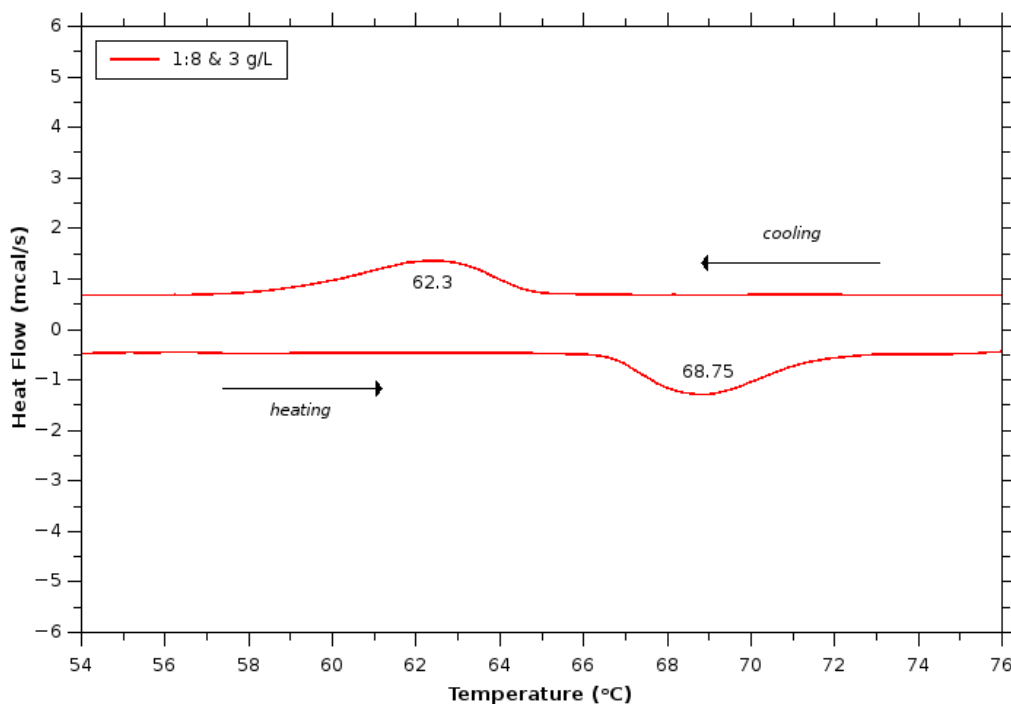


Figure 3.38 Narrow DSC curves ($\approx 50^{\circ}C \leq T \leq 80^{\circ}C$) of “1:8 & 3g/L” sample.

From the DSC curve of the “1:8 & 3 g/L” configuration sample (Figure 3.38) we can calculate the T_c = 65.53 °C and the ΔT_c = 6.45 °C. The area under the curves is very small, with small heat flow values, indicating a low VO₂(M) or (R) crystallinity in the sample composition, a conclusion which is in accordance with the XRD results of this sample.

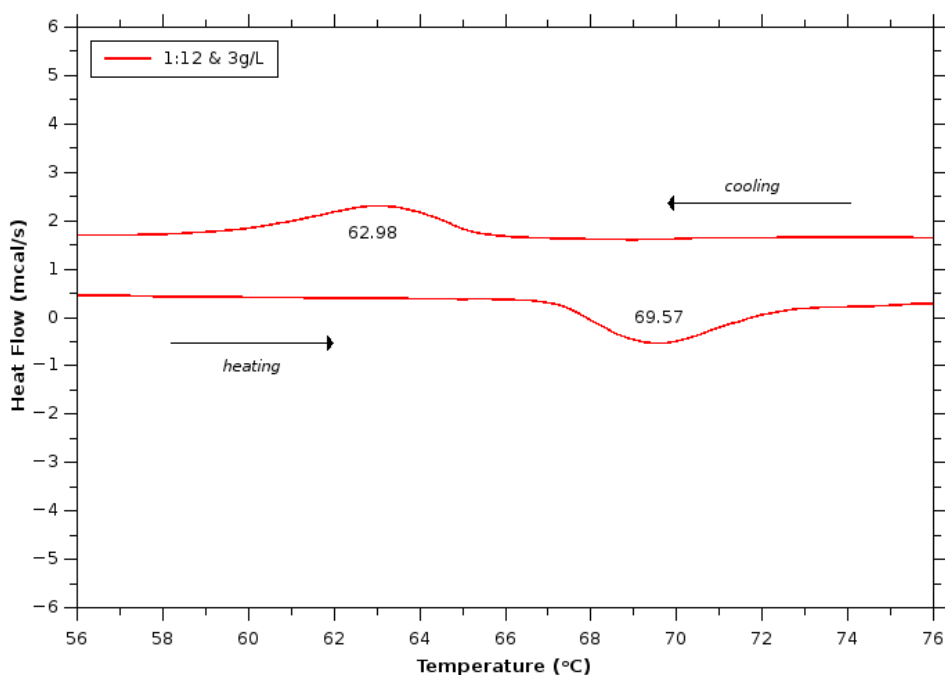


Figure 3.39 Narrow DSC curves ($\approx 50^\circ\text{C} \leq T \leq 80^\circ\text{C}$) of “1:1.2 & 3g/L” sample.

From the DSC curve of the “1:1.2 & 3 g/L” configuration sample (Figure 3.39) we can calculate the $T_c = 66.28^\circ\text{C}$ and the $\Delta T_c = 6.59^\circ\text{C}$. The area under the curves is very small, with small heat flow values, indicating a low $\text{VO}_2(\text{M})$ or (R) crystallinity in the sample composition, a conclusion which is in accordance with the XRD results of this sample.

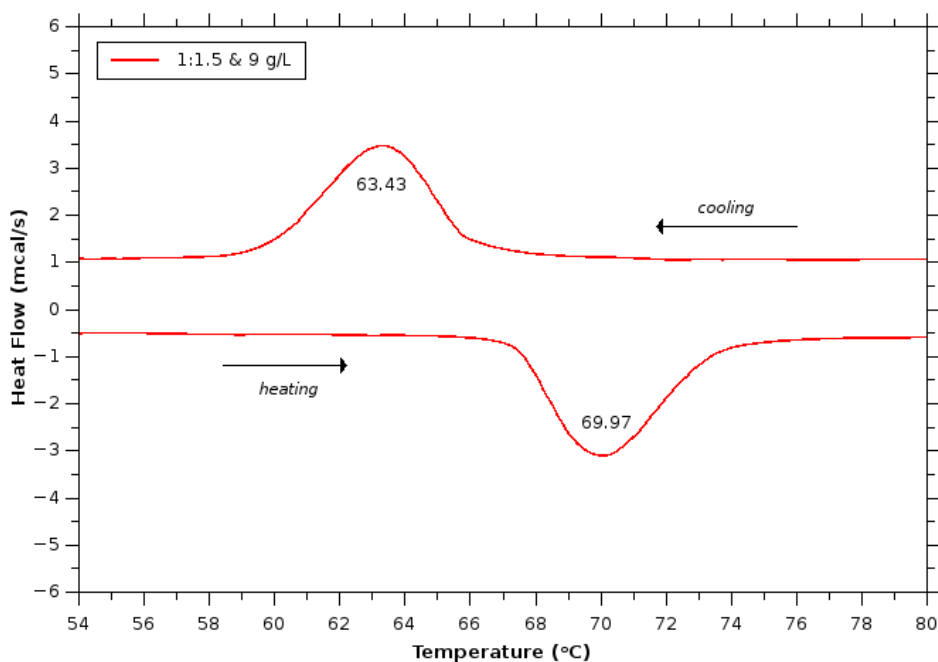


Figure 3.40 Narrow DSC curves ($\approx 50^\circ\text{C} \leq T \leq 80^\circ\text{C}$) of “1:1.5 & 9g/L” sample.

From the DSC curve of the “1:1.5 & 9 g/L” configuration sample (*Figure 3.40*) we can calculate the $T_c = 66.70\text{ }^\circ\text{C}$ and the $\Delta T_c = 6.54\text{ }^\circ\text{C}$. The area under the curves are moderate, with medium heat flow values, indicating a good $\text{VO}_2(\text{M})$ or (R) crystallinity in the sample composition, a conclusion which is in accordance with the XRD results of this sample.

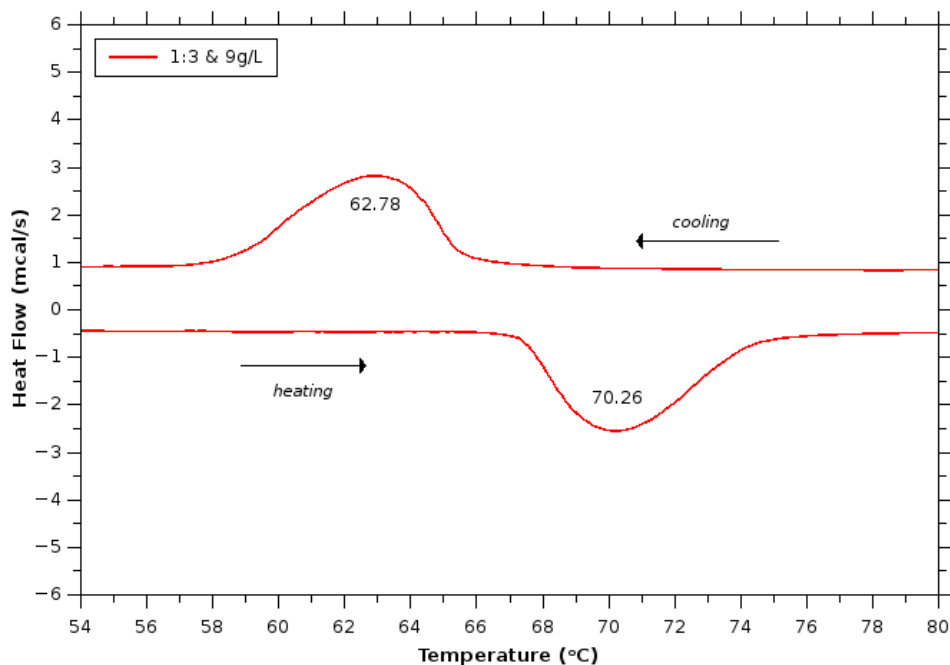


Figure 3.41 Narrow DSC curves ($\approx 50^\circ\text{C} \leq T \leq 80^\circ\text{C}$) of “1:3 & 9g/L” sample.

From the DSC curve of the “1:3 & 9 g/L” configuration sample (*Figure 3.41*) we can calculate the $T_c = 66.52\text{ }^\circ\text{C}$ and the $\Delta T_c = 7.48\text{ }^\circ\text{C}$. The area under the curves is moderate, with medium heat flow values, indicating a good $\text{VO}_2(\text{M})$ or (R) crystallinity in the sample composition, a conclusion which is in accordance with the XRD results of this sample.

From the DSC curve of the “1:4 & 9 g/L” configuration sample (*Figure 3.42*) we can calculate the $T_c = 65.79\text{ }^\circ\text{C}$ and the $\Delta T_c = 9.02\text{ }^\circ\text{C}$. The area under the curves is moderate to large, with medium heat flow values, indicating a good $\text{VO}_2(\text{M})$ or (R) crystallinity in the sample composition, a conclusion which is in accordance with the XRD results of this sample.

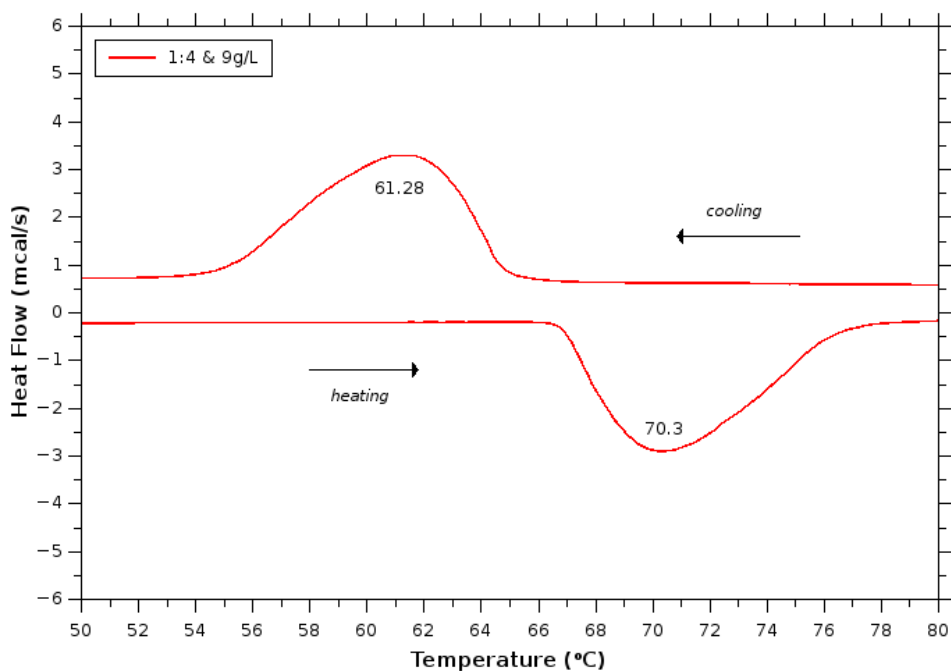


Figure 3.42 Narrow DSC curves ($\approx 50^{\circ}C \leq T \leq 80^{\circ}C$) of “1:4 & 9g/L” sample.

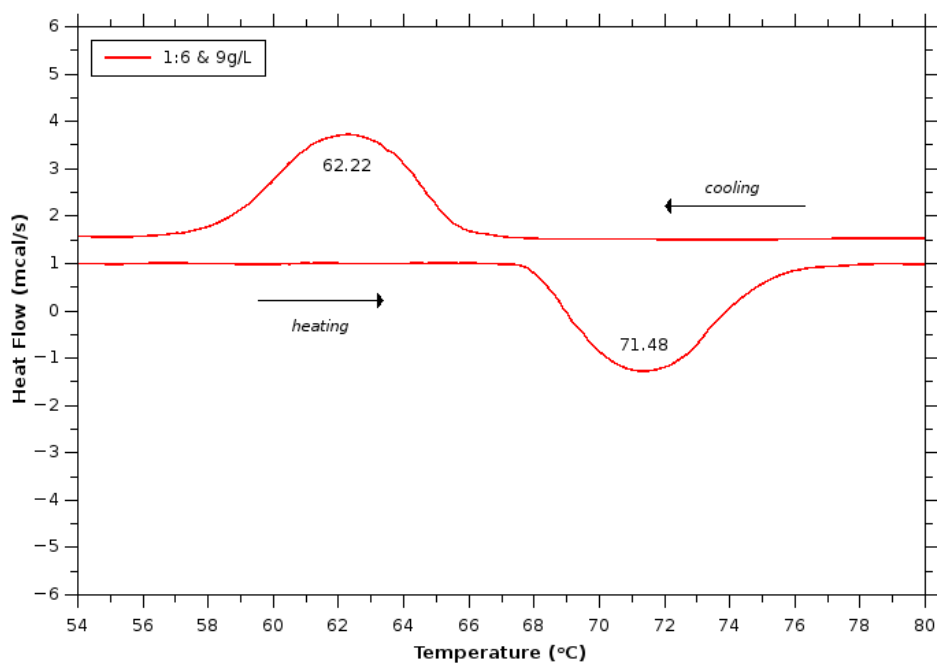


Figure 3.43 Narrow DSC curves ($\approx 50^{\circ}C \leq T \leq 80^{\circ}C$) of “1:6 & 9g/L” sample.

From the DSC curve of the “1:6 & 9 g/L” configuration sample (Figure 3.43) we can calculate the $T_c = 66.85^{\circ}C$ and the $\Delta T_c = 9.26^{\circ}C$. The area under the curves is moderate to small, with medium heat flow values, indicating a good $VO_2(M)$ or (R) crystallinity in the sample composition, a conclusion which is in accordance with the XRD results of this sample.

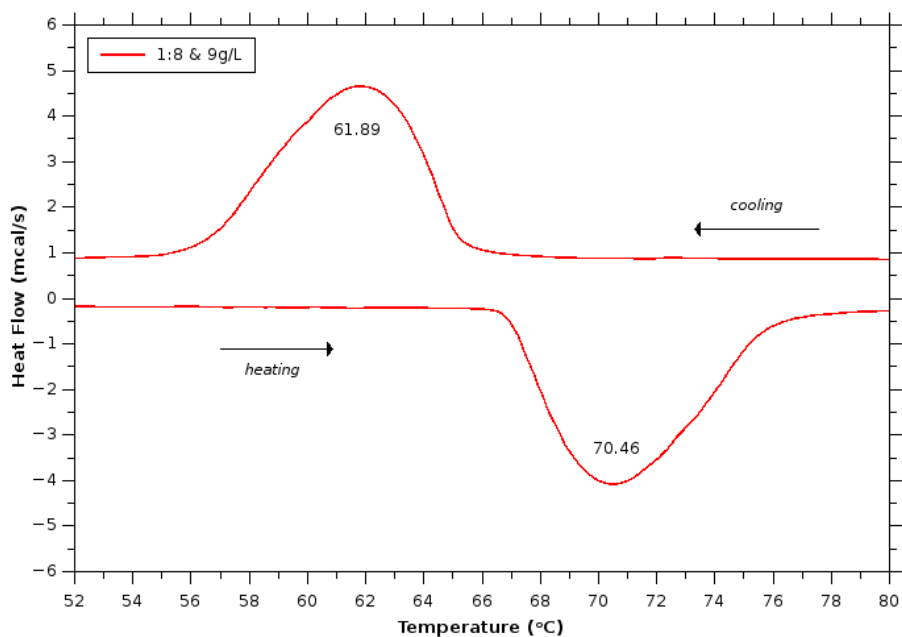


Figure 3.44 Narrow DSC curves ($\approx 50^{\circ}C \leq T \leq 80^{\circ}C$) of “1:8 & 9g/L” sample.

From the DSC curve of the “1:8 & 9 g/L” configuration sample (Figure 3.44) we can calculate the $T_c = 66.18^{\circ}C$ and the $\Delta T_c = 8.57^{\circ}C$. The area under the curves is large, with high heat flow values, indicating a good VO₂(M) or (R) crystallinity in the sample composition, a conclusion which is in accordance with the XRD results of this sample.

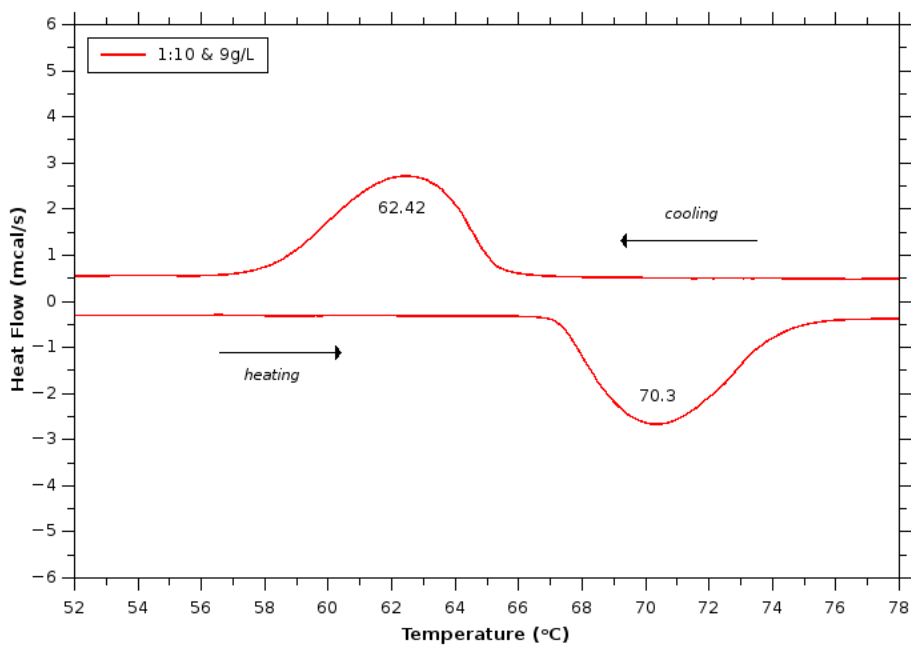


Figure 3.45 Narrow DSC curves ($\approx 50^{\circ}C \leq T \leq 80^{\circ}C$) of “1:10 & 9g/L” sample.

From the DSC curve of the “1:10 & 9 g/L” configuration sample (*Figure 3.45*) we can calculate the $T_c = 66.36\text{ }^\circ\text{C}$ and the $\Delta T_c = 7.88\text{ }^\circ\text{C}$. The area under the curves is moderate to small, with medium heat flow values, indicating a good $\text{VO}_2(\text{M})$ or (R) crystallinity in the sample composition, a conclusion which is in accordance with the XRD results of this sample.

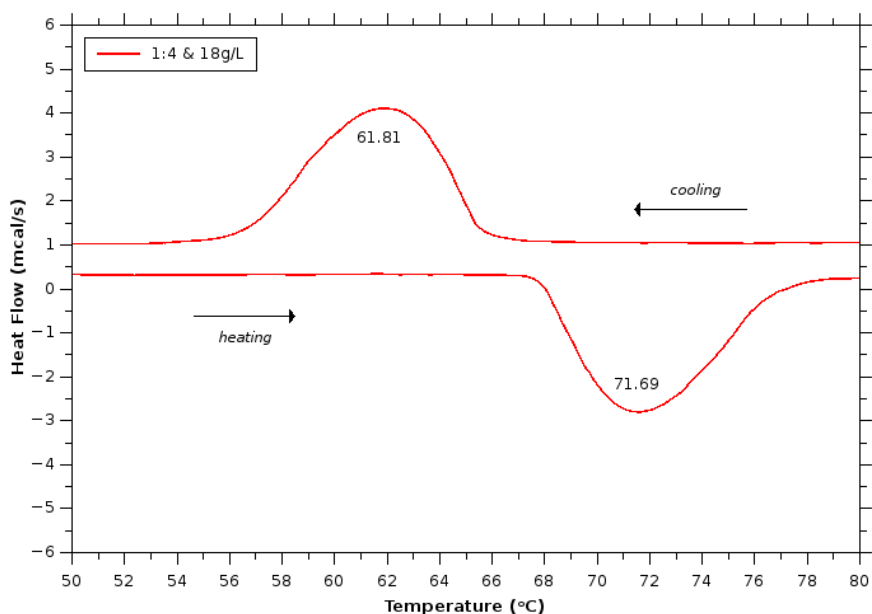


Figure 3.46 Narrow DSC curves ($\approx 50^\circ\text{C} \leq T \leq 80^\circ\text{C}$) of “1:4 & 18g/L” sample.

From the DSC curve of the “1:4 & 18 g/L” configuration sample (*Figure 3.46*) we can calculate the $T_c = 66.75\text{ }^\circ\text{C}$ and the $\Delta T_c = 9.88\text{ }^\circ\text{C}$. The area under the curves is moderate, with high heat flow values, indicating a good $\text{VO}_2(\text{M})$ or (R) crystallinity in the sample composition, a conclusion which is in accordance with the XRD results of this sample.

From the DSC curve of the “1:8 & 18 g/L & half volume synthesis” configuration sample (*Figure 3.47*) we can calculate the $T_c = 66.88\text{ }^\circ\text{C}$ and the $\Delta T_c = 8.61\text{ }^\circ\text{C}$. The area under the curves is moderate to small, with medium heat flow values, indicating a good $\text{VO}_2(\text{M})$ or (R) crystallinity in the sample composition, a conclusion which is in accordance with the XRD results of this sample.

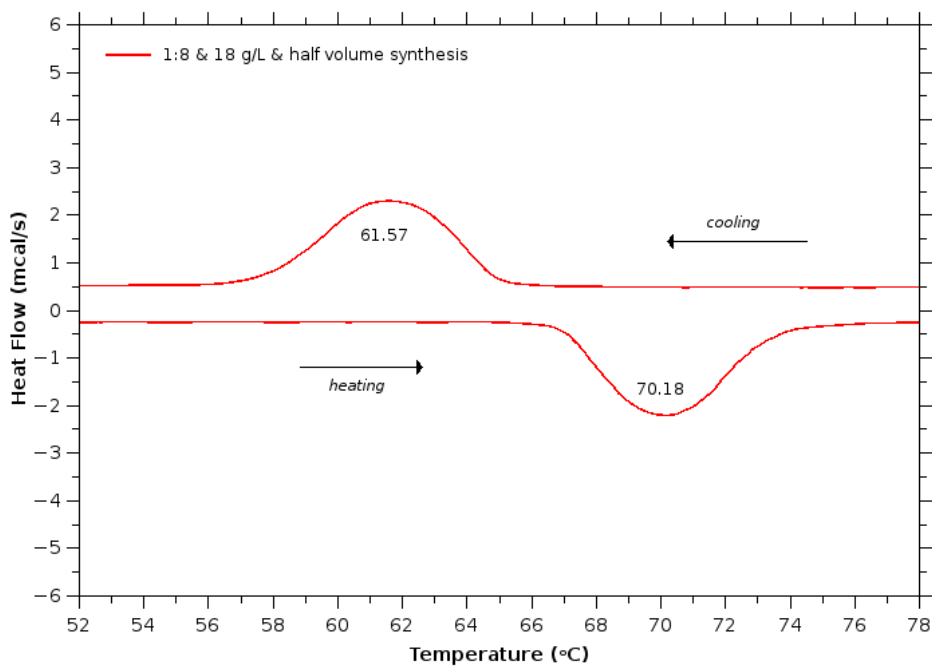


Figure 3.47 Narrow DSC curves ($\approx 50^{\circ}\text{C} \leq T \leq 80^{\circ}\text{C}$) of “1:8 & 18g/L & half volume” synthesis sample.

3.8.2. DSC results of configurations with additives

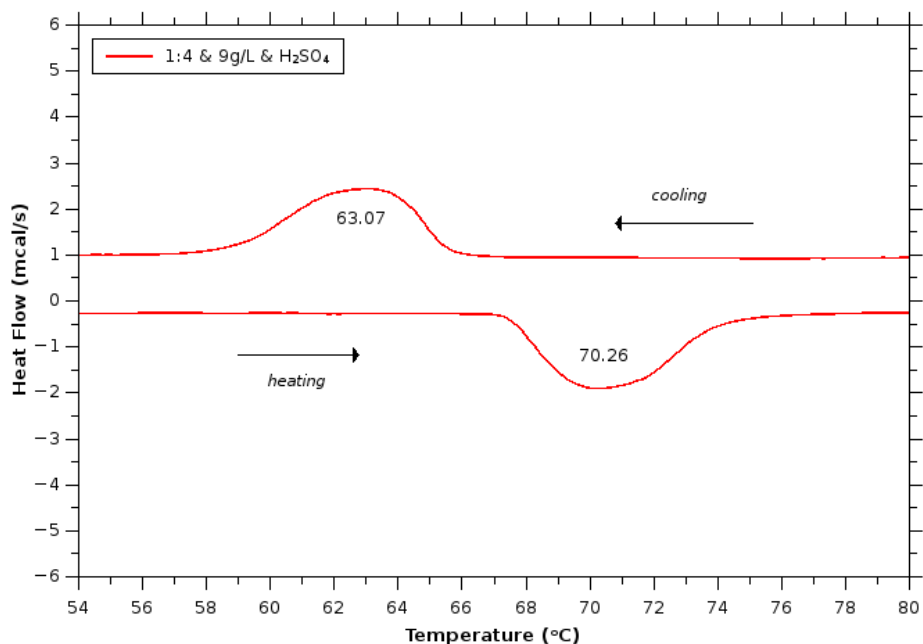


Figure 3.48 Narrow DSC curves ($\approx 50^{\circ}\text{C} \leq T \leq 80^{\circ}\text{C}$) of “1:4 & 9g/L & H_2SO_4 ” sample.

From the DSC curve of the “1:4 & 9g/L & H_2SO_4 ” configuration sample (Figure 3.48) we can calculate the $T_c = 66.67^{\circ}\text{C}$ and the $\Delta T_c = 7.19^{\circ}\text{C}$. The area under the curves is small, with medium heat flow values, indicating a lower $\text{VO}_2(\text{M})$ or (R) crystallinity in the sample composition, a conclusion which is in accordance with the XRD results of this sample.

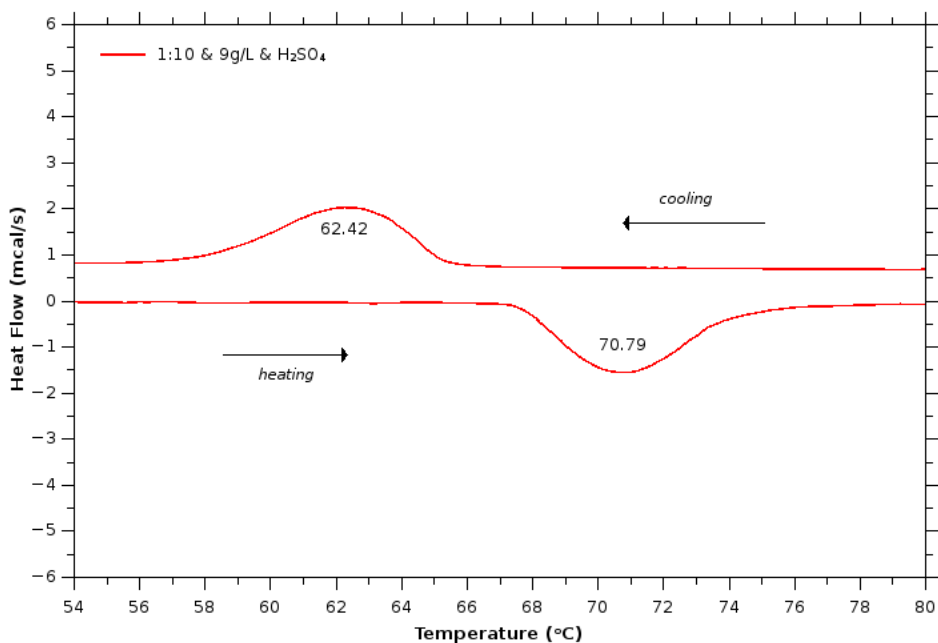


Figure 3.49 Narrow DSC curves ($\approx 50^{\circ}C \leq T \leq 80^{\circ}C$) of “1:10 & 9g/L & H₂SO₄” sample.

From the DSC curve of the “1:10 & 9g/L & H₂SO₄” configuration sample (Figure 3.49) we can calculate the $T_c = 66.61^{\circ}C$ and the $\Delta T_c = 8.37^{\circ}C$. The area under the curves is small, with small heat flow values, indicating a lower VO₂(M) or (R) crystallinity in the sample composition, a conclusion which is in accordance with the XRD results of this sample.

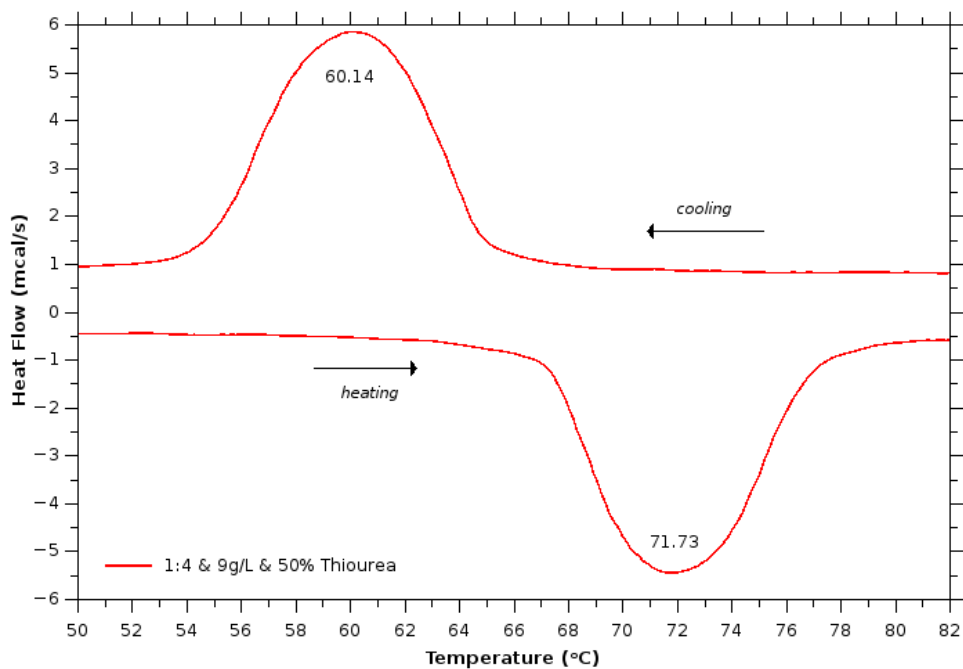


Figure 3.50 Narrow DSC curves ($\approx 50^{\circ}C \leq T \leq 80^{\circ}C$) of “1:4 & 9g/L & 50% Thiourea” sample.

From the DSC curve of the “1:4 & 9g/L & 50% Thiourea” configuration sample (Figure 3.50) we can calculate the $T_c = 65.9\text{ }^\circ\text{C}$ and the $\Delta T_c = 11.59\text{ }^\circ\text{C}$. The area under the curves is very large, with very high heat flow values, indicating a high $\text{VO}_2(\text{M})$ or (R) crystallinity in the sample composition, a conclusion which is in accordance with the XRD results of this sample.

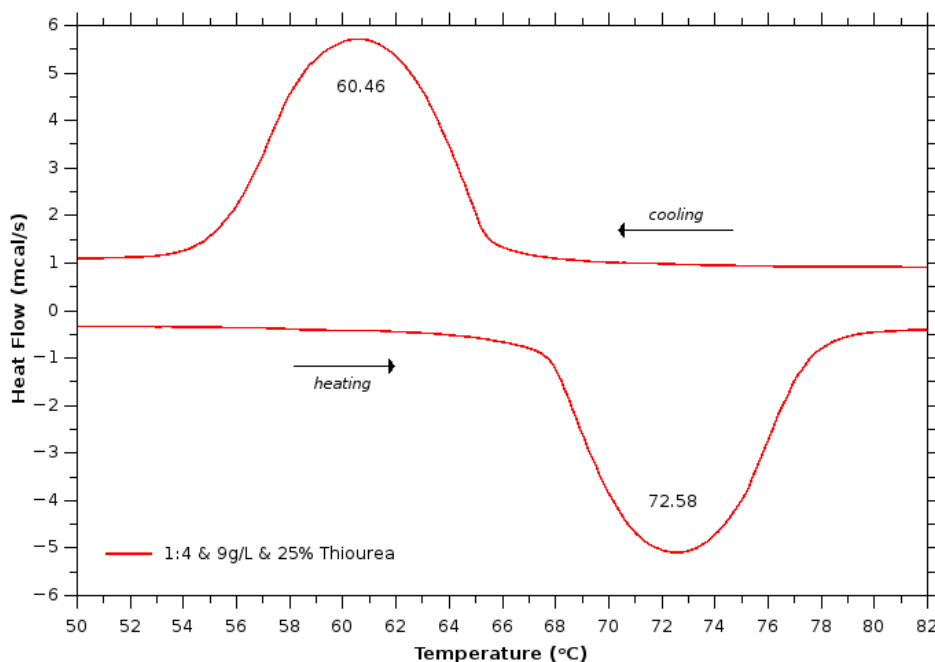


Figure 3.51 Narrow DSC curves ($\approx 50^\circ\text{C} \leq T \leq 80^\circ\text{C}$) of “1:4 & 9g/L & 25% Thiourea” sample.

From the DSC curve of the “1:4 & 9g/L & 25% Thiourea” configuration sample (Figure 3.51) we can calculate the $T_c = 66.52\text{ }^\circ\text{C}$ and the $\Delta T_c = 12.12\text{ }^\circ\text{C}$. The area under the curves is very large, with very high heat flow values, indicating a high $\text{VO}_2(\text{M})$ or (R) crystallinity in the sample composition, a conclusion which is in accordance with the XRD results of this sample.

3.8.3. DSC results of configurations with dopants

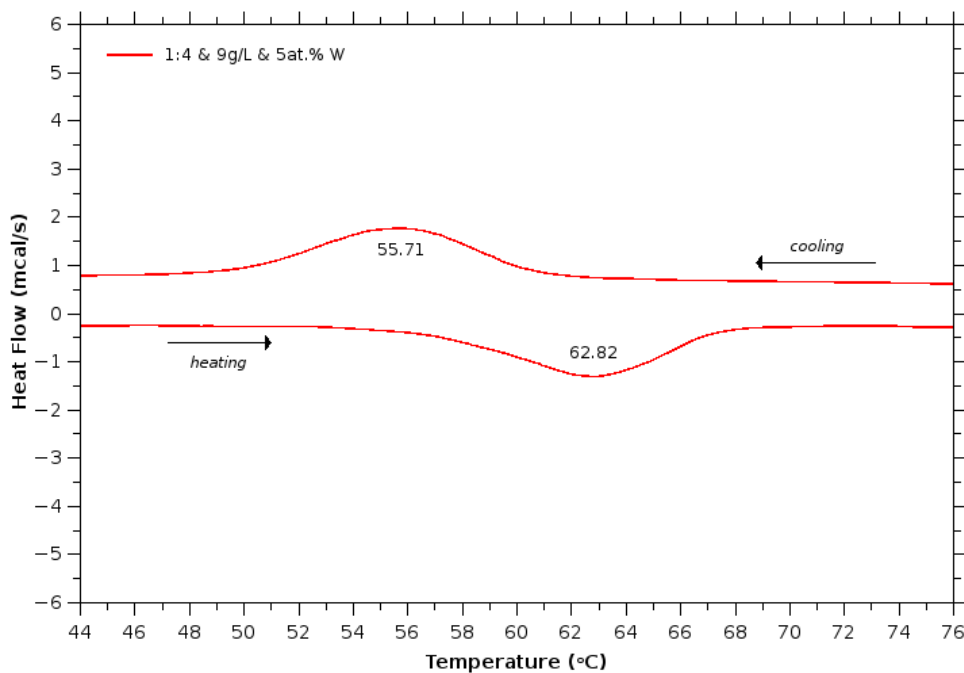


Figure 3.52 Narrow DSC curves of “1:4 & 9g/L & 5at.% W” sample.

From the DSC curve of the “1:4 & 9g/L & 5at.% W” configuration sample (Figure 3.52) we can calculate the $T_c = 59.27$ °C and the $\Delta T_c = 7.11$ °C. The area under the curves is small, with low heat flow values, indicating a lower $VO_2(M)$ or (R) crystallinity in the sample composition, a conclusion which is in accordance with the XRD results of this sample.

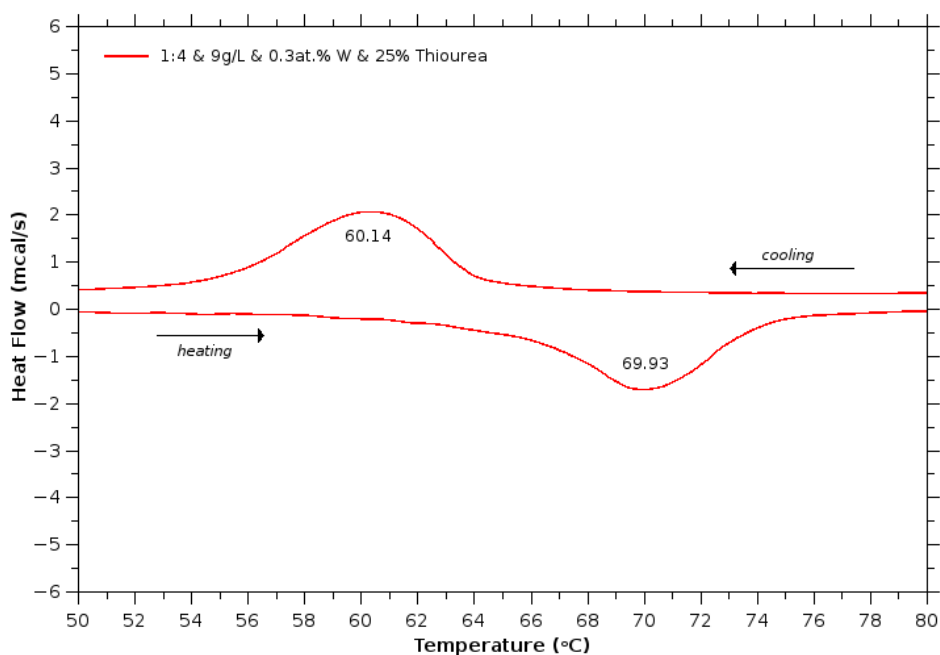


Figure 3.53 Narrow DSC curves of “1:4 & 9g/L & 0.3at.% W & 25% Thiourea” sample.

From the DSC curve of the “1:4 & 9g/L & 0.3at.% W & 25% Thiourea” configuration sample (Figure 3.53) we can calculate the $T_c = 65.04$ °C and the $\Delta T_c = 9.79$ °C. The area under the curves is small, with medium to low heat flow values, indicating a good VO₂(M) or (R) crystallinity in the sample composition, a conclusion which is in accordance with the XRD results of this sample.

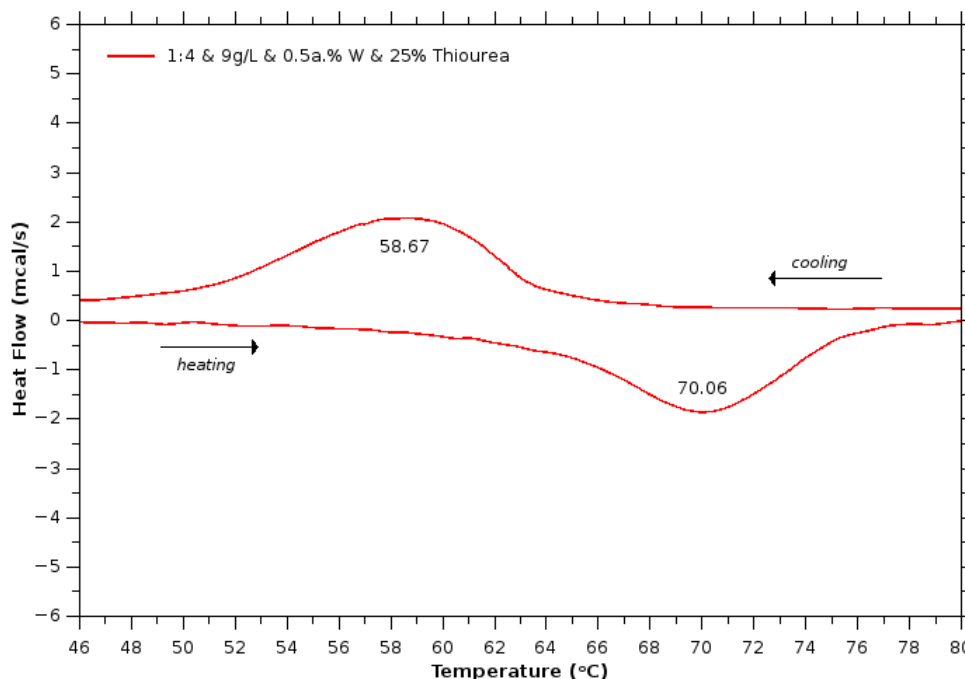


Figure 3.54 Narrow DSC curves of “1:4 & 9g/L & 0.5at.% W & 25% Thiourea” sample.

From the DSC curve of the “1:4 & 9g/L & 0.5at.% W & 25% Thiourea” configuration sample (Figure 3.54) we can calculate the $T_c = 64.37$ °C and the $\Delta T_c = 11.39$ °C. The area under the curves is moderate, with medium to low heat flow values, indicating a good VO₂(M) or (R) crystallinity in the sample composition, a conclusion which is in accordance with the XRD results of this sample.

From the DSC curve of the “1:4 & 9g/L & 0.8at.% W & 25% Thiourea” configuration sample (Figure 3.55) we can calculate the $T_c = 64.53$ °C and the $\Delta T_c = 9.11$ °C. The area under the curves is moderate, with medium to low heat flow values, indicating a good VO₂(M) or (R) crystallinity in the sample composition, a conclusion which is in accordance with the XRD results of this sample.

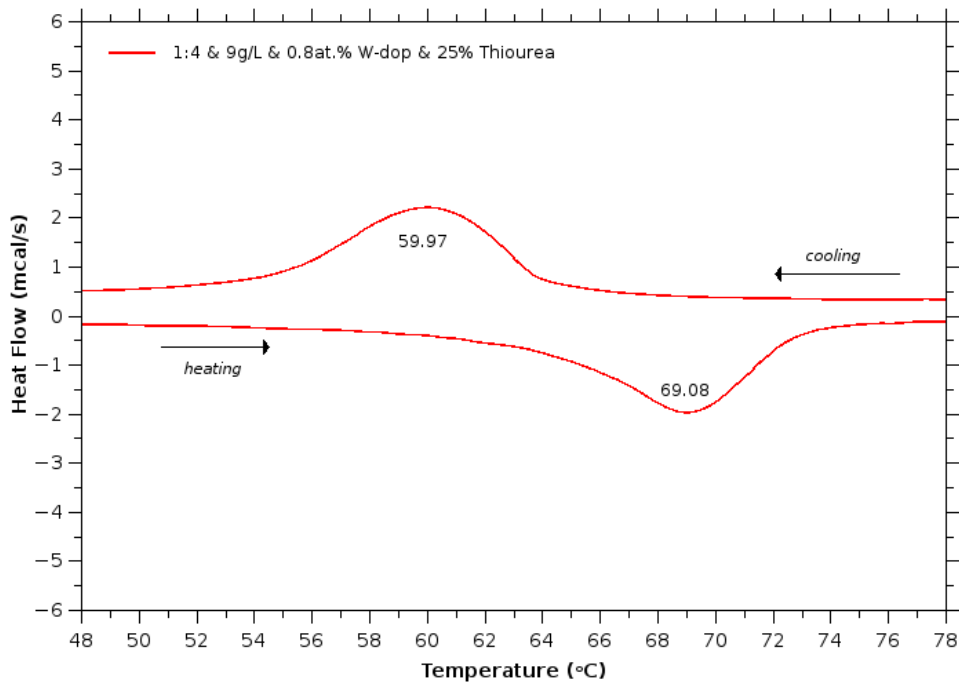


Figure 3.55 Narrow DSC curves of “1:4 & 9g/L & 0.8at.% W & 25% Thiourea” sample.

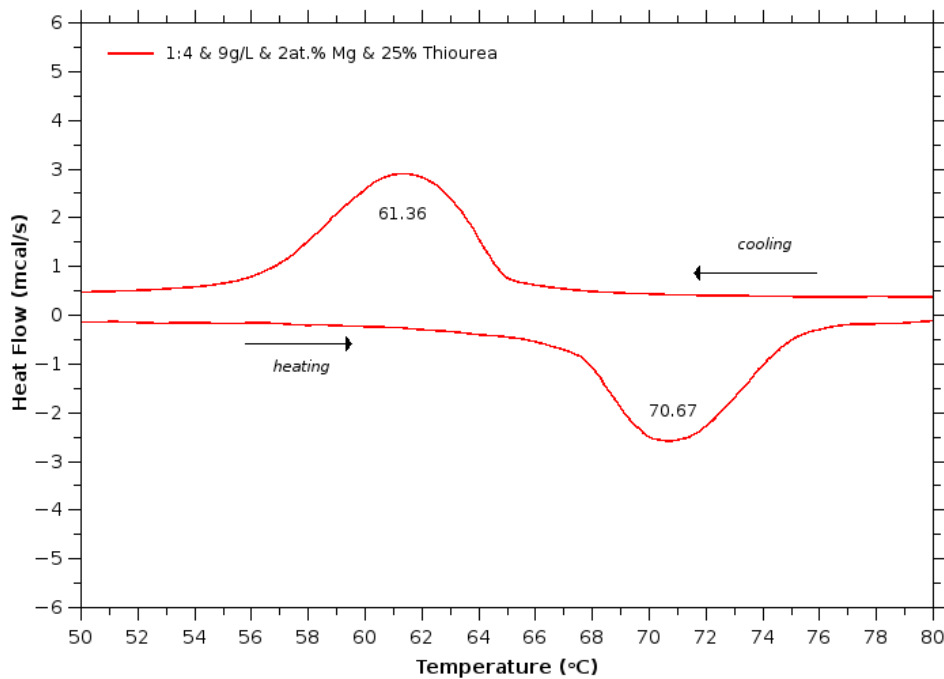


Figure 3.56 Narrow DSC curves of “1:4 & 9g/L & 2at.% Mg & 25% Thiourea” sample.

From the DSC curve of the “1:4 & 9g/L & 2at.% Mg & 25% Thiourea” configuration sample (Figure 3.56) we can calculate the $T_c = 66.02$ °C and the $\Delta T_c = 9.31$ °C. The area under the curves is moderate, with medium heat flow values, indicating a good VO₂(M) or (R) crystallinity in the sample composition, a conclusion which is in accordance with the XRD results of this sample.

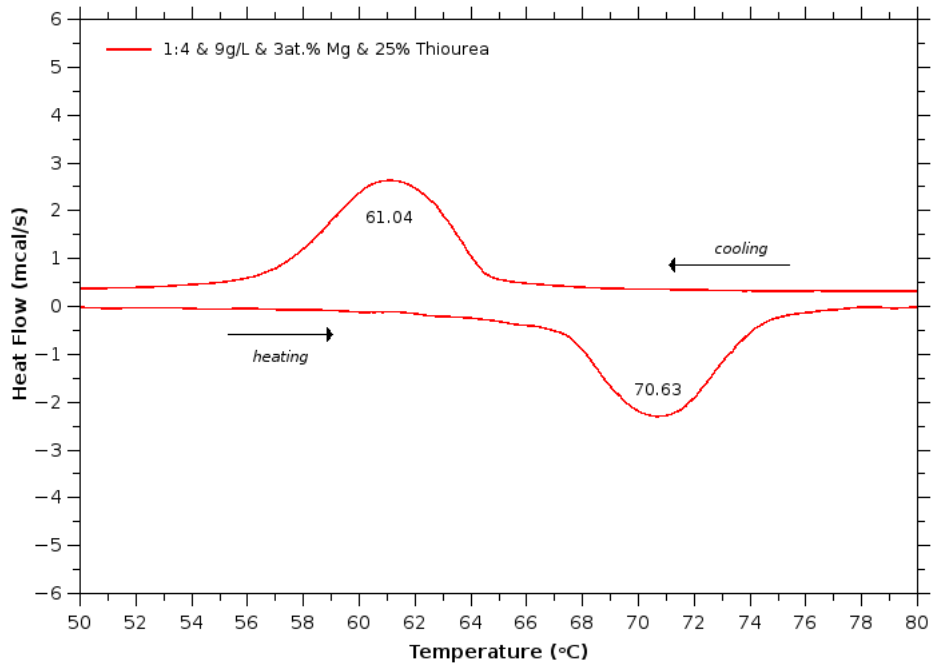


Figure 3.57 Narrow DSC curves of “1:4 & 9g/L & 3at.% Mg & 25% Thiourea” sample.

From the DSC curve of the “1:4 & 9g/L & 3at.% Mg & 25% Thiourea” configuration sample (Figure 3.57) we can calculate the $T_c = 65.84$ °C and the $\Delta T_c = 9.59$ °C. The area under the curves is moderate, with medium to low heat flow values, indicating a good VO₂(M) or (R) crystallinity in the sample composition, a conclusion which is in accordance with the XRD results of this sample.

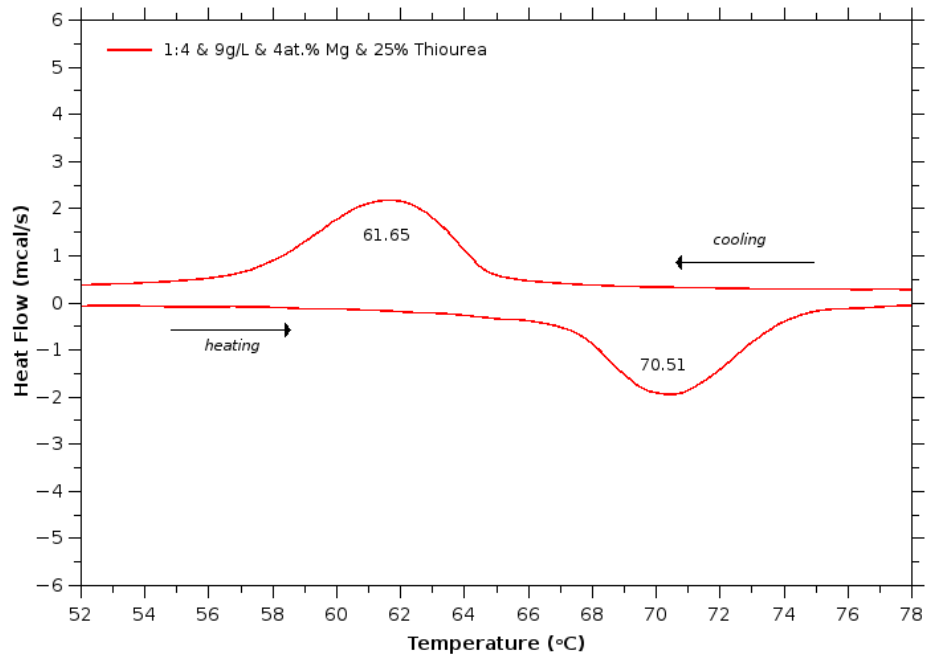


Figure 3.58 Narrow DSC curves of “1:4 & 9g/L & 4at.% Mg & 25% Thiourea” sample.

From the DSC curve of the “1:4 & 9g/L & 4at.% Mg & 25% Thiourea” configuration sample (Figure 3.58) we can calculate the $T_c = 66.08 \text{ }^\circ\text{C}$ and the $\Delta T_c = 8.86 \text{ }^\circ\text{C}$. The area under the curves is moderate, with lower heat flow values, indicating a moderate $\text{VO}_2(\text{M})$ or (R) crystallinity in the sample composition, a conclusion which is in accordance with the XRD results of this sample.

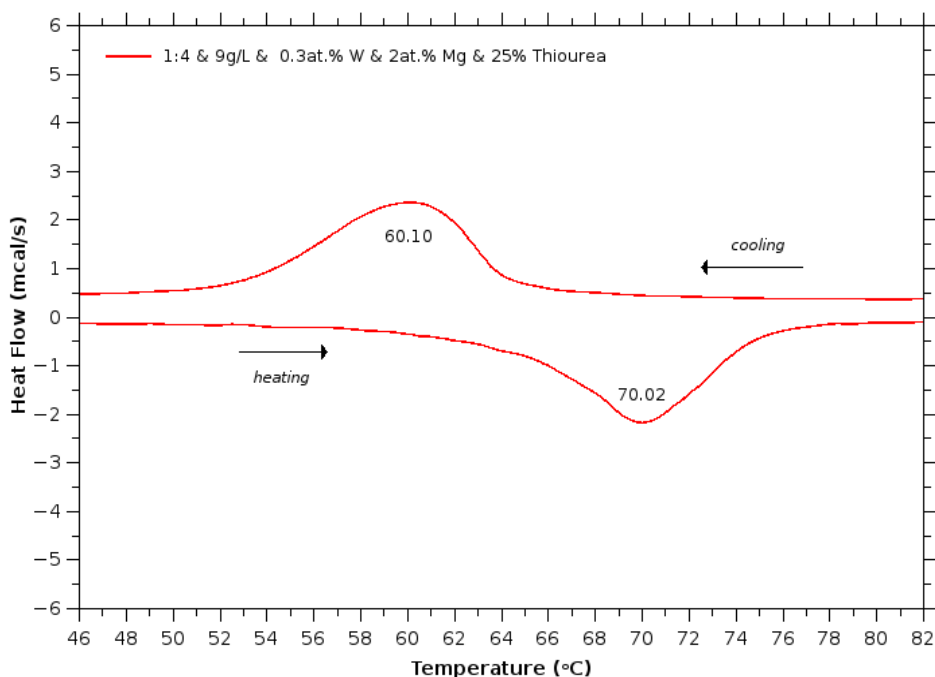


Figure 3.59 Narrow DSC curves of “1:4 & 9g/L & 0.3at.% W & 2at.% Mg & 25% Thiourea” sample.

From the DSC curve of the “1:4 & 9g/L & 0.3at.% W & 4at.% Mg & 25% Thiourea” configuration sample (Figure 3.59) we can calculate the $T_c = 65.06 \text{ }^\circ\text{C}$ and the $\Delta T_c = 9.92 \text{ }^\circ\text{C}$. The area under the curves is moderate to small, with lower heat flow values, indicating a moderate $\text{VO}_2(\text{M})$ or (R) crystallinity in the sample composition, a conclusion which is in accordance with the XRD results of this sample.

From the DSC curve of the “1:4 & 9g/L & 0.3at.% W & 3at.% Mg & 25% Thiourea” configuration sample (Figure 3.60) we can calculate the $T_c = 65.36 \text{ }^\circ\text{C}$ and the $\Delta T_c = 9.96 \text{ }^\circ\text{C}$. The area under the curves is moderate, with lower heat flow values, indicating a moderate $\text{VO}_2(\text{M})$ or (R) crystallinity in the sample composition, a conclusion which is in accordance with the XRD results of this sample.

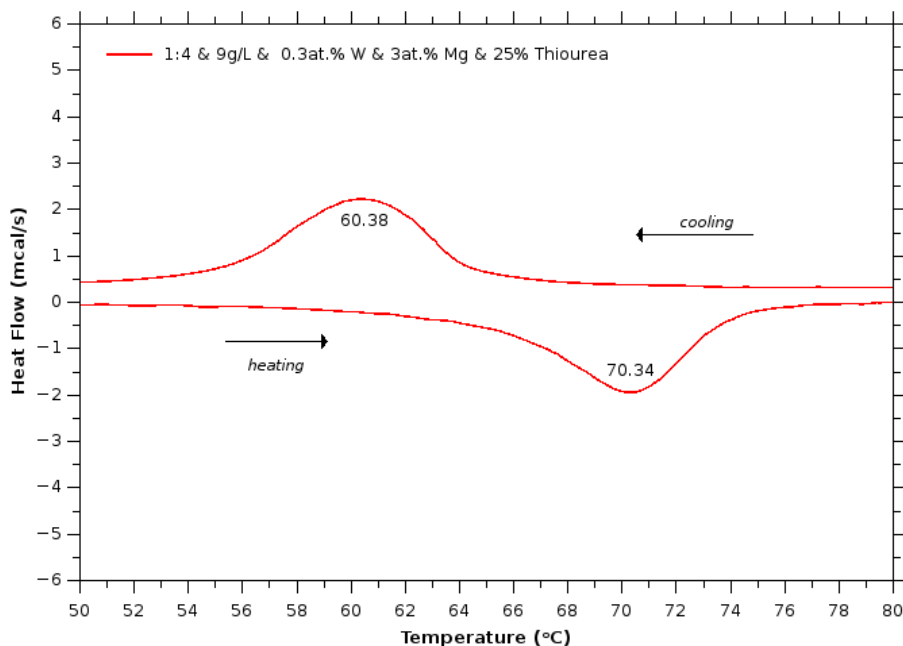


Figure 3.60 Narrow DSC curves ($\approx 50^{\circ}\text{C} \leq T \leq 80^{\circ}\text{C}$) of “1:4 & 9g/L & 0.3at.% W & 3at.% Mg & 25% Thiourea” sample.

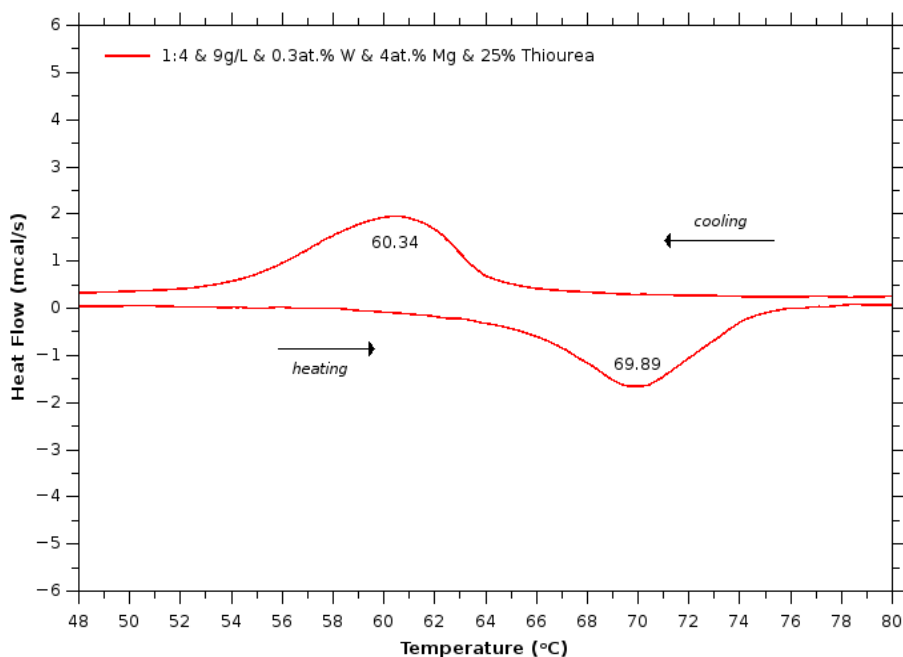


Figure 3.61 Narrow DSC curves ($\approx 50^{\circ}\text{C} \leq T \leq 80^{\circ}\text{C}$) of “1:4 & 9g/L & 0.3at.% W & 4at.% Mg & 25% Thiourea” sample.

From the DSC curve of the “1:4 & 9g/L & 0.3at.% W & 4at.% Mg & 25% Thiourea” configuration sample (Figure 3.61) we can calculate the $T_c = 65.12^{\circ}\text{C}$ and the $\Delta T_c = 9.55^{\circ}\text{C}$. The area under the curves is moderate, with low heat flow values, indicating a moderate $\text{VO}_2(\text{M})$ or (R) crystallinity in the sample composition, a conclusion which is in accordance with the XRD results of this sample.

3.8.4. Conclusions over the structural transition

Out of the 44 configurations presented in this thesis (with 44 samples prior and 44 samples after annealing), 26 of the annealed samples were tested by differential scanning calorimetry for structural transition exhibition, of which 24 found to be thermochromic, as presented in this section, and 2 gave no peaks. These samples with configurations “1:1.5 & 9 g/L & 5at.% W” and “1:8 & 9 g/L & 5at.% W” have been identified by the xrd identification programs as mixtures of vanadium oxide without any evident presence of VO₂(M) polymorph, and were tested for the sole reason of examining the possibility of structural transition from a possibly undetectable by the XRD VO₂(M).

All of the 24 samples presented exhibit an inherent structural transition that can be repeated with the same results acquired. Unfortunately no more tests to define the maximum number possible of repeatable cycles have been made, since the focus of this project was more towards an optimization of the synthetic routes. All the samples feature a transition temperature in the area: $64\text{ }^{\circ}\text{C} \leq T_c \leq 67\text{ }^{\circ}\text{C}$, with the unique exception of “1:4 & 9 g/L & 5at.% W” configuration sample which has a $T_c = 59.27\text{ }^{\circ}\text{C}$. Samples with the lower transition temperature were the ones with Tungsten doping, as expected, but no correlation between the smaller tungsten atomic percentages (0.3, 0.5 and 0.8 at.% W) and temperature value was noted.

ΔT_c hysteresis loop between the cooling and heating structural transitions of the same samples varied from $6\text{ }^{\circ}\text{C}$ to $12\text{ }^{\circ}\text{C}$, with one of our basic configuration “1:8 & 3 g/L” sample scoring the lower $\Delta T_c = 6.45\text{ }^{\circ}\text{C}$ and the “1:4, 9g/L, 25% Thiourea” configuration sample the higher $\Delta T_c = 12.12\text{ }^{\circ}\text{C}$. This last observation is relevant to all of our configurations with additive thiourea, where a rise in the hysteresis values can be noticed. As shown on *Figure 3.62* there is a correlation between T_c and ΔT_c , that if generalized suggests that on lower transition temperatures, T_c , the hysteresis, ΔT_c , will increase. Obviously there are exceptions to this generalization, as in our “1:4 & 9 g/L & 5at.% W” configuration sample, that displays the best transition properties for smart glazing applications.

As mentioned in the introductory part of this thesis, doping the vanadium dioxide lattice with tungsten yields a depression in the transition temperature of 20 to 26 $^{\circ}\text{C}$ per W %atom^{[1.2.36],[1.2.37],[1.2.38]}. Of course, this experimentally deduced prediction does not correspond to our experimental result, suggesting that the incorporation of dopant in the material lattice is less than the equivalent quantity provided in the reagents solution, meaning that our synthetic mechanism suffers from dopant-loss towards the supernatant of our as obtained product. An effective way to confirm the actual doping achieved for these samples is with an elemental composition analysis, with some examples being: Inductively coupled plasma atomic emission spectroscopy (ICP-AES), X-ray photo-electron spec-

troscopy (XPS), Energy-dispersive X-ray spectroscopy (EDX) and others. In following chapter we will discuss the elemental analysis results from EDX measurements data.

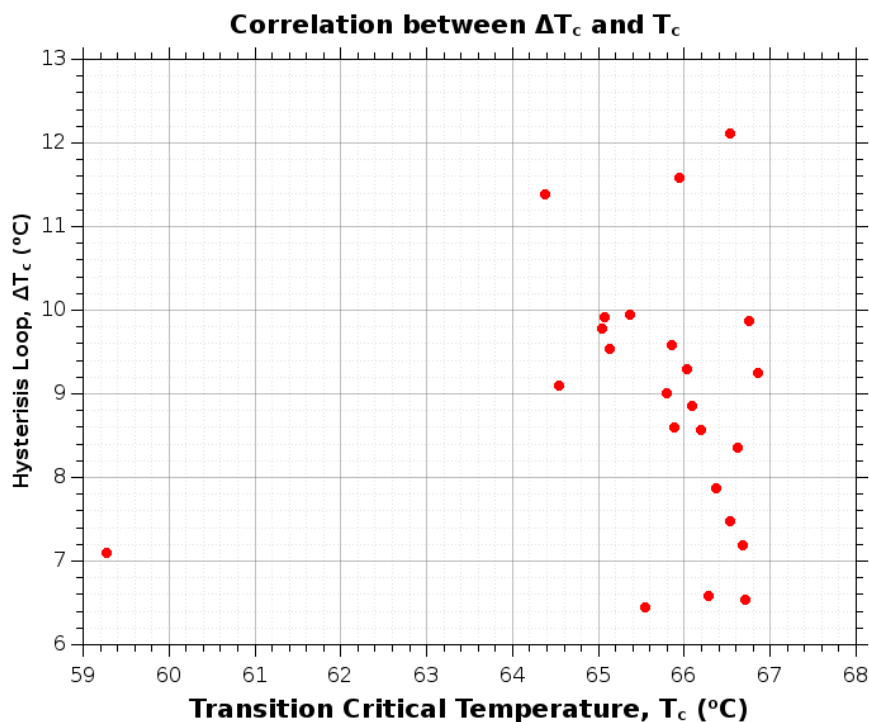


Figure 3.62a Plot of Transition temperatures vs Hysteresis loop for our thermochromic materials

The last thing done to examine structural properties of our samples was the XRD in situ, where XRD measurements were executed in various temperatures inside a special heated apparatus in a constant temperature value, with an instrumental systematic error of ± 10 °C, during the heating and the cooling process. We examined two samples, the “1:4 & 9 g/L & 50% thiourea” configuration sample and the “1:4 & 9 g/L & 5at.% W” configuration sample. The first one was measured only during the heating process. The results are presented on Figure 3.62b.

Due to the special apparatus used in these measurement, the sample quantities used were very small, thus the xrd peaks are more weak here than were in the rest of our xrd data presented. This makes our quest of monitoring the structural phase change from polymorph M to R more difficult, so we are going to focus on the major peak of 27.8° only.

On Figure 3.62b we can observe the major peak of our thermochromic VO₂ in different temperatures from 13 °C to 98 °C. For sample of “1:4 & 9 g/L & 50% thiourea” configuration there is an evident shift towards values of smaller degrees during the heating process, from 28.12° (at 13 °C) to 27.96°C (at 98 °C). For sample of “ 1:4 & 9 g/L & 5at.% W” configuration there is a much smaller,

almost non-existent shift towards values of smaller degrees during the heating, from 27.50° (at 38 °C) to 27.46 °C (at 98 °C), and back again towards values of greater degrees during the cooling process, from 27.46 °C (at 98 °C) to 27.48° (at 38 °C), which can be easily dismissed due to the various systematic errors of our xrd measurement.

This shift observed for our “1:4 & 9 g/L & 50% thiourea” sample, which sample consists of pure VO₂(M) as identified from xrd identification programs, has been reported before through the various works^{[3.11][3.12][3.13]} works. Okimura, Sakai, and Ramanathan^[3.12] monitored the shift of the (020) 2θ = 40° peak towards values of lower degrees, whereas Banerjee et al.^[3.13] monitored the shift of the major (011) 2θ = 27.8° VO₂(M) peak and the (013) VO₂(M) peak towards values of lower degrees, up to the equivalent peaks of VO₂(R), (110)R and (130)R.

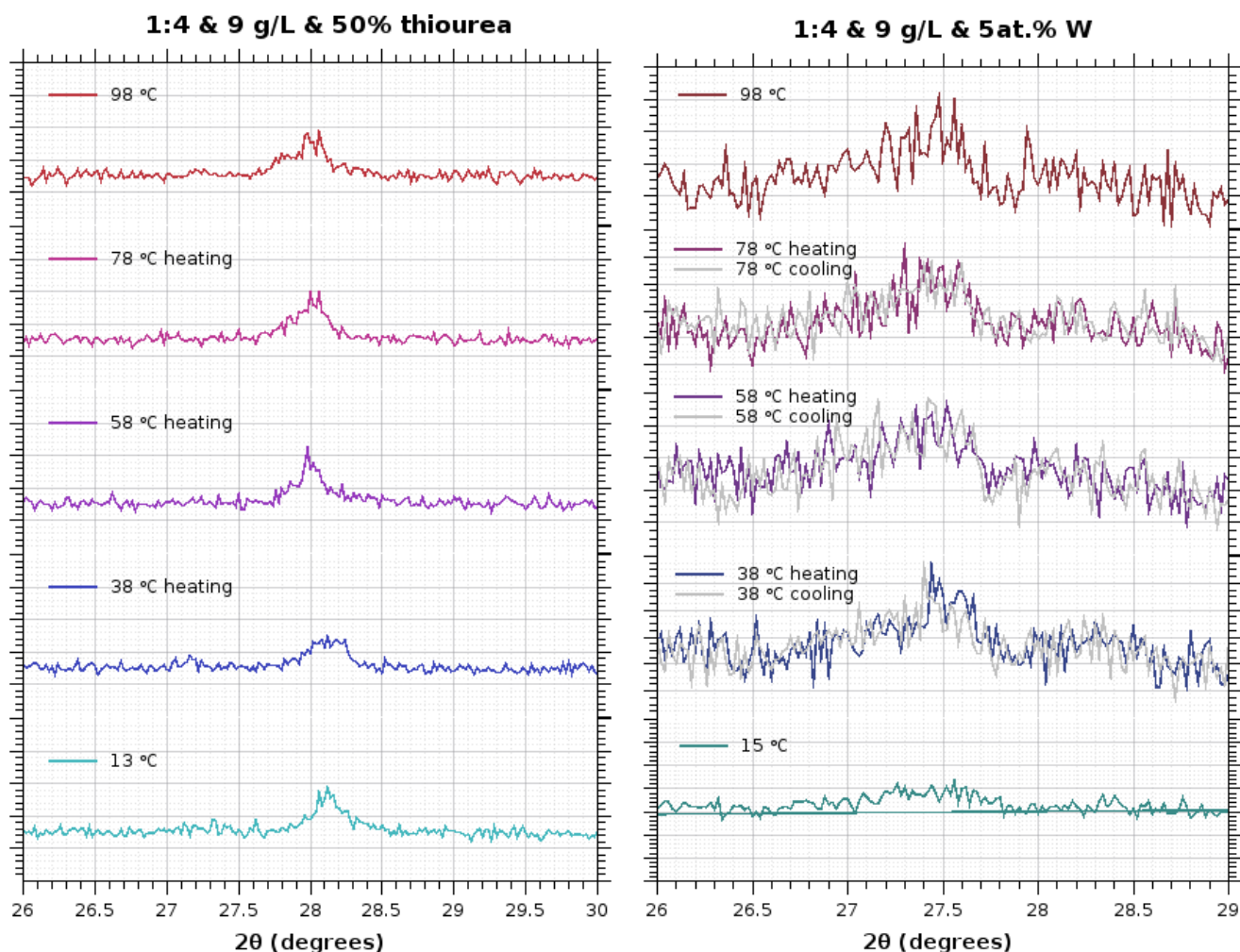


Figure 3.62b XRD in situ of “1:4 & 9 g/L & 50% thiourea” and “1:4 & 9 g/L & 5at.% W” configuration samples

3.9 Elemental analysis

In order to examine the dopants incorporation on our materials lattice, an elemental analysis of our doped products was conducted by an Energy Dispersive X-ray (EDX) spectrometry system, prior and after the annealing procedure. After the e-beam bombardment of our samples, emitted X-rays that have sufficient energy to escape the material surface can be detected, resulting in a spectrum with peaks at the characteristic energies for the elements present. The areas under selected peaks can also be used to provide semi-quantitative elemental composition information, which is presented in the tabulated inset of each spectrum figure. The SEM image inset shows an inspection field within which EDX data were collected by rastering the e-beam to produce the spectrum shown. These EDX results will be presented and discussed in this chapter.

3.9.1. EDX results of *W*-doped samples

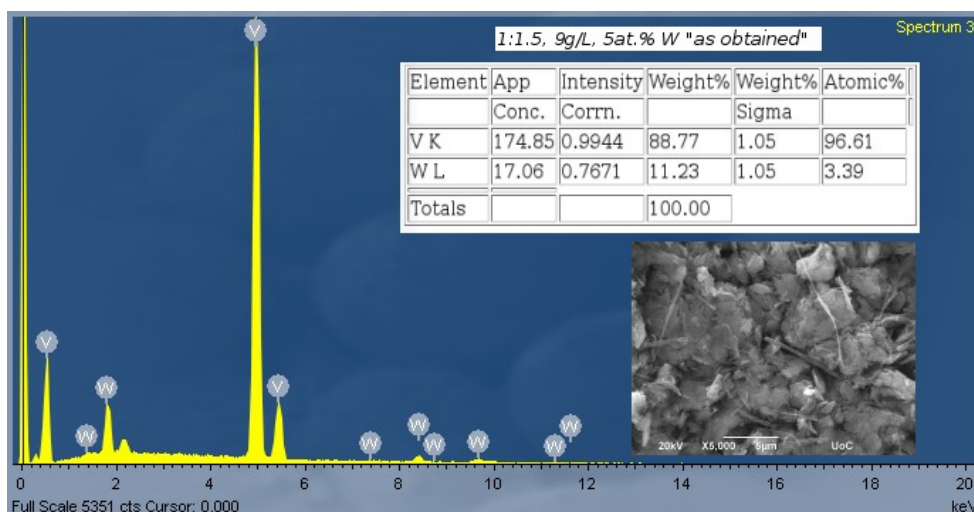


Figure 3.63 EDX results of “1:1.5 & 9 g/L & 5at.% W” configuration “as obtained” sample

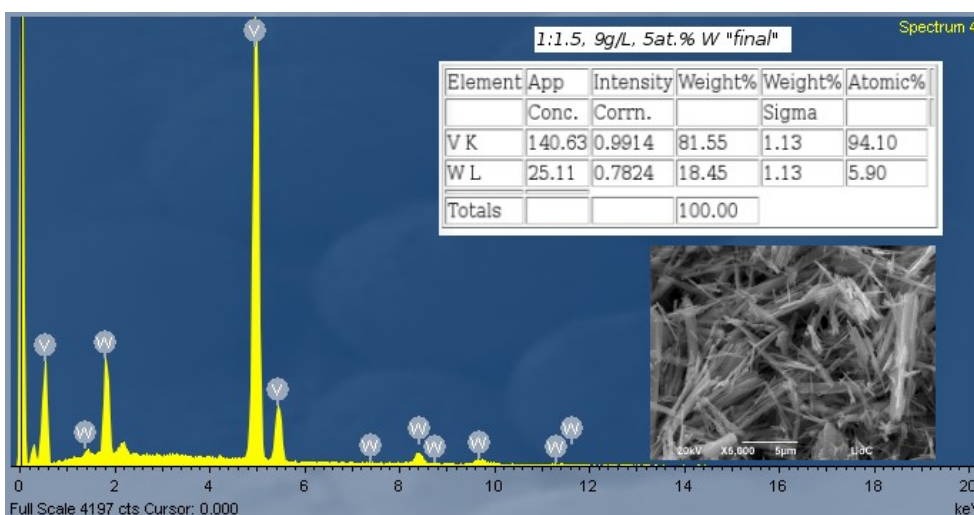


Figure 3.64 EDX results of “1:1.5 & 9 g/L & 5at.% W” configuration “final” sample

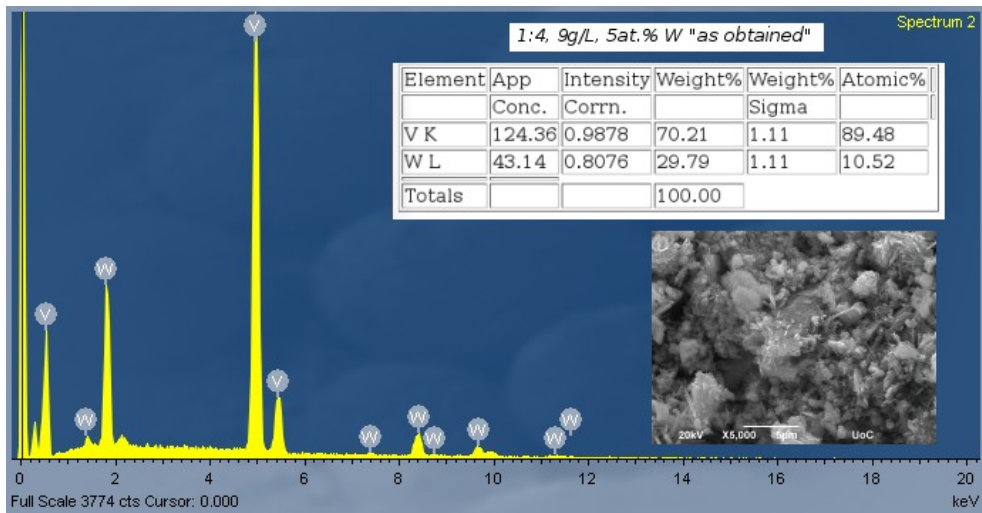


Figure 3.65 EDX results of “1:4 & 9 g/L & 5at.% W” configuration “as obtained” sample

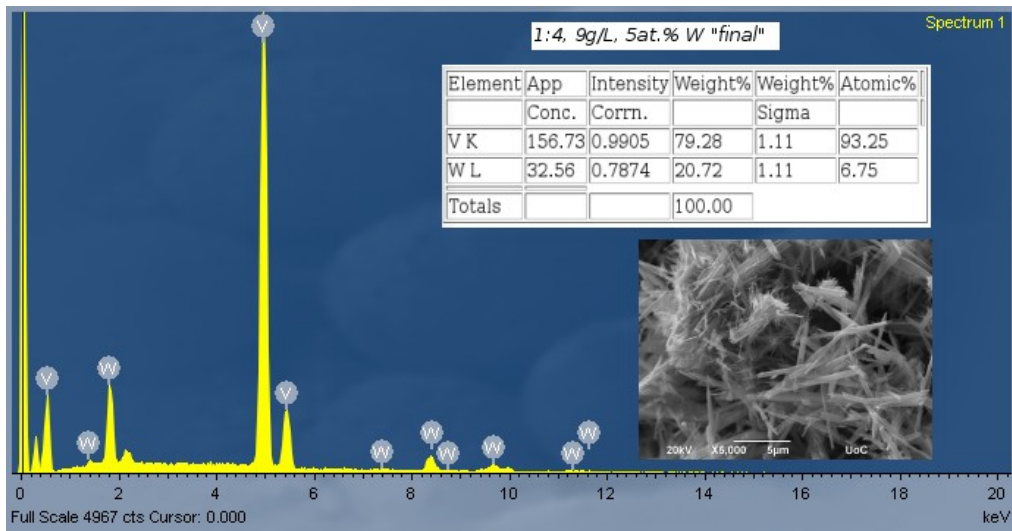


Figure 3.66 EDX results of “1:4 & 9 g/L & 5at.% W” configuration “final” sample

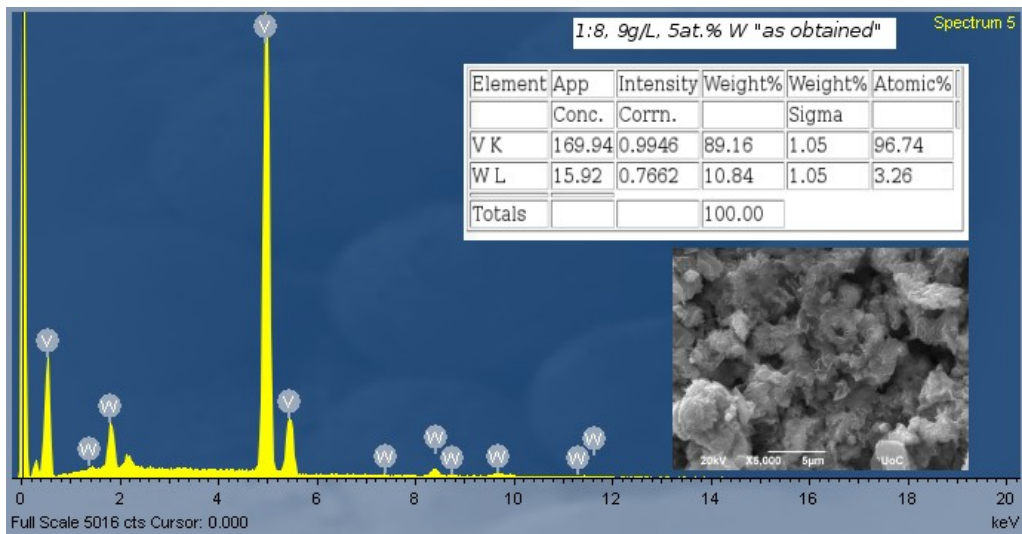


Figure 3.67 EDX results of “1:8 & 9 g/L & 5at.% W” configuration “as obtained” sample

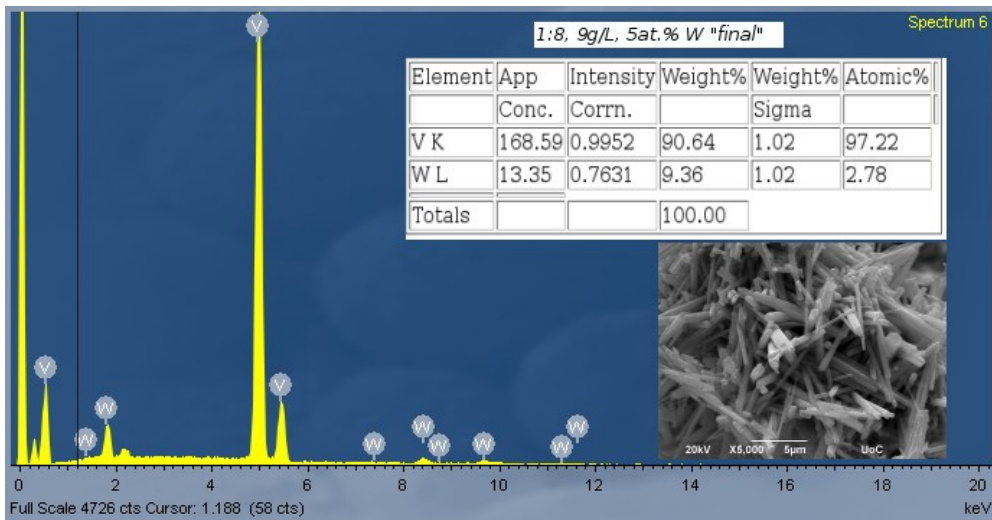


Figure 3.68 EDX results of “1:8 & 9 g/L & 5at.% W” configuration “final” sample

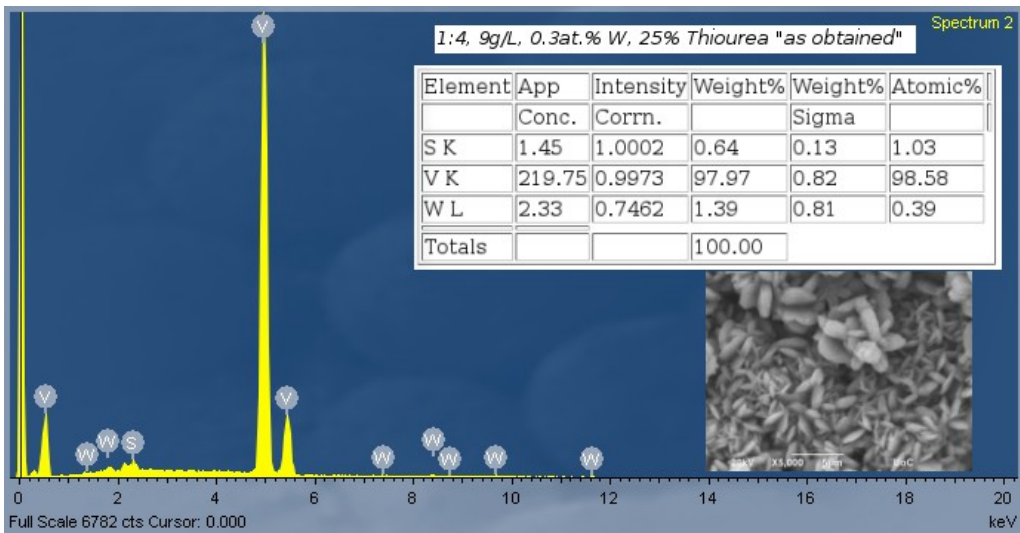


Figure 3.69 EDX of “1:4, 9 g/L, 0.3at.% W, 25% Thiourea” configuration “as obtained” sample

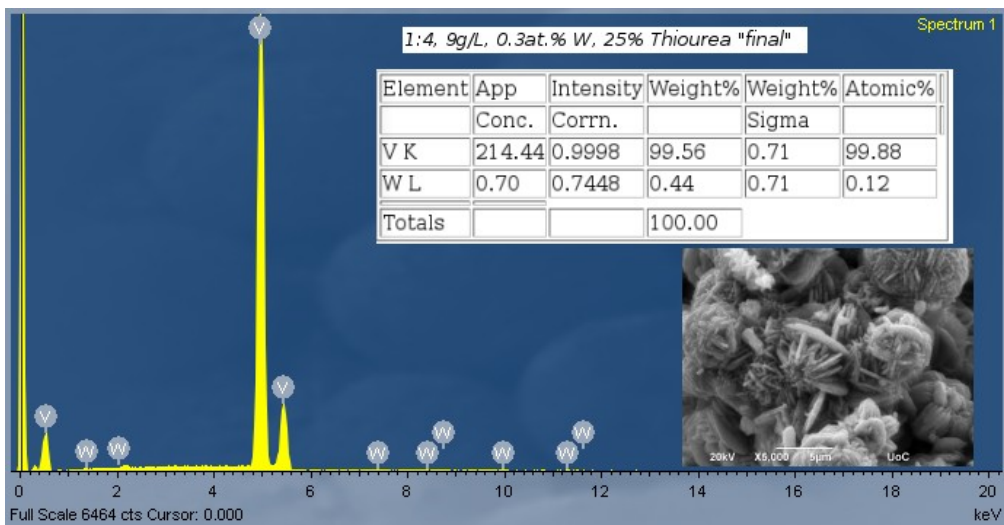


Figure 3.70 EDX results of “1:4, 9 g/L, 0.3at.% W, 25% Thiourea” configuration “final” sample

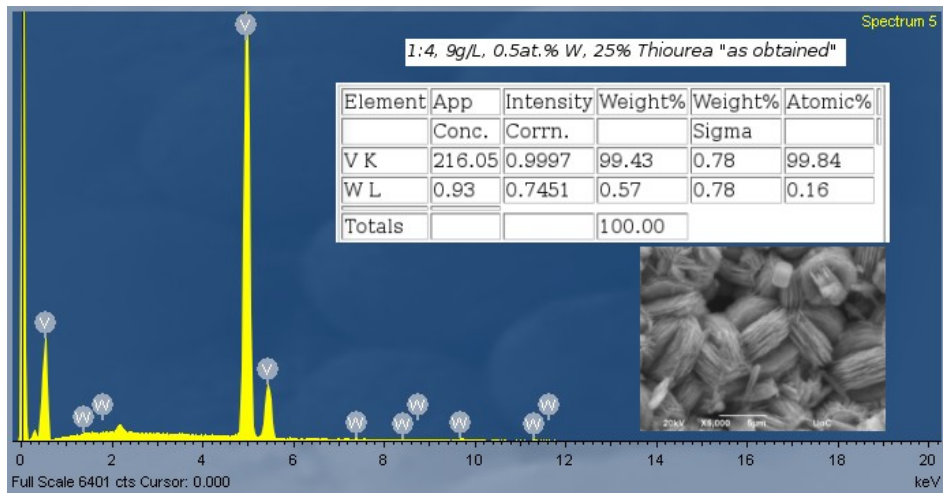


Figure 3.71 EDX of “1:4, 9 g/L, 0.5at.% W, 25% Thiourea” configuration “as obtained” sample

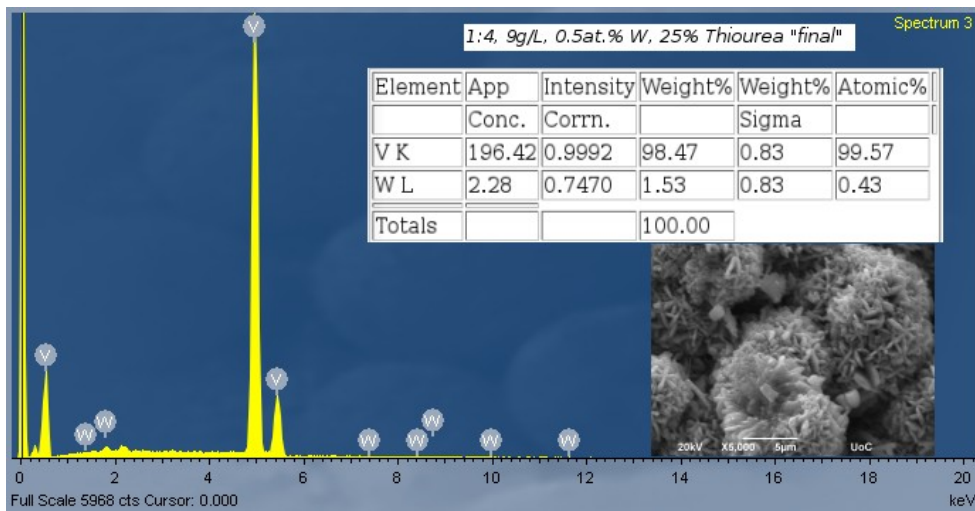


Figure 3.72 EDX results of “1:4, 9 g/L, 0.5at.% W, 25% Thiourea” configuration “final” sample

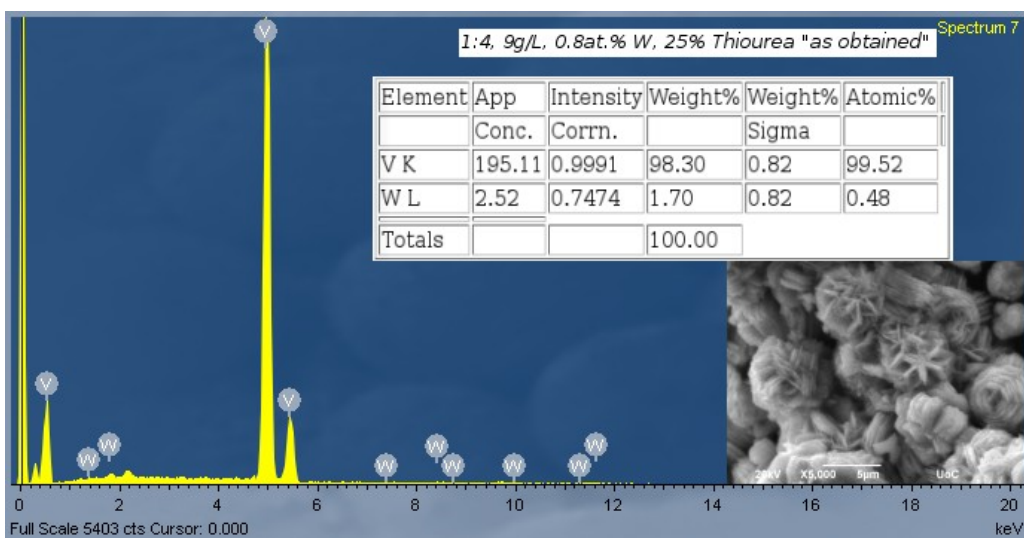


Figure 3.73 EDX results of “1:4, 9 g/L, 0.8at.% W, 25% Thiourea” configuration “as obtained” sample

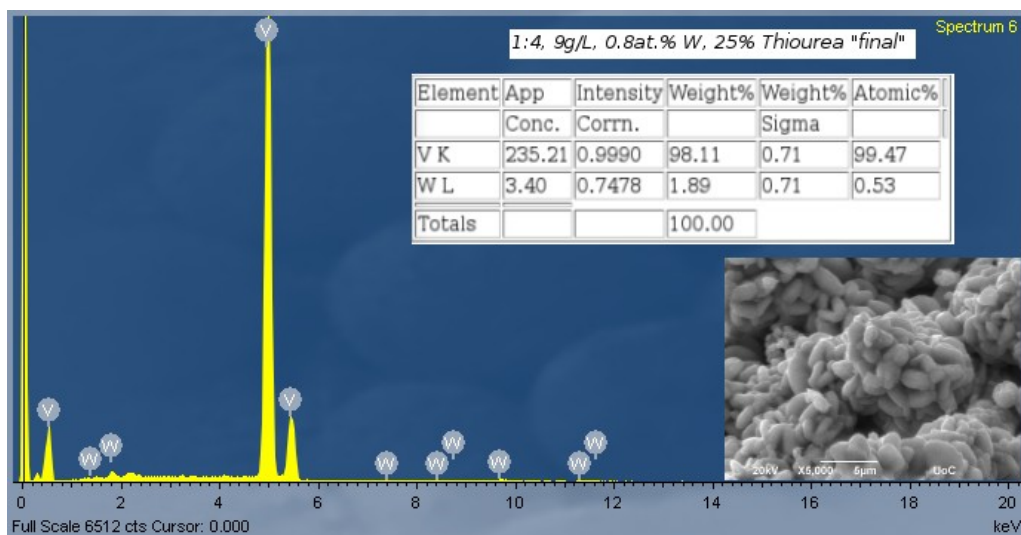


Figure 3.74 EDX results of “1:4, 9 g/L, 0.8at.% W, 25% Thiourea” configuration “final” sample

For the majority of our “W-doped” samples, results reveal that V and W are the main elements present within the inspection field, with V being the most abundant of the two. This is a confirmation of the dopant being present inside our material structure. The sole exception is “1:4, 9 g/L, 0.3at.% W, 25% Thiourea” configuration “as obtained” sample the results of which show it consists of elements V, S and W, with V being the most abundant, followed by S and then W. This is a direct evidence of the contribution of the S element and its entities, originating from additive thiourea, to our synthesis mechanism results.

Regarding the actual percentage of the dopant in our structures, EDX provide us with some semi-quantified results that should be considered as such along with their high systematic and random errors, since the accuracy and precision of this quantitative analysis is affected by various factors. These errors can be observed on our own measurements, with samples of the same W atomic percentage (at.% W) showing different EDX experimental Atomic% values. However, from a more general point of view, we can discuss some of the quantitative observations, such as the deviation of the experimental tungsten Atomic% values from our calculated at.% W. This indicates either a loss of dopant towards the supernatant of the “as obtained” product (as already hypothesized in a previous section of this thesis), a low dopant incorporation on the structures of samples at the specific inspection fields measured (by pure chance, low repeatability), or a tendency inherent to our synthetic route or of the material itself to result in more inhomogeneous doping in regards to the particles composition, resulting in a nucleation of our doping elements and thus a lower incorporation of W in our material. Morphological homogeneity of our materials will be discussed in the following chapter. These results also explain the reduced effect of the dopant on the T_c .

3.9.2. EDX results of Mg-doped samples

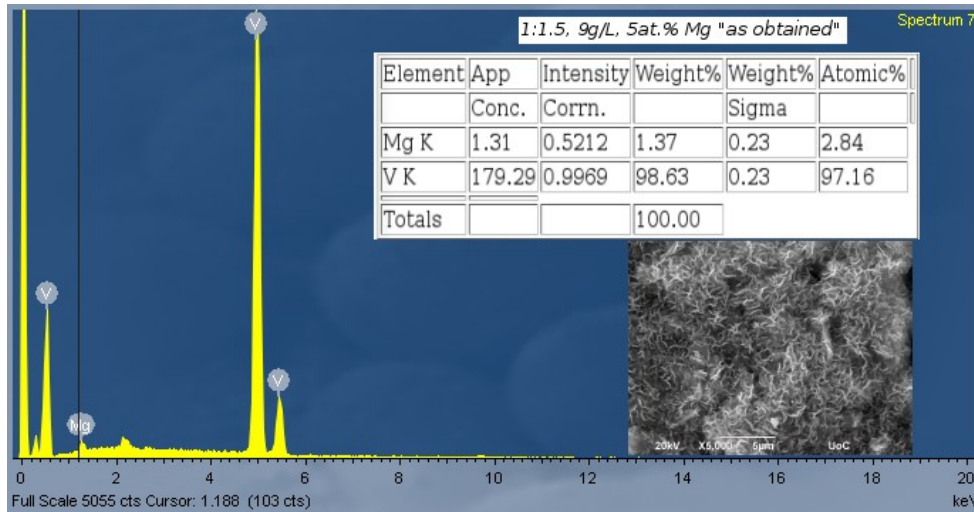


Figure 3.75 EDX results of “1:1.5 & 9 g/L & 5at.% Mg” configuration “as obtained” sample

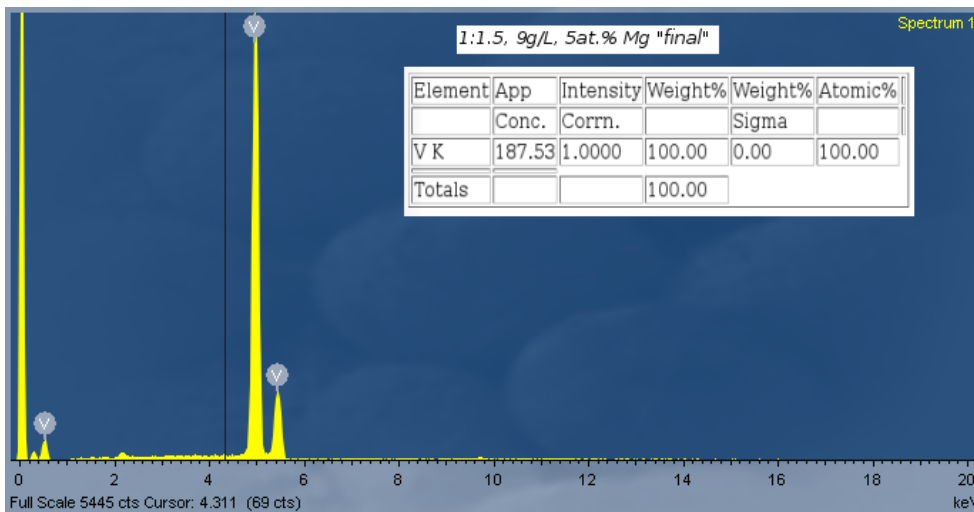


Figure 3.76 EDX results of “1:1.5 & 9 g/L & 5at.% Mg” configuration “final” sample

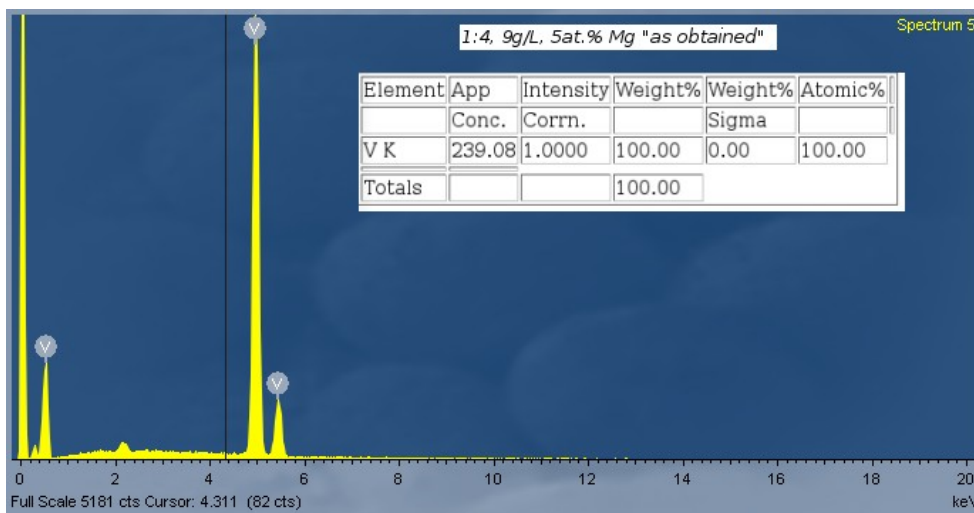


Figure 3.77 EDX results of “1:4 & 9 g/L & 5at.% Mg” configuration “as obtained” sample

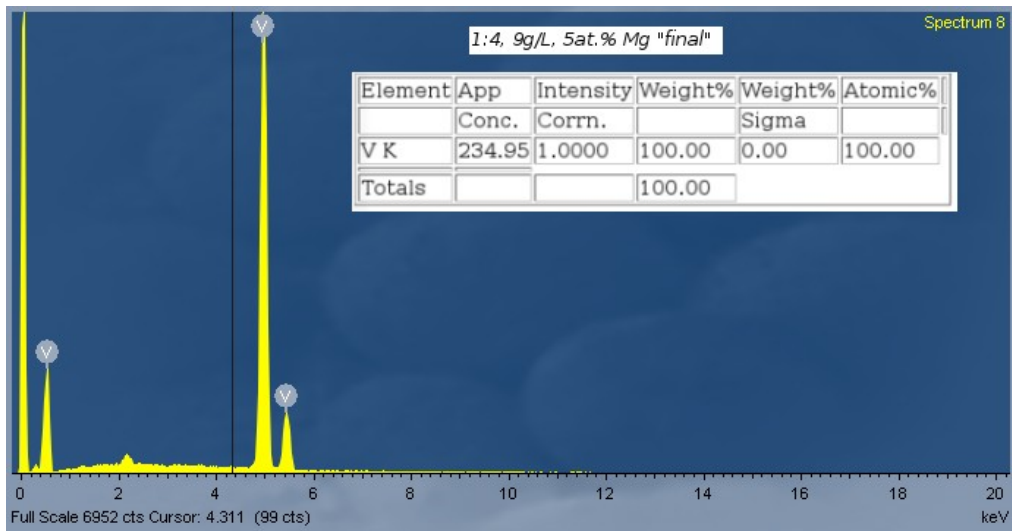


Figure 3.78 EDX results of "1:4 & 9 g/L & 5at.% Mg" configuration "final" sample

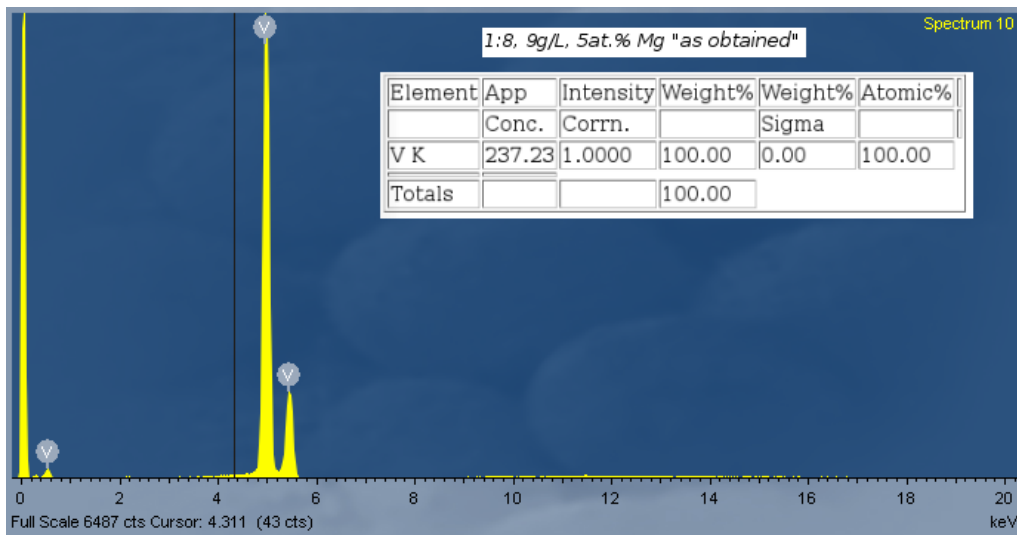


Figure 3.79 EDX results of "1:8 & 9 g/L & 5at.% Mg" configuration "as obtained" sample

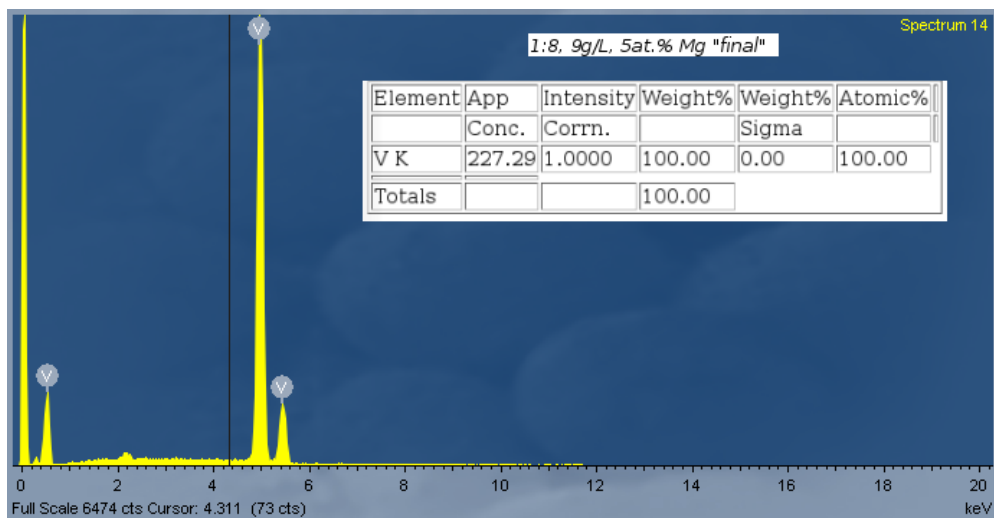


Figure 3.80 EDX results of "1:8 & 9 g/L & 5at.% Mg" configuration "final" sample

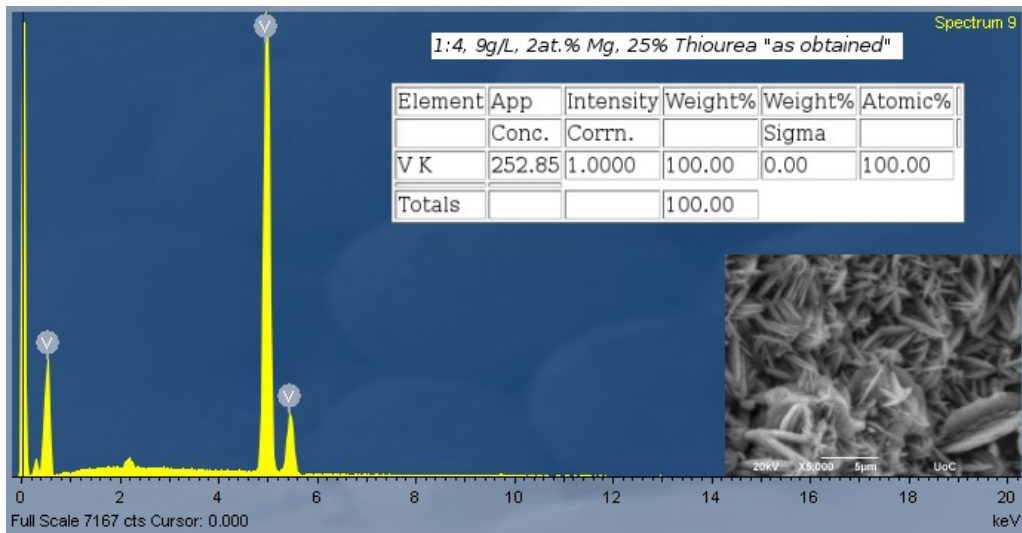


Figure 3.81 EDX of “1:4, 9 g/L, 2at.% Mg, 25% Thiourea” configuration “as obtained” sample

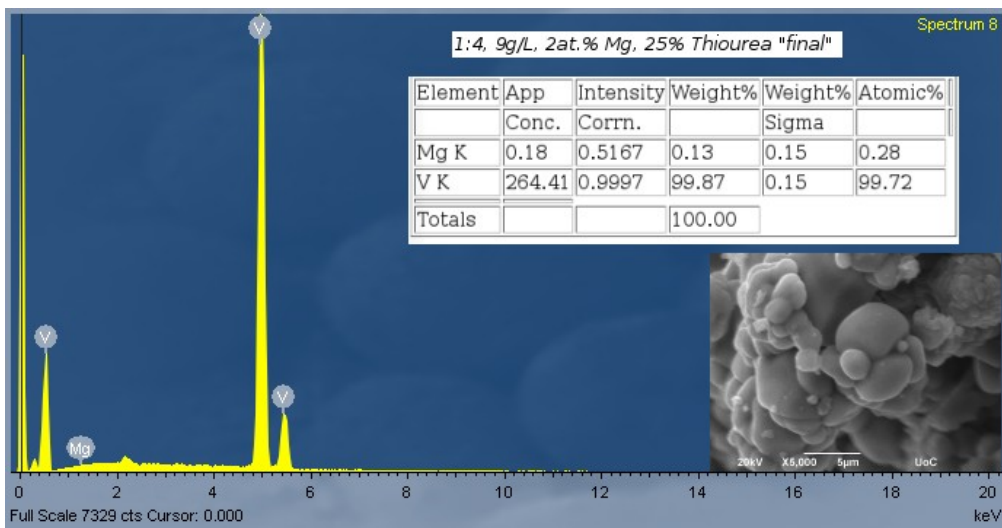


Figure 3.82 EDX results of “1:4, 9 g/L, 2at.% Mg, 25% Thiourea” configuration “final” sample

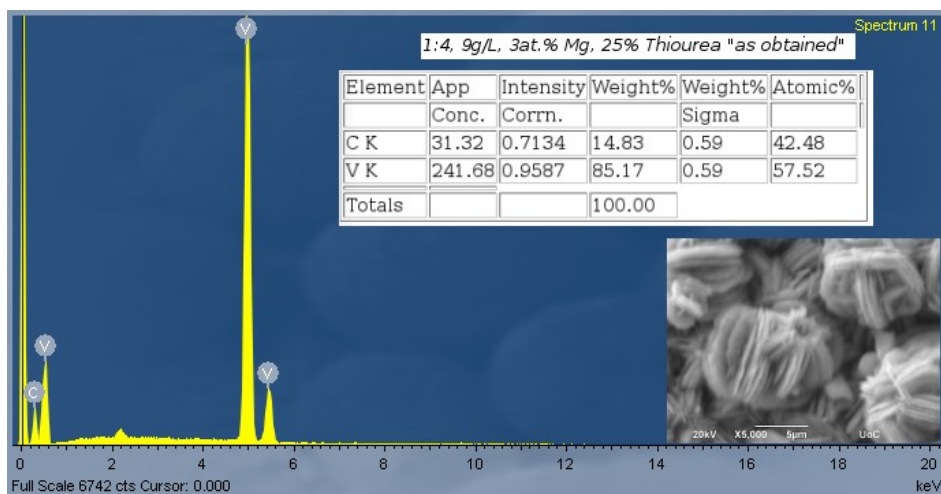


Figure 3.83 EDX of “1:4, 9 g/L, 3at.% Mg, 25% Thiourea” configuration “as obtained” sample

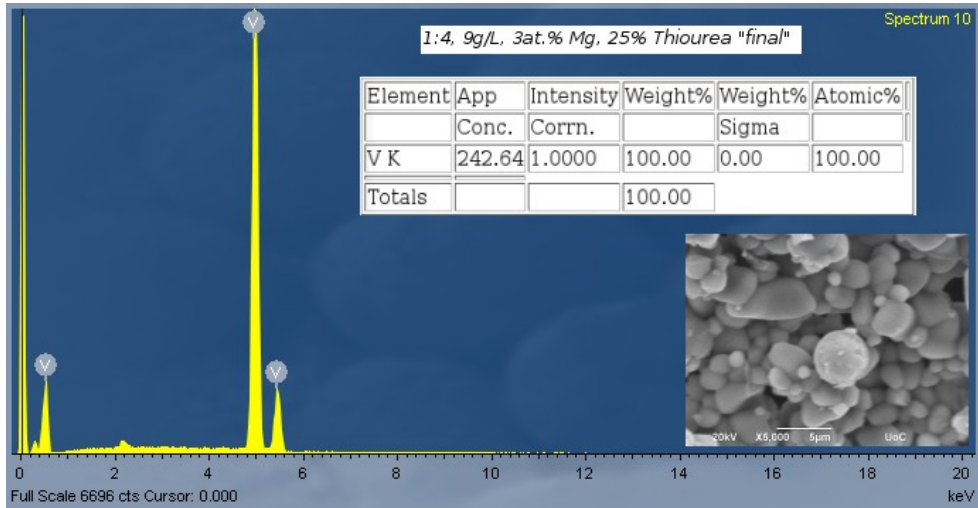


Figure 3.84 EDX results of “1:4, 9 g/L, 3at.% Mg, 25% Thiourea” configuration “final” sample

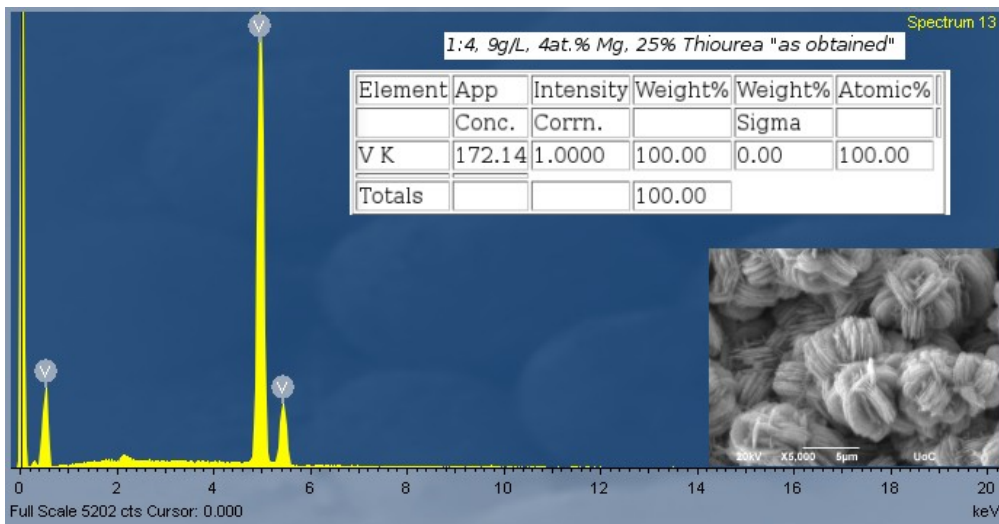


Figure 3.85 EDX of “1:4, 9 g/L, 4at.% Mg, 25% Thiourea” configuration “as obtained” sample

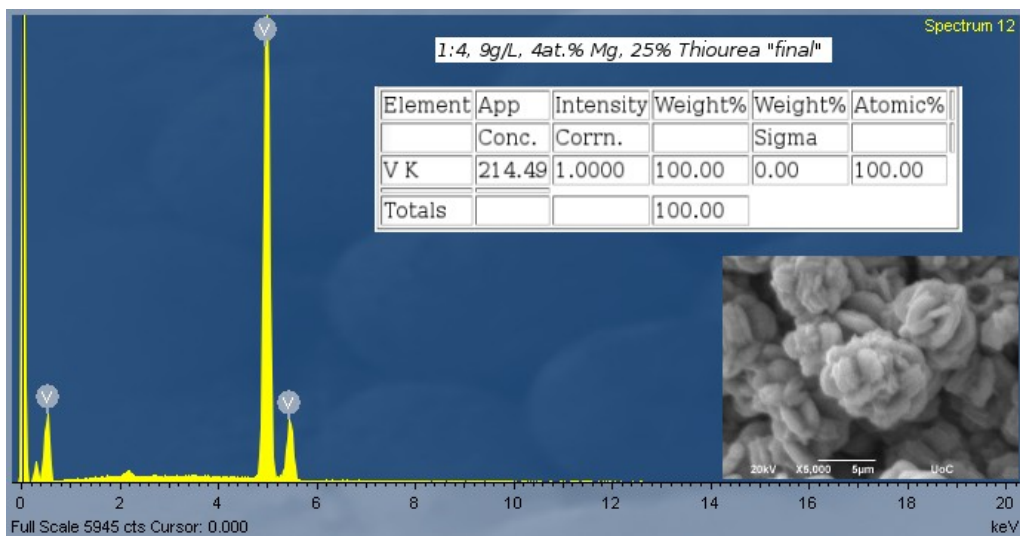


Figure 3.86 EDX results of “1:4, 9 g/L, 4at.% Mg, 25% Thiourea” configuration “final” sample

For the majority of our “Mg-doped” samples, results reveal that V is the sole elements present within the inspection field, with 100 Atomic%. Exception are ““1:1.5 & 9 g/L & 5at.% Mg” configuration “as obtained” sample and “1:4, 9 g/L, 2at.% Mg, 25% Thiourea” configuration “final” sample the results of which show they consist of elements V and Mg, with V being the most abundant. This is a confirmation of the dopant being present inside our material structure. However it is troubling that only two out of the 12 samples have detectable Mg quantities, with no obvious relation between these results and the at.% Mg supplied or the morphology or any other parameter of our configuration or measured sample property. Another exception on the elemental analysis results is “1:4, 9 g/L, 3at.% Mg, 25% Thiourea” configuration “as obtained” sample, which shows an elemental composition of V and C, in an almost equivalent percentage each. The high presence of carbon can be easily attributed to possible organic residues, of either oxalic acid or thiourea, since no carbon structures where detected during xrd measurements, and considering that “as obtained” solid samples are thermally treated at a low temperature of 80°C during the drying process.

3.9.3. EDX results of W, Mg co-doped samples

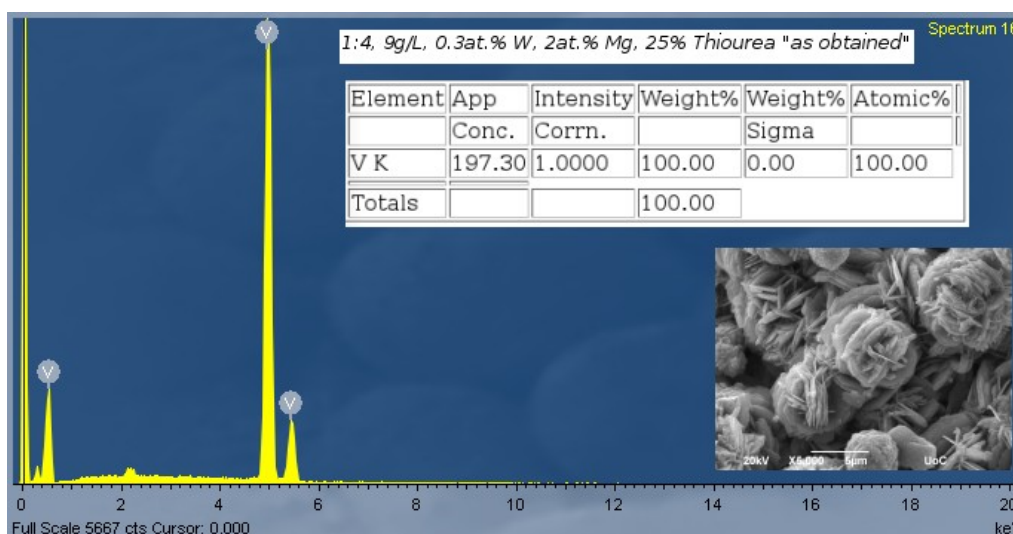


Figure 3.87 EDX results of “1:4, 9 g/L, 0.3at.% W, 2at.% Mg, 25% Thiourea” configuration “as obtained” sample

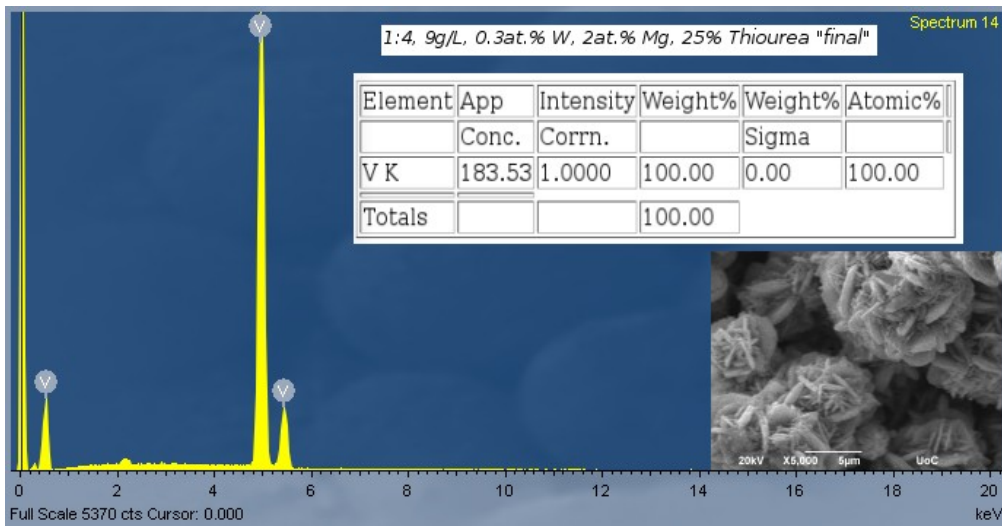


Figure 3.88 EDX of “1:4, 9 g/L, 0.3at.% W, 2at.% Mg, 25% Thiourea” configuration “final”

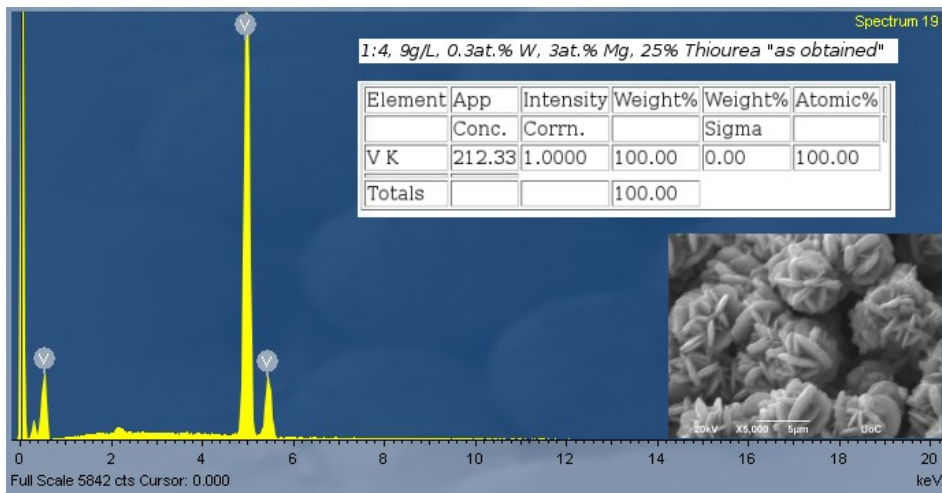


Figure 3.89 EDX results of “1:4, 9 g/L, 0.3at.% W, 3at.% Mg, 25% Thiourea” configuration “as obtained” sample

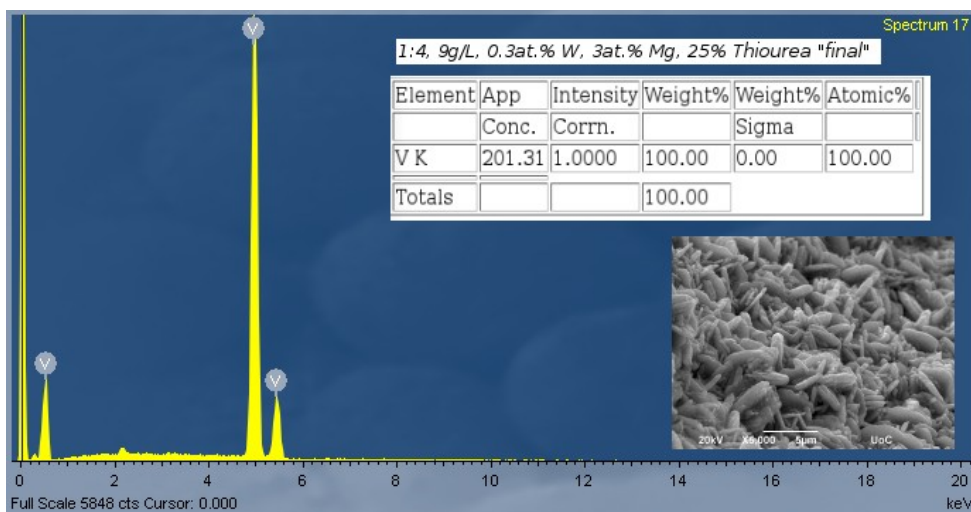


Figure 3.90 EDX of “1:4, 9 g/L, 0.3at.% W, 3at.% Mg, 25% Thiourea” configuration “final”

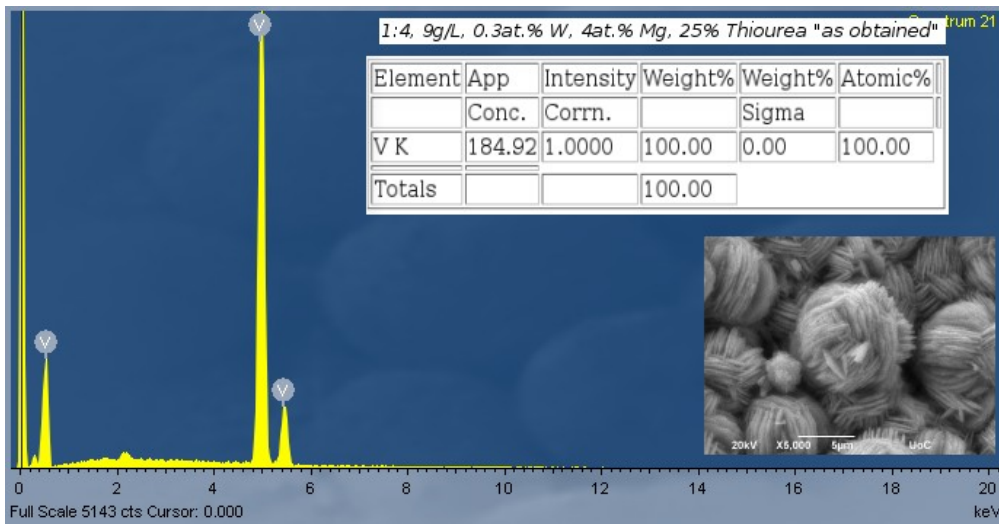


Figure 3.91 EDX of “1:4, 9 g/L, 0.3at.% W, 4at.% Mg, 25% Thiourea” configuration “as obtained” sample

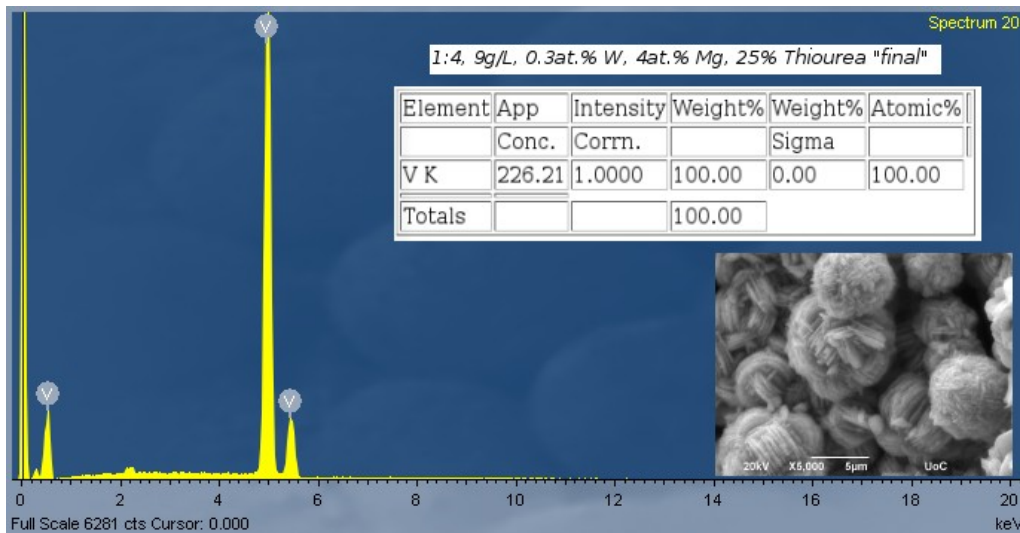


Figure 3.92 EDX of “1:4, 9 g/L, 0.3at.% W, 4at.% Mg, 25% Thiourea” configuration “final”

For all of our “co-doped samples”, results reveal that V is the sole elements present within the inspection field, with 100 Atomic%, with no exception. Since EDX results our “0.3at.% W-doped” samples revealed the presence of W element in the materials structures, and results of “2at.% Mg” and “5at.% Mg” samples revealed the presence of Mg element, we would expect that the “co-doped” samples of the specific at.% to give similar results. Yet, no dopant presence has been detected on these samples, suggesting either a loss of dopants towards the supernatant during hydrothermal treatment, an unsuccessful dopant incorporation at the specific inspection fields measured, or a nucleation of the dopant elements elsewhere in our samples morphology. An extended analysis of the dopant incorporation during hydrothermal treatment is highly advised for future works, as reported elsewhere^[3.11], in order to unravel more on the VO₂ hydrothermal synthesis mechanism.

3.10 Morphology

The morphology of 16 of our products was examined by Field Emission Scanning Electron Microscopy (SEM), both prior and after the annealing process (31 samples in total). In this chapter, images of the SEM measurements will be presented and discussed.

3.10.1. SEM results on the thiourea effect

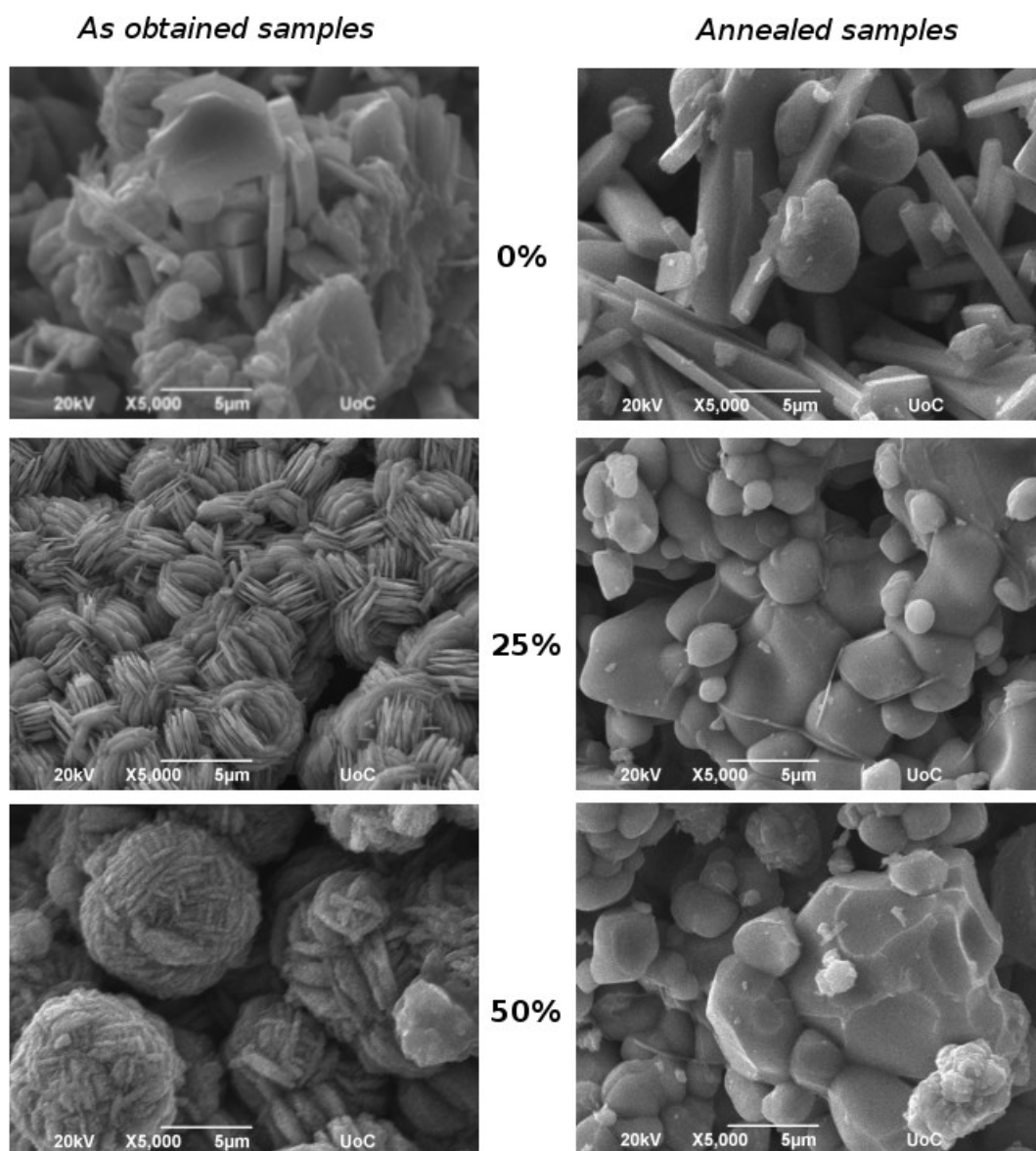


Figure 3.93 SEM images of “1:4, 9 g/L” configuration samples with and without thiourea, prior and after annealing

On Figure 3.93 the morphologies of our basic “1:4, 9 g/L” configuration samples and of our basic configuration with additive thiourea samples are presented. The particles vary greatly from sample

to sample. For the as obtained morphologies we notice an increase on the organization of particles, from more bulky rock-like structures for our basic configuration sample, with dimensions of few μm , to the more thin flake-like structures for 25% thiourea additive configuration samples, with dimensions of less than 1 μm , and aggregated flakes forming spherical structures for 50% thiourea additive, with diameters of $\approx 5 \mu\text{m}$. After annealing, particles tend to aggregate and form big bulky rock-like structures with various forms, and dimensions ranging from 0.5 to 10 μm . Additive thiourea seem to promote a more fine, nano-structured morphology for our as obtained particles, whereas after annealing particles seem to aggregate more easily.

3.10.2. SEM results on W-doping effect

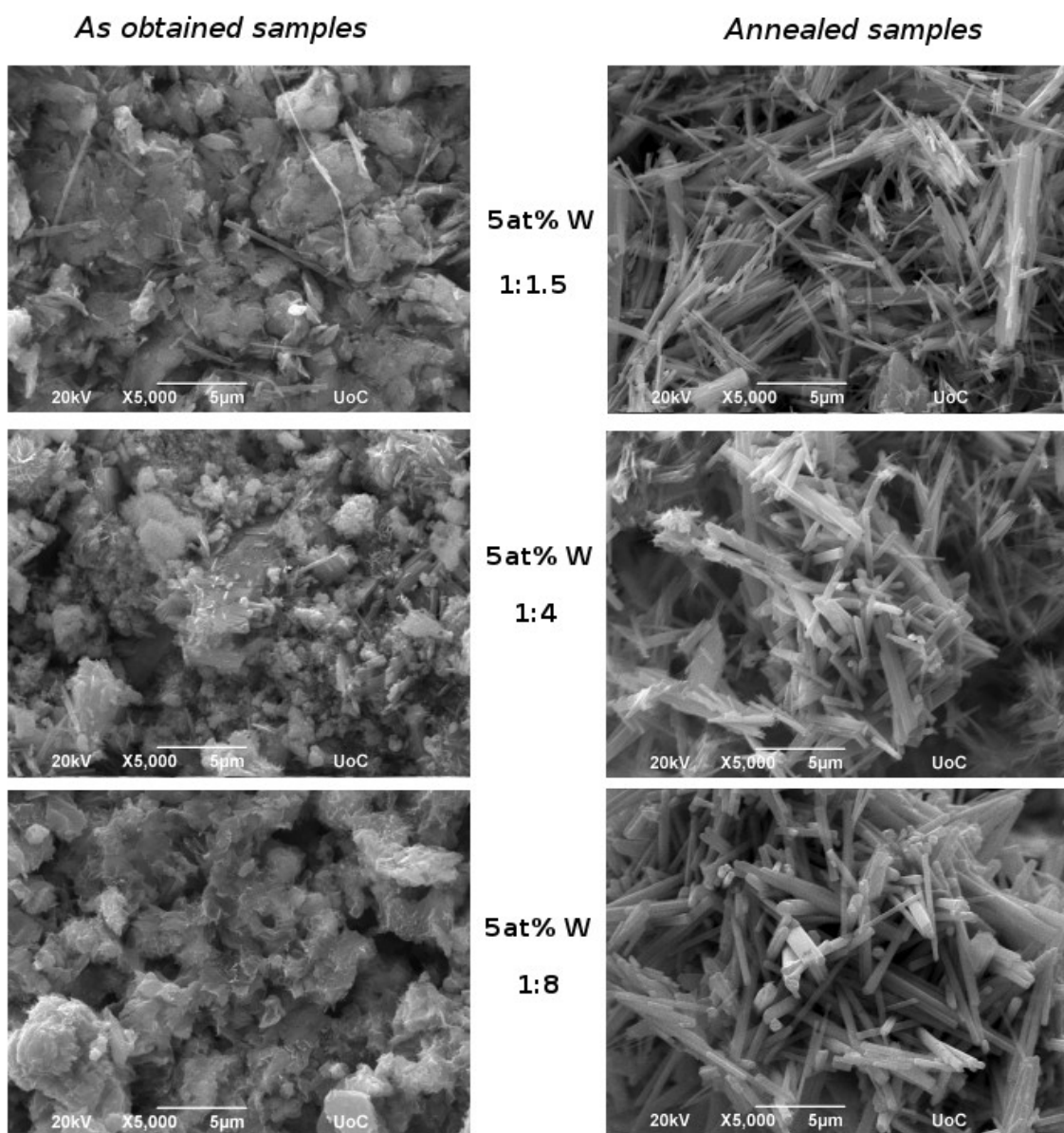


Figure 3.94 SEM images of “9 g/L, 5at.% W” configuration samples with various molar ratios, prior and after annealing

On *Figure 3.94* the morphologies of our 5at.% W-doped configuration samples of various molar ratios are presented. For the as obtained morphologies we notice no obvious effect from 1:1.5 to 1:4 and 1:8 reagents molar ratios, with not much distinguishable particles and on a dense distribution that seems to form a bulky layer of our material. After annealing, particles tend to separate and form fine nano-rods (width ≈ 0.5 to $1 \mu\text{m}$), which stick together in bigger less dense structures, especially on configuration samples with higher oxalic acid reagent presence. Tungsten dopant seem to promote a more continuous bulky morphology for our as obtained particles, whereas after annealing the promotion to a more fine, nano-structured morphology is evident.

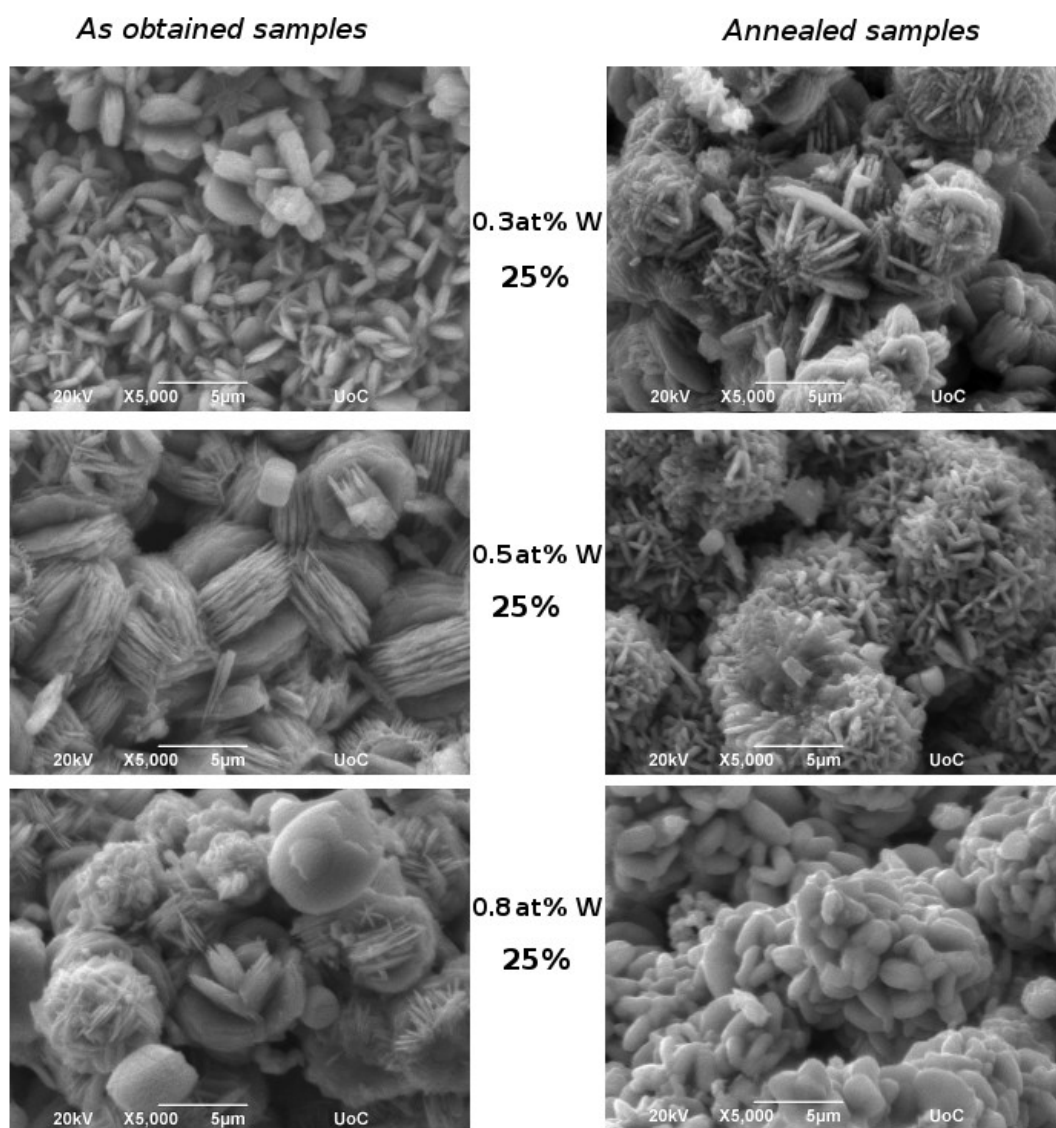


Figure 3.95 SEM images of “1:4, 9 g/L, 25% Thiourea” configuration samples with various at.% W-dopant, prior and after annealing

On *Figure 3.95* the morphologies of our configuration samples with thiourea additive and various at.% W-doping are presented. For the as obtained morphologies we notice results more similar to

the basic configuration with 25% thiourea additive samples of *Figure 3.93*, with particles varying greatly from sample to sample. After annealing, particles tend to rearrange their micro-structure while changing morphology to more spherical particles aggregations, with particles dimensions ranging from 0.5 to a few μm . The same effect mentioned above from additive thiourea is also evident here, only this time the addition of tungsten dopant reagent seem to act in contrast of the thiourea effects and promote less aggregated structures of particles, on our samples after annealing.

3.10.3. SEM results on Mg-doping effect

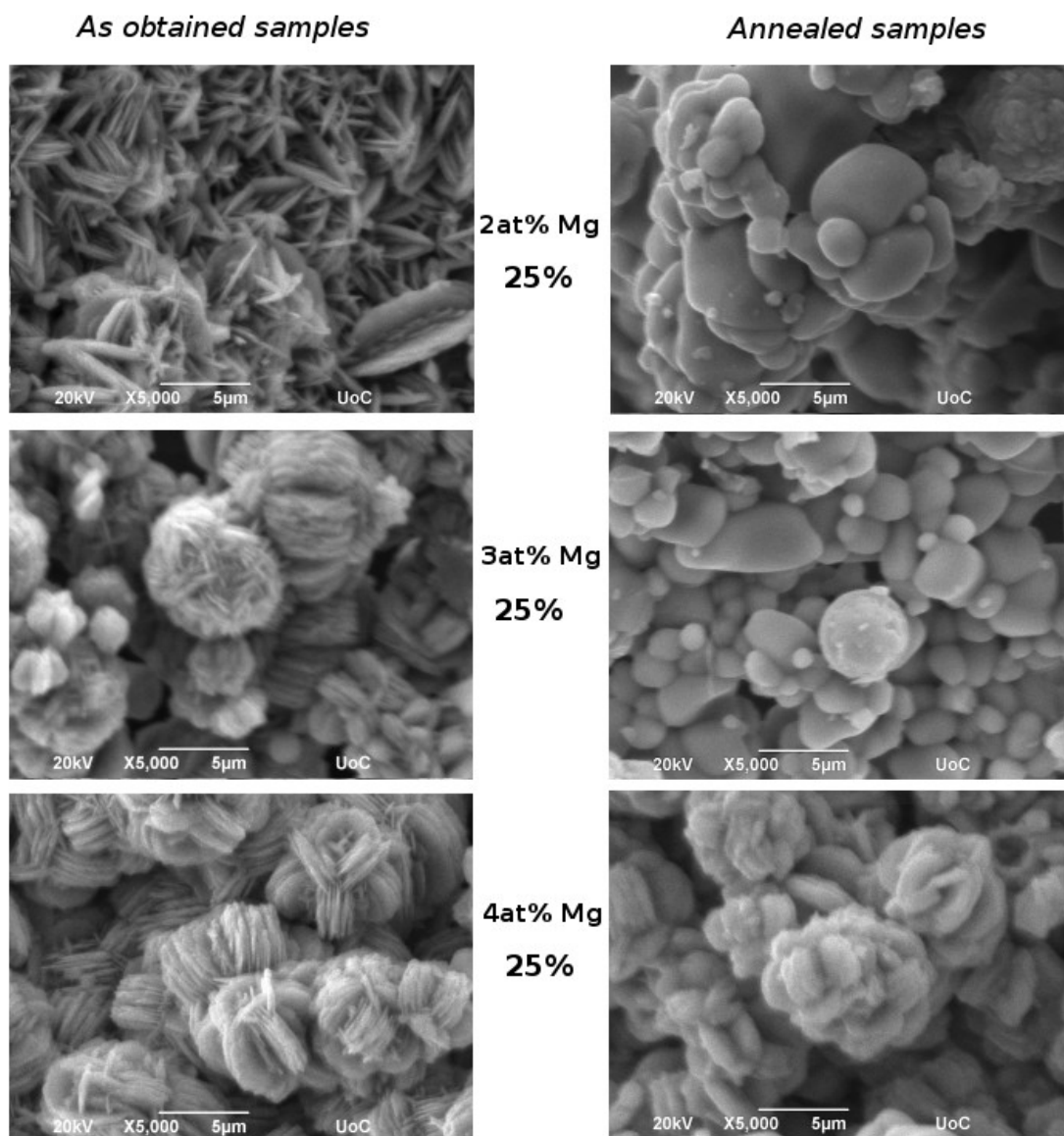


Figure 3.96 SEM images of “1:4, 9 g/L, 25% Thiourea” configuration samples with various at.% Mg-dopant, prior and after annealing

On *Figure 3.95* the morphologies of our configuration samples with thiourea additive and various at.% Mg-doping are presented. For the as obtained morphologies we notice results more similar to

the basic configuration with 25% thiourea additive samples of *Figure 3.93*, with flake-like particles of widths fewer than 1 μm forming bigger more volumed structures of $\approx 5 \mu\text{m}$ dimensions. After annealing, particles tend to aggregate in the same manner as *Figure 3.93* 25% thiourea configuration sample and form big bulky rock-like structures with various forms and dimensions ranging from 1 to 5 μm . The same effect mentioned above from additive thiourea is also evident here, however Mg dopant reagent seem to have no obvious effect on morphology.

3.10.4. SEM results on W, Mg co-doping effect

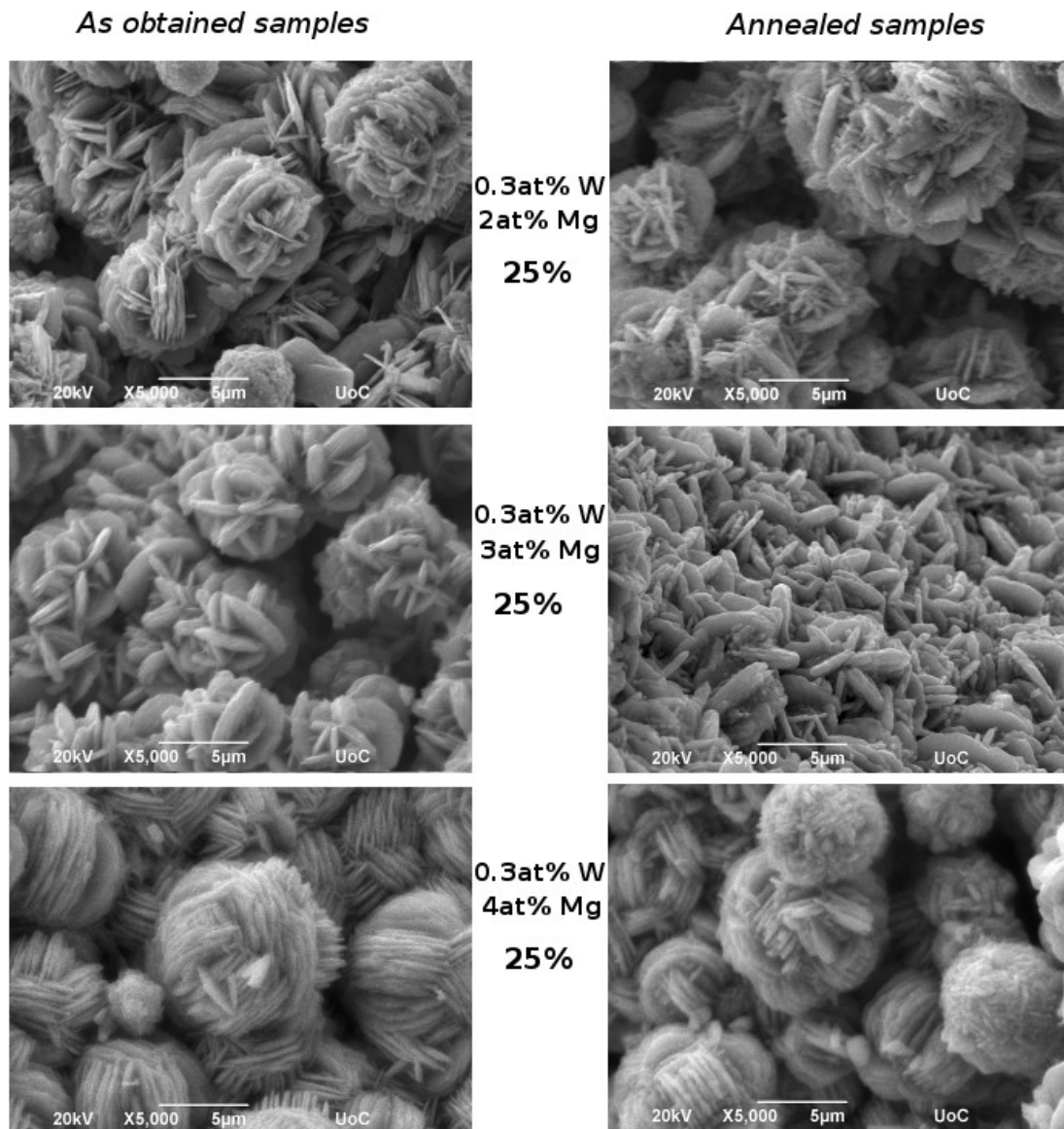


Figure 3.97 SEM images of “1:4, 9 g/L, 25% Thiourea” configuration samples with 0.3at.% W-dopant and various at.% Mg-dopant, prior and after annealing

On *Figure 3.95* the morphologies of our configuration samples with thiourea additive, 0.3at% W and various at.% Mg-doping are presented. For the as obtained morphologies again we notice re-

sults more similar to the basic configuration with 25% thiourea additive sample of *Figure 3.93*, only this time particles from different configurations have similar morphology with flake-like structures of $\approx 0.5 \mu\text{m}$ width packing in greater spherical structures of $\approx 5 \mu\text{m}$. After annealing, particles seem to keep a similar flake-like morphology packed into bigger spheres, rather than aggregating in bulky volumes as the 25% thiourea additive sample of *Figure 3.93*. Although the flake-like particles effect from additive thiourea mentioned is evident on the as obtained samples, no thiourea morphology effect is taking place after annealing. Again the addition of tungsten dopant reagent seem to act in contrast of the thiourea effects and promote less aggregated structures of particles, on our final samples.

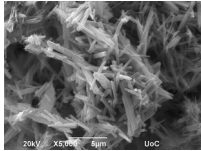
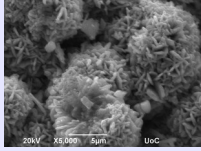
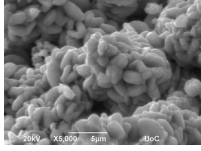
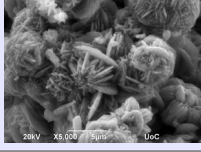
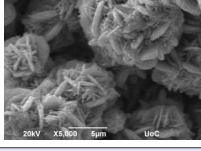
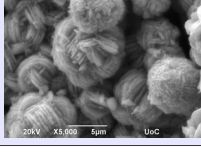

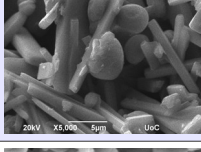
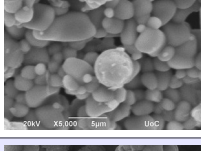
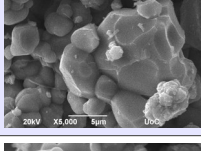
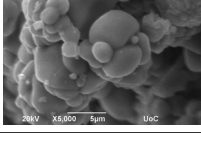
3.10.5. Conclusions over morphology of samples

In this section the morphology of some of our most promising products were discussed. As mentioned, the overall samples tested consist of particles of an average size in the scale of hundreds of nm to few μm , most of which are arranged in micro-structures of an average size in the scale of 5 to 10 μm . We showed the effect on morphology of samples with additive thiourea, which, compared to our basic configurations, showed a more fine morphology with flake-like particles (as obtained) and aggregated spheres (final products). Doping with Tungsten reagent, H_2WO_3 , resulted in more nano-structured particles, whereas Magnesium dopant reagent did not seem to have a specific effect on morphology.

As some published works have discussed before^{[3.13][3.14][3.15][3.16][3.17]} the size of thermochromic VO_2 particles seem to play a key role to its thermochromic properties, like affecting the T_c and even ΔT_c of samples. Here we will present our own observations regarding our samples morphology/particle size and T_c .

Table 3.10 shows the same DSC data presented on Table 3.9, only this time only our samples characterized with SEM were displayed, and xrd identification column has been substituted with the morphology column which contains the corresponding SEM images in order to get a qualitative value of the particle size. Results are arranged by ascending T_c .

As the T_c presented increases, we notice an increase in the particle sizes, starting with some fine rods of the scale of hundreds of nm, followed by various intermediates, up to the more bulky spherical particles of the scale of few μm . The explanation of this phenomena can be easily understood, since a higher density of grain boundaries (smaller particle size) provides a greater number of nucleating defects which in turn reduces T_c . Regarding our ΔT_c no general trend can be observed.

Configuration	Morphology	T _c (°C)	ΔT _c (°C)
1:4, 9g/L, 5at.% W		59.27	7.11
1:4, 9g/L, 0.5at.% W, 25% Thiourea		64.37	11.39
1:4, 9g/L, 0.8at.% W, 25% Thiourea		64.53	9.11
1:4, 9g/L, 0.3at.% W, 25% Thiourea		65.04	9.79
1:4, 9g/L, 0.3at.% W, 2at.% Mg, 25% Thiourea		65.06	9.92
1:4, 9g/L, 0.3at.% W, 4at.% Mg, 25% Thiourea		65.12	9.55
1:4, 9g/L, 0.3at.% W, 3at.% Mg, 25% Thiourea		65.36	9.96
1:4 & 9 g/L		65.79	9.02
1:4, 9g/L, 3at.% Mg, 25% Thiourea		65.84	9.59
1:4, 9g/L, 50% Thiourea		65.94	11.59
1:4, 9g/L, 2at.% Mg, 25% Thiourea		66.02	9.31

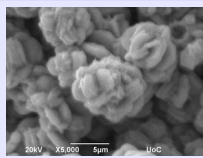
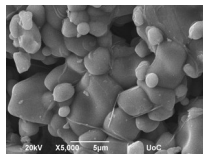
1:4, 9g/L, 4at.% Mg, 25% Thiourea		66.08	8.86
1:4, 9g/L, 25% Thiourea		66.52	12.12

Table 3.10 DSC overall data from various configurations “final” samples measured, arranged by ascending T_c , along with comments on samples morphology.

3.11 Thermal decomposition and annealing step

As indicated by all of the results discussed in previous sections, the annealing of our as obtained samples is a crucial step in the acquisition of higher purity, high crystallinity, thermochromic products. Still, in order to move towards synthetic procedure that is more environmentally friendly, energy efficient and easier to scale up for industrial productions, we need to examine energy costly and time consuming step of our procedures and try to avoid their usage as much as possible and to a feasible extend. Such a step is the annealing process of our materials. In our project the aim was to examine and optimize the synthetic procedure by means of the solution chemistry of the system. Thus, no experimentation with different annealing temperatures was conducted.

However, thermogravimetric analysis measurements were used in order to examine the material mass loss during the annealing step, as well as the extend of excess in the procedure usage. We thermally decomposed samples of our basic “1:4 & 9g/L” configuration, our “25% thiourea additive” and “50% thiourea additive” configuration. Results are presented in *Figure 3.98*.

Starting at 100% mass loading, after gradually increasing the temperature applied on our samples, water molecules, organic residues and other impurities start to decompose and the mass percentage starts to drop, until it reaches a plateau. The temperature where our data reaches the plateau corresponds to the lower possible temperature for the annealing process. From all of our three samples measured, this temperature is about 500 °C. On thermal treatment at farther temperatures there is an excess of energy input in the system, that could promote transitions in the structure of the solid material, activating the irreversible transition $VO_2(A) \rightarrow VO_2(R)$ or even advance the crystal growth creating morphologies with larger particles. Since our annealing procedures where carried out at 700 °C this results would explain the particle size growth noted on our SEM results discussion.

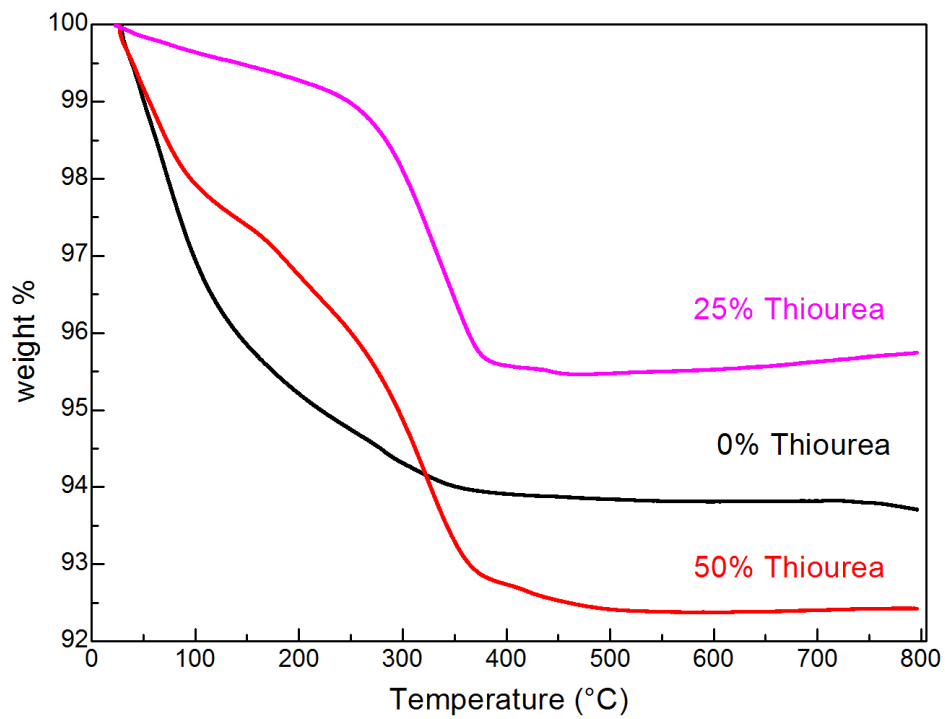


Figure 3.98 TGA results of “1:4, 9 g/L”, “1:4, 9 g/L, 25% Thiourea” and “1:4, 9 g/L, 50% Thiourea” configuration samples (prior annealing).

CHAPTER 4. Conclusions

4.1 Summary and conclusions

In this project, the optimization of the hydrothermal synthesis and the characterization of VO₂ powders has been carried out. From the analysis of the results of samples characterization, conclusions can be summarized as follows:

- › The hydrothermal method shows to be a good tool of solution-based techniques for synthesizing good quality thermochromic VO₂, as well as for the vanadium dioxide metastable polymorphs.
- › The method is chemically much flexible and can be tuned to achieve different results by changing various synthetic parameters.
- › Best results on producing VO₂(M) powders are possible in the optimized area of 1:4 to 1:8 reagents V₂O₅ : oxalic acid molar ratio, high V₂O₅ concentration ~ 9 g/L, and acidic pH in the region of 0.5 to 1.
- › Synthesis volume should be considered carefully since a low reagents solution volume will result to less pressure applied inside the autoclave, thus giving products with an overwhelming presence of impurities.
- › Sulphuric acid additive seemed to be of better use as a pH regulator and assistant additive for the more efficient formation of the metastable phases of VO₂, rather than the VO₂(M) thermochromic polymorph.
- › Thiourea additive exhibited optimal effectiveness on promoting the formation of pure and high crystallinity thermochromic VO₂, thus making it our preferred candidate for the hydrothermal synthesis regulation.
- › A mechanism of the effect of additive thiourea was proposed and discussed, based on our novel results, suggesting that decomposition of thiourea inside the autoclave during our hydrothermal synthesis applies an accelerated gradual pH increase on the synthesis solution and promotes the pentavanadyl cation (VO₂⁺) precipitation.
- › Thiourea can be also used to alter the morphology of our products, promoting the formation of flake-like particles, organized to bigger micro-

spheres.

- › Dopants were used to exploit our synthesis products to acquire thermochromic VO₂ with critical transition temperatures closer to the application requirements.
- › However, as dsc measurements showed and edx elemental analysis confirmed, there is still an issue of low incorporation of the dopants in our products. From result of the various configurations with doping used, we can speculate that an interaction with other entities in our hydrothermal procedure may be the cause, although no hard-core evidence can be exposed to defend this.
- › Tungsten as a dopant seem to play a crucial role on lowering the T_c of thermochromic VO₂, as well as promoting more nano-structured morphologies producing nano-rods and spikes.
- › Magnesium as a dopant seem to incorporate very difficulty, most probably due to the selected reagent used as its source. No generalized conclusions can be made for this dopant, since low incorporation to our characterized products makes them almost trivial.
- › A relation between particle sizes and the T_c was observed, with T_c values rising from smaller nano-sized particles to bigger micro-sized particles.
- › Thermal decomposition of our most promising products suggested a possibility for reducing the annealing temperature about 200 °C lower than the one used through this project.

4.2 Future suggestions - perspectives

As future suggestions, we would recommend some of the following experimental procedures and analysis:

- › One of the parameters we experimented the less is the filling of the autoclave which can be described by the volume of the synthesis. Since lower synthesis volume gives products with high impurities, the opposite method should be examined by increasing the filling of the autoclave by scaling up the synthesis configurations. We can go as far as to speculate that if pressure inside the autoclave reached an optimized higher level both efficient and secure, we would probably reach our desired products by a single-step route.

- › Another subject to be more extensively experimented with is the dopant usage. We would highly recommend for future works to test different kind of doping reagents for the same dopants, as well as different atomic percentages of each, in order to unravel the mechanism of dopant incorporation for our hydrothermal system.
- › Also, an elemental analysis with more quantitative precise techniques would be of great interest for both undoped and doped products.
- › As already mentioned, the temperature of the annealing treatment of our samples could be lowered, in order to reduce energy consumption and examine the differentiation, if any, from our results in this project.
- › The the thermochromic properties lifespan of these materials could be tested by measuring multiple dsc cycles and defining the maximum number of possible repeatable thermochromic cycles.
- › And last, but definitely not least, the next step for future works should also examine the methods for thin film production, in order to measure the thermochromic properties of our materials in action, as well as to achieve a realizable application exhibition in a step towards future industrial fabrication.

References

Chapter 1

- [1.1.1] BUILDINGS AND CLIMATE CHANGE Summary for Decision-Makers, © United Nations Environment Programme, 2009
- [1.1.2] Adv. Mat. Lett. 2010, 1(2), 86-105
- [1.1.3] Morin, F. J. (1959). *Oxides which show a metal-to-insulator transition at the neel temperature*. Physical Review Letters, 3(1), 34–36. <https://doi.org/10.1103/PhysRevLett.3.34>
- [1.1.4] Y. Zhang et al. /*Influence of different additives on the synthesis of VO₂ polymorphs*. Ceramics International 39 (2013) 8363–8376
- [1.1.5] S.A. Lawton, E.A. Theby, *Effect of tungsten and molybdenum doping on the semiconductor–metallic transition in vanadium dioxide produced by evaporative decomposition of solutions and hydrogen reduction*, Journal of the American Ceramic Society 78 (1) (1995) 238–240.
- [1.1.6] Y. Zhang, M. Fan, W. Wu, L. Hu, J. Zhang, Y. Mao, C. Huang, X. Liu, *A novel route to fabricate belt-like VO₂(M)@C core–shell structured composite and its phase transition properties*, Materials Letters 71 (2012) 127–130.
- [1.1.7] C.M. Zheng, X.M. Zhang, J.H. Zhang, K.R. Liao, *Preparation and characterization of VO₂ nanopowders*, Journal of Solid State Chemistry 156 (2) (2001) 274–280.
- [1.1.8] Z.F. Peng, W. Jiang, H. Liu, *Synthesis and electrical properties of tungsten-doped vanadium dioxide nanopowders by thermolysis*, Journal of Physical Chemistry C 111 (3) (2007) 1119–1122.
- [1.1.9] S. Yamamoto, N. Kasai, Y. Shimakawa, *Preparation of monodisperse and spherical rutile VO₂ fine particles*, Chemistry of Materials 21 (2) (2008) 198–200.
- [1.1.10] J.Q. Shi, S.X. Zhou, B. You, L.M. Wu, *Preparation and thermochromic property of tungsten-doped vanadium dioxide particles*, Solar Energy Materials and Solar Cells 91 (19) (2007) 1856–1862.
- [1.1.11] J. Li, C.Y. Liu, L.J. Mao, *The character of W-doped one-dimensional VO₂(M)*, Journal of Solid State Chemistry 182 (10) (2009) 2835–2839.
- [1.1.12] X. Liu, C. Huang, S. Yi, G. Xie, H. Li, Y. Luo, *A new solvothermal method of preparing VO₂ nanosheets and petaloid clusters*, Solid State Communications 144 (2007) 259–263.
- [1.1.13] Y. Zhang, M. Fan, F. Niu, W. Wu, C. Huang, X. Liu, H. Li, X. Liu, *Belt-like VO₂(M) with a rectangular cross section: a new route to prepare, the phase transition and the optical switching properties*, Current Applied Physics 12 (3) (2012) 875–879.
- [1.1.14] C.Z. Wu, J. Dai, X.D. Zhang, J.L. Yang, F. Qi, C. Gao, Y. Xie, *Direct confined-space combustion forming monoclinic vanadium dioxides*, Angewandte Chemie International Edition 49 (1) (2010) 134–137.
- [1.1.15] S. Ji, F. Zhang, P. Jin, *Preparation of high performance pure single phase VO₂ nanopowder by hydrothermally reducing the V₂O₅ gel*, Solar Energy Materials and Solar Cells 95 (12) (2011) 3520–3526.
- [1.1.16] L. Whittaker, T.L. Wu, C.J. Patridge, G. Sambandamurthy, S. Banerjee, *Distinctive finite size effects on the phase diagram and metal–insulator transitions of tungsten-doped vanadium(IV) oxide*, Journal of Materials Chemistry 21 (15) (2011) 5580–5592.
- [1.1.17] C.X. Cao, Y.F. Gao, H.J. Luo, *Pure single-crystal rutile vanadium dioxide powders: synthesis, mechanism and phase-transformation property*, Journal of Physical Chemistry C 112 (48) (2008) 18810–

18814.

- [1.1.18] J.H. Son, J. Wei, D. Cobden, G.Z. Cao, Y.N. Xia, *Hydrothermal synthesis of monoclinic VO₂ micro- and nanocrystals in one step and their use in fabricating inverse opals*, Chemistry of Materials 22 (10) (2010) 3043–3050.
- [1.1.19] S.D. Ji, Y. Zhao, F. Zhang, P. Jin, *Direct formation of single crystal VO₂(R) nanorods by one-step hydrothermal treatment*, Journal of Crystal Growth 312 (2) (2010) 282–286.
- [1.1.20] C.X. Cao, Y.F. Gao, L.T. Kang, H.J. Luo, *Self-assembly and synthesis mechanism of vanadium dioxide hollow microspheres*, CrystEngComm 12 (12) (2010) 4048–4051.
- [1.1.21] F. Théobald, *Étude hydrothermale du système VO₂–VO_{2,5}–H₂O*, Journal of the Less Common Metals 53 (1) (1977) 55–71.
- [1.1.22] Z. Gui, R. Fan, X.H. Chen, Y.C. Wu, *A new metastable phase of needle-like nanocrystalline VO₂ center dot H₂O and phase transformation*, Journal of Solid State Chemistry 157 (2) (2001) 250–254.
- [1.1.23] Y. Zhang, J. Zhang, X. Zhang, C. Huang, Y. Zhong, Y. Deng, *The additives W, Mo, Sn and Fe for promoting the formation of VO₂(M) and its optical switching properties*, Materials Letters 92 (2013) 61–64.
- [1.1.24] Li, G., Chao, K., Zhang, C., Zhang, Q., Peng, H., & Chen, K. (2009). Synthesis of urchin-like VO₂ nanostructures composed of radially aligned nanobelts and their disassembly. Inorganic Chemistry, 48(3), 1168–1172. <https://doi.org/10.1021/ic801620n>
- [1.1.25] Wu, C., Zhang, X., Dai, J., Yang, J., Wu, Z., Wei, S., & Xie, Y. (2011). Direct hydrothermal synthesis of monoclinic VO₂(M) single-domain nanorods on large scale displaying magnetocaloric effect. Journal of Materials Chemistry, 21(12), 4509. <https://doi.org/10.1039/c0jm03078c>
- [1.1.26] Cao, X., Wang, N., Law, J. Y., Loo, S. C. J., Magdassi, S., & Long, Y. (2014). Nanoporous thermochromic VO₂ (M) thin films: Controlled porosity, largely enhanced luminous transmittance and solar modulating ability. Langmuir, 30(6), 1710–1715. <https://doi.org/10.1021/la404666n>
- [1.1.27] M, T. V. O., Popuri, S. R., Miclau, M., Artemenko, A., Labrugere, C., & Villesuzanne, A. (2013). Rapid Hydrothermal Synthesis of VO₂ (B) and Its Conversion to Thermochromic VO₂ (M1). Inorganic Chemistry, 2, 4780–4785.
- [1.1.28] Alie, D., Gedvilas, L., Wang, Z., Tenent, R., Engtrakul, C., Yan, Y., ... Ban, C. (2014). Direct synthesis of thermochromic VO₂ through hydrothermal reaction. Journal of Solid State Chemistry, 212, 237–241. <https://doi.org/10.1016/j.jssc.2013.10.023>
- [1.1.29] Zhang, Y. F., Huang, Y. F., Zhang, J. C., Wu, W. B., Niu, F., Zhong, Y. L., ... Huang, C. (2012). Facile synthesis, phase transition, optical switching and oxidation resistance properties of belt-like VO₂(A) and VO₂(M) with a rectangular cross section. Materials Research Bulletin, 47(8), 1978–1986. <https://doi.org/10.1016/j.materresbull.2012.04.015>
- [1.1.30] Lv, W., Huang, D., Chen, Y., Qiu, Q., & Luo, Z. (2014). Synthesis and characterization of Mo-W co-doped VO₂(R) nano-powders by the microwave-assisted hydrothermal method. Ceramics International, 40(8 PART B), 12661–12668. <https://doi.org/10.1016/j.ceramint.2014.04.113>
- [1.1.31] Nagashima K, Yanagida T, Tanaka H, Kawai T (2006) Stress relaxation effect on transport properties of strained vanadium dioxide epitaxial thin films. Phys Rev B 74(17):172106–4

- [1.1.32] Jin P, Yoshimura K, Tanemura S (1997) Dependence of microstructure and thermochromism on substrate temperature for sputter-deposited VO₂ epitaxial films. *J Vac Sci Technol A* 15: 1113–1117
- [1.1.33] Hood PJ, Denatale JF (1991) Millimeter-wave dielectric-properties of epitaxial vanadium dioxide thin-films. *J Appl Phys* 70(1):376–381
- [1.1.34] Chae BG, Kim HT, Yun SJ, Kim BJ, Lee YW, Youn DH, Kang KY (2006) Highly oriented VO₂ thin films prepared by sol-gel deposition. *Electrochem Solid State Lett* 9(1):C12–C14
- [1.1.35] Sahana MB, Subbanna GN, Shivashankar SA (2002) Phase transformation and semiconductor-metal transition in thin films of VO₂ deposited by low-pressure metalorganic chemical vapor deposition. *J Appl Phys* 92(11):6495–6504
- [1.1.36] Kitchen WJ, Proto GR (1971) Properties of vanadium dioxide thermal filaments. *J Appl Phys* 42(5):2140–2142
- [1.1.37] Case FC (1988) Simple resistance model fit to the oxidation of a vanadium film into VO₂. *J Vac Sci Technol A* 6(1):123–127
- [1.2.0.] Wikipedia
- [1.2.1] Vanadium and Vanadium Compounds, © 2012 Wiley-VCH Verlag GmbH & Co. KGaA, Weinheim, DOI: 10.1002/14356007.a27_367
- [1.2.2] J. Haber et al./*Applied Catalysis A: General* 157 (1997) 3-22
- [1.2.3] *Phys. Chem. Chem. Phys.*, 2011, 13, 15873–15881, DOI: 10.1039/c1cp20838a
- [1.2.4] Li, Y., Ji, S., Gao, Y., Luo, H. & Kanehira, M.; *Sci. Rep.* 3, 1370; DOI:10.1038/srep01370 (2013).
- [1.2.5] Yao; Oka; Yamamoto; *Structural Phase Transition of VO₂ (B) to VO₂ (A)*. *J. MATER. CHEM.*, 1991, 1 (5), 815-818
- [1.2.6] Yao; Oka; Yamamoto; *Phase Transition and V⁴⁺-V⁴⁺ Pairing in VO₂ (B)*. *J. SOLID STATE CHEM.*, 1993, 105, 271-278
- [1.2.7] Yao; Oka; Yamamoto; *A Structural Study of the High-Temperature Phase of VO₂ (A)*. *J. SOLID STATE CHEM.*, 1994, 112, 196-198
- [1.2.8] Pragna Kiri, Geoff Hyett, Russell Binions; *Solid-state thermochromic materials*, *Adv. Mat. Lett.* 2010, 1(2), 86-105
- [1.2.9] Zylbersztein A, Mott N. F.; *Metal-insulator transition in vanadium dioxide*, *Physical Review B* 1975, 11, 4383
- [1.2.10] Goodenough, J. B.; *The Two Components of the Crystallographic Transition in VO₂*, *Journal of Solid State Chemistry* 1971, 3(4), 490
- [1.2.11] Lee S. et al. (2017). *Anomalously low electronic thermal conductivity in metallic vanadium dioxide*. *Science*, 355(6323), 371–374. <https://doi.org/10.1126/science.aag0410>
- [1.2.12] Qazilbash MM et al. (2007) Mott transition in VO₂ revealed by infrared spectroscopy and nano-imaging. *Science* 318(5857):1750–1753
- [1.2.13] Choi HS, Ahn JS, Jung JH, Noh TW, Kim DH (1996) Mid-infrared properties of a VO₂ film near the metal-insulator transition. *Phys Rev B* 54(7):4621–4628
- [1.2.14] Morin, F. J. (1959). *Oxides which show a metal-to-insulator transition at the neel temperature*.

Physical Review Letters, 3(1), 34–36. <https://doi.org/10.1103/PhysRevLett.3.34>

[1.2.15] Monfort, O., Roch, T., Satrapinsky, L., Gregor, M., Plecenik, T., Plecenik, A., & Plesch, G. (2014). Reduction of V₂O₅ thin films deposited by aqueous sol-gel method to VO₂(B) and investigation of its photocatalytic activity. *Applied Surface Science*, 322. <https://doi.org/10.1016/j.apsusc.2014.10.009>

[1.2.16] Pergament, A. L., Stefanovich, G. B., & Velichko, A. A. (2013). Oxide Electronics and Vanadium Dioxide Perspective : A Review. *Journal on Selected Topics in Nano Electronics and Computing*, 1(1), 24–43. <https://doi.org/10.15393/j8.art.2013.3002>

[1.2.17] Li, W.; Dahn, J. R.; Wainwright, D. S. *Science* 1994, 264, 1115. (18) Tsang, C.; Manthiram, A. J. *Electrochem. Soc.* 1997, 144, 520

[1.2.18] Tsang, C.; Manthiram, A. J. *Electrochem. Soc.* 1997, 144, 520.

[1.2.19] Wu, C., Zhang, X., Dai, J., Yang, J., Wu, Z., Wei, S., & Xie, Y. (2011). *Direct hydrothermal synthesis of monoclinic VO₂(M) single-domain nanorods on large scale displaying magnetocaloric effect*. *Journal of Materials Chemistry*, 21(12), 4509. <https://doi.org/10.1039/c0jm03078c>

[1.2.20] Ningyi, Y., Jinhua, L., & Chenglu, L. (2002). Valence reduction process from sol-gel V₂O₅ to VO₂ thin films. *Applied Surface Science*, 191(1–4), 176–180. [https://doi.org/10.1016/S0169-4332\(02\)00180-0](https://doi.org/10.1016/S0169-4332(02)00180-0)

[1.2.21] Monfort, O., Roch, T., Satrapinsky, L., Gregor, M., Plecenik, T., Plecenik, A., & Plesch, G. (2014). Reduction of V₂O₅ thin films deposited by aqueous sol-gel method to VO₂(B) and investigation of its photocatalytic activity. *Applied Surface Science*, 322. <https://doi.org/10.1016/j.apsusc.2014.10.009>

[1.2.22] J.H. Son, J. Wei, D. Cobden, G.Z. Cao, Y.N. Xia, *Hydrothermal synthesis of monoclinic VO₂ micro- and nanocrystals in one step and their use in fabricating inverse opals*, *Chemistry of Materials* 22 (10) (2010) 3043–3050.

[1.2.23] L. Whittaker, T.L. Wu, C.J. Patridge, G. Sambandamurthy, S. Banerjee, *Distinctive finite size effects on the phase diagram and metal–insulator transitions of tungsten-doped vanadium(IV) oxide*, *Journal of Materials Chemistry* 21 (15) (2011) 5580–5592.

[1.2.24] F. Théobald, *Étude hydrothermale du système VO₂–VO_{2,5}–H₂O*, *Journal of the Less Common Metals* 53 (1) (1977) 55–71.

[1.2.25] Z. Gui, R. Fan, X.H. Chen, Y.C. Wu, *A new metastable phase of needle-like nanocrystalline VO₂ center dot H₂O and phase transformation*, *Journal of Solid State Chemistry* 157 (2) (2001) 250–254.

[1.2.26] C.X. Cao, Y.F. Gao, L.T. Kang, H.J. Luo, *Self-assembly and synthesis mechanism of vanadium dioxide hollow microspheres*, *CrystEngComm* 12 (12) (2010) 4048–4051.

[1.2.27] J.H. Son, J. Wei, D. Cobden, G.Z. Cao, Y.N. Xia, *Hydrothermal synthesis of monoclinic VO₂ micro- and nanocrystals in one step and their use in fabricating inverse opals*, *Chemistry of Materials* 22 (10) (2010) 3043–3050.

[1.2.28] S.D. Ji, Y. Zhao, F. Zhang, P. Jin, *Direct formation of single crystal VO₂(R) nanorods by one-step hydrothermal treatment*, *Journal of Crystal Growth* 312 (2) (2010) 282–286.

[1.2.29] C.X. Cao, Y.F. Gao, H.J. Luo, *Pure single-crystal rutile vanadium dioxide powders: synthesis, mechanism and phase-transformation property*, *Journal of Physical Chemistry C* 112 (48) (2008) 18810–18814.

[1.2.30]] L. Whittaker, T.L. Wu, C.J. Patridge, G. Sambandamurthy, S. Banerjee, *Distinctive finite size ef-*

fects on the phase diagram and metal–insulator transitions of tungsten-doped vanadium(IV) oxide, *Journal of Materials Chemistry* 21 (15) (2011) 5580–5592.

[1.2.31] Y. Zhang, et al. *Facile synthesis, phase transition, optical switching and oxidation resistance properties of belt-like VO₂(A) and VO₂(M) with a rectangular cross section*, *Materials Research Bulletin* 47 (8) (2012) 1978–1986.

[1.2.32] Y. Zhang, Y. Huang, et al. /Facile synthesis, phase transition, optical switching and oxidation resistance properties of belt-like VO₂(A) and VO₂(M) with a rectangular cross section, *Materials Research Bulletin* 47 (8) (2012) 1978–1986.

[1.2.33] Dai, L., Cao, C., Gao, Y. & Luo, H. Synthesis and phase transition behavior of undoped VO₂ with a strong nano-size effect. *Sol. Energy Mater. Sol. Cells* 95, 712–715 (2011)

[1.2.34] Pouget, J. P.; Launois, H.; Rice, T. M.; Dernier, P.; Gossard, A.; Villeneuve, G.; Hagenmuller, P. Dimerization of a Linear Heisenberg chain in the Insulating Phases of V_{1-x}Cr_xO₂. *Phys. Rev. B* 1974, 10, 1801–1815.

[1.2.35] Pouget, J. P.; Launois, H.; Dhaenens, J. P.; Marendia, P.; Rice, T. M. Electron Localization Induced by Uniaxial Stress in Pure VO₂. *Phys. Rev. Lett.* 1975, 35, 873–875.

[1.2.36] Manning, T. D.; Parkin, I.; Pemble, M. E.; Sheel, D.; Vernardou, D. Intelligent Window Coatings: Atmospheric Pressure Chemical Vapor Deposition of Tungsten-Doped Vanadium Oxide. *Chem. Mater.* 2004, 16, 744–749.

[1.2.37] Grassel, O.; Frommeyer, G. Effect of Martensitic Phase Transformation and Deformation Twinning on Mechanical Properties of Fe-Mn-Si-Al Steels. *Mater. Sci. Technol.* 1998, 14, 1213–1217.

[1.2.38] Chae, B.-G.; Kim, H. T.; Yun, S. J. Characteristics of W- and Ti- Doped VO₂ Thin Films Prepared by Sol-Gel Method. *Electrochem. Solid-State Lett.* 2008, 11, D53–D55.

[1.2.39] Tang, C.; Georgopoulos, P.; Fine, M. E.; Cohen, J. B.; Nygren, M.; Knapp, G. S.; Aldred, A. Local Atomic and Electronic Arrangements in W_xV_{1-x}O₂. *Phys. Rev. B* 1985, 31, 1000–1011.

[1.2.40] Netsianda, M.; Ngoepe, P. E.; Catlow, C. R. A.; Woodley, S. M. The Displacive Phase Transition of Vanadium Dioxide and the Effect of Doping with Tungsten. *Chem. Mater.* 2008, 20, 1764–1772.

[1.2.41] Lv, W., Huang, D., Chen, Y., Qiu, Q., & Luo, Z. (2014). *Synthesis and characterization of Mo-W co-doped VO₂(R) nano-powders by the microwave-assisted hydrothermal method*. *Ceramics International*, 40(8 PART B), 12661–12668. <https://doi.org/10.1016/j.ceramint.2014.04.113>

[1.2.42] 1. Kam, K. C. & Cheetham, A. K. Thermochromic VO₂ nanorods and other vanadium oxides nanostructures. *Mater. Res. Bull.* 41, 1015–1021 (2006).

[1.2.43] Haber, J., Witko, M. & Tokarz, R. Vanadium pentoxide I. Structures and properties. *Appl. Catal. A Gen.* 157, 3–22 (1997).

[1.2.44] Y. Zhang, J. Zhang, X. Zhang, C. Huang, Y. Zhong, Y. Deng, *The additives W, Mo, Sn and Fe for promoting the formation of VO₂(M) and its optical switching properties*, *Materials Letters* 92 (2013) 61–64.

Chapter 2

[2.1] Wikipedia

[2.2] Byrappa, K. & Yoshimura, M. Handbook of Hydrothermal Technology, Technology for Crystal Growth and Materials Processing. Materials science and processing technology series (2001). doi:10.1016/B978-081551445-9.50002-7

[2.3] PerkinElmer's Beginners Guide to Differential Scanning Calorimetry @2013-2014, PerkinElmer, Inc.

[2.4] PerkinElmer's Beginners Guide to Thermogravimetric Analysis @2010, PerkinElmer, Inc.

[2.5] Presentation: Introduction to X-Ray Powder Diffraction Data Analysis, by Scott A Speakman, Center for Materials Science and Engineering at MIT.

Chapter 3

[3.1] Ji, S., Zhao, Y., Zhang, F. & Jin, P. *Direct formation of single crystal VO₂(R) nanorods by one-step hydrothermal treatment*. J. Cryst. Growth 312, 282–286 (2010).

[3.2] Li, R. & Liu, C. *VO₂(B) nanospheres: Hydrothermal synthesis and electrochemical properties*. Mater. Res. Bull. 45, 688–692 (2010).

[3.3] Tavakoli, M. R., Dornian, S. & Dreisinger, D. B. *The leaching of vanadium pentoxide using sulfuric acid and sulfite as a reducing agent*. Hydrometallurgy 141, 59–66 (2014).

[3.4] Weizhong Lv, Dezhen Huang, Yanmei Chen, Qi Qiu, Zhongkuan Luo; *Synthesis and characterization of Mo–W co-doped VO₂(R) nano-powders by the microwave-assisted hydrothermal method*. Ceramics International 40 (2014) 12661–12668

[3.5] Li, W. et al. *Synthesis of VO₂ nanoparticles by a hydrothermal-assisted homogeneous precipitation approach for thermochromic applications*. RSC Adv. 4, 13026 (2014).

[3.6] Yan, X. P. et al. *Fabrication of hollow VO₂ microspheres by a facile template-free process*. Mater. Lett. 64, 278–280 (2010).

[3.7] Qiao, L. & Swihart, M. T. *Solution-phase synthesis of transition metal oxide nanocrystals: Morphologies, formulae, and mechanisms*. Adv. Colloid Interface Sci. 244, 199–266 (2017).

[3.8] Wang, Z. D., Yoshida, M. & George, B. *Theoretical study on the thermal decomposition of thiourea*. Comput. Theor. Chem. 1017, 91–98 (2013).

[3.9] Wang, S., Gao, Q. & Wang, J. *Thermodynamic analysis of decomposition of thiourea and thiourea oxides*. J. Phys. Chem. B 109, 17281–17289 (2005).

[3.10] Shaw, W. H. R. & Walker, D. G. *The Decomposition of Thiourea in Water Solutions*. J. Am. Chem. Soc. 78, 5769–5772 (1956).

[3.11] Zhang, Y. et al. *Influence of different additives on the synthesis of VO₂ polymorphs*. Ceram. Int. 39, 8363–8376 (2013).

[3.12] Okimura, K., Sakai, J. & Ramanathan, S. *In situ x-ray diffraction studies on epitaxial VO₂ films grown on c-Al₂O₃ during thermally induced insulator-metal transition*. J. Appl. Phys. 107, 63503 (2010).

[3.13] Banerjee, S. et al. *Distinctive finite size effects on the phase diagram and metal–insulator transitions of tungsten-doped vanadium(IV) oxide*. J. Mater. Chem. 21, 5580 (2011).

- [3.14] Dai, L., Cao, C., Gao, Y. & Luo, H. Synthesis and phase transition behavior of undoped VO₂ with a strong nano-size effect. *Sol. Energy Mater. Sol. Cells* 95, 712–715 (2011).
- [3.15] Miller, M. J. & Wang, J. *Influence of grain size on transition temperature of thermochromic VO₂*. *J. Appl. Phys.* 117, (2015).
- [3.16] Melnik, V. et al. *Low-temperature method for thermochromic high ordered VO₂ phase formation*. *Mater. Lett.* 68, 215–217 (2012).
- [3.17] Lopez, R., Haynes, T. E., Boatner, L. A., Feldman, L. C. & Haglund, R. F. *Size effects in the structural phase transition of VO₂ nanoparticles*. *Phys. Rev. B* 65, 224113 (2002).

[page intentionally left blank]

CURRICULUM VITAE

Name **Leila Zouridi**
Telephone **+30 6947586979**
E-mail **l.zouridi@campus.fct.unl.pt**
Linkedin contact **www.linkedin.com/in/leilazouridi**

Education/Qualifications

2017-current ***Master of Science student in Materials Science***
University of Crete, Department of Materials Science and Technology

2011-2017 ***Bachelor degree in Chemistry***
University of Crete, Department of Chemistry

2005-2011 ***High school degree***
High School of Arts, in Heraklion Crete, Greece

Personal Soft Skills

- Able to work under pressure
- Understanding how to work in a team as well as feeling comfortable to work individually
- Quick learner
- Confident working on several projects simultaneously
- Experience in solving problems
- Organising working laboratory environment
- Presentation Skills
- Ability to plan research projects

Work Experience/Activities

2017 ***CENIMAT|i3, Universidade Nova de Lisboa***, Lisbon, Portugal.
Post: *Traineeship Research Student.*
Responsibilities: Training on Inkjet Printing technology, Research in the field of Printed Electronics: *Inkjet printed Gallium Indium Zinc Oxide based Thin Film Transistors*, Chemical Synthesis, Ink development and Storage Testing, Inkjet Printer operation, Electronic Device Assembly and Performance Testing, Data Treatment, Project Planning, Presenting the Ideas, Plans and Results for my Project.

2015-2016 ***Foundation for Research and Technology - Hellas (FORTH) Institute of Electronic Structure***, Heraklion, Crete, Greece.
Post: *Thesis Research Student.*
Responsibilities: Research in the field of Material Science: *Synthesis of Vanadium Dioxide for Energy Saving Applications*, Chemical Synthesis, Organization of working laboratory environment, Planning the course of my Thesis Project, Presenting the Ideas, Plans and Results for my Project, Helping other Thesis Students with their works.

Publications

to be submitted Works regarding recent research activities

Other Experience/Activities

2017 **Poster Presentation**
M. Moschogiannaki, M. Charalampakis, L. Zouridi, G. Kiriakidis, V. Binas

Solution based synthesis of Cobalt Nickel tungstates as efficient photocatalysts. European Materials Research Society, E-MRS, 2017, Spring Meeting

2017 Poster Presentation

L. Zouridi, E. Aperathitis, E. Gagaoudakis, G. Kiriakidis, V. Binas.

Solution based thermochromic VO₂ particles for energy saving applications. 19th

Postgraduates Conference on Chemistry

Place/time: University of Crete, Voutes, Heraklion, Crete – Greece.

2016 Poster Presentation

L. Zouridi, E. Aperathitis, E. Gagaoudakis, G. Kiriakidis, V. Binas.

Solution based thermochromic VO₂ particles for energy saving applications. 6th

International Symposium of Transparent Conductive Materials, Platanias – Chania, Crete – Greece.

2016 Poster Presentation

L. Zouridi, E. Aperathitis, E. Gagaoudakis, G. Kiriakidis, V. Binas.

Solution based thermochromic VO₂ particles for energy saving applications. European Materials Research Society, E-MRS, Lille Grand Palais, France, Spring Meeting 2016

2016 Attendance in the 18th Chemistry Postgraduates Conference

Place/time: University of Crete, 26-28 March 2016

2011 Participation and First Prize in the ‘Fotochemica’ Science Photography Contest.

Post: Co-participant of project.

Responsibilities: Co-Responsible for all the phases of projecting, designing and rendering.

Languages

Italian: native speaker;

Greek: native speaker;

English: B2 level; Certificate of Competency in English (ECCE)
Examinations of the University of Michigan;

Other Skills

Laboratory Skills:

Basic Chemistry Laboratory Skills in the fields of: Material Synthesis, Organic, Inorganic, Analytical and Physical Chemistry.

Hydrothermal Synthesis, X-ray Diffraction, Ultraviolet–Visible Spectroscopy, Infrared Spectroscopy, Differential scanning calorimetry, Dynamic Light Scattering, Viscometry, Scanning Electron Microscopy, Semiconductor Parameter Analyser

Data Analysis and Data Plotting Computer Programs:

OriginLab, QtiPlot, Gnuplot (learning)

Other Programs:

Microsoft Office, LibreOffice, Email Services, Adobe Photoshop CS6 (learning), Visual Molecular Dynamics (learning)

General Scientific and Research Interests

Inorganic Materials and Metal Oxides synthesis, Solution-based synthesis, Green chemistry, Soft condensed matter, Layer deposition, Thin films, Novel technologies and techniques, Printing technologies, Nanotechnology, Responsive and Smart materials, Energy Storage and Production Applications, Water Splitting and Photocatalysis, Sensing Applications, Medical Implants Applications, Wearable Applications

Other Interests Fine Arts, Reading, Contemporary Dance, Travelling, Animal Welfare

References

Available upon request.